AERODYNAMIC PARAMETER IDENTIFICATION FOR AN UNMANNED AERIAL VEHICLE

Kreelan Padayachee

A dissertation submitted to the Faculty of Engineering and the Built Environment, School of Mechanical, Industrial and Aeronautical Engineering, University of the Witwatersrand, in fulfilment of the requirements for the degree of Master of Science in Engineering.

Johannesburg, May 2016

DECLARATION

I declare that this dissertation is my own unaided work. It is being submitted to the Degree of Master of Science to the University of the Witwatersrand, Johannesburg. It has not been submitted before for any degree or examination to any other University. The flight test data used in this dissertation was obtained while employed by the Council for Scientific and Industrial Research, Pretoria.

____

Signature
Kreelan Padayachee

______ day of ____________________, 2016

ABSTRACT

The present work describes the practical implementation of systems identification techniques to the development of a linear aerodynamic model for a small low-cost UAV equipped with a basic navigational and inertial measurement systems. The assessment of the applicability of the techniques were based on determining whether adequate aerodynamic models could be developed to aid in the reduction of wind tunnel testing when characterising new UAVs. The identification process consisted of postulating a model structure, flight test manoeuvre design, data reconstruction, aerodynamic parameter estimation, and model validation. The estimators that were used for the post-flight identification were the output error maximum likelihood method and an iterated extended Kalman filter with a global smoother. SIDPAC and FVSysID systems identification toolboxes were utilised and modified where appropriate. The instrumentation system on board the UAV consisted of three-axis accelerometers and gyroscopes, a three-axis vector magnetometer and GPS tracking while data was logged at 25 Hz. The angle of attack and angle of sideslip were not measured directly and were estimated using tailored data reconstruction methods. Adequate time domain lateral model correlation with flight data was achieved for the cruise flight condition. Adequacy was assessed against Theil's inequality coefficients and Theil's covariance. It was found that the simplified estimation algorithms based on the linearized equations of motion yielded the most promising model matches. Due to the high correlation between the pitch damping derivatives, the longitudinal analysis did not yield valid model parameter estimates. Even though the accuracy of the resulting models was below initial expectations, the detailed data compatibility analysis provided valuable insight into estimator limitations, instrumentation requirements and test procedures for systems identification on low-cost UAVs.

PREFACE

The current study of systems identification applied to aerodynamic model development on a low-cost unmanned aerial vehicle (UAV) was undertaken with the support of the Council for Scientific and Industrial Research (CSIR) and the University of the Witwatersrand.

The study was intended to aid in the understanding and application of system identification techniques to reduce the time taken to characterise a small, low cost UAV. My hope is that the current study will provide a strong grounding in the practical advantages and disadvantages of parameter identification techniques for future modelling of UAV within the CSIR and greater South African aeronautical industry.

ACKNOWLEDGEMENTS

I would like to express my sincere appreciation to my colleagues at the CSIR that provided the necessary technical guidance and motivation throughout this study. I am also thankful to my research supervisors, Prof Craig Law and Dr Benjamin Broughton, for their guidance and approachability with regards to technical discussions on flight dynamics and system identification. A special thank you to my wife and family for providing unwavering support, constant motivation, and encouragement throughout this study.

TABLE OF CONTENTS

LIST OF FIGURES

LIST OF TABLES

NOMENCLATURE

Abbreviations

CFD	Computational Fluid Dynamics
UAV	Unmanned Aerial Vehicle
IMU	Inertial Measurement Unit
GPS	Global Positioning System
AGL	Above Ground Level
CSIR	Council for Scientific and Industrial Research
NASA	National Aeronautics and Space Administration
R/C	Radio controlled
IEKF	Iterated Extended Kalman Filter
AMSL	Above mean sea level
QNH	Barometric pressure adjusted to sea level

Symbols	**Description**	**Units**
Dynamics		
m	The mass of the aircraft including all systems	$[kg]$
V, ω	The translational and rotational velocity vectors	$[{}^{m}/_{s}], \left[{}^{rad}/_{s}\right]$
I	The inertia tensor	
F, M	Applied force and moment vectors	$[N], [N.m]$
u	Control vector	
ξ	Euler angle vector	$[rad]$
θ	Vector of aerodynamic parameters	
A, B, C, D	The linearized system state, control and observations matrices	
x	The system kinematic state vector	
y	The observation vector	
z	The measurement vector for the dynamic system	
ν	The Gaussian measurement noise vector	
S_w	Wing area	$[m^2]$
b_w	Wing Span	$[m]$
$\bar{c}$	Mean aerodynamic chord	$[m]$
ω_n	Natural frequency	$\left[{}^{rad}/_{s}\right]$

a	Accelerations	$[{}^{m}/_{s^2}]$
C_D, C_L, C_Y	Non-dimensional forces (drag, lift and side force)	
C_l, C_n, C_m	Non-dimensional moments (roll, yaw, and pitch moments)	
λ	Rigid body dynamics: characteristic roots	
u, v, w	The body-axis linear velocities	$[{}^{m}/_{s}]$
ϕ, θ, ψ	Euler angles (roll, pitch, and yaw)	$[rad]$
p, q, r	Angular velocities (roll, pitch, and yaw)	$[{}^{rad}/_{s}]$
V, α, β	Air relative states (Velocity, angle of attack, and sideslip)	$[{}^{m}/_{s}], [rad]$
$\delta_e, \delta_a, \delta_r$	Control deflections (Elevator, Aileron, Rudder)	$[rad]$
δ_T	Change in non-dimensionalized thrust	
x, y, z	The aircraft locations in the three orthogonal Earth axes directions (N,E,D)	$[m]$
W_x, W_y, W_z	The constant wind vector components in the Earth axes	$[{}^{m}/_{s}]$
$magX, magY, magZ$	The constant magnetic field vector components in the body fixed axes	$[tesla]$
ΔV_{pitot}	The pitot tube bias	$[{}^{m}/_{s}]$
$\overline{q_0}$	Dynamic pressure at the start of a manoeuvre	$[Pa]$
F_X, F_Y, F_Z	Applied forces in the X,Y,Z body axis directions	$[N]$
L_X, M_Y, N_Z	Applied moments about the X,Y,Z body axis directions	$[N.m]$

Regression Analysis

y	The identified system vector (modelled output)
x	The regressor vector
ξ	Linear or non-linear function of the regressors
θ	Vector of unknown parameters to be estimated
X	The matrix representation of the regressors
z	The model representing the measured output of the system

v	Uncorrelated measurement noise vector
J	The quadratic cost function
σ^2	Statistical variance
R^2	Coefficient of determination
$\hat{R}_{vv}(k)$	The autocorrelation function as a function of k, the discrete time-shift index
N	The data sample length
i	Discrete time index (i.e. sample point reference)
v	Residual vector
F_0	F-ratio: Statistical parameter
SS_R	Regression sum of squares for the entire model
$PRESS$	Prediction sum of squares

Maximum Likelihood

L	Likelihood function
z	The kinematic response at each time step
N	The dataset size
θ	The vector of estimated parameters
R	Measurement-error covariance matrix
k	The sample index
y	The dynamic model output
n_y	The number of model responses
t_k	The time at sample index k
$\left(\frac{\partial J^2(\theta)}{\partial\theta\partial\theta^T}\right), M$	Information matrix
$\frac{\partial J(\theta)}{\partial\theta}, g$	Gradient matrix

Data Compatibility

y	The measured variable or instrument output
K_y	Instrument scale factor
τ	The instrument measurement time lag
Δy	The instrument bias error
$\tilde{x}_{a}, \hat{x}_a$	Predicted and corrected augmented state vector

$\tilde{P}, \hat{P}$	Predicted and corrected augmented-state prediction-error covariance matrices
$\bar{u}_m$	The mean control input vector
K	Kalman gain matrix
A, B, C	Linearized system, control matrix, and observation matrices
Q	The process noise covariance matrix;
k	The discretised time index ranging from k = 1,2,3,…N
R	The measurement-error covariance matrix
Φ	The state transition matrix or the Wiener filter function
Ψ	The state transition matrix integral
C_s	The signal model coefficient for the Wiener filter
C_n	The noise model coefficient for the Wiener filter
M_k	Grammian matrix
Δ	Bias parameter

Validation

σ	Goodness of fit parameter or model standard deviation
U_i	Theil's inequality coefficient
U_i^M	Theil's bias coefficient
U_i^S	Theil's variance coefficient
U_i^C	Theil's covariance coefficient
ρ	The correlation coefficient

Subscripts

G	Contribution due to Gravity
T	Contribution due to Thrust
A	Contribution due to Aerodynamics
0	Initial Values
ML	Maximum Likelihood
m	Measured variable

x	Component in the X body-axis
y	Component in the Y body-axis
z	Component in the Z body-axis
rel	Relative components
$wind$	Wind component

1 INTRODUCTION

1.1 BACKGROUND

Flight vehicle development has always been associated with a continuous requirement to understand and mathematically model the dynamic behaviour of aircraft. Such models are used in stability and control analyses, control law development, aerodynamic optimisations, to safely plan the expansion of the flight envelope, or for the development of flight simulators of varying fidelity. Attaining an adequate mathematical model allows aircraft design teams to make informed design decisions in the effort to extract maximum efficiency and develop a high level of predictability from the aircraft and sub-systems.

As described by Klein and Morelli (2006), comprehensive flight dynamic modelling would include the consideration of the elasticity of the aircraft, the varying mass density of components including the structure, and position changes of various components (e.g. Fuel slosh or structural deformation). The concept of model adequacy, however, must be taken into account. In a majority of modelling cases, simplifications are made and the aircraft is considered as a rigid body within a uniform gravitational field. If the model is required to represent atmospheric flight in a localised airspace, the curvature of the earth can be considered negligible, simplifying the analysis considerably. By using these assumptions and applying Newton's second law of motion to the translation and rotation (about the centre of mass) of the rigid aircraft Eq. 1-1 and 1-2 are derived.

$$m\dot{\boldsymbol{V}} + \boldsymbol{\omega} \times m\boldsymbol{V} = \boldsymbol{F_G}(\boldsymbol{\theta}, \boldsymbol{\phi}) + \boldsymbol{F_T} + \boldsymbol{F_A}(\boldsymbol{V}, \boldsymbol{\omega}, \boldsymbol{u}, \boldsymbol{\Lambda}) \qquad \text{1-1}$$

$$I\dot{\boldsymbol{\omega}} + \boldsymbol{\omega} \times I\boldsymbol{\omega} = \boldsymbol{M_T} + \boldsymbol{M_A}(\boldsymbol{V}, \boldsymbol{\omega}, \boldsymbol{u}, \boldsymbol{\Lambda}) \qquad \text{1-2}$$

Where: m is the mass of the aircraft including all systems;

$\boldsymbol{V}$ and $\boldsymbol{\omega}$ are the translational and rotational velocity vectors;

I is the inertia tensor about the centre of gravity;

$\boldsymbol{F}$ and $\boldsymbol{M}$ are the applied forces and moments distinguished by the subscripts G, T and A respectively representative of gravity, thrust and aerodynamic influences;

$\boldsymbol{u}$ is the control vector;

$\boldsymbol{\theta}$ and $\boldsymbol{\phi}$ are the pitch and roll attitude angles relative to a fixed earth coordinate system;

and $\boldsymbol{\Lambda}$ is the vector of aerodynamic parameters unique to the given aircraft model.

In Eq. 1-1 and Eq. 1-2, the applied forces and moments are due to the gravitational force, the thrust force, and the aerodynamic forces acting on the aircraft. By utilising a flat-earth assumption in conjunction with uniform gravitational acceleration, the gravitational vector components are direct functions of the aircraft attitude at a given point in time. The thrust force is modelled on data from grounded experimental techniques. The remaining external forces are due to aerodynamic influences that can be obtained via techniques ranging from theoretical analyses to experimental analyses using flight test data. A significant effort goes into modelling the aerodynamics when a flight dynamic model is required.

Aerodynamic model structures vary in complexity ranging from simple one degree of freedom transfer functions, to linear models parameterized by the current aircraft states (Etkin, 1959; Cook, 2007; Roskam, 1979), to non-linear b-spline representations of the aerodynamic influences (Batterson, 1981), to complex time-dependent non-linear indicial functions (Tobak, 1984). With the variety of model structure techniques available, the correct choice of structure is paramount to achieving an effective aerodynamic model. The most common model structure used in a vast majority of reference publications such as Etkin (1959), Cook (2007), and Roskam (1979), is based on a multi-variable Taylor series expansion about a reference condition, truncated at the first order terms. The models are independent of time and are parameterized by the instantaneous aircraft states (i.e. angle of attack, angle of sideslip, airspeed, and rotational speeds about the three orthogonal body axes) and control deflections. The model coefficients are referred to as stability and control derivatives. This type of linear model structure is suitable for dynamic modelling where only small excursions from the reference conditions are expected (Klein and Morelli, 2006). It is common practice to non-dimensionalize the forces and moments to remove the model dependencies on dynamic pressure and geometric properties. Due to its simplicity and adequacy, the linear parametric structures are used extensively in aerodynamic modelling, especially in the early design and evaluation stages of an aircraft development cycle.

Numerous methods exist for estimating the aerodynamic model coefficients for a prescribed structure. Listed in the order of increasing fidelity these include empirical methods, low order analytical methods, higher order computational methods and experimental methods. Empirical methods such as DATCOM use historic data based on aircraft of similar geometry. Lower order analytic methods include vortex lattice codes such as AVL and Tornado or panel methods such as CMARC. The advantage of the lower order methods is the low computational overhead allowing large test matrices to be analysed within short time periods. The disadvantage is the low achievable fidelity of the models and the flight regime limitations (i.e. these model estimation methods are limited to linear aerodynamic models). The higher fidelity methods include computational fluid dynamics (CFD) solvers that are based on the Navier-Stokes equations and experimental methods such as wind tunnel testing and flight testing. The advantage of these latter methods is the rich data content, containing linear or non-linear aerodynamic information beyond the capabilities of the lower-order methods. The high fidelity methods are, however, characterised by higher facility overheads. The choice of method is based on the requirements of the aerodynamic model and which stage of the design cycle is being implemented.

When experimental data sets are used in the development of physically realistic model structures and the estimation of the respective model parameters, the process is defined as systems identification. As mentioned, this is a high fidelity modelling technique. The broad definition of systems identification is given by Babister (1961) and Klein and Morelli (2006), as being one of the three types of inverse problems commonly encountered:

- Given the output and the system, find the input. The type of problem is common in control theory where control deflections or control system characterisation is required.
- Given the input and the system, determine the output. An example of this problem is the simulation environment where the dynamic responses of the system need to be replicated.
- And lastly, given the output and input, find the system characteristics. The solution to this problem requires the modelling of the system when measured dynamic output data and measured inputs are available. The inputs can range from control inputs to environmental inputs.

Various types of aircraft systems identification are possible based on input-output experimental flight data. These can be divided into two categories allowing for four different combinations. The categories are offline or online analyses, and the physically realistic models or 'black-box' models (Jategaonkar, 2006). Each of these categories and combinations has particular merits based on the modelling requirements.

Category One:

- Offline analyses are suitable when complete flight datasets defined by a prescribed period are available. These analyses have the potential to be as complex as required because all modelling data is available for a given period and computation time is less of a priority than for real-time analyses. This method is ideal for characterising time invariant systems as it averages the model across a given dataset.
- Online analyses make use of recursive algorithms that utilise data as it becomes available. Because of the limited information, the resulting parameters are of lower accuracy than those attained from offline analyses. The advantage of recursive analyses is the ability to model time-varying systems where model parameters change throughout the dataset. This advantage is useful when adaptive system characterisation is required, for example, in cases where in-flight damage occurs.

Category Two:

Whereas the first category dealt with how the models are to be generated, the second category deals with the type of model required.

- Physically realistic models account for actual phenomena based on the physics describing the system. The terms within the model represent, to an extent, the actual interactions of the system with the environment. This type of model is utilised when detailed insight into the system behaviour is required as in the case of aerodynamic characterisations. An example of this type of modelling is the use of stability and control derivatives, where each derivative has a physical interaction linked to its existence.
- 'Black-box' modelling disregards any meaningful physical interactions, allowing for a simplified model construction tailored to the test conditions. The advantage of this type of modelling is that complex dynamics can readily be

modelled by simplified model functions. An example of this type of modelling includes the use of low order transfer functions.

This dissertation deals with the application of commonly used offline system identification techniques and algorithms utilised through unique combinations to achieve an acceptable, physically realistic, parametric aerodynamic model. An emphasis was placed on the use of flight testing as the main experimental method where static wind tunnel test data was used as supplementation when required. All further references to systems identification will refer to offline analyses of flight data and the development of physically realistic aerodynamic models.

When characterising aircraft, the offline system identification algorithm consists of a few mutually dependent analysis subgroups. These are the design of the experiment; data compatibility checks; model structure determination; parameter estimation; and, finally, model validation (Klein, 1989; Iliff, 1989; and Maine and Iliff, 1985, 1986).

Regarding the objectives of system identification, the core module of the process is the parameter estimation technique. The trends followed within the systems identification fraternity favour the use of regression estimation methods and various adaptations of the offline maximum likelihood methods (i.e. Equation Error, Output Error, and Filter Error methods) for the parameter identification. Other significant and widely used methods are based on the least squares modelling techniques (Morelli and Klein, 2005). Due to the direct dependency of system identification to the input and output data, the quality of the data is an attribute that should not be ignored. This makes the design of the experiment and data compatibility modules significant. The design of experiment deals with the process of achieving information-rich data where the level of information is determined by a combination of the structure of the dynamic system and the parameter identification method used. Well-designed experiments are used to maximise the efficacy of the parameter identification. Data compatibility, on the other hand, has an indirect impact on the parameter estimation results. This module deals with extracting a dynamically consistent dataset from instrument measurements of the system dynamics, which includes systematic and random errors, ensuring the creation of realistic model structures. The predictive capability of the resulting model is also increased because the model is not required to implicitly describe the instrumentation errors, thus characterising the actual system dynamics more accurately. Data compatibility is dominated by the use of Kalman filter variations and recursive maximum likelihood procedures (Mulder et al., 1999). The interdependency of the various modules of the system identification algorithm is clear and should be exploited during the estimation process to maximise the algorithm efficacy.

The overall system identification approach has been extensively researched between 1960 and 1980 during which a mature theory base for the estimation procedures was developed (Morelli and Klein, 2005). Significant reference publications by Maine and Iliff (1985) and Iliff (1987) provide detailed explanations of the statistical nature of system identification techniques with a strong emphasis on the mathematical derivations. Maine and Iliff (1985, 1986) also provide a theoretical background to maximum likelihood estimators and state estimation techniques for both stochastic and deterministic systems (i.e. the output error method) of which the latter concentrates on deterministic systems. Mulder et al. (1994) emphasise the theory and application of maximum likelihood methods to nonlinear systems.

Other substantial references more recently published by Jategaonkar (2006) and Klein and Morelli (2006) provide a comprehensive presentation of the system identification analysis modules as well as the commonly encountered problems experienced within each module domain and includes proposed solutions. These particular publications consolidate the system identification knowledge-base and provide the flight data analyst with a sufficient theoretical grounding as well as practical techniques to successfully apply the common system identification algorithms. They provide practical examples of system identification based on real flight test data of manned aircraft. Klein (1989) provides a similar, although less comprehensive, presentation of system identification theory. Unmanned aerial vehicles (UAVs) are not dealt with in any of the above-mentioned publications. The prior two publications do, however, make reference to and provide significant examples in which autonomous control inputs were utilised.

According to Wang and Iliff (2004), the practical advancements in system identification applied to aircraft can be attributed largely to a group of institutions consisting of NASA Dryden, NASA Langley, and DLR in Germany, Delft University of Technology, and the National Aerospace Laboratory. Three significant publications by Wang and Iliff (2004), Morelli and Klein (2005) and Jategaonkar et al. (2004), present a comprehensive account of the historical advancements of system identification as used and developed by NASA Dryden, NASA Langley and DLR respectively. Wang and Iliff (2004) provide a partial list of the various aircraft that system identification was applied to, with a more detailed overview of a few substantial projects including the X-29A, F/A-18, SR-71 and the space shuttles. These examples encompass linear, non-linear, steady, unsteady, and high-speed aerodynamic modelling techniques and are good advocates for system identification used for flight dynamic modelling of a variety of aircraft. Morelli and Klein (2005) provide a similar retrospective analysis of the successful application of system identification at NASA Langley with an extensive bibliography covering the major modules of the system identification algorithm. The authors placed an emphasis on the advancements of real-time estimation, wind tunnel data modelling (i.e. both steady and unsteady), and low order equivalent system (LOES) modelling. Much of the modelling in these publications involved the use of maximum likelihood estimation techniques.

An important characteristic of the system identification applied by Wang and Iliff (2004), Morelli and Klein (2005) and Jategaonkar et al. (2004) is that the aircraft were instrumented to meet the requirements of specific systems identification objectives and high accuracy measurements of all relevant properties were recorded by the authors. In these documented cases a comprehensive set of sensors based on the systems identification requirements were available and included a set of angular rate gyroscopes, accelerometers, air data sensors, control surface deflection sensors and GPS. The unknown aerodynamic parameters were estimated using measurements from these high accuracy instrumentation sets and the system identification algorithms described above. Each system identification procedure was based upon the mature theory-base but used particular modifications tailored to the specific requirements of the postulated model. The modifications and simplifications included accounting for measurement and process noise, data partitioning and unique flight testing techniques. Morelli and Klein (2005) and Wang and Iliff (2004) show that a systematic approach to parameter estimation is available when carried out in conjunction with a fully instrumented aircraft.

More recently, systems identification has been applied to a low-cost UAV by Dorobantu et al. (2013). The authors demonstrated a practical approach to model the dynamics of a low-cost UAV with a limited set of inertial sensors. The analysis was carried out in the frequency domain and produced good models correlating well with the flight test data. The disadvantage of this approach is that longer, automated, less efficient manoeuvres (e.g. frequency sweeps) are required. Frequency domain parameter identification has advantages when low-quality measurements are available (e.g. sensor biases are removed). However, the expansion to more unsteady, non-linear, coupled dynamic models is limited. A time domain approach alleviates these non-linear limitations and allows for global aerodynamic model expansion. The practicality of identifying aerodynamic models, of a low-cost fixed-wing UAV, using a time domain approach has not been completely addressed in research to date.

1.2 MOTIVATION AND RESEARCH PROBLEM

As mentioned in Sec. 1.1, a theory base and a variety of model structures and estimation techniques are available for use when creating an aircraft aerodynamic model. The applications of these techniques have documented the use of these techniques as used in highly instrumented, manned aircraft. With the advancements in automation technologies and theories, and the continuously increasing use of unmanned aerial vehicles by operators from small, local research institutions to multinational aerospace agencies, the requirements for cost-effective, efficient systems characterisation methods has become an important research area. Due to the level of automation, reduced flight test costs, and the reduced risk through remote piloting, systems identification provides the ideal post-design characterisation tool. It allows for a reduction of the extensive test time involved in comprehensive wind tunnel testing programmes by reducing the complexity of the test matrix while still providing the potential to fulfil the requirements of higher fidelity aerodynamic characterisations. Although systems identification has many advantages when utilised on small to medium unmanned aircraft characterisations, many limitations including spatial (i.e. airframe size), environmental and legal constraints (i.e. airspace restrictions) must be considered. Therefore, the application of system identification algorithms within the unmanned aircraft systems domain yields many, as yet unanswered, questions and challenges, providing a multitude of research opportunities based on the type of system being analysed.

In recent years, the Council for Scientific and Industrial Research (CSIR) has developed a range of small to medium-sized unmanned aerial vehicles (UAVs) as technology demonstrators and research vehicles varying from conventional configurations to blended wing body designs. The cost of accurately characterising each airframe through extensive wind tunnel testing as well as the lack of critical equipment makes detailed characterisation impractical. Due to the relatively low cost involved in the flight testing of UAVs, system identification is an attractive supplementation to preliminary aerodynamic models or basic wind tunnel data. This class of aircraft is commonly used for short-range, low-endurance reconnaissance missions or for simple aeronautical research tasks and do not have high-quality instrumentation. The instrumentation systems on-board the aircraft only provide basic navigational information with a fair degree of uncharacterised noise. This leads to unique challenges within the data compatibility module of the system identification algorithm. Preliminary wind tunnel test matrices for UAV development undertaken at the CSIR generally includes only static, power off tests. Furthermore, due to civil aviation regulatory restrictions imposed on unmanned aerial vehicles the available flight test airspace is limited. This leads to the exclusion of many of the commonly used frequency-based system identification flight test techniques such as frequency sweeps. The feasibility of the application of time domain system identification to estimate the open loop aerodynamics of such a UAV was thus required. If feasible, the algorithm and data conditioning techniques involved can be applied to all UAVs similarly sized and instrumented. The research also determined what improvements to the sensor suite, if any, were required.

This dissertation addresses the issues involved in characterising a small to medium sized, propeller driven UAV (Unmanned Aerial Vehicle) using system identification techniques.

1.3 RESEARCH OBJECTIVES

The main research objective was to determine the viability of using a known system identification algorithm on the aerodynamic modelling of a UAV equipped with basic navigational instrumentation. The specified aerodynamic model was that based on stability and control derivatives for a single flight condition.

During the implementation of the algorithm, solutions to various sub-objectives were required that resulted in the development of unique combinations of solution processes to maximise the potential success of the system identification. These sub-objectives are described below in the order in which they were achieved:

1. To develop and verify the systems identification algorithms and the parameter estimation techniques via simulated data.
2. To develop an initial aerodynamic model based on available static, power-off wind tunnel data as well as previously generated aerodynamic stability and control derivatives determined via lower order analyses such as AVL and theoretical methods as found in Roskam (1979).
3. To implement the tailored system identification algorithm on a low-cost UAV. The systems identification algorithm includes the development of a flight test plan, the application of data compatibility procedures, parameter estimation, and model validation.

1.4 APPROACH

The approach taken was governed by the sub-objectives specified in Sec. 1.3, where the system identification algorithm development is followed by an initial aircraft model development and thereafter the actual system identification.

The use of simulated data in the algorithm development provided a controlled test environment for the development of data compatibility solution methods where different levels of noise could be applied to the datasets (i.e. Kalman filtering techniques and optimal filtering techniques); for the analysis of various flight test manoeuvre designs; and to validate the parameter estimation algorithms that were used.

The initial model development that followed involved combining the available data and deriving the best aerodynamic model weighted by the relative accuracies of the various aerodynamic analyses. The purpose of developing an initial model was to create a model to be used in the system identification algorithm and to aid in the model structure development. The model structure was based on traditional stability and control parameters (refer to Sec. 1.1) since only one flight condition was analysed.

The system identification that followed was based on the offline system identification algorithm. By applying the respective steps, it was possible to draw conclusions on the efficacy of the processes involved with application to the UAV. The flight test planning and implementation provided information on the restrictions, capabilities, and requirements to generate data of high information content as well as establishing the areas that differ from traditional flight testing of sophisticated systems. In the same light, the data compatibility process provided insight into the shortcomings of the traditional solution procedures and the modifications required when applied to the data generated from the instrumentation system on board the UAV. Similar objectives were met by the parameter estimation process. The adequacy of the traditional methods regarding the accuracy of results and the robustness of the processes was determined.

Through application of this approach on a UAV, the various shortcomings of the different generic modules as used on manned aircraft with high-quality data systems were evident. Additionally, the unique combinations of known techniques that were required were developed in a controlled simulated environment, maximising the potential for the algorithm while determining the minimum requirements for the aircraft systems for a successful characterisation to be achieved through systems identification.

1.5 LIMITATIONS

The scope of this dissertation was limited to an open loop aerodynamic analysis of a small to medium sized, navigationally equipped, UAV for a typical cruise flight condition via data generated from a single flight test.

The particular aircraft that was analysed, utilised an instrumentation set including an IMU (Inertial Measurement Unit) consisting of a three-axis angular rate gyroscope; linear accelerometers and magnetometers aligned with the three principle aircraft body axes; a calibrated pitot tube; a static pressure port; and a GPS (Global Positioning System). Telemetry of these measurements was possible up to 25Hz and included an anti-aliasing filter. The reader should be drawn to the fact that no sensors measuring control surface deflection, airflow angles, engine parameters, or on-board temperature were present.

Due to civil aviation airspace regulations, flight testing was limited to a flight ceiling of 200m AGL (Above Ground Level) and a planar spatial limitation of a 1000m by 500m rectangular circuit. Static, power-off, wind tunnel test data and lower fidelity stability and control derivatives were available for the cruise flight condition allowing for the construction of an adequate initial aerodynamic model. A detailed power model was not available and was beyond the scope of this dissertation.

1.6 DISSERTATION OVERVIEW

This dissertation describes the theory, method, and results of systems identification applied to the aerodynamic model development of a small unmanned aerial vehicle. Chapter one introduced the basic principles and described the scope and limitations of the current study. Particular objectives were defined in Sec. 1.3 followed by the research approach. Chapter two will provide a rigorous presentation of the available theory and current state of the art of systems identification when applied to aerodynamic parameter identification. The advantages and disadvantages of each technique will be discussed. Chapter three details the structured investigative method. Chapter three is divided into subsections appropriate to the different steps in systems identification as applied to low-cost unmanned aerial vehicles i.e. experiment design, data compatibility, parameter identification, detailed analysis of the method and results. Chapter four presents the results of the system identification process and provides a critical discussion of characteristics of the results in relation to the objectives of the study. The conclusions of the study are then presented in chapter five. Results and discussions related to the current study but not directly influencing the conclusions (e.g. validation data) are presented in the appendices.

2 LITERATURE REVIEW

2.1 INTRODUCTION

To determine the viability of the system identification algorithm on the flight dynamics characterisation of a poorly instrumented UAV, an analysis of work done by previous authors was required to build on the theoretical and practical base that already existed.

Table 2-1 Commonly Used Offline System Identification Methods

Module:	Methods:
Parameter Identification	• Regression Analyses • Maximum Likelihood Estimators ○ Equation Error ○ Output Error ○ Filter Error
Model Structure Determination	• Stepwise Regression Analyses • B-Spline Representations • Table Lookups
Data Compatibility	• Kalman Filtering ○ Kalman Filter ○ Extended Kalman Filter ○ Iterated Extended Kalman Filter • Maximum Likelihood
Manoeuvre Design	• Standard Performance Manoeuvres • Frequency based ○ Frequency Sweeps ○ Optimised Harmonics • Time based ○ Step, Ramp, Doublets ○ Optimised Multi-Steps

As noted in Section 1.1, there are well-established methodologies within the aircraft system identification field applied to each module of the process (Maine and Iliff, 1985; Maine and Iliff, 1986; Iliff, 1987; Jategaonkar, 2006; and Klein and Morelli, 2006). The modules and associated solutions are provided in Table 2-1. Various developments of these solution processes have led to more efficient estimators and reliable systems identification. At the same time, these developments have provided insight into the shortcomings of the methods when applied to practical problems. Such application challenges are numerous and an extensive amount of literature is available. An attempt to present all the significant cases is beyond the scope of this study.

This chapter introduces the reader to the significant sources of theoretical information within the field of rigid-body, fixed-wing aircraft system identification. Detailed descriptions of the various methods as well as the cautionary factors to note during implementation are provided. The chapter also provides a brief overview of the applications of the algorithm and unique techniques used on manned and unmanned systems. A concluding subsection summarising the critical points will be provided at the end of the chapter. The rationale behind which algorithms were utilised in the accomplishment of the objectives will be described.

2.2 PARAMETER ESTIMATION AND MODEL STRUCTURES

As mentioned in Section 1.1 and presented in Table 2-1, the parameter estimation of the unknown model coefficients forms the core of the offline systems identification algorithm. The two most widely used statistical methods to achieve the estimates are the maximum likelihood methods and least squares regression methods (Cook, 2007).

2.2.1 Regression Analysis

Regression methods are explicit curve fitting algorithms. The system model used for identification is presented in Eq. 2-1, simplified to Eq. 2-2. The measurement model inclusive of added noise is given by Eq. 2-3.

$$y = \theta_0 + \sum_{j=1}^{n} \theta_j \xi_j (x_1, x_2, \dots, x_s) \qquad 2\text{-}1$$

This can be simplified to matrix form:

$$y = X\theta \tag{2-2}$$

By adding uncorrelated measurement noise, Eq. 2-2 leads to:

$$z = X\theta + \nu \tag{2-3}$$

Where: y is the identified system;

x are the known regressors;

ξ is the linear or non-linear function of the regressors;

θ is the vector of unknown parameters to be estimated;

X is the matrix representation of the model regressors;

z is the model representing the measured output of the system;

and ν is the added uncorrelated measurement noise vector.

By analysis of these models, regression modelling is based on models that are linear with regard to the unknown parameters, where each regressor is assumed to be free of noise. The model parameters are estimated by minimising a cost function, which, for the least squares fit is Eq. 2-4. This cost function is equal to the square of the error between the measured variable and the model output. The optimal parameter vector is given by Eq. 2-5.

$$J(\theta) = \frac{1}{2}(z - X\theta)^T(z - X\theta) \tag{2-4}$$

Where: J is the quadratic cost function.

$$\theta = (X^T X)^{-1} X^T z \tag{2-5}$$

For aerodynamic modelling, the measurement (i.e. the dependent variable within the resulting model) is the time history of the aerodynamic forces while the model inputs (i.e. independent variables or regressors) are the aircraft states and control deflections. When the model is linear with respect to the independent variables, the cost function is quadratic, yielding a unique solution to the minimization for a given dataset. The advantage of the regression technique is the computational efficiency it provides. When the model is non-linear with respect to the regressors the solution process is more complex and requires an iterative algorithm such as Newton-Raphson.

Regarding the quality of the parameter estimation results, two significant statistical properties are used. These are the covariance of the estimates and the coefficient of determination of the resulting model. With the assumption of the measurement error being of zero mean and constant uncorrelated variance, the covariance of the estimated parameters are given by Eq. 2-6.

$$Cov(\theta) = \sigma^2 (X^T X)^{-1} \qquad 2\text{-}6$$

Where: σ^2 is the model output statistical variance.

Due to the lack of repeated measurements at the same conditions, Klein and Morelli (2006) suggest an estimated value for the model output variance equal to the residual variance of the model, s^2, given by Eq. 2-7.

$$\sigma^2 \cong \frac{v^T v}{N - n_p} \equiv s^2 \qquad 2\text{-}7$$

The second criteria, the coefficient of determination, ranges from 0 to 1, where 1 represents an ideal model fit to the measured data is given by Eq. 2-8.

$$R^2 = \frac{\theta^T X^T z - N\bar{z}^2}{z^T z - N\bar{z}^2} \qquad 2\text{-}8$$

Where: $\bar{z}$ is the mean of the measured variable.

Cautionary factors to acknowledge when using the least squares estimator method, as noted by Jategaonkar (2006), are based on the following assumptions:

- The pool of regressors (i.e. independent variables) is selected before estimation.
- The regressors are measured without noise.
- The model varies linearly with respect to the regressors.

- The output measurement (i.e. the dependent variable) noise has a constant variance, is uncorrelated and has a zero mean value.

These are important assumptions to take note of because the regressors, in practical cases, do contain a degree of system noise that consists of sensor measurement noise as well as biases or unknown scaling factors (Jategaonkar, 2006) which can significantly deteriorate the quality of a model based on this assumption. As detailed in Jategaonkar (2006), biases and scale factors within the measured regressors lead to biassed estimation of the unknown model parameters. Jategaonkar (2006) concludes, via a mathematical proof, that if systematic errors are zero, then the estimates will be unbiased provided the measurement noise of each regressor is independent. The parameter variances, however, will still be dependent on the measurement noise, whether or not the systematic errors are zero.

One of the methods of determining the adequacy of the regression models and whether the above assumptions hold is the analysis of the model fit residuals (Klein and Morelli, 2006). Various residual analysis methods are commonly suggested. The simplest of which is to plot the residuals against time and visually determine whether there are any deterministic components. If the assumption of the residuals being based on white noise with a zero mean is true, then the residuals would be distributed randomly about zero throughout the time segment. Another method of validating the assumptions is to calculate the autocorrelation function (Klein and Morelli, 2006), Eq. 2-9. If the residuals are truly uncorrelated then a plot of the elements of the autocorrelation matrix would resemble an impulse function. Because a coloured residual vector (i.e. correlated residual vector) significantly effects the parameter estimation variance, a correction factor is usually applied to the calculated parameter variances (Jategaonkar, 2006 and Klein and Morelli, 2006).

$$\hat{R}_{vv}(k) = \frac{1}{N-k}\sum_{i=1}^{N-k} v(i)v(i+k) \qquad 2\text{-}9$$

Where: $\hat{R}_{vv}(k)$ is the autocorrelation function as a function of k, the discrete time shift index;

N is the data sample length;

i is a discrete time index (i.e. sample point reference);

and v is the residual vector.

The corrected parameter covariances are described by Eq. 2-10.

$$Cov(\theta) \approx (X^T X)^{-1} \left\{ \sum_{i=1}^{N} x^T(i) \sum_{j=1}^{N} \hat{R}_{vv}(i-j)x(j) \right\} (X^T X)^{-1} \tag{2-10}$$

The third method described is to plot the residuals in ascending order against a function of the cumulative probability distribution of a random variable with the ideal Gaussian distribution of zero mean and unit variance. Linearity in the resulting plot is an indication that the assumptions made about the distribution of the residuals (i.e. Gaussian distribution) are likely to be plausible (Klein and Morelli, 2006).

When applying the least squares algorithm, the extent of data (i.e. regressors) collinearity should also be acknowledged (Klein and Morelli, 2006). Data collinearity or regressor collinearity is a source of parameter ambiguity within the least squares estimation procedure. Particular attention should be placed on this phenomenon when dealing with flight test data because of the inherent correlation between particular aircraft states. These correlations may be caused by the flight control feedback system or simply because of kinematic relationships. This potential collinearity has a direct impact on the accuracy (i.e. increased variance) of the resulting model estimates.

Due to the adverse effects of collinearity, various methods are commonly utilised to either account for or to quantify the significance of this factor. Morelli (1995) describes the use of orthogonal regressors to eliminate collinearity within the estimation process. This method is based on creating new regressors from the unique components of the original regressors. A cautionary property of this technique is that the new orthogonal functions are dependent on the order in which the orthogonal regressors are derived. Therefore, it is important to start the orthogonalisation with the critical regressors. Furthermore, the ability to detect the existence of collinearity is presented by Klein and Morelli (2006). The methods involving the assessment of the regression correlation matrix, the ratios of singular values found by singular value decomposition, and parameter variance decomposition are explained. It was noted that none of the methods can guarantee a complete assessment of the level of collinearity on an individual basis, but are used as indicators of the probable origins of problems in the estimation algorithm.

Advanced applications of the least squares estimation algorithm involve model structure determination and non-linear aerodynamic modelling. Model structure development is commonly based on a stepwise regression routine as depicted by Klein et al. (1981). Regressors are added to the model iteratively, prioritised by the polynomial order (i.e. lower order terms have a higher priority) and the statistical significance of the model performance (Klein and Morelli, 2006). This method still requires an initial pool of regressors but reduces the possibility of including an insignificant regressor in the model. A more detailed explanation of stepwise regression is given in Sec. 2.2.2. Techniques to accommodate non-linear aerodynamic models are also addressed by Batterson (1981), Klein and Batterson (1981), and Klein et al. (1983). They depict methods based on data partitioning, higher order polynomial regressors, or splines. Application of these methods showed a good correlation of the aerodynamic coefficients with models generated via linearization dynamics about many trimmed conditions. Effective application of the model structure development and non-linear modelling was also demonstrated by Klein and Morelli (2006) via a well-conditioned data set.

2.2.2 Model Structure Determination via Stepwise Regression

An advantage of stepwise regression is the simplistic development of aerodynamic model structures based on selecting a combination of regressors that are statistically relevant to a dataset. This differs from the standard regression algorithm discussed in Sec. 2.2.1 where all of the postulated regressors are used for the model structure. Stepwise regression is particularly useful when the model structure is not known as in the case of large amplitude or rapid manoeuvres (Klein, 1989). It is also presented in publications by Klein and Batterson (1981), Klein and Batterson (1983) and Batterson (1981). The method is used to simultaneously generate a plausible model structure and corresponding coefficients that may ultimately be used in the more complex maximum likelihood methods that require an a priori model definition.

As described by Klein and Morelli (2006), stepwise regression is an iterative combination of forward selection and backwards elimination. At every step of the iteration, parameters are introduced into the model based on their unique contribution relative to the parameters already in the model. An initial measure of this contribution is defined by the partial correlation factor calculated via Eq. 2-11.

$$r_{jz} = \frac{\sum_{i=1}^{N}\left[\xi_j(i) - \bar{\xi}_j\right]\left[z(i) - \bar{z}\right]}{\sqrt{S_{jj}S_{zz}}}, j = 1,2,\dots,n$$
$$S_{jj} = \sum_{i=1}^{N}\left[\xi_j(i) - \bar{\xi}_j\right]^2 \; and \; S_{zz} = \sum_{i=1}^{N}\left[z(i) - \bar{z}\right]^2 \qquad 2\text{-}11$$

Where: ξ_j and $\bar{\xi}_j$ are the jth regressor vector and the corresponding vector mean respectively;

and z and $\bar{z}$ are the dependent variable vector and the corresponding mean.

The dependent variable is the difference between the current model and the measurement to be modelled and is thus changed with each new regressor inclusion into the model. The parameters constituting the regressor pool is also changed at each iteration via a similar process to the dependent variable. The iterative regressors are representative of the difference between their original values and a representative regression model based on the parameters already included in the dependent variable model. This process, defined as the forward selection, allows for the selection of the regressors to be based on the unique contributions to the final model.

The backwards elimination component is introduced after a regressor is included into the model using the forward selection criterion. This component ensures that the included regressors are still statistically significant after further additions and are judged by the partial F-ratio evaluations. The partial F-ratio is a measure representing the contribution of a particular regressor to the final model fit based on the regression sum of squares. It is calculated via Eq. 2-12, where F_{out} is the backwards elimination threshold.

$$F_0 = \min_j \frac{SS_R(\hat{\theta}_p) - SS_R(\hat{\theta}_{p-j})}{s^2} < F_{out}$$
$$SS_R \equiv \sum_{i=1}^{N}\left[\hat{y}(i) - \bar{z}\right]^2 \qquad 2\text{-}12$$

Where: $SS_R(\hat{\theta}_p)$ is the regression sum of squares for the entire model;

and $SS_R(\hat{\theta}_{p-j})$ is the regression sum of squares of the model excluding the jth regressor.

If the partial F-ratio is less than the prescribed $F_{out,}$ then the corresponding regressor is eliminated from the model. This elimination must be considered because it is possible for a regressor to become insignificant after additional regressors are included (Klein and Morelli, 2006).

The combination of selection and elimination steps is repeated until no further regressor inclusions or eliminations are deemed necessary. In practice, however, it is suggested that multiple criteria are used in determining the set of regressors to be used. Klein et al. (1981) suggest the coefficient of determination as one of the additional criteria. Since the coefficient increases whenever a parameter is added it is only useful when the amount that it increases by (i.e. percentage change) is taken into account. Further criteria suggested by Klein et al. (1981) include the residual sum of squares and an *F*-statistic measure. The *F*-statistic is the ratio of the regression mean square to the residual mean square. The best-fit model according to this criterion would be chosen at the point when this value is at its maximum. An additional selection criterion is the predicted sum of squares (PRESS). An approximation to the PRESS value is given by Eq. 2-13. This criterion is used as a measure of the prediction capabilities of the model, where the best predictor is when the PRESS function is at a minimum (Klein et al. 1981).

$$PRESS = \sum_{i=1}^{N} \left[\frac{v(i)}{1 - k_{ii}}\right]^2 \qquad \text{2-13}$$

$$k_{ii} = x^T(i)(X^TX)^{-1}x(i)$$

Where: v is the residual vector;

$x(i)$ is a vector of the *i*th samples of the regressor matrix;

and X is the complete matrix of included regressors.

By using a combination of these criteria, it is possible to achieve an accurate model structure for regression analysis. As noted by Klein and Morelli (2006) the individual characteristics of each criterion lead to very rare cases when all are simultaneously satisfied; thus, a decision based on engineering judgement is required.

2.2.3 Maximum Likelihood Analysis

The maximum likelihood estimator, as opposed to the explicit modelling nature of the least squares estimator, is an implicit curve fitting technique for systems based on the Fisher model. The method is characterised by modelling the dynamic system by utilising parameters (linear or non-linear) that maximise the statistical probability of the system kinematics (i.e. the likelihood function) at each time step of the given dataset. Maximum likelihood methods, as opposed to regression methods, do not treat the unknown parameters as statistically random variables, but rather as optimal values that maximise the conditional probability density (referred to as the likelihood function) of the observation vector. Of significant importance is that the maximum likelihood methods are efficient, asymptotically unbiased estimation techniques (N.B.: A detailed proof is given in Jategaonkar (2006)).

A flow diagram of the method is presented in Figure 2-1, describing the basic maximum likelihood algorithm. The iterative solution system is enclosed by the dashed boundary signifying the computational attributes of the solution procedure. These modules will be discussed in brief in this section.

The cost function as seen in Figure 2-1 is known as the likelihood function of the maximum likelihood methods and is given as Eq. 2-14.

$$L(z;\theta,R)=p(z_1|\theta,R)\cdot p(z_2|\theta,R)\cdots p(z_N|\theta,R)=\prod_{k=1}^{N}p(z_k|\theta,R) \qquad 2\text{-}14$$

Where: p is the conditional probability function;

z is the kinematic response at each time step;

N is the data sample size;

θ is the vector of estimated parameters;

R is the measurement error covariance matrix for the measured responses;

and k is the sample index.

By applying an assumption of a Gaussian probability distribution the likelihood function can be expanded to Eq. 2-15.

$$L(z;\theta,R)=(\{2\pi\}^{n_y}|R|)^{-\frac{N}{2}}exp\left(-\frac{1}{2}\sum_{k=1}^{N}\{z(t_k)-y(t_k)\}^{T}R^{-1}\{z(t_k)-y(t_k)\}\right) \qquad 2\text{-}15$$

Where: $y(t_k)$ is the dynamic model output (i.e. $h(\theta)$ or$H\theta$);

n_y is the number of model responses;

and t_k is the time at sample index k.

A common procedural practice employed when using the maximum likelihood method is to minimise the negative natural logarithm of the likelihood function. This simplification is mathematically valid because both methods yield an identical optimised solution (N.B.: Mathematical proof is provided in Jategaonkar (2006)). Using this simplification the revised likelihood function is as Eq. 2-16.

$$-\ln p(z|\theta,R)=\frac{1}{2}\sum_{k=1}^{N}\{z(t_k)-y(t_k)\}^{T}\{z(t_k)-y(t_k)\}+\frac{N}{2}ln\,\{det(R)\}+\frac{Nn_y}{2}ln\,(2\pi)=J(\theta,R) \qquad 2\text{-}16$$

From Eq. 2-16 it is evident that the likelihood function is dependent on the set of parameters,θ that are implicit to $y(t_k)$, as well as the measurement covariance matrix, R. Hence, the minimisation of the likelihood function also involves solving for these independent parameters. According to Klein and Morelli (2006) and Jategaonkar (2006), an iterative solution procedure based on alternating between the two variables yields a more stable solution algorithm when compared to solving for both variables simultaneously. This approach to minimisation of the likelihood function is termed the relaxation technique.

In many instances, it may be assumed that the external noise (i.e. process noise such as turbulence; refer to Figure 2-1) may be negligible. This may be the case when flight testing is done in calm, predictable environmental conditions. The application of this assumption in conjunction with the maximum likelihood algorithm is known as the output error method. In such a case the system is considered deterministic and the algorithm only considers measurement noise as being significant (Jategaonkar, 2006). Using a linearized state space model (i.e. the mathematical model depicted in Figure 2-1), the discrete system output model is given by Eq. 2-19, where the continuous kinematic and observation relationships are given in Eq. 2-17 and Eq. 2-18. For non-linear dynamic models, the state space model may be replaced by the deterministic set of non-linear relationships provided in Appendix A. The deterministic kinematic relationships do not significantly affect the generality of the description of the output error algorithm and therefore, the simpler state space model will be utilised in this section.

$$\dot{x}(t) = Ax(t) + Bu(t) \tag{2-17}$$

$$y(t) = Cx(t) + Du(t) \tag{2-18}$$

$$z(t_k) = y(t_k) + v(t_k) \tag{2-19}$$

Where: A, B, C and D are the system state, control and observations matrices;

x is the system kinematic state vector;

y is the observation vector;

u is the control vector;

z is the measurement model for the system;

and v is the assumed Gaussian measurement noise.

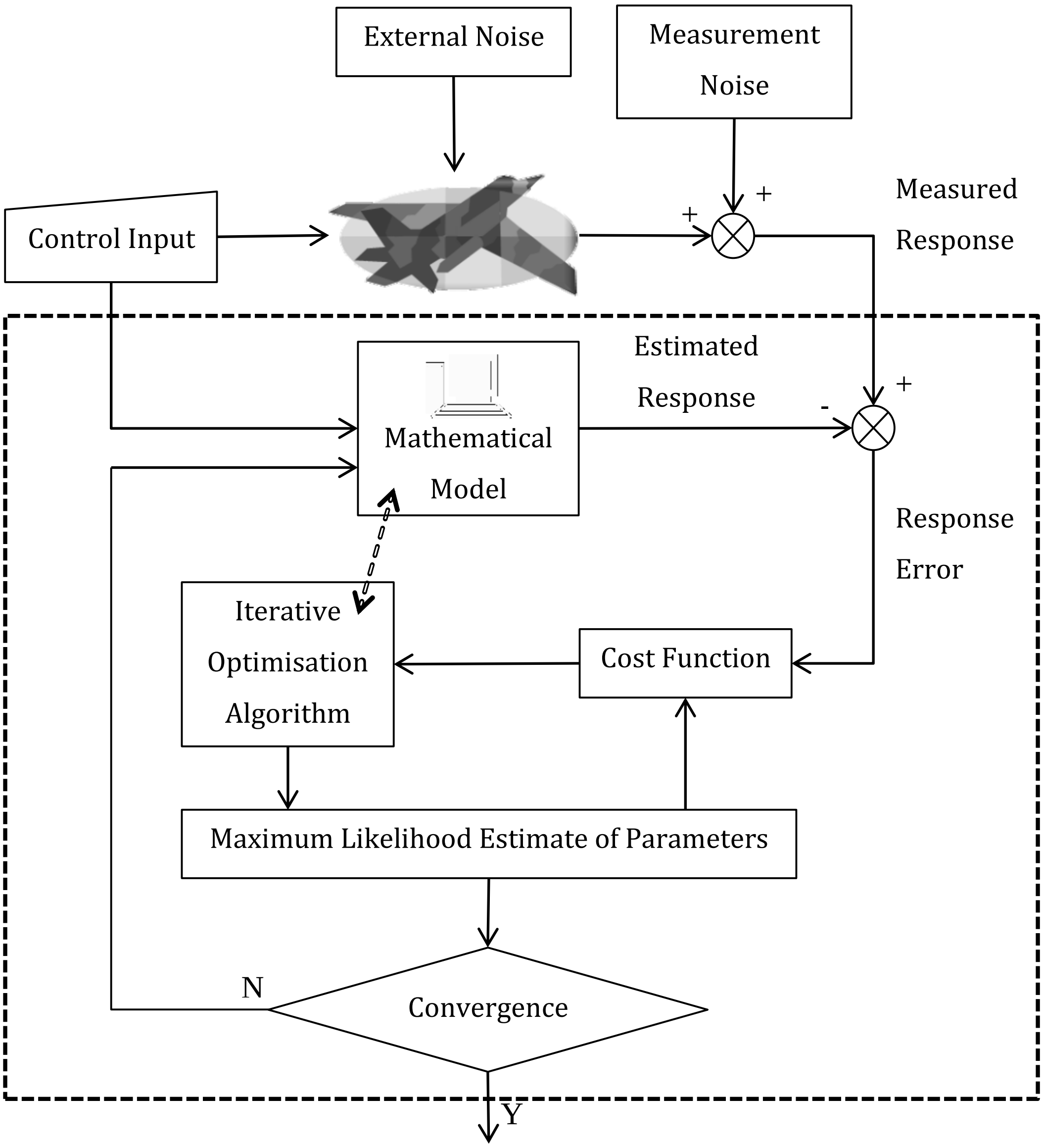

Figure 2-1 Maximum Likelihood Algorithm (Iliff, 1987)

Greater stability of the solution process can be achieved by applying the relaxation technique. The cost function is thus optimised with respect to R while keeping θ constant, and vice versa (Klein and Morelli, 2006). The steps are repeated iteratively until a convergence criterion is met. Differentiating the cost function, $J(\theta, R)$, with respect to R (assuming that the residuals at each time point are statistically independent), and then equating to zero yields the intermediate optimised value of the measurement covariance matrix:

$$R = \frac{1}{N}\sum_{i=1}^{N} \nu(i)\nu^T(i) \qquad 2\text{-}20$$

Upon substitution of this intermediate measurement covariance matrix into the cost function (i.e. Eq. 2-16) and dropping the constant parameters yields:

$$J(\theta) = \frac{1}{2}\sum_{i=1}^{N} \nu(i)R^{-1}\nu^T(i) \qquad 2\text{-}21$$

Many different optimisation schemes can be used to determine the parameter vector that minimises Eq. 2-21. A commonly used algorithm is the modified Newton-Raphson method (Klein, 1989; Klein and Morelli, 2006; and Jategaonkar, 2006). This is a gradient-based, iterative optimisation procedure that yields the local minimum of a given cost function. To reduce the complexity of the optimisation, the cost function is approximated by a second order Taylor series, resulting in a change in the parameter vector for the iterative procedure defined by Eq. 2-22. The parameter updates are repeated until defined convergence criteria are met. Once this is achieved, the measurement covariance matrix is updated via Eq. 2-20 and the modified Newton-Raphson process is repeated until the entire algorithm is converged.

$$\Delta\theta = -\left(\frac{\partial J^2(\theta)}{\partial\theta\partial\theta^T}\right)^{-1} \frac{\partial J(\theta)}{\partial\theta}\bigg|_{\theta=\theta_0} \qquad 2\text{-}22$$

Where: $\left(\frac{\partial J^2(\theta)}{\partial\theta\partial\theta^T}\right)$ is the second partial derivative of the cost function;

and $\frac{\partial J(\theta)}{\partial\theta}$ is the first partial derivative.

The convergence criteria commonly utilised for the convergence of the Newton-Raphson optimisation on the maximum likelihood method include (Klein and Morelli, 2006):

- The percentage change of the parameter update with successive iterations:

$$\frac{\|\theta_k - \theta_{k-1}\|}{\|\theta_{k-1}\|} < 0.001 \qquad 2\text{-}23$$

Where: $\theta_k$is the parameter vector at the k-th iteration of the scheme and a threshold of 0.1% is selected.

- The change in the cost function must be less than 0.1% of the magnitude of the previous value of the cost function:

$$\left|\frac{J(\theta_k) - J(\theta_{k-1})}{J(\theta_{k-1})}\right| < 0.001 \qquad 2\text{-}24$$

Where: $J(\theta_k)$ is the cost function corresponding to the k-th parameter vector estimation.

- The magnitude of the change in the diagonal elements of the measurement error covariance matrix reach values below 5% of the previous values:

$$\left|\frac{(r_{jj})_k - (r_{jj})_{k-1}}{(r_{jj})_{k-1}}\right| < 0.05, \forall j, j = 1,2,\dots,n_o \qquad 2\text{-}25$$

Where: $(r_{jj})_k$ is the j-th diagonal element of the measurement covariance matrix at the k-th iteration of the maximum likelihood method.

- And lastly, a value of the cost gradient, for each unknown parameter, of below 0.05 is required for convergence:

$$\left|\left(\frac{\partial J(\theta)}{\partial \theta_j}\right)_{\theta=\theta_k}\right| < 0.05, \forall j, j = 1,2,\dots,n_p \qquad 2\text{-}26$$

Where: $\left(\frac{\partial J(\theta)}{\partial \theta_j}\right)$ is the partial derivative of the cost function with regard to the j-th parameter.

The second partial derivative of the cost function, as included in Eq.2-22, is commonly referred to as the information matrix, symbolised by M, while the first derivative is referred to as the gradient matrix, g. The solution to these matrices involves the derivation of the system sensitivity matrix $\frac{\partial y(i)}{\partial x}$ via either analytical or numerical methods (e.g. central differencing). According to Klein and Morelli (2006), and Jategaonkar (2006) the numerical approach lends itself to being less complicated when a non-linear system is being analysed. This process is detailed in Appendix B.2 along with the appropriate mathematical simplifications.

Although creating a parameter identification model from the above algorithm may be achieved relatively easily, various computational problems arise. These computational problems may lead to divergence of the iterative procedure or erroneous results (Klein and Morelli, 2006). A sizable concern is given to nearly singular information matrices, M. If the information matrix is nearly singular, its inversion has two main detrimental effects on the algorithm. The first is a divergent cost function and the second is large parameter step sizes within the modified Newton-Raphson optimisation scheme (Klein and Morelli, 2006). Three established techniques are commonly used to accommodate the nearly singular information matrix. These are the rank deficient method; the Levenberg-Marquardt method; and the Bayes-like method. The characteristic attributes of each method are provided in the following bulleted list. The reader is also advised to refer to Appendix B.3 for a more detailed description of each method.

- Levenberg-Marquardt: Involves an additional positive definite matrix being added to the information matrix to improve the condition of the information matrix used.
- Bayes-like method: The cost function is modified by imposing prior parameter information on the information matrix reducing the possibility of ill-conditioning.
- Rank-deficient method: This technique is based on singular value decomposition of a matrix. The ratio of each singular value to the largest singular value is monitored for an indication of ill-conditioning and is set to zero if the ratio threshold is reached.

To this point, the algorithm specified in Figure 2-1 has been addressed together with the special computational techniques that are applied for algorithm stability. The natural progression of the maximum likelihood review leads to the discussion of parameter accuracy. A brief description of the accuracy parameters used within the maximum likelihood method (i.e. The Cramer-Rao bounds) and the corrective techniques applied when the measurement noise assumptions are breached is provided below.

As stated previously, when using the maximum likelihood method, the parameter estimates are not considered random numbers. They do not have variances or mean values. A mathematical proof determining the maximum theoretical accuracy of the parameters is given in Jategaonkar (2006). The result is:

$$cov(\theta_{ML}) \geq M^{-1} \qquad 2\text{-}27$$

Where: θ_{ML} is the maximum likelihood estimate of the unknown system parameters;
and M is the information matrix described earlier.

The accuracy of the parameter estimates is directly related to the information content within the flight data (Jategaonkar, 2006). The elements of the inverse of the information matrix are known as the lower Cramer-Rao bounds and are the measure of the accuracy of estimated parameters. This method of determining the error bounds for the estimates yields consistently accurate results when simulated data is used and the residual vector is based on a white noise assumption. In practice, when experimental flight data is utilised, these residuals deviate somewhat from the assumption of white noise. The use of the above accuracy method in these cases results in accuracy measurements that are optimistic (Klein and Morelli, 2006). The methods used to overcome coloured residuals are described in Morelli and Klein (1995).

The first method breaks away from the assumption that the white noise has a constant power spectral density throughout all frequencies up to the Nyquist frequency. In this case, the white noise is limited to white noise over a certain bandwidth. This results in a correction factor that is a function of the bandwidth to which the white noise is deemed to be limited to. The correction factor is given as $\frac{1}{2\Delta tB}$, where Δt is the measurement sampling-period and B is the limiting bandwidth. This factor is multiplied by the inverse of the information matrix, yielding estimates of the covariances corrected for coloured measurement noise.

The second method involves the use of an autocorrelation matrix given as:

$$R_{vv}(k) = \frac{1}{N}\sum_{i=1}^{N-k} v(i)v^{T}(i+k) = R_{vv}(-k), where\ k = 1,2,\dots,r \qquad 2\text{-}28$$

Where: r is the largest sample index difference used to calculate the autocorrelation function;

N is the total number of samples in the dataset;
and v is the noise vector.

According to Klein and Morelli (2006), the value of r need not be too large since the significant portion of the colouring in actual flight test measurements is at low frequencies. A useful estimate is given as $r = \frac{N}{5}$. It was found that the parameter variances calculated using this correction yields good results that correlate well with estimates determined from repeated manoeuvres at the same flight condition (Klein and Morelli, 2006).

2.3 DESIGN OF EXPERIMENT

2.3.1 Introduction

The design of experiment module of the system identification algorithm encompasses both the design and implementation of an objective-specific flight test programme. The available information content of aircraft modes, aerodynamics, propulsion and instrumentation characteristics (i.e. Range, resolution, sensitivity, etc.) must be used to maximise efficiently the information content of the flight data, thus reducing required flight test time.

A high-level description of this process is presented by Klein (1989); wherein particular emphasis was placed on recommended resolutions of instrumentation. It must be considered that technological advances since the publication date lead to significantly higher quality sensors available to the public at reduced costs. The significance of Klein (1989), although reduced, lies in the principles applied to the design of the experiment and the selection of instrumentation for systems identification of aircraft. Other significant sources that provide a high-level description of the design of experiment include Klein and Morelli (2006) and Jategaonkar (2006). The remainder of this section will elaborate on the subsections of the design of experiment module.

2.3.2 Instrumentation

Characterising a given instrumentation set or defining an instrumentation set for flight testing plays a pivotal role in obtaining adequate information content for systems identification analyses. Too low a resolution or sensitivity could lead to modal information being lost. Characterising the noise variance gives the analyst an indication of measurement accuracy and is a requirement in many of the parameter identification and data compatibility algorithms (e.g. Maximum likelihood methods or Kalman filters). Extremely high-quality sensors, on the other hand, may prove costly and unnecessary when lower modal frequencies are being analysed. Balance must be achieved between accuracy requirements and instrumentation costs. The available payload volume should also be considered, especially when small unmanned aerial systems are concerned. The instrumentation aspects described above are discussed by Klein (1989), and Maine and Iliff (1986).

Along with the adequate characterisation of the on-board sensors, descriptions of the important flight variables that require measurement are also presented by Maine and Illif (1986). These include the correct measurements of time, control surface positions, angular rates, and linear accelerations; all of which are essential to achieving dependable system parameter estimates. Depending on the expected accuracy of the estimation procedure and flight regime being analysed, independent measurements of the Euler angles, flow angles, angular accelerations, and air data may also be critical.

The importance of defining sensor time lags and drift rates should be acknowledged as these directly attribute to unwanted systematic errors if not modelled properly or removed from the data source. Sensor lags, in many cases, are either modelled as a fixed time shift (Blackwell, 1990), a dynamic lag (i.e. first or second order lag), or a combination of both. Fixed time shifts are restricted to the sample rate due to the discrete time modelling of the parameter estimation algorithms (Blackwell, 1990). Drift rates are modelled effectively as linear functions of elapsed time within the dataset. When these sub-model parameters are unknown, they may be modelled within the data compatibility module of the systems identification algorithm. It is advised to model these parameters under laboratory conditions to reduce the number of system parameters to be estimated.

2.3.3 Specific Flight Test Objectives and Associated Manoeuvre Designs

Flight-testing in the aircraft systems identification domain, in general, is carried out with either of two main objectives: flight performance and control evaluation or model parameter estimation. The first is more qualitative and involves the evaluation of the stability and control characteristics (i.e. modal analyses), while the second involves the estimation of a greater array of specific system model parameters (e.g. Aerodynamic parameters via statistical analyses on datasets) (Babister, 1961). It is a natural conclusion that the specific flight test objectives and imposed flight test constraints should be closely linked to the quality or reliability of the available mathematical model and the flight conditions that such models are associated with. Established manoeuvre designs are available for both analyses mentioned above. Babister (1961) offers descriptions of these generic types of manoeuvres to implement when establishing traditional longitudinal or lateral linear dynamic models. This section will address these set of manoeuvres as well as the special techniques to maximise the information content with regards to system identification flight testing of a UAV.

As previously mentioned, there may be requirements to develop higher fidelity aircraft aerodynamic models. Detailed manoeuvre designs are then required. These are based on exciting specific responses, that when modelled, maximise the effect of the specified parameters on the simulated responses. This design objective is highlighted by Maine and Iliff (1985) in which an emphasis is placed on good modal excitation of the aircraft via a fairly broad spectrum of control surface frequency inputs. The requirement for modal excitation ties in with the frequency response of each model parameter intuitively falling within the modal frequency bands of the system. This is detailed in Jategaonkar (2006). Because no system model is perfectly accurate, a degree of uncertainty as to the specific modal frequency exists. Broad spectrum inputs are required and are achieved via band-limited frequency sweeps. For UAV systems, however, spatial limitations may disqualify the application of frequency sweeps. In these cases, optimised manoeuvres are required to effectively excite the relevant dynamic modes of the aircraft.

Jategaonkar (2006) details a typical set of input manoeuvre categories that is useful for holistic aerodynamic modelling. These categories, together with the respective response classes, are as follows:

- Short period excitation – Longitudinal
- Phugoid excitation – Longitudinal
- Push-over pull-up – Longitudinal
- Level turn – Lateral
- Thrust variation – Longitudinal

- Bank-to-bank roll – Lateral
- Dutch-roll excitation – Lateral
- Steady heading steady sideslip – Lateral
- Acceleration-deceleration manoeuvre - Longitudinal

Manoeuvres within these categories, when optimised for a specific aircraft, lead to high information content (i.e. higher energy content within identified spectral bands) in the gathered datasets to determine the aerodynamic parameters.

With the maturation of systems identification on aircraft aerodynamic modelling, various authors have attempted to optimise control input functions within the categories mentioned above, in both, the time and frequency domain. These input designs rely significantly on the prior aerodynamic model and the selected set of parameters within the model to be estimated. These methods are based on single as well as multiple control surface excitations, ranging from simple impulses to optimal multi-steps and harmonic inputs (Jategaonkar 2006).

Common inputs optimised in the time domain are:

- Pulse inputs
- Doublet inputs (Multi-step)
- 3-2-1-1 inputs (Multi-step)

The above manoeuvres are combinations of respective equal amplitude step inputs about the trimmed control surface deflection. A pulse input is an asymmetric control pulse of a specified Δt. The doublet inputs are symmetric with equal $\Delta t's$. The 3-2-1-1 inputs, are commonly used due to the broad frequency spectrum, and are combinations of positive and negative steps with adjacent time steps of $3\Delta t$, $2\Delta t$, Δt and Δt. These inputs are described and summarised in terms of their spectral comparisons by Jategaonkar (2006). A graphical representation of the summarised results in terms of normalised frequencies is given in Figure 2-2. In practice, the respective step times for each of the above manoeuvres are optimised to have a broad spectral density curve with the highest energy content around the frequency of interest. By optimising the inputs, the margin for error of exciting a specific frequency response is increased.

Maine and Iliff (1986) also note that important aspects of designing a manoeuvre for the adequate excitation of an aircraft involve adhering to additional constraints such as structural and control system limitations. Publications including these constraints and dealing with multi-surface optimisations of complex multistep inputs in the time domain are Morelli and Klein (2005) and Morelli (1993). Morelli (1993) describes a procedure that incorporates direct control and output constraints. The cost function for this method was either to set the variance goals (lower Cramer-Rao bounds) to tend to zero with an undefined time limit (unconstrained) or to prescribe a set manoeuvre time and minimise the Cramer-Rao bounds (constrained optimisation) within this period. The process involves the utilisation of dynamic programming that dramatically reduces the computation time when compared to a process whereby all possible control sequences are computed. The method is based on choosing the appropriate input signal (restricted to either a maximum, minimum or zero amplitude) at particular time intervals, inclusive of the state constraints. The result would be a manoeuvre that maximises the sensitivities of all the parameters of interest (i.e. minimising the norm of the inverse information matrix).

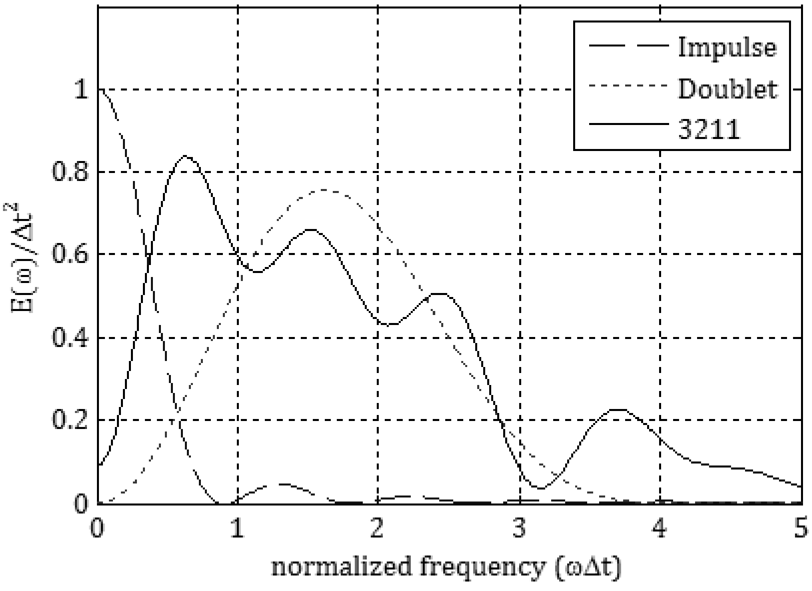

Figure 2-2 Energy comparisons of different control input types (Jategaonkar, 2006)

The above-mentioned method was applied to actual flight tests and parameter identification from the collected flight data and is described in Morelli (1999). Results were compared on an equivalent energy basis to the traditional doublet and 3-2-1-1 inputs. All estimated parameters for either longitudinal or lateral manoeuvres showed increased accuracies when the optimal input was utilised. Standard deviations for the lateral manoeuvres using the optimal input compared to the 3-2-1-1 inputs showed an average decrease of 20% in parameter standard errors. An average decrease of 72% was deduced for the longitudinal cases. As noted by Morelli (1999) this was also because higher amplitudes could be achieved by the complex multi-steps since the state constraints were directly applied. Also noted was the fact that the differences between the commanded and actual control inputs did not have detrimental effects on the results, showing good robustness. This conclusion is logical since the modal frequencies of interest are situated in a low-frequency band. This property enhances the practicality of the process, especially when dealing with unmanned aerial systems.

Another approach to optimisation is described by Mulder et al (1994). It details the approach used at the Delft University of Technology and utilises a combination of weighted orthonormal sinusoidal functions to achieve a resultant signal with concentrated frequency bands. The constraint with regard to the form of the input signal (control amplitudes) is applied indirectly via an energy constraint adhering to a fixed time interval. Since the weighting vector is related to the energy constraint as described by Mulder et al. (1994), the signal form is controlled via a constraint applied to the weighting vector. This method of optimal design yields an optimal signal with comparatively lower frequency content when compared to that of other multistep inputs (i.e. Doublets, pulse, etc.). The results achieved via this method are reported to compare well with other input types but with the advantage of restricting the frequency response spectrum to certain ranges.

It should be understood from the above descriptions that both the complex multistep and the control inputs based on sinusoidal functions have the capability to reduce the Cramer-Rao bounds to an extent bettering the traditional inputs (3-2-1-1 and doublets). Although this is the case, the practicality of each process should be weighted accordingly. When dealing with pilot inputs, multistep inputs are far easier to perform than carefully constructed sinusoidal inputs, especially those at either very low or very high frequencies. But if an automatic control system is available the more complicated sinusoidal manoeuvres can be achieved with relative ease. The engineer must determine the devices available to him and make a decision appropriate to the situation. In conclusion, it should be noted that the significant decreases in parameter standard deviations of the optimised input sequences, effectively reduces the overall testing time in addition to the higher accuracy. In most cases this factor should offset the computation and analysis time required compared to simple doublet and 3-2-1-1 manoeuvres. More detail on the selected manoeuvres particular to the current research topic are presented in Sec. 3.2.5.

2.4 DATA COMPATIBILITY

To successfully apply the maximum likelihood method or any other parameter identification procedure, the set of raw data needs to be of good quality and should be bound by the physical constraints of dynamic systems. This is the principle from which data compatibility arises. After superficial checks (e.g. sign conventions) have been carried out on the flight data, data compatibility checks serve to determine any unknown instrumentation characteristics such as time lags, scale factors or biases. This process involves applying a parameter identification technique using the measured aircraft states in conjunction with the kinematics laws that should unite them. By-products of this process are reconstructed state variables that may not have been directly measured during experimental testing but are required for further parameter identification analyses (e.g. angle of attack, angle of sideslip).

The two tiers of the data compatibility algorithm will now be described in more detail. The first objective is to correctly model the instrumentation characteristics.

A commonly used model for this analysis is given by Eq. 2-29.

$$y(t) = K_y y(t - \tau) + \Delta y \qquad \text{2-29}$$

Where: y is the measured variable or instrument output;
K_y is the scale factor;
τ is the measurement time lag;
and Δy is the bias error.

Data compatibility involves the estimation of the model defined by Eq. 2-29 via parameter estimation procedures. The maximum likelihood method (i.e. output error method) is one of the more popular methods used in data compatibility analyses.

Common inputs into this estimator, for the purpose of data compatibility, are the linear accelerometer measurements and the angular-rate gyroscopes. The output measurements are those from any available instrumentation related to air data or aircraft kinematics.

For cases involving a relatively high degree of measurement noise a filter error method or a Kalman filter is utilised. Each of these methods requires knowledge of the instrumentation error covariance matrices divided into a measurement error covariance matrix and an input error covariance matrix. As opposed to the measurement error covariance matrix, the input error covariance matrix can be estimated within the filter error algorithm by setting the elements of the matrix as unknown parameters. This restriction on the estimation of the measurement error covariance matrix is due to potential identification problems as described in Jategaonkar (2006).

The filter error method utilises a Kalman filtering process to estimate the aircraft states that are propagated through time, which, as mentioned above, is the second objective (or second 'tier') of the data compatibility process. If there is a strong degree of confidence in the input and output noise covariance matrices, then the extended Kalman filter can be used as a stand-alone estimator for the aircraft states as well as the system parameters. This is achieved by including the system parameters in the state vector resulting in the augmented state vector as described in Jategaonkar (2006), Jonkers (1976), and Mulder et al. (1999). The states are propagated through time steps via an integration scheme (usually a 4th order Runge-Kutta numerical scheme) and then corrected via a Kalman gain matrix before moving to the next successive time step. The constant parameters are carried over and corrected through all the time steps, maintaining their constant attributes by setting the respective time derivatives to zero in the integration scheme. For a more stable analysis, the constant value is replaced by a Markov process where either a constant drift term may be imposed; or a random walk may be represented by using a time constant tending to infinity (Mulder et al., 1999). Appropriate initialisation of the Kalman filter properties (i.e. Input, measurement, and initial prediction-error covariance matrices) also affects the estimates.

In the case of linear aircraft dynamic systems, Kalman filter state corrections are based on an optimal Kalman gain matrix (A formal proof of this can be found in Jategaonkar, 2006) but for non-linear systems, a mixed-estimator approach is required to obtain the best estimate of the gain matrix. The mixed-estimator as described by Jategaonkar (2006) utilises a non-linear integration of states in the prediction step and linearized system approximations for estimating the Kalman gain and prediction-error covariance matrices. This solution method is provided in both Jategaonkar (2006) and Mulder et al. (1999). The main steps of this algorithm are depicted below:

Prediction Step:

$$\tilde{x}_a(k+1) = \hat{x}_a(k) + \int_{t_k}^{t_{k+1}} f_a[\hat{x}_a(t), \bar{u}_m(k)]dt \tag{2-30}$$

$$\begin{aligned}\tilde{P}(k+1) = \Phi(k+1)\hat{P}(k)\Phi^T(k+1) \\ + \Psi(k+1)B(k)\mathrm{Q}(k)B^T(k)\Psi^T(k+1)\end{aligned} \tag{2-31}$$

Correction Step:

$$K(k) = \tilde{P}(k)C^T(k)[C(k)\tilde{P}(k)C^T(k) + R(k)]^{-1} \tag{2-32}$$

$$\hat{x}_a(k) = \tilde{x}_a(k) + K(k)\big[z(k) - g_a\big(\tilde{x}_a(k)\big)\big] \tag{2-33}$$

$$\hat{P}(k) = [I - K(k)C(k)]\tilde{P}(k)[I - K(k)C(k)]^T + K(k)R(k)K^T(k) \tag{2-34}$$

Where: $\tilde{x}_a$ is the predicted augmented state vector;

$\hat{x}_a$ is the corrected augmented state vector;

$\bar{u}_m$ is the mean control input matrix;

$\tilde{P}$ is the predicted augmented state prediction-error covariance matrix;

$\hat{P}$ is the corrected prediction-error covariance matrix ;

K is the Kalman gain matrix;

B is the linearized control matrix;

C is the linearized observation matrix;

Q is the process noise covariance matrix;

I is an identity matrix;

k is the discretised time index ranging from k = 1,2,3,…N where N is the total number of samples;

R is the measurement-error covariance matrix;

and Φ and Ψ are the state transition matrix and its integral respectively.

The state transition matrix and integral are derived via the use of linearized systems representations. These parameters are approximated via a Taylor series and given by Eqs. 2-35 and 2-36 respectively.

$$\Phi(k+1) = I + A(k)\Delta t + A^2(k)\frac{\Delta t}{2!} + \cdots \tag{2-35}$$

$$\Psi(k+1) = I\,\Delta t + A(k)\frac{\Delta t^2}{2!} + A^2(k)\frac{\Delta t^3}{3!} + \cdots \tag{2-36}$$

Where: I is an identity matrix;

A is the linearized aircraft state matrix;

and Δt is the discrete time increments.

The Taylor series approximation above may be truncated to between 8 and 12 terms (Jategaonkar, 2006). This is regarded as a good representative model for the transition matrix for aircraft dynamics. The linearized system, control, and observation matrices are derived via Eq.Set 2-37, where a central difference computational scheme is used.

$$\begin{aligned} A(k) &= \left(\frac{\partial f_a}{\partial x_a}\right)_{\hat{x}_a(k-1),u(k-1)} \\ B(k) &= \left(\frac{\partial f_a}{\partial u}\right)_{\hat{x}_a(k-1),u(k-1)} \\ C(k) &= \left(\frac{\partial g_a}{\partial x_a}\right)_{\hat{x}_a(k-1),u(k-1)} \end{aligned} \tag{2-37}$$

Where: f is the dynamic system non-linear function;

and g is the observation function.

When the systems being analysed are significantly non-linear, a more advanced Kalman filtering scheme is used called the iterated extended Kalman filter. This process consists of an iteration loop on the calculation of the observation matrix until a better estimate of the estimated augmented state vector is achieved. The iterated augmented state vector leads to better estimates of the observation matrix that in turn lead to more appropriate estimates of the Kalman gain matrix. A detailed explanation and derivation of the iterated extended Kalman filter are given by Mulder et al. (1999). Another additional procedure utilised to achieve better estimates of the augmented state vector is to apply a post-calculation smoother. A smoother commonly used in conjunction with a Kalman filter for aircraft state estimation is a fixed-interval smoother (Jategaonkar, 2006). The scheme works backwards regarding the sequential time points of the data set (i.e. from the last data sample to the first data sample). It is based on all the measurements of the particular dataset. The process is represented by Eq. 2-38, Eq. 2-39 and Eq. 2-40 as derived in Jategaonkar (2006).

Many established methods are available for the data compatibility process and should be chosen on merit based on the instrumentation set at hand. It should be noted that increasing the fidelity of the algorithm also significantly increases the calculation time. Because this dissertation deals with offline analyses, a time constraint is of less importance than accuracy.

$$K_s(k) = \tilde{P}(k)\Phi^T(k+1)\tilde{P}^{-1}(k+1) \tag{2-38}$$

$$x_{as}(k) = \hat{x}_a(k) + K_s(k)[x_{as}(k+1) - \tilde{x}_a(k+1)] \tag{2-39}$$

$$\begin{aligned} P_s(k) = {} & [I - K_s(k)\Phi(k+1)]\hat{P}(k)[I - K_s(k)\Phi(k+1)]^T \\ & + K_s(k)[\tilde{P}(k+1) \\ & + \Psi(k+1)B(k)Q(k)B^T(k)\Psi^T(k+1)]K_s^T(k) \end{aligned} \tag{2-40}$$

Where: All definitions are unchanged, while the subscript *s* refers to smoothed values.

2.5 MODEL VALIDATION AND VERIFICATION

The model verification and validation processes are significant steps in the system identification algorithm (Morelli and Klein, 2005). The determination of whether or not the model accurately represents the real aircraft behaviour (to within defined error bounds) determines the success of the estimation.

Verification deals with the correctness of the actual solution process of the model. It deals with whether or not the mathematical model structure correctly describes the flight regime in question. The verification process also involves a data compatibility check. As described in Sec. 2.4, this step deals with the fact that even though the data may be handled correctly, constant bias and scale factor errors may still occur due to the characteristics of the sensors. A large part of this step is based on reconstructing flight paths and matching them with the measured values.

On the other hand, validation deals with whether the parameters estimated are within practical bounds or how well the model describes the measured data. Data sets used for the validation process must come from theoretical estimates, wind tunnel data, or any other form of estimation dissimilar to the estimation algorithm (Morelli and Klein, 2005 and Klein, 1989). The comparison of the results for specific flight regimes must also account for the error bounds of the estimates.

Jategaonkar (2006) presents three significant statistical measures to describe the model fit based on an analysis of the residuals. Similar processes are suggested by Klein and Morelli (2006). The first method is to determine the total standard deviations of the residuals for each dataset being analysed by Eq. 2-41. This statistical measure gives the analyst an idea of how close the modelled responses are to the measured responses but fails to provide insight on system accuracy or predictive potential.

$$\sigma_i = \sqrt{\frac{1}{N}\sum_{k=1}^{N}[z_i(t_k) - y_i(t_k)]^2}\, , where\ i = 1,2,\dots,n_y \qquad \text{2-41}$$

Where: N is the total number of sample points;

n_y is the number of output parameters of the system being analysed;

z is the measured variable;

and y is the model output.

The second statistical measure is based on the Theil's inequality coefficient. Unlike the standard deviations, the Theil's coefficient defined by Eq. 2-42 provides some quantitative insight into the correlation between the measured outputs and the modelled responses. The ratio given by its definition bounds the coefficient to between zero and one, where zero represents an ideal fit. This property creates the advantage over the standard deviations because it is independent of response units and, therefore, all output fit properties can be compared by equal weightings.

$$U_i = \frac{\sqrt{\frac{1}{N}\sum_{k=1}^{N}[z_i(t_k) - y_i(t_k)]^2}}{\sqrt{\frac{1}{N}\sum_{k=1}^{N}[z_i(t_k)]^2} + \sqrt{\frac{1}{N}\sum_{k=1}^{N}[y_i(t_k)]^2}}, where\ i = 1,2,\ldots,n_y \qquad 2\text{-}42$$

Additional ratios based on the residuals are the Theil's bias, variance, and covariance coefficients defined respectively by Eq. 2-43, Eq. 2-44 and Eq. 2-45 (Jategaonkar, 2006). As described by Jategaonkar (2006), the bias proportion gives the analyst an indication to the level of systematic error evident in the model where a target value close to zero is desired. The covariance proportion also provides an indication of systematic error. A value as close as possible to one is desired. The variance proportion given by Eq. 2-44 provides a measure as to the similarity between the model response variances and the measured variances. A good quality model would generate an output variance very similar to the measured variance and thus this coefficient should be as close as possible to zero.

$$U_i^M = \frac{(\bar{z}_i - \bar{y}_i)^2}{\frac{1}{N}\sum_{k=1}^{N}[z_i(t_k) - y_i(t_k)]^2} \qquad 2\text{-}43$$

$$U_i^S = \frac{\left(\sigma_{zi} - \sigma_{yi}\right)^2}{\frac{1}{N}\sum_{k=1}^{N}[z_i(t_k) - y_i(t_k)]^2} \qquad 2\text{-}44$$

$$U_i^C = \frac{2(1-\rho_i)\sigma_{zi}\sigma_{yi}}{\frac{1}{N}\sum_{k=1}^{N}[z_i(t_k) - y_i(t_k)]^2} \qquad 2\text{-}45$$

Where: σ_{zi}, σ_{yi} are the standard deviations of the measured parameters and model responses respectively defined by Eq. 2-46;

and ρ_i is the correlation coefficient given by Eq. 2-47.

$$\sigma_{zi} = \sqrt{\frac{1}{N}\sum_{k=1}^{N}[z_i(k) - \bar{z}_i]^2} \quad and \quad \sigma_{yi} = \sqrt{\frac{1}{N}\sum_{k=1}^{N}[y_i(k) - \bar{y}_i]^2} \qquad \text{2-46}$$

$$\rho_i = \frac{1}{\sigma_{zi}\sigma_{yi}}\frac{1}{N}\sum_{k=1}^{N}[z_i(k) - \bar{z}_i][y_i(k) - \bar{y}_i] \qquad \text{2-47}$$

Where: all variables were defined previously.

The final method of validation based on the residuals is a test for whiteness. As seen in Sec. 2.2 and 2.4 the parameter identification algorithms assumed white noise when measurement noise was considered. White noise is defined as noise that is statistically independent, has an infinite bandwidth and a constant power spectrum over the entire range of frequencies. By this description, it is clear that white noise is a theoretical idealisation that is approximated by real measurements. A test for whiteness is the evaluation of the autocorrelation function similar to Eq. 2-28, but with the residuals being replaced by the residual variances.

By applying these residual checks on the identified model responses, it is possible to evaluate the validity or quality of the identified model. These parameters also serve as methods of measurement allowing relative comparisons between various models based on the same system.

2.6 DATA SMOOTHING

As with any analysis based on real data, noise in measured signals is inevitable. A variety of methods have been used and proposed to efficiently reduce the effect of noise on the results of the various identification techniques. A common method suggested by Jategaonkar (2006) is based on local smoothing of data by means of fitting a local polynomial. As opposed to this smoothing in the time domain, Morelli (1995) describes a method to differentiate between the true signal and the noise in the frequency domain through an optimal low-pass filter.

The algorithm is described as being a global optimal filtering technique. It involves modelling the signal in the frequency domain and then removing the frequencies that approximately characterise the noise. The process exploits the trend that the magnitude of the Fourier coefficients of a Fourier series exhibit when used to model a conventional signal in the frequency domain. The trend is an asymptotic decrease of k^{-3}, while the coefficients used, in part, to model the noise frequencies converge at a slower rate following a k^{-1} trend where k is the sine function coefficient index used in the Fourier series modelling. By exploiting these different trends it was possible to create a low-pass filter with a smooth power reduction across the optimal cut-off frequency. The filter is also known as the Wiener filter and is given by Eq. 2-48.

$$\begin{gathered}\Phi(k) = \frac{\tilde{y}^2(k)}{\tilde{y}^2(k) - \tilde{v}^2(k)}, \qquad 0 \leq k \leq N-1 \\ \tilde{y}(k) = \frac{C_s}{k^3} \\ \tilde{v}(k) \approx C_n\end{gathered} \tag{2-48}$$

Where: k is the discrete frequency index;

N is the number of samples in the dataset;

and C_s and C_n are the model coefficients for the signal and noise trends respectively.

The signal model coefficient, C_s is determined by a least squares fit to a specified number of Fourier sine coefficient peaks about a threshold coefficient peak. Peaks are specified as coefficient magnitudes that are higher than adjacent coefficients. The coefficient peak threshold is based on relative changes between successive peak magnitudes. In terms of the noise model, the coefficient C_n is determined from the root mean square of the peaks associated with the noise.

The component of the noise model falling in a frequency spectrum similar to the signal cannot be removed by these methods, but is also at a relatively lower power band than that of the signal. The method is used to estimate the measurement covariance matrix, R in the output error maximum likelihood algorithm or to determine the instrument error covariance matrices for the Kalman filter algorithms via Eq. 2-49.

$$R = \frac{[z-y]^T[z-y]}{N-1} \tag{2-49}$$

2.7 SYSTEMS IDENTIFICATION SOFTWARE

The use of off-the-shelf systems identification software packages is common among the research domain. As noted in Sec. 2.8 Neeland et al. (2007) describe the use of SIDPAC (Morelli E.A., 2006) in their systems identification analyses. SIDPAC is a systems identification toolset developed for the Matlab® environment. It contains many of the analyses functions required within systems identification such as data handling, general equations of motion, parameter identification algorithms for linearized systems and analyses in the frequency domain. Additionally, functions for data smoothing, or filtering are available. A software suite, FVSysID (Jategaonkar, 2006), with similar capabilities was developed by Jategaonkar (2006). This software package is based mostly on the time domain systems identification analyses.

These collections of systems identification tools provide the researcher with a platform from which to carry out comprehensive systems identification analyses on fixed wing aircraft. Because systems identification requires iterative and sometimes unique solution strategies, many of the algorithms or functions supplied with these software suites have to be modified to suit the aircraft being analysed as well as the research objectives.

Additional systems identification packages are proprietary and thus require licence fees in most cases. An example of this is the systems identification toolbox developed for Matlab® by Mathworks®. This toolbox is not restricted to aircraft dynamics and, therefore, presents a general approach to systems identification. Once again, because of the unique requirements of every airframe being analysed via systems identification, intelligent user inputs and modifications are frequently required. A full list of functions available for SIDPAC 2.0 and FVSysID can be found in Morelli (2006) and Jategaonkar (2006) respectively.

2.8 APPLICATIONS OF SYSTEM IDENTIFICATION

A multitude of publications dealing with the application of system identification on manned aircraft is available as was described in Sec. 1.1. Important to this dissertation was the structural component of the algorithm used on manned aircraft and the application to UAVs in particular.

One of the comprehensively presented publications, within the scope of system identification application, is by Paris and Bonner (2004). The authors provided an example of the application of the system identification algorithm to a manned aircraft, the F/A-18 Super Hornet. The publication dealt with an incremental aerodynamic model development of an asymmetric aerodynamic case (i.e. asymmetric leading edge flap deflections). Practical issues of the various system identification modules applied to flight test data were raised. An equation error method was utilised, yielding a significant improvement of the initial aerodynamic model regarding the predictive nature of the model and the model fit to experimental flight data. The complexity of the aerodynamic modelling task and the structured method that was used in achieving models of high quality provided a good methodical structure that can be applied to any aircraft system identification task. Other similar case studies, although dated, were published by Batterson (1981), Rajamurthy (1985), Suit (1972) and Tanner and Montgomery (1979). These publications were characterised by linear aerodynamic modelling problems. It should be noted that high quality of flight data, extensive instrumentation and piloted flight, sets these types of case studies apart from the application of system identification to unmanned aerial vehicles. The general procedures, however, are universal and are evident in UAV domain through publications by Chumalee and Whidborne (2010), Suk et al. (2003), and Neeland et al. (2007).

Chumalee and Whidborne (2010) provide a comprehensive overview of work done to achieve an aerodynamic and propulsion model for a 65 kg UAV (i.e. Royal Thai Air Force aerial target). The objective was to determine whether a model could be achieved with sufficient accuracy to create three autopilot functions for a particular flight condition. Linear aerodynamic and propulsion models were postulated and an equation error parameter identification method was employed. It is important to note that Chumalee and Whidborne (2010) used high accuracy digital output systems where the avionics instrumentation and telemetry rates were selected on the basis of system identification being the primary driver. Two critical UAV-related issues addressed by Chumalee and Whidborne (2010) were the requirement for remote piloting and the higher level of noise evident in the measured data. These problems were partially surmounted by utilising a racetrack manoeuvre that included simple modal excitation manoeuvres, and a detailed data compatibility analysis. The parameter identification process yielded an adequate parametric model for a single flight condition; the resulting flight control functions effectively achieved the desired functionalities for the small scale remotely piloted aircraft. This result was aided by good a priori aerodynamic data in conjunction with high accuracy instrumentation. Chumalee and Whidborne (2010) thus highlight the flight test planning and data acquisition problems unique to UAV’s, providing a base to build upon.

Suk et al. (2003) detail the parameter identification process applied to a slightly larger fixed wing UAV than that described by Chumalee and Whidborne (2010). The UAV that was analysed was 290 kg with a wing span of 6.4 m. The critical difference, however, was the utilisation of an automatic flight control system for achieving a higher accuracy aerodynamic model. The initial flight dynamic model was derived from a Datcom analysis for a given flight condition. Regarding parameter identification techniques, a maximum likelihood method was used in conjunction with a postulated linear aerodynamic structure. The technique was adapted to weight each of the different flight modes within the analysis. This allowed for a balanced identification of the different modes using a limited set of data. Open loop longitudinal system identification manoeuvres, such as optimised 3-2-1-1 multisteps, were designed and implemented allowing for a high data content. Suk et al. (2003) also placed a significant emphasis on the utilisation of the automatic flight control system. The improvements offered by the utilisation of the flight control system were two-fold. Firstly, the system was used to decouple the longitudinal and lateral modes allowing the data to reflect specific modes required by the parameter identification. The second advantage was that additional closed loop manoeuvres could be performed that yielded aerodynamic information for longitudinal modelling within the same flight condition. A pitch command following manoeuvre was carried out at constant throttle. The closed loop elevator and pitch rate responses to the pitch command were then modelled. Since both open and closed loop models in part used the same aerodynamic parameterisations for the given flight conditions, concurrent model estimations were possible, yielding higher accuracy aerodynamic parameters. Suk et al. (2003) describe the implementation of the concurrent modelling for the linear longitudinal model. The model parameters were bounded within realistic ranges for each parameter, thus maintaining the physical meaning of each aerodynamic parameter during estimation. As presented by Suk et al. (2003), good results for both longitudinal and lateral linear aerodynamic parameters were achieved.

Neeland et al. (2007) provide a largely qualitative account of the progress made on systems identification of a fixed-wing UAV at Monash University, Australia. Once again decoupled, linear modelling structures were used. A standard maximum likelihood method was utilised for aerodynamic parameter estimation. High accuracy instrumentation and data acquisition techniques were used to achieve the highest quality data possible. A sample rate of 100Hz was used. Once again the airspace restrictions placed on UAV's was found to be a significant factor in flight test planning. The authors carried out the flight tests at a model aircraft club where a figure of eight flight path was employed for the duration of the flight test. Relatively simple remotely piloted manoeuvres were used to excite the various rigid body modes of the aircraft. The authors have also utilised the SIDPAC suite of system identification tools in the estimation process.

From the above three UAV system identification publications, it was evident that the instrumentation systems on board the various aircraft were geared towards systems identification rather than standard flight control and navigation. Acceptable models were achievable without considerable data conditioning. This contrasted with the characteristics of the UAV used in this dissertation where noisy data was significant thus requiring a data conditioning process. Also, of notable significance within the presented literature were the various experimental techniques used, from simple manoeuvres to optimised manoeuvres and additional closed loop testing. The airspace restrictions and remote piloting constraints were also factors in the design of flight testing manoeuvres. Due to the open loop nature of the research and degree of uncertainty regarding the initial aerodynamic model and control law limitations, an R/C piloted flight performing a combination of simple and optimised manoeuvres applied to the scope of this dissertation. It is evident from these applications that systems identification applied to UAV's does bring additional dimensions to the modelling domain not seen in large aircraft analyses.

2.9 CONCLUSIONS

The references detailed in Chapter 2, show that a strong theory base does exist. Due to the dependence of systems identification on real flight test data and on the aircraft characteristics, however, the identification algorithm cannot be viewed as an autonomous solution process. The application must be tailored for each case based on engineering experience and the identification objective. It has been explained in Sec. 1.2

that the UAV analysed in this dissertation was restricted in terms of automated flight capabilities and adequate systems identification instrumentation. This resulted in the exclusion of some of the reviewed methods from the initial research method. A significant portion of the restrictions was placed on the design of experiment and data compatibility processes. These restrictions, however, should not be placed on future systems identification analyses where the airframe may be modified to the extent that the rationale becomes invalid.

As mentioned in Sec. 2.3, the selection and characterisation of the onboard instrumentation is an important part of the design of experiment step. The selection of instrumentation was beyond the scope of this dissertation, while the onboard sensors were characterised through the filtering methods described in Sec. 2.6. Sensors measuring aerodynamic model parameters such as angle of attack and sideslip were not installed on the airframe, thus detailed data reconstruction using an iterated extended Kalman filter as described in Sec. 2.4 was necessary. Due to the low inertia of the UAV, non-linear dynamics were assumed a more likely occurrence and thus the extended Kalman filter was used instead of a linear optimal filter. The iterative algorithm was also implemented to reduce the effect of the combination of the linear state transition matrices and low sample rates.

An important difference between the current UAV system identification research and those described in Sec. 2.8 is that the UAV in this study is significantly smaller with lower instrumentation specifications. A comprehensive data compatibility process was thus required. Regarding the actual parameter identification, there was no restriction placed on the validity of the algorithms as seen by the successful application of regression, maximum likelihood and Kalman filter estimators on both large aircraft and smaller UAVs. Within this dissertation, the effectiveness of system identification on the test aircraft was analysed through a multitude of methods starting with the simpler regression and methodically progressing to the maximum likelihood algorithms.

The flight testing method used in this dissertation involved a piloted figure of eight manoeuvres as detailed in Neeland et al. (2007). The encouraging results obtained by Chumalee and Whidborne (2010) using a single flight test meant that significant information could be extracted from limited data if the manoeuvres were adequately planned. Although the high-level autopilot capabilities of the airframe used in this dissertation were not utilised, Suk et al. (2003) showed that the possibility of predefined automated control inputs would significantly enhance the manoeuvre implementation. An effort was thus made to create an experimental design method that seamlessly combined remotely piloted flight and predefined manoeuvre inputs. These optimal control inputs were based on simple predefined combinations of sequential step inputs (3-2-1-1 and doublet inputs), implemented by the control system, about the trimmed control deflections achieved through R/C piloting. The multistep inputs would not yield data as rich in information content as the optimal multisteps or optimised harmonics, but have broad spectral properties and thus forgiving error margins.

Also noted, are the existence of systems identification software packages containing many of the tools required within each module of the systems identification algorithm. Because SIDPAC 2.0 and FVSysID collectively contain a vast majority of analyses tools developed specifically for aircraft analyses, they were the preferred toolsets for the current research. However, due to the unique data analysis requirements of low-cost UAVs, as discussed in Sec. 1.2, many additional solution techniques were required for the flight test design, data compatibility, and parameter identification modules.

3 INVESTIGATIVE METHOD AND IMPLEMENTATION

3.1 INTRODUCTION

The investigative method was constructed based on the practical constraints of the available airframe and instrumentation, the limitations placed on flight testing an unmanned aerial vehicle, and the various parameter identification and data compatibility algorithms available.

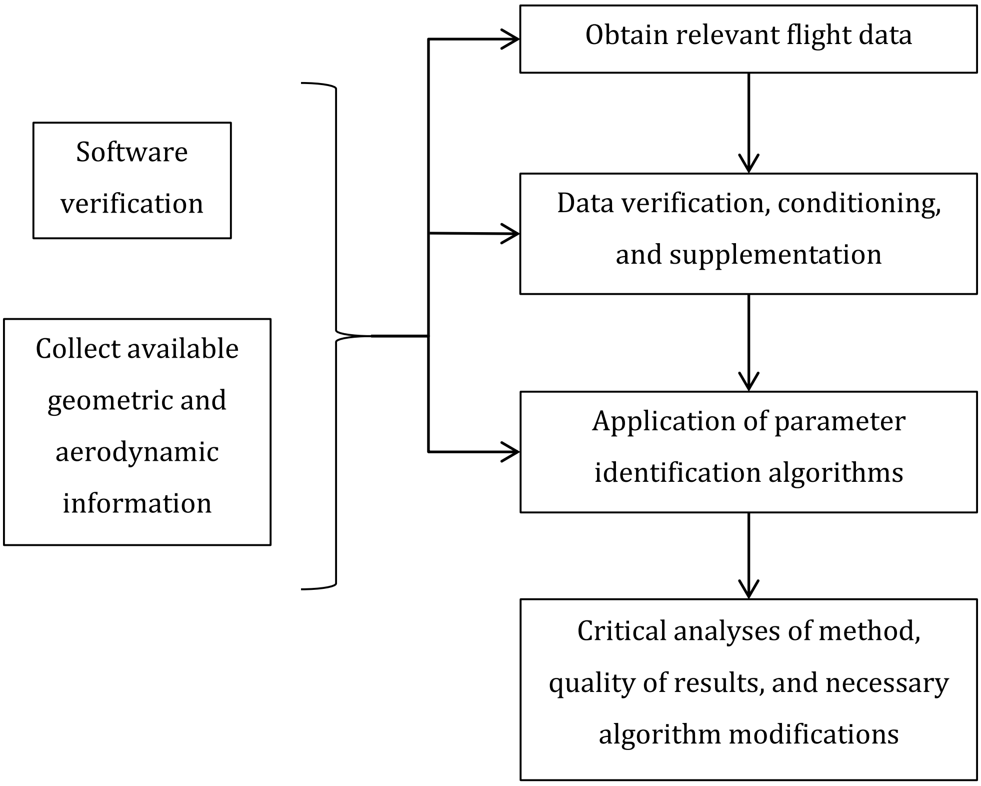

Figure 3-1 Investigative Method

The high-level flowchart describing the method is given in Figure 3-1. The first three modules are consistent with the system identification algorithm discussed in Chapter 2 and include flight testing, data compatibility and parameter identification respectively. As noted in Figure 3-1, software verification of each of these modules was initially carried out on the algorithms used. In conjunction with the software verification was the collection of geometric information and aerodynamic data from sources of varying degrees of fidelity to develop the initial flight dynamic model. The sub-sections that follow within this chapter will discuss the specific details of the implementation of each module presented in Figure 3-1. The final process described in the flowchart is associated with the objective of this dissertation and thus is the critical analysis of the method and results obtained for each system identification module.

3.2 FLIGHT TESTING

3.2.1 Introduction

To assess the parameter identification algorithms discussed in Chapter 2, information-rich flight data had to be obtained. This process involved flight test planning, manoeuvre implementation and data recording. The following sub-sections detail the method employed for this stage of the analysis.

3.2.2 Objectives and Defined Solutions

As mentioned previously, due to financial constraints, only a single flight test was possible for this phase of the system identification. Further flight tests would rely on the experience gained and information gathered during this particular flight. The flight test objectives were defined with regards to specific, achievable targets. Since the endurance of the test vehicle was approximately 50 minutes, the planned flight test time was restricted to 30 minutes to allow for manoeuvre repetitions.

Flight testing proposed objectives:

- To identify the atmospheric conditions. This included determination of the average wind vector, pressure, and air temperature measurements.
- To achieve adequate longitudinal and lateral modal responses at the cruise condition to maximise the information content of the data relative to the specific parameter identification algorithm requirements. The importance of this criterion was described in Sec. 2.3.3. The manoeuvres were limited to small amplitude control inputs (about the reference trim condition) in order to reduce the flight test risk related to the differences between the designed (i.e. intended) and experienced manoeuvre responses.
- To collect quasi-steady flight data for the validation of static force and moment coefficients obtained via external procedures (e.g. Wind tunnel testing).

Along with the proposed objectives, a set of flight testing limitations was constructed based on the restrictions placed on the test environment, the capabilities of the control system and the accuracy of the initial aerodynamic information. These limitations are listed below:

- Due to airspace regulation limitations placed on unmanned aircraft at the time of testing, flights were restricted to a zone of dimensions: 1000m by 500m by 200m AGL (height above ground level). This spatial restriction meant that manoeuvre times were subsequently restricted as well.
- For this flight test programme, the control system was adapted to accept and implement predefined multi-step and sinusoidal commands on individual control surfaces. At the time of testing, simultaneous control of the various control surfaces by the control system was not possible. This problem was alleviated by using pilot inputs when simultaneous inputs were required. Navigation and stability augmentation capabilities of the control system were disabled for the parameter identification tests because the control system operational envelope was not cleared for the type of manoeuvres required. The test procedures were carried out via remote controlled piloting where the pilot was required to acquire the planned test reference conditions before the manoeuvres were implemented using the predefined control system commands. This meant that a further line-of-sight restriction was implicit in the test procedure.
- Although comprehensive performance related tests were carried out on previous flight test campaigns, the existing correlations of the flight dynamic simulation outputs, based on the initial aerodynamic model to the actual flight dynamics, were not adequate to safely model large amplitude or rapid manoeuvres. Because of this simulation limitation, all planned manoeuvres to be implemented by the control system were restricted to small amplitude control deflections of less than 10° of deflection (33% of control range).

The proposed manoeuvres were largely based on the generic systems identification manoeuvres described in Sec. 2.3.3 and by Jategaonkar (2006) because of the above limitations and the reliance on a single flight. Drawing from the conclusions in Sec. 2.9, due to the poor quality of the initial flight dynamic model, multistep 3-2-1-1, 1-1-2-3, and doublet control inputs were preferred over the optimal multi-step inputs described by Morelli (1993) or the optimised harmonic inputs detailed by Mulder et al. (1994). This decision was taken to minimise potential departure of the aircraft caused by the uncertainties of the initial flight dynamic model.

The flight test was performed at the White Hills Radio Flyers Club in Pretoria. The final flight test card included the following manoeuvre sets:

Manoeuvres to establish atmospheric data:

- Pressure and temperature – The UAV onboard instrumentation did not include an air temperature sensor, while the static pressure was indirectly measured via the altimeter. These parameters were needed to evaluate the air density and were requirements for true airspeed evaluation. These conditions were attained via a thermometer reading at the ground station and a QNH reference pressure measurement was supplied by a local control tower (AFB Swartkop) approximately 10 km away (Refer to Figure 3-2). The temperature variation between the ground station altitude and the flight altitude was approximated from the Standard Atmosphere table variations.

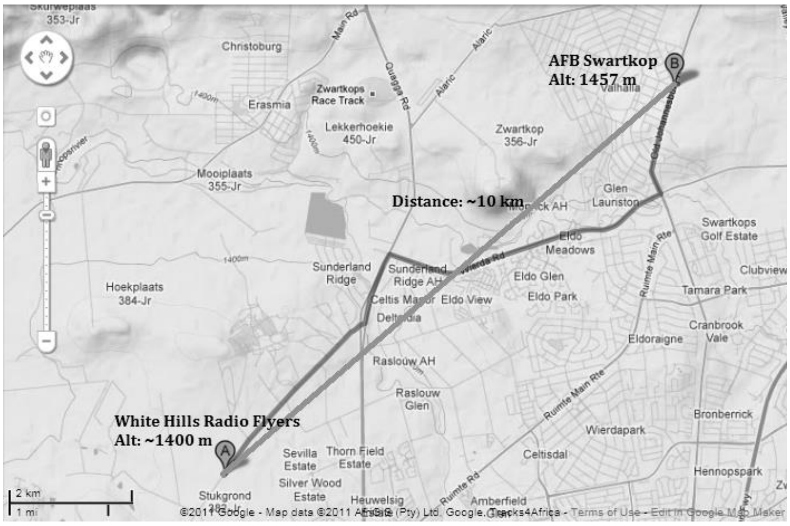

Figure 3-2 QNH Pressure Measurement: Location Differences (Source: Google Maps, August 2011)

- Box manoeuvres – A rectangular circuit was flown, where each segment was characterised by trimmed straight and level flight. All segments were carried out at approximately the same altitude and calibrated airspeed. The airspeed and ground speed (determined from GPS measurements) information obtained from this manoeuvre was used to determine the wind velocity vector approximated as a constant throughout the flight test period.

Steady State Data: The design specification for manoeuvres within this category stipulated a requirement for a constant throttle setting.

- Push-over pull-up manoeuvre – A low frequency (i.e. 0.1 Hz), small amplitude (i.e. $\delta_e < \pm 5°$) sinusoidal command was given to the elevator control. The objective of this manoeuvre was to obtain flight data required to estimate steady lift and drag characteristics as well as longitudinal trimming information. The design specified that a quasi-steady state be maintained throughout the manoeuvre and no oscillatory modes should be excited.
- Steady heading sideslip (SHS) – Defined by a coordinated sideslip with increasing magnitudes of rudder step deflections. The ailerons were used to trim the aircraft at a constant heading for the various rudder step inputs. The objective of this manoeuvre was also to obtain information on the lateral coupling of the aircraft and hence lateral trim conditions.

Dynamic Data: Much like the steady state manoeuvres, a constant throttle setting was required for each of the following manoeuvres.

- Longitudinal short period excitation – Usually excited by elevator doublets, multistep manoeuvres or frequency sweeps, however as mentioned above, this will be achieved via 3-2-1-1or 1-1-2-3 manoeuvres due to the broad bandwidth of such inputs (See Figure 2-2). The objectives of these manoeuvres were to provide information on the dynamic stability of the aircraft, and hence the dynamic derivatives at the specific reference condition.
- Bank to bank manoeuvre – This manoeuvre was performed to determine the coupling between the roll and yaw characteristics of the aircraft. The aircraft was slowly banked via an aileron input until the desired bank angle (30°) was reached. The manoeuvre was then reversed.
- Excitation of the Dutch-roll mode – Excitation of this lateral mode provided information on the lateral dynamic derivatives of the aircraft for the particular reference condition. A rudder doublet was sufficient to excite this moderately

damped mode. This manoeuvre was performed immediately after the bank to bank manoeuvre to maximise the dutch-roll coupled dynamic response.

All manoeuvres were initiated from a steady state condition at the calibrated cruise speed (i.e. 22 m/s). This reference state was achieved via remote controlled piloting. Where possible (i.e. Push-over or pull-up, longitudinal short period excitation, and Dutch-roll excitation) the autonomous predefined control input capabilities were utilised. To ensure maximum efficacy of the design process, the aircraft dynamic response resulting from the application of the predefined manoeuvres were modelled through representative flight dynamic simulations. The simulation model was based on prior aerodynamic and geometric data.

3.2.3 Experimental Setup

The flight test setup consisted of three major components i.e. the UAV system including instrumentation, the ground station, and the pilot.

The available airframe was a twin boom, electrically powered and aerodynamically stable configuration shown in Figure 3-3. The significant geometric and mass properties are provided in Table 3-1 and Table 3-2. The Y and Z centre of gravity locations were approximated measurements based on a low fidelity component-wise mass build-up, whereas the critical X (longitudinal) location was accurately established via balance tests before the flight test. This check also served as an indication as to whether the results of the mass build-up were realistic. The moments of inertia were also derived from the component-wise mass build-up with the assumption of an X-Z plane of symmetry.

The centre of gravity location presented in Table 3-2 is provided in the structural frame of reference. The x axis is defined as projected from the origin to the rear of the aircraft, parallel with the centreline. The y axis is perpendicular to the x axis in the starboard direction, and the z axis is pointed upward, completing the set of mutually orthogonal structural set of axes. The origin of the axis in the x and z direction is in line with the tip of the propeller hubs and coincides with the centreline in the y direction. The moments of inertia reported in Table 3-2 are with respect to the stated centre of gravity location. The aerodynamic reference point was also selected to coincide with the centre of gravity for the configuration that was tested.

The main wing has an aspect ratio of 11.5, has a taper ratio of 1, and has a 0° sweep angle. The payload pod that houses the IMU and battery packs are located below the main wing, along the centreline. The mean aerodynamic chord is 0.36 m, with the leading edge located at 0.64 m. The UAV has twin vertical tails, one mounted on each fuselage. Each vertical tail has a reference area of 0.03 m^2 and a moment arm of 0.43 m between the main wing quarter chord and the quarter chord of the mean aerodynamic chord (MAC) of the vertical tail. Each vertical tail has an aspect ratio of 1.2 and a MAC of 0.15 m. The horizontal tail is located between the two vertical tails with a planform area of 0.08 m^2. The moment arm from the main wing quarter chord to the horizontal tail quarter chord is 0.80 m. The horizontal tail has an aspect ratio of 4.44, a taper ratio of 1, and a MAC equal to 0.14 m. The aircraft is powered by two electric motors mounted at the tip of each fuselage. The battery packs are located within the payload pod.

The aircraft systems included an instrumentation set containing an IMU (Inertial Measurement Unit) consisting of three-axis rate gyroscopes, linear accelerometers and magnetometers; a calibrated pitot tube; and a GPS sensor. The magnetometer reference was initialised to the standard magnetic field reference at the flight test location (i.e. GPS coordinates: $25°52'2''S\ 28°5'13''E$) and thus only approximated the actual magnetic field. The location of the IMU was measured on the airframe and is provided in Table 3-3. An on-board, linear Kalman filter estimator was also utilised to provide real-time estimates of Euler angles based on the angular rate gyroscope measurements.

Table 3-1 Modular UAV Geometric Properties

Geometric Property	Value	Metric
Wing area, S_w	1.486	m^2
Wing Span, b_w	4.128	m
Mean aerodynamic chord, $\bar{c}$	0.360	m

Table 3-2 Modular UAV Mass Properties

Property	Value	Metric
Mass	26.382	kg
I_{xx}	11.238	$kg.m^2$
I_{yy}	7.891	$kg.m^2$
I_{zz}	18.456	$kg.m^2$
I_{xz}	0.840	$kg.m^2$
CG X-location	-0.655	m
CG Y-location	0	m
CG Z-location	0.052	m

Table 3-3 IMU Location in the Structural Frame

Coordinate	Value	Unit
X location	-0.91	m
Y location	0.00	m
Z location	-0.08	m

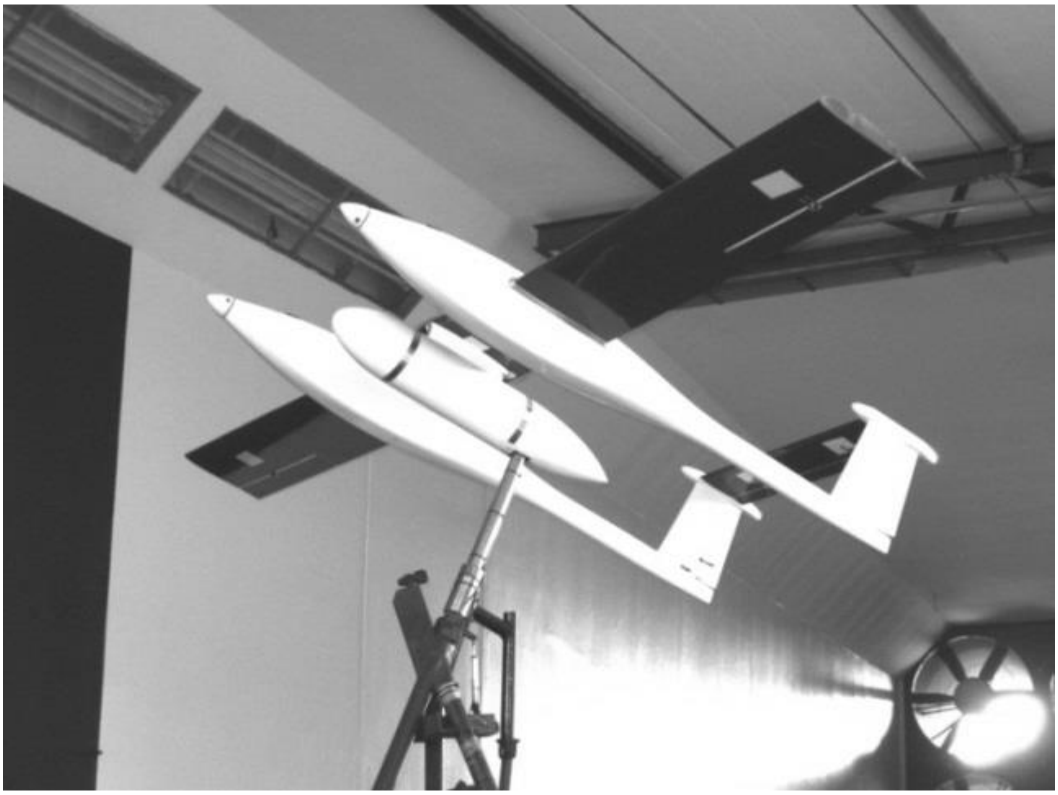

Figure 3-3 The Modular UAV

As mentioned in Sec. 3.2.2, the flight control system (FCS) used for preliminary systems identification flight tests was only utilised to implement predefined control surface commands when the pilot had attained the relevant test condition.

Data logging of flight-related parameters was achieved via the onboard systems. All sensor data, flight control data, and other miscellaneous health monitoring parameters were saved onto the on-board SD memory card. The sample rate was limited to 25 Hz. A high-frequency threshold analogue filter was implemented via the onboard data conditioning systems. The cut-off frequency for this filter was greater than 100 Hz. Considering the rigid body lateral and longitudinal dynamic modes of the UAV to be safely below 5 Hz (As determined by the initial flight dynamic model), it was assumed that a 25 Hz sampling frequency would be high enough to reduce the effects of data aliasing to fairly insignificant levels. However, the possibility of higher frequency structural modes being excited during the flight could not be eliminated yielding some uncertainty.

The ground station consisted of telemetry equipment required for the monitoring of the UAV in flight. This afforded the human pilot real-time flight data that supplemented the line of sight visual information. The ground control software was used to trigger the FCS predefined manoeuvres when the reference test conditions were attained. Constant and clear communication between the ground control personnel and the pilot was a vital component in successfully coordinating the planned manoeuvres.

3.2.4 Simulation Platform

As mentioned in Sec. 3.2.2, to optimise the required manoeuvre inputs it was essential to simulate the flight dynamic responses. This was achieved through the use of JSBSim, an open source flight dynamics simulation environment. A summary of the software capability is provided in Appendix C. The data used to populate the flight dynamic model was extracted from the data produced during the development phases of the airframe, where various methods of characterisation and geometric modelling were carried out.

The available a priori information is listed below:

- Engineering drawings
- Moments of inertia via a component-wise spread-sheet build-up

- Preliminary aerodynamic characterisation
- Static power-off wind tunnel tests at the cruise airspeed

The engineering drawings were used to extract the basic reference information needed in the flight dynamic models. The moments of inertia as described in Sec. 3.2.3 were generated from a component-wise spreadsheet build-up. These properties were provided in Table 3-1 and Table 3-2.

Regarding aerodynamic characterisation, a linear aerodynamic model consisting of force and moment coefficients was also available from the preliminary design stages of the UAV development cycle. These were achieved via analysis tools based on vortex lattice theory (AVL) as well as a panel method (CMARC). Semi-empirical methods found in Roskam (1979) were also utilised. These models were created about a zero angle of attack, straight and level flight condition at 22 m/s (the designed cruise speed). It should be noted that the vortex lattice theory and panel methods did not account for power effects or the fixed landing gear thus increasing the uncertainty of the longitudinal aerodynamic results.

At a later stage in the design cycle, wind tunnel tests were also performed at 22 m/s. The test matrix consisted of alpha and beta sweeps at a series of control deflections. The controls used were elevator, rudders, and ailerons at approximately two-degree increments. These tests, much like the previous analyses, did not account for power effects or the fixed landing gear. The flight dynamic static stability and control coefficients were derived from the wind tunnel force and moment database for a zero angle of attack reference flight condition.

The initial simulated model (within JSBSim) was created to correlate to the reference conditions of the available data and assuming the following initial states: $\phi = \alpha = \beta = 0$ deg. and $p = q = r = 0$ deg/s. The aerodynamic results from the above mentioned analyses were selected and yielded a linear aerodynamic model parameterised by the non-dimensional force and moment coefficients given in Table 3-4. The model included the static stability and control coefficients derived from wind tunnel data and dynamic stability derivatives from the vortex lattice method. As mentioned in Sec. 3.2.3. The aerodynamic reference point was set to the centre of gravity position also correlating to the characterisation methods.

Table 3-4 Simulation Data - Aerodynamic Force and Moment Model Coefficients

Parameter	Unit	JSBSim	Parameter	Unit	JSBSim (Source)
C_{L_0}	$[-]$	0.381 (WT)	C_{D_0}	$[-]$	0.023 (WT)
C_{L_α}	$[\mathrm{rad}^{-1}]$	4.987 (WT)	C_{D_α}	$[\mathrm{rad}^{-1}]$	0.141 (WT)
$C_{L_{\dot{\alpha}}}$	$[\mathrm{rad}^{-1}]$	1.372 (AVL)			
$C_{L_{\hat{q}}}$	$[\mathrm{rad}^{-1}]$	4.639 (AVL)			
$C_{L_{\delta e}}$	$[\mathrm{rad}^{-1}]$	0.274 (WT)			
C_{m_0}	$[-]$	0.054 (WT)	C_{Y_β}	$[\mathrm{rad}^{-1}]$	-0.582 (WT)
C_{m_α}	$[\mathrm{rad}^{-1}]$	-1.218 (WT)	$C_{Y_{\hat{p}}}$	$[\mathrm{rad}^{-1}]$	-0.006 (AVL)
$C_{m_{\hat{q}}}$	$[\mathrm{rad}^{-1}]$	-17.421 (AVL)	$C_{Y_{\hat{r}}}$	$[\mathrm{rad}^{-1}]$	0.080 (AVL)
$C_{m_{\dot{\alpha}}}$	$[\mathrm{rad}^{-1}]$	-1.687 (AVL)	$C_{Y_{\delta a}}$	$[\mathrm{rad}^{-1}]$	-0.045 (WT)
$C_{m_{\delta e}}$	$[\mathrm{rad}^{-1}]$	-1.377 (WT)	$C_{Y_{\delta r}}$	$[\mathrm{rad}^{-1}]$	0.210 (WT)
C_{l_β}	$[\mathrm{rad}^{-1}]$	-0.083 (WT)	C_{n_β}	$[\mathrm{rad}^{-1}]$	0.097 (WT)
$C_{l_{\hat{p}}}$	$[\mathrm{rad}^{-1}]$	-0.113 (AVL)	$C_{n_{\hat{p}}}$	$[\mathrm{rad}^{-1}]$	0.020 (AVL)
$C_{l_{\hat{r}}}$	$[\mathrm{rad}^{-1}]$	0.033 (AVL)	$C_{n_{\hat{r}}}$	$[\mathrm{rad}^{-1}]$	-0.085 (AVL)
$C_{l_{\delta a}}$	$[\mathrm{rad}^{-1}]$	-0.172 (WT)	$C_{n_{\delta a}}$	$[\mathrm{rad}^{-1}]$	0.010 (WT)
$C_{l_{\delta r}}$	$[\mathrm{rad}^{-1}]$	0.020 (WT)	$C_{n_{\delta r}}$	$[\mathrm{rad}^{-1}]$	-0.065 (WT)

*WT – Wind tunnel; AVL – Vortex Lattice Method

The propulsion model consisted of electric motors with the appropriate propeller power characteristics. The moment of inertia was estimated at 0.3 g.m^2 per propeller about the respective rotational axes and a maximum propeller speed (in revolutions per minute) of 5000 rpm was set. The approximated maximum rotational speed correlated with the maximum expected rotational rate of the actual propellers. The variation of the thrust generated with advance ratio (C_{T_U}) was assumed to be negligible for the purposes of small dynamic perturbations of the aircraft about a reference condition within the simulation. This assumption was expected to affect the phugoid mode because of the dependence on the velocity perturbations (Refer to Roskam, 1979). Due to the uncertainties around the propulsion model, the basic model was only used to provide an approximately constant thrust force and to provide the coupled dynamics of the propulsion system on the total dynamics based on inertial considerations. The line of action of the thrust was assumed to be parallel to the X body axis of the aircraft.

A simplified autopilot was also developed for use within the flight dynamic simulation. The autopilot was capable of simulating both the multistep control inputs as well as sinusoidal inputs. No delays were specified for the actuator models; hence commanded inputs were instantaneously applied. This approach was deemed reasonable due to the rapid response time of the actual actuators relative to the lower modal frequencies of the rigid body dynamics.

3.2.5 Manoeuvre Design and Implementation Method

After establishing the required manoeuvre set for the test flight, the details (i.e. Reference condition, control deflections and frequencies of interest) of each manoeuvre were determined in conjunction with the aspects of practical implementation based on the UAV characteristics as detailed in Sec. 3.2.3. As previously mentioned, the simulation platform provided the test-bed for the required manoeuvre optimisations.

Since the initial aerodynamic information characterised a reference flight condition of trimmed, straight and level flight at 22 m/s, the designed flight test conditions were set up to generate data at similar conditions. The pilot was responsible for achieving the required reference conditions of each manoeuvre. An altitude of between 150 m and 200 m above ground level was deemed sufficient in terms of safety (i.e. adequate manoeuvre failure recovery margin).

The implementation of the selected manoeuvres was achieved through a mixture of pilot and predefined control commands due to the control system limitations. The steady sideslip and box manoeuvres were performed solely via remote piloting due to the complexity of the manoeuvre and the capability of the FCS. The steady sideslip was performed using rudder deflections of magnitudes: 3°, 7° and 15°. The respective deflections were held for 10 seconds and trimmed via aileron commands thus maintaining a constant heading. The box manoeuvre was based on a rectangular flight path of dimensions 1000 m by 500 m and was performed at the beginning and the end of the flight test plan to determine whether the wind vector changed significantly throughout the flight test. This assumed that the flight test was short enough that the atmospheric conditions did not vary nonlinearly between the start and end of the flight. Because these two manoeuvres were based on largely qualitative objectives (see Sec. 3.2.2), accurate simulations before the flight were not required. The pilot had to ensure that the opposing flight paths were approximately parallel to easily extract the wind vector from pitot tube and GPS data.

Another manoeuvre that was implemented via remote piloting alone was the bank-to-bank manoeuvre. It consisted of the pilot banking the aircraft to $+30°$. The implementation was then reversed to achieve a $-30°$ bank angle. The aircraft was then returned to wings level trimmed flight. The specification of $\pm 30°$ was largely qualitative and was adequate for the generation of the lateral dynamic coupling effects. The details of the actual manoeuvre, including a time history of the predicted and actual aileron deflections are provided in Sec. 4.4.5. The actual bank angles achieved during the bank-to-bank manoeuvres were between a minimum of 31.4° and maximum of 52° (refer to Figure 4-31 for the time history).

The push-over pull-up manoeuvre was simulated via a predefined sinusoidal elevator command through the control system. The design variables for the sinusoidal inputs consisted of the amplitude and frequency. The resultant manoeuvre was restricted to a period of 30 seconds and thus a distance of 660 m. An elevator amplitude of 3° was implemented as an initial estimate based on simulated dynamic responses.

The longitudinal short period modal excitation was achieved via 3-2-1-1 multistep inputs (see. Sec. 2.3.3). The 3-2-1-1 multistep control design input variables and FCS multistep input parameters were the length (i.e. period) and magnitude (i.e. control amplitude) of each step. The time interval was based on Eq. 3-1.

$$\Delta t \approx \frac{0.3}{f_c} \qquad 3\text{-}1$$

Where: f_c is the natural frequency of the particular mode to be excited.

This approximation is advised by Jategaonkar (2006) and is based on designing the 3-2-1-1 manoeuvre such that the required excitation frequency falls towards the centre or upper third of the input energy spectrum (refer to Figure 2-2) thus allowing for a maximum modelling error margin and a greater probability of exciting the required mode. Additionally, two 3-2-1-1 inputs were concatenated for each manoeuvre to increase the energy content of the excitation. The natural frequencies for the short period longitudinal mode and lateral modes respectively are approximated by the characteristic polynomial method of solving the aircraft's defining ordinary differential equations and is found in most graduate and undergraduate flight dynamics reference books dealing with linearized stability and control of aircraft. Examples of these are Babister (1961), Etkin (1959), Cook (2007), and Roskam (1979). The method is based on the solution of the characteristic polynomial of the approximated aircraft using the linearized, decoupled system assumptions.

The resulting longitudinal conjugate roots were:

$$\lambda_1, \lambda_2 = 0.03 \pm 0.53i$$
$$\lambda_3, \lambda_4 = -2.89 \pm 4.37i$$

The short period longitudinal mode was characterised by the second conjugate pair of which the damped natural frequency was 4.38 rad/s. Derived from the conjugate pair was the natural frequency and damping ratio of 5.24 rad/s and 0.55 respectively. Converting the frequency to Hertz and substituting into Eq. 3-1 yielded the time step parameter $\Delta t = 0.36\,s$ for the 3-2-1-1 elevator manoeuvre. The elevator control amplitudes were $\pm 4°$ and $\pm 6°$. The larger amplitude manoeuvres were 1-1-2-3 (reverse 3-2-1-1) manoeuvres in order to limit possible departures from the reference condition, while maintaining the same frequency content as the 3-2-1-1 (Jategaonkar, 2006).

The simulated response for the 6° elevator 1-1-2-3 manoeuvre is given in Figure 3-4. The figure presents the significant longitudinal parameters of the simulation. The format of Figure 3-4 is used in all input-response presentations within this report, where plot (a) is the control input followed by the relevant state responses experienced by the aircraft. All subplots are representative of the same time scale on the X-axis. Plots of this nature, within this report, are used as a visual aid in the analysis of the response of an aircraft to a control input. When analysing these figures, the reader should take note of the initially trimmed conditions of all parameters identified by an unchanging value before the relevant control input for the manoeuvre. For both longitudinal and lateral responses to doublets or multi-step inputs, the response plots give the reader an idea of the stability of the system. Figure 3-5 shows an extract of the dataset presented in Figure 3-4 emphasising the short term response of the aircraft as well as the 1-1-2-3 control input repetition. The response parameters, alpha and pitch rate, important to the short period mode is highlighted by an ellipse in both Figure 3-4 and Figure 3-5. The stability of the short period response correlated with the estimated second pair of longitudinal conjugate roots above. The phugoid (long term) response of the aircraft as seen in the response plots between 18s and 40s in Figure 3-4 shows a stable mode characterised by the decreasing amplitude of the response oscillations. This was in contrast to the predicted unstable conjugate roots,λ_1, λ_2. The difference was attributed to the absence of the C_{T_U} derivative within the approximated system used to determine the eigenvalues. Due to a propulsion model within the simulation, the C_{T_U} coefficient was implicit to the model yielding the stabilising effect seen in Figure 3-4 and Figure 3-5.

In conclusion, four multi-step longitudinal manoeuvres were simulated yielding the expected response characteristics of the actual aircraft. Multiple manoeuvres were required to obtain data for use in the validation stages of the parameter identification.

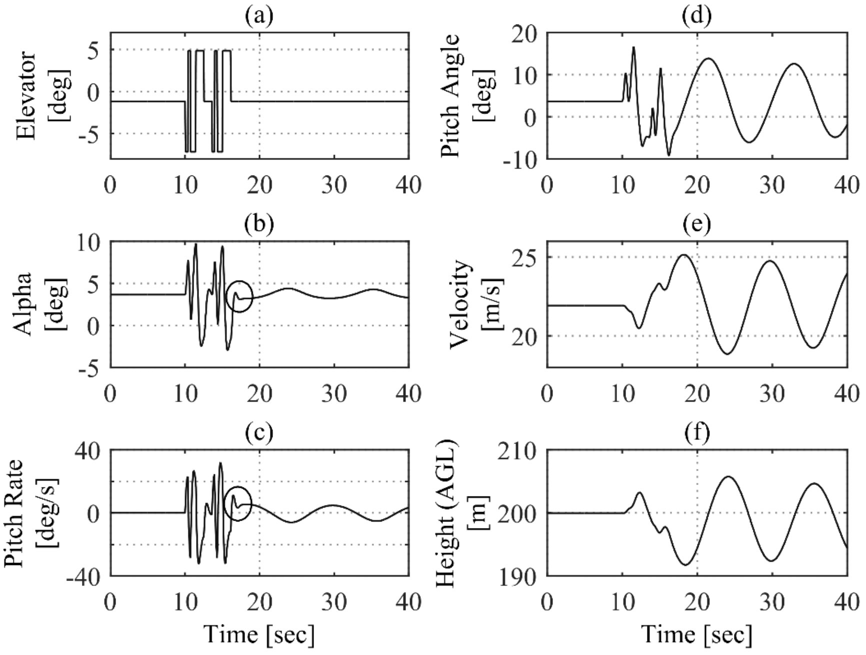

Figure 3-4 Simulated Data - 1-1-2-3 Elevator Manoeuvre (a) Elevator deflection angle (b) Angle of attack response (c) Pitch rate response (d) Euler pitch angle response (e) True airspeed (f) Height (AGL)

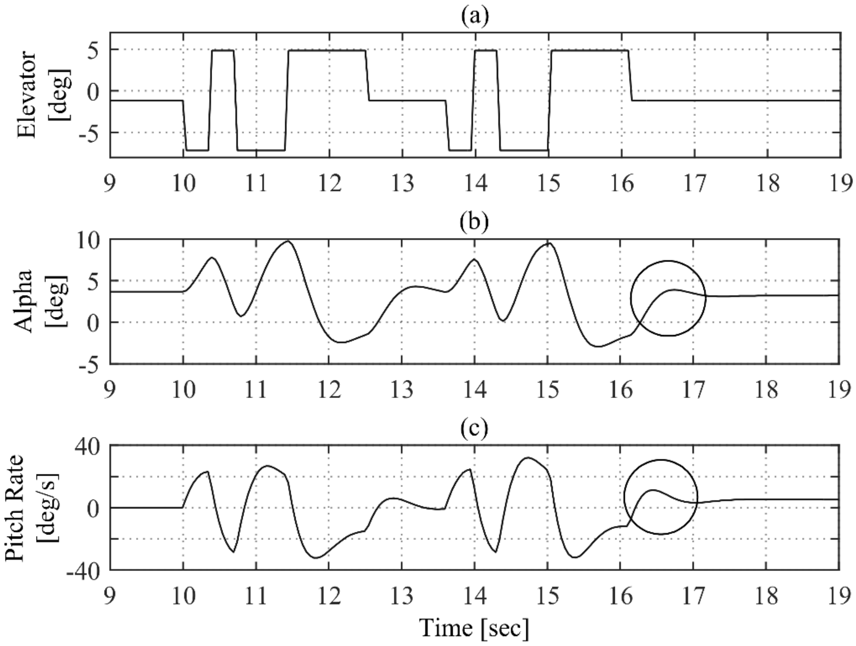

Figure 3-5 Simulated Data - 1-1-2-3 Elevator Manoeuvre (Data Extract) (a) Elevator deflection angle (b) Angle of attack response (c) Pitch rate response

The manoeuvre design details for the dutch-roll excitation were determined in a similar manner to the longitudinal short period excitation, where the roots of the approximated system's characteristic polynomial were evaluated using the linearized, decoupled equations of motion. The difference was that the commanded input was a rudder doublet instead of a multistep manoeuvre. This approach to the modal excitation was due to the expected low damping characteristics of the aircraft and thus relative ease of exciting this lateral mode. The resulting roots of the lateral characteristic polynomial derived from the initial flight dynamic model were:

$$\lambda_1 = -0.13$$

$$\lambda_2 = -1.73$$

$$\lambda_3, \lambda_4 = -0.28 \pm 2.77i$$

The roots associated with the Dutch-roll were λ_3 and λ_4. The dutch-roll damped frequency was 2.77 rad/s. This evaluated to a natural frequency of 2.79 rad/s and a damping factor of 0.10. By using the normalised frequency corresponding to the peak energy content of a doublet manoeuvre (see Figure 2-2) one can derive Eq. 3-2. Using this relationship, an optimal Δt of 0.83 s was calculated.

$$\Delta t = \frac{2.3}{\omega_n} \tag{3-2}$$

The lateral input-response plot from the dynamic simulation utilising this optimised doublet is given in Figure 3-6. Once again, the manoeuvres were initiated from a trimmed condition. Figure 3-6(a) shows the rudder doublet input of fairly large amplitude (12°). The doublet manoeuvre was sufficient to adequately excite the dutch-roll mode as noted by the stable oscillatory behaviour of the corresponding lateral directional states of the aircraft given in Figure 3-6(b) to Figure 3-6(d) (yaw rate, yaw angle and sideslip angle). The resulting damping ratio derived from the logarithmic decrement of the responses to the doublet input correlated with the damping ratio represented by the roots provided above (i.e. damping ratio of 0.1).

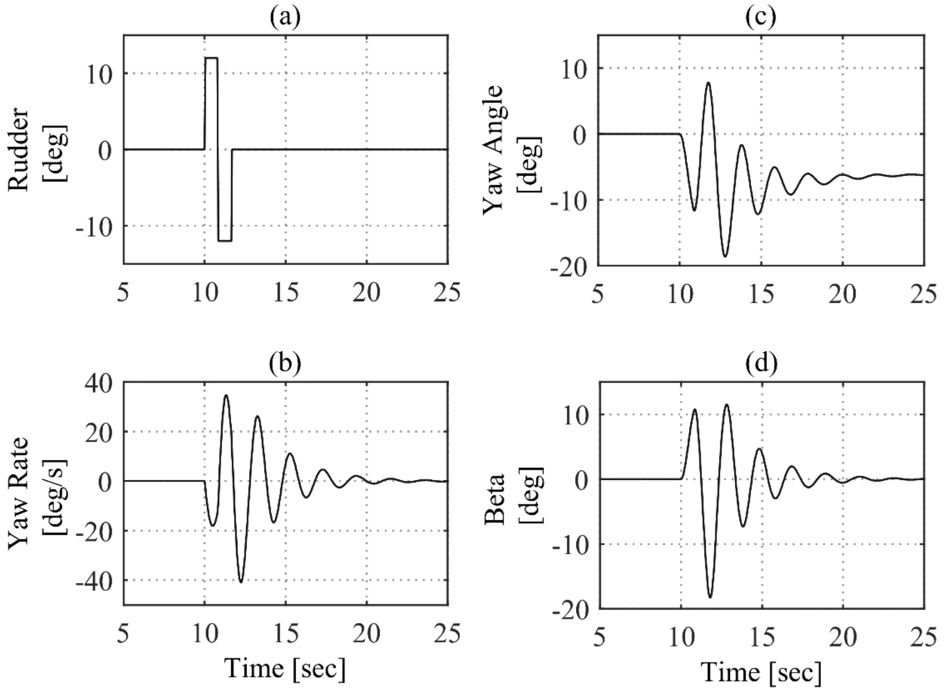

Figure 3-6 Simulated Data - Dutch Roll Excitation (a) Rudder deflection (b) Yaw rate response (c)Euler yaw angle (d) Sideslip angle

The successful implementation of the designed manoeuvres required a combination of both remote inputs as well as the FCS. Because telemetry of the aircraft states was possible at the ground station information could be transferred to the pilot verbally at regular intervals or when required. The pilot was thus able to attain the reference conditions more accurately than would be possible by just line-of-sight piloting with no telemetry.

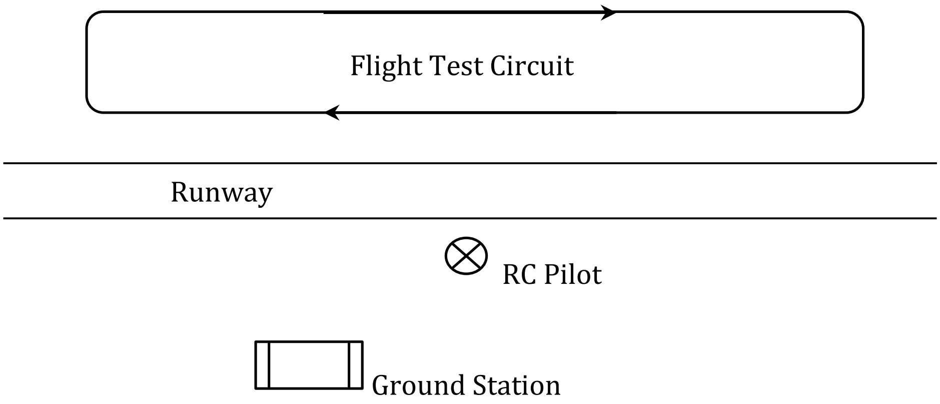

Figure 3-7 Flight Test Operational Setup

As mentioned in Sec. 3.2.2, the rudder doublet was performed immediately after the bank to bank manoeuvre to maximise the coupled response. When the pilot was satisfied the reference conditions were met, the bank to bank manoeuvre was performed via remote piloting followed by the predefined rudder doublet implemented via the FCS. The rudder commands were triggered by the ground control station. During the rudder command and response period, the pilot refrained from additional control input unless a recovery was required.

Through the above-mentioned method the generation of adequate dynamic information through a single flight test was possible but relied heavily on the pilot inputs and the quality of the initial flight dynamic model. Perfect practical replication of all simulated manoeuvres was unlikely, but the choice of manoeuvres using the initial model allowed for a higher possibility of satisfactory information content within the flight data.

3.2.6 Manoeuvre Verification Procedures

Various procedures were employed during and after the flight test to ensure that the required manoeuvres were adequately implemented. The manoeuvre verifications carried out during the flight test were based on visual cues. The telemetry (i.e. indicated airspeed) and visual observations were compared with a set of success criteria decided upon before the flight test. Simple success criteria were based on achieving the correct trimmed airspeed prior to the manoeuvre, whether the correct input commands were implemented, and whether or not a significant visual modal response was apparent. Where necessary, the results of this analysis were then compared to the simulated inputs and responses post flight to qualitatively determine a measure of the accuracy of the simulated model.

These manoeuvre verifications of adequate modal excitation assisted in the selection procedure of manoeuvres that were utilised in the parameter identification analysis. Data obtained via this process would also serve as reference information for follow-on flight test programmes.

3.2.7 Section Synopsis

The flight test programme was carried out in a structured manner to maximise the overall information content of the recorded data. A manoeuvre set was chosen based on the quality of the initial flight dynamic model, the UAV instrumentation, flight test restrictions, and control system capabilities. Control inputs that were implemented by the FCS were simulated, before the flight, in JSBSim to determine whether a stable response was expected and to optimise the manoeuvre design parameters. Of significant importance to a successful flight test was the communication between the human pilot and the ground station equipped with a telemetry system. The pilot was therefore supplied with real-time flight data information, in addition to visual observations, allowing a greater probability of attaining the required reference conditions prior to FCS implementations. This additional information also aided in the successful implementation of the manoeuvres based solely on remote piloting.

3.3 DATA COMPATIBILITY AND RECONSTRUCTION

3.3.1 Introduction

The necessity of a data compatibility and reconstruction procedure within the systems identification algorithm as described in Sec. 2.4 was to verify that a dynamically consistent dataset was used in the parameter estimation procedure. The process made use of the kinematic relationships (between accelerations, velocities and displacements) to derive aircraft state or observation data that were not measured directly during flight, but was required in the aerodynamic model development. The method consequently relied on the characteristics of the instrumentation, onboard data conditioning, and requirements of the postulated aerodynamic models. A simulation platform was used to validate the various aspects of the chosen data compatibility algorithm. This provided a controlled test environment to optimise the algorithm parameters applied to the real flight data. The following sub-sections provide information on the simulation environment and the details of the solution process.

3.3.2 Algorithm Selection

As described in Sec. 2.4, two commonly used algorithms and the respective modifications and derivations have resulted in adequate data compatibility results in a variety of applications. These were the maximum likelihood based algorithms and the Kalman filter methods. Due to the noisy sensor measurements generated from flight testing, the kinematic system was considered stochastic and either the filter error or Kalman filter methods were applicable. Through the filter error method, it was possible to implicitly determine the required measurement noise covariance matrices within the estimation procedure. This is a computationally costly algorithm due to the calculation of the sensitivity matrices (Eq. 2-22) at every iteration. The iterated extended Kalman filter with smoother (IEKF) was selected instead. The measurement covariance matrices in this case were explicitly achieved via the utilisation of the optimal filter algorithm detailed in Sec. 2.6. The adequacy of this method of estimating sensor noise within the required accuracy was determined via simulated data analyses.

3.3.3 Simulation Environment

A simulation environment was created as a validation testbed for the chosen data compatibility algorithm.

The simulated data was generated with JSBSim, using an aircraft model based on a generic flight dynamics model (Roskam, 1979) and by applying optimised lateral and longitudinal multistep control inputs. The variables from the simulated data used in the data reconstruction process were similar to the dataset that was available from the Modular UAV, with the exception of magnetometer measurements. These are listed below:

Input Variables:

- Three angular rates about the three orthogonal body axes – p, q, r
- Three linear accelerations along the three orthogonal body axes – a_x, a_y, a_z

Output Variables:

- Three Euler angles – Φ, Θ, Ψ
- Three location measurements along the respective Earth axes – altitude, north, and east
- Three velocity measurements along the respective Earth axes – vertical velocity, and velocity components in the northerly and easterly directions respectively.

Bias errors and added Gaussian noise (with a specified variance) were superimposed on the simulated data to be representative of a real flight dataset. Artificial time delays between each parameter were excluded from the simulation because these would commonly be accounted for by adequate data conditioning and recording processes (applicable to the Modular UAV). No error was imposed on the initial conditions of each simulated measurement. For analysis of the real flight dataset, the noise-induced initial condition error was reduced by finding the mean of the first ten data points. Given Gaussian noise assumptions and the application of data compatibility analyses, the averaging of the first ten points was deemed adequate to estimate the mean, trimmed, state measurements.

The data compatibility algorithm validation was a two-step process. The first step utilised the optimal Weiner filter to estimate the noise variances of a set of typical flight test parameters with signals typical of small perturbation, multistep, flight test manoeuvres. The estimated noise variances were the variances of the residuals between the filtered and unfiltered data. This exercise empirically indicated the adequacy of this filter for approximating the actual measurement error covariance matrices of real flight test data. The off-diagonal terms of the covariance matrices were zero as the noise imposed on each measurement was independently derived. The second step involved using these predicted measurement error covariance matrices within the IEKF algorithm to estimate the applied data biases. The simulated data provided a good platform for empirical validation of the algorithm because external influences could be controlled.

The validation of the algorithm involved analysing the estimation results, the residuals, and the state variances. Residual analysis was based on the verification of Gaussian characteristics by utilising residual plots, the cumulative probability function, and the autocorrelation function.

3.3.4 Data Reconstruction Method

The data reconstruction requirements were dependent on a linear objective aerodynamic model consisting of stability and control derivatives. The time histories of all the dynamic states of the UAV were required and determined through the IEKF algorithm. Some significant states such as the angle of attack were not measured directly but were reconstructed from the combination of kinematic relationships and the set of available, recorded measurements. The detail of the IEKF reconstruction is presented in a stepwise manner within this section. The kinematic model is described first, followed by the algorithm-specific information such as the input vector selection and preconditioning, output vector selection, and algorithm conditioning checks.

An estimation of the average wind vector was required and included in the kinematic model because of the direct influence it has on the angle of attack, sideslip, and true airspeed. Due to a combination of the relatively short flight test period (thirty minutes) in steady atmospheric conditions, and the spatially limited flight test circuit, an approximately constant wind vector was postulated and validated through the data reconstruction procedure. The kinematic equations of motion based on rigid body dynamics and a constant wind vector are given by Eq. 3-3.

$$\begin{aligned}
\dot{u}_{rel} &= \left(\dot{u}_{body} - \dot{u}_{wind}\right) = -qw_{rel} + rv_{rel} - gsin\Theta + a_x \\
\dot{v}_{rel} &= \left(\dot{v}_{body} - \dot{v}_{wind}\right) = -ru_{rel} + pw_{rel} + gcos\Theta sin\Phi + a_y \\
\dot{w}_{rel} &= \left(\dot{w}_{body} - \dot{w}_{wind}\right) = -pv_{rel} + qu_{rel} + gcos\Theta cos\Phi + a_z
\end{aligned} \tag{3-3}$$

Where: u_{rel}, v_{rel}, w_{rel} are the airspeed vector components in the X, Y, and Z body axes;

p, q, r are the angular rotational rates;

Θ and Φ are the pitch and roll Euler angles respectively;

and a_x, a_y, a_z are the linear accelerations in the X, Y, and Z body axes generated by all external forces except gravity.

The Euler angles associated with the angular orientation of the aircraft were determined by the integration of Eq. 3-4, where *p*, *q*, and *r* were the angular rates about the body axes measured via the angular rate gyroscopes.

$$\begin{aligned} \dot{\Phi} &= p + q sin\Phi tan\Theta + \mathrm{r} cos\Phi tan\Theta \\ \dot{\Theta} &= q cos\Phi - \mathrm{r} sin\Phi \\ \dot{\Psi} &= q sin\Phi sec\Theta + \mathrm{r} cos\Phi sec\Theta \end{aligned} \qquad 3\text{-}4$$

The final set of kinematic equations (Eq. 3-5), allowed for the dissociation of the relative airspeed into the ground speed and wind vector in the earth-fixed axes.

$$\begin{aligned} \dot{x} &= u(cos\Psi cos\Theta) + v(cos\Psi sin\Theta sin\Phi - sin\Psi sin\Phi) \\ &\qquad + w(cos\Psi sin\Theta cos\Phi + sin\Psi sin\Phi) + W_x \\ \dot{y} &= u(sin\Psi cos\Theta) + v(sin\Psi sin\Theta sin\Phi + cos\Psi cos\Phi) \\ &\qquad + w(sin\Psi sin\Theta cos\Phi - cos\Psi sin\Phi) + W_y \\ \dot{h} &= u(sin\Theta) - \mathrm{v}(\mathrm{cos\Theta sin\Phi}) - \mathrm{w}(\mathrm{cos\Theta cos\Phi}) - W_z \end{aligned} \qquad 3\text{-}5$$

Where: $\dot{x}$, $\dot{y}$, $\dot{h}$ are the aircraft inertial velocity components in the X, Y and –Z Earth axes;

and W_x, W_y, and W_z are the constant wind vector components in the X, Y, and Z Earth axes.

By utilising GPS-derived ground speeds, linear accelerometer measurements and angular rate gyroscope measurements combined with the kinematic relationships it was possible to estimate the constant wind vector components through the IEKF algorithm. The IEKF augmented state vector (see Sec. 2.4) therefore consisted of the parameter set:

$$x_{aug} = [x, \theta] = \cdots$$
$$[u, v, w, \Phi, \Theta, \Psi, x, y, z, W_x, W_y, W_z, magX, magY, magZ, \Delta V_{pitot}]^T \qquad 3\text{-}6$$

Where: u, v, w are the body axis linear velocities;

Φ, Θ, Ψ are the Euler angles;

x, y, z are the aircraft locations in the three orthogonal Earth axes directions;

W_x, W_y, W_z are the constant wind vector components in the Earth axes;

$magX, magY, magZ$ are the magnetic field vector components in the body fixed axes;

and ΔV_{pitot} is the pitot tube bias parameter.

The input vector, Eq. 3-7, for the IEKF, made use of the linear accelerometers and angular rate gyroscopes housed within the IMU enclosure.

$$u = [p_m, q_m, r_m, a_{xm}^{cg}, a_{ym}^{cg}, a_{zm}^{cg}] \qquad 3\text{-}7$$

Where: $p_m, q_m$and $r_m$are the angular rate measurements about the X, Y, Z body axes;

and a_{xm}^{cg}, a_{ym}^{cg} and $a_{zm}^{cg}$are the measured accelerations along the X,Y and Z body axes respectively.

The location of the IMU in the structural frame was given in Table 3-3 and was offset from the centre of gravity. The accelerometer data thus had to be adjusted to the centre of gravity for compatibility with the dynamic model used in the IEKF algorithm. This was achieved by applying Eq. 3-8. The correction was also consistent with the reference location for the final aerodynamic model in the parameter identification module.

$$\begin{aligned} a_{xm}^{cg} &= a_{xm}^{s} + (q^2 + r^2)x_{scg} - (pq - \dot{r})y_{scg} - (pr + \dot{q})z_{scg} \\ a_{ym}^{cg} &= a_{ym}^{s} - (pq + \dot{r})x_{scg} + (p^2 + r^2)y_{scg} - (qr - \dot{p})z_{scg} \\ a_{zm}^{cg} &= a_{zm}^{s} - (pr - \dot{q})x_{scg} - (qr + \dot{p})y_{scg} + (p^2 + q^2)z_{scg} \end{aligned} \qquad 3\text{-}8$$

Where: x_{scg}, y_{scg}, and z_{scg} are the location offsets from the centre of gravity;

a_{xm}^{s}, a_{ym}^{s}, and a_{zm}^{s} are the accelerations measured at the sensor locations;

and a_{xm}^{cg}, a_{ym}^{cg}, and a_{zm}^{cg} are the measured accelerations corrected to the centre of gravity.

The measurement (observation) vector, Eq. 3-9, was constructed based on the available instrumentation and to enhance the reconstructive characteristics of the algorithm.

$$\begin{gathered} z = [h, \dot{h}, magX, magY, magZ, velN, velE, north, east, \ldots \\ magXref, magYref, magZref, velP] \end{gathered} \tag{3-9}$$

Where: $h, \dot{h}$ are the height and vertical velocity respectively;

$magX, magY, magZ$ are the magnetometer measurements in the X,Y, and Z Earth axes respectively;

$velN, velE$ are the velocity components in the north and east directions;

$magXref, magYref, magZref$ are the magnetometer reference values in the X,Y, and Z Earth axes;

$velP$ is the true airspeed derived from the calibrated pitot tube measurements.

The true airspeed was derived from the indicated airspeed measurements by correcting for the actual air density based on a derived pressure (from QNH readings) and measured temperature. In order to match the reconstructed airspeed to the measured and corrected true airspeed at the location of the pitot tube, the reconstructed airspeed was corrected using Eq. 3-10.

$$\begin{aligned} u_{pitot} &= u_{cg} - rY_{cg_{pitot}} + qZ_{cg\_pitot} \\ v_{pitot} &= v_{cg} - pZ_{cg_{pitot}} + rX_{cg\_pitot} \\ w_{pitot} &= w_{cg} - qX_{cg_{pitot}} + pY_{cg\_pitot} \end{aligned} \tag{3-10}$$

Where: u_{pitot}, v_{pitot} and w_{pitot} are the velocity components at the pitot locations;

u_{cg}, v_{cg} and w_{cg} are the velocity components at the centre of gravity;

X_{cg_pitot}, Y_{cg_pitot}, and $Z_{cg_{pitot}}$ represent the pitot tube location offset from the centre of gravity;

and p, q and r are the rotational rates of the aircraft

The error variance of each output variable was estimated via Eq. 3-11 where the dependence on the estimated state error covariance was noted by the term CPC^T, thus differing from the output error covariance of a deterministic system that is based solely on the outputs of the estimator.

$$R = C\tilde{P}C^T + GG^T \tag{3-11}$$

Where: C is the linearized output matrix;
$\tilde{P}$ is the estimated state error covariance matrix;
and GG is the instrument measurement noise covariance matrix.

In terms of determining whether the augmented state vector was reconstructable given the set of measured parameters, the rank of the Grammian matrix was calculated. This method was described by Mulder et al. (1999). If the Grammian matrix (i.e. Eq. 3-12) was of full rank, then the non-linear system was considered re-constructible. This check was done at the end of the algorithm and was used to determine the validity of the reconstruction algorithm used on the system parameter set.

$$M_k = \sum_{k=1}^{N} \Phi_{a,k}^T \, C_{a,k}^T C_{a,k} \Phi_{a,k} \tag{3-12}$$

Due to initial algorithm stability problems caused by the lack of additional independent kinematic measurements, erroneous initial state covariance matrices and an observed systematic noise of the magnetometer measurements, the data compatibility method was decomposed into a combination of simpler processes. This simplification was achieved by removing the estimation of input vector biases from the IEKF algorithm to a post process. The manoeuvres were also separated into two sets differing by the level of information content. The method was defined by the flowchart in Figure 3-8 where the dashed boundaries demarcate the manoeuvre separation. This separation allows for a two-step procedure that led to a more stable iterative solution process that yielded acceptable results.

The first step consisted of the analysis of the rectangular circuits (box manoeuvres) that were relatively long manoeuvres with high directional information content. The second step involved the analysis of the more specialised system identification manoeuvres (limited spatial content but high dynamic content; see Sec. 3.2.2). Because the rectangular circuit dataset was relatively large (improved statistical properties) and contained mostly steady state information, it allowed for the efficient elimination of any systematic errors of the postulated dynamic model. It also allowed for the effective evaluation of necessary adjustments to the input and output measurement noise covariance matrices initially estimated through the optimal filter analyses. The resulting dynamic model and measurement noise covariance matrices were used as constants in the second step, along with a higher accuracy initial wind vector (based on step one results). A good initial estimate of the wind vector for the shorter manoeuvres of step two was important due to the lower degree of directional variation. The first step was therefore seen as a 'calibration and initialization' step before the analysis of the primary system identification manoeuvres.

During iterations of each step of the data compatibility process, the input vector time histories were reconstructed based on the smooth reconstructed state vectors. As defined by the method flowchart, Figure 3-8, this post analysis was required to determine and remove any input vector biases. A comprehensive residual analysis was also carried out on the input vector results and served as an indication of efficacy and thus adequacy of the Kalman filter process as well as to determine whether systematic errors had occurred. These analyses were similar to the analyses applied to the simulated data (Sec. 3.3.3) where the autocorrelation function and residual time histories were checked for consistency with the Gaussian noise assumption.

The significant points of both steps in Figure 3-8 can be defined by the following:

1. Specification of datasets to be analysed
2. Setup of the data compatibility algorithm and instrument position corrections
3. Execution of the IEKF algorithm
4. Analysis of residuals
5. Removal of biases in input measurements or adjustments in measurement variances if necessary

The process was repeated until satisfactory residuals were achieved for the reconstructed states.

To maximise the accuracy of the results, successive iterations of each step allowed for the correction of the initial state vector that had initially been calculated using the following process and thus was affected by measurement noise:

- The initial Euler angles, Φ_0, Θ_0 and Ψ_0, were obtained from the Euler angles estimated by the onboard real-time Kalman filter (refer to Sec. 3.2.3).
- The GPS information was used as the initial positional estimates.
- The initial airspeed components were derived from Eq. 3-13, using a zero magnitude wind vector (for the rectangular circuit manoeuvres), the initial Euler angles explained above, and the initial earth relative velocities obtained from the time rate of change of the GPS positional measurements. Initial airspeed components for the dynamic manoeuvres included the initial wind vector estimates from step one.

$$\begin{aligned}
u &= \dot{x}(cos\Theta cos\Psi) + \dot{y}(cos\Theta sin\Psi) - \dot{z}(sin\Theta) \\
v &= \dot{x}(sin\Phi sin\Theta cos\Psi - cos\Phi sin\Psi) \\
&\qquad + \dot{y}(sin\Phi sin\Theta sin\Psi + cos\Phi cos\Psi) + \dot{z}(sin\Phi cos\Theta) \\
w &= \dot{x}(cos\Phi sin\Theta cos\Psi + sin\Phi sin\Psi) \\
&\qquad + \dot{y}(cos\Phi sin\Theta sin\Psi - sin\Phi cos\Psi) + \dot{z}(cos\Phi cos\Theta)
\end{aligned} \tag{3-13}$$

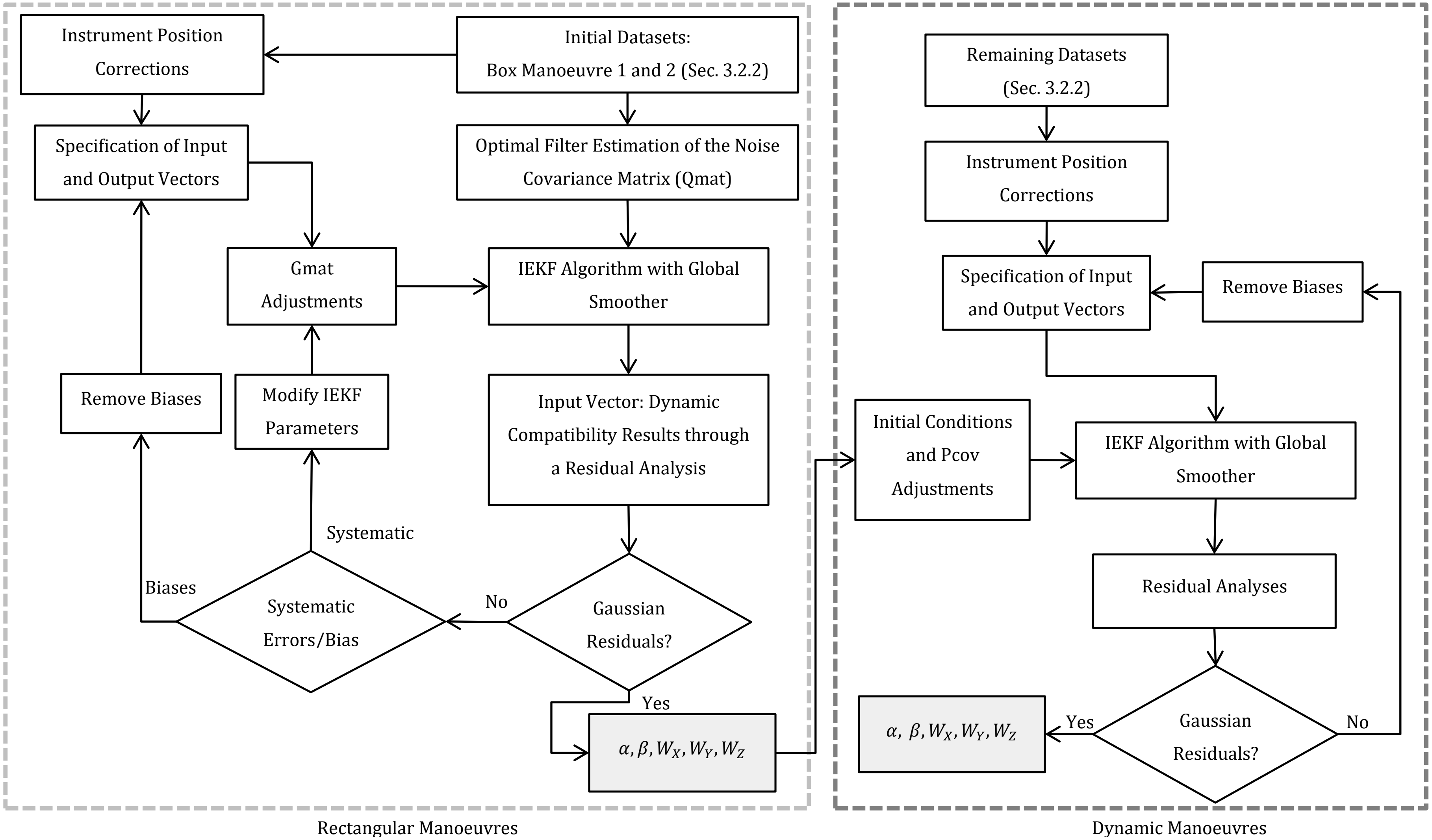

Figure 3-8 Data Compatibility Method Flowchart

3.3.5 Section Synopsis

After providing the motivation for selection of the IEKF algorithm, the details of implementation were described. A simulation platform was generated to determine the adequacy of combining the measurement covariance matrices determined via the optimal filter with the IEKF estimation algorithm. A two-step validation of the combination comprised of first determining the accuracy of the measurement error covariances from the optimal filter and second determining the accuracy of the estimated parameters via the IEKF algorithm. The application of this method in conjunction with the stepwise data compatibility method to the real flight data was also described including the corrections for biases, the initial state estimates, and adjustments to the covariance matrices within the IEKF algorithm. The input vector, output vector and augmented state vector were also defined. The implemented method correlated in part to the analysis of the system identification adequacy for a low-cost UAV, in which standard methods had to be modified to yield acceptable results.

3.4 PARAMETER IDENTIFICATION

3.4.1 Introduction

Parameter identification was based on the theoretical methods described in Sec. 2.2. A structured approach based on increasing model complexity was adopted to gain significant insight into the adequacy of the estimation algorithms given the information available through the flight test and data compatibility procedures. As specified in Sec. 1.3, the final aerodynamic model was based on linear aerodynamic assumptions about a single reference flight condition (i.e. the designed cruise condition). Algorithm verifications were based on secondary data within SIDPAC 2.0 and Klein and Morelli (2006) and are presented in Appendix E. A flowchart of the parameter identification method (demarcated by the dashed boundary) is presented, as a part of the entire system identification framework, in Figure 3-9. The process involved an analysis of the current model, initialization of the algorithm, application, and analysis of the results. Figure 3-9 also shows the dependence of each step of the parameter identification process on the manoeuvre design, data compatibility, and algorithm verifications.

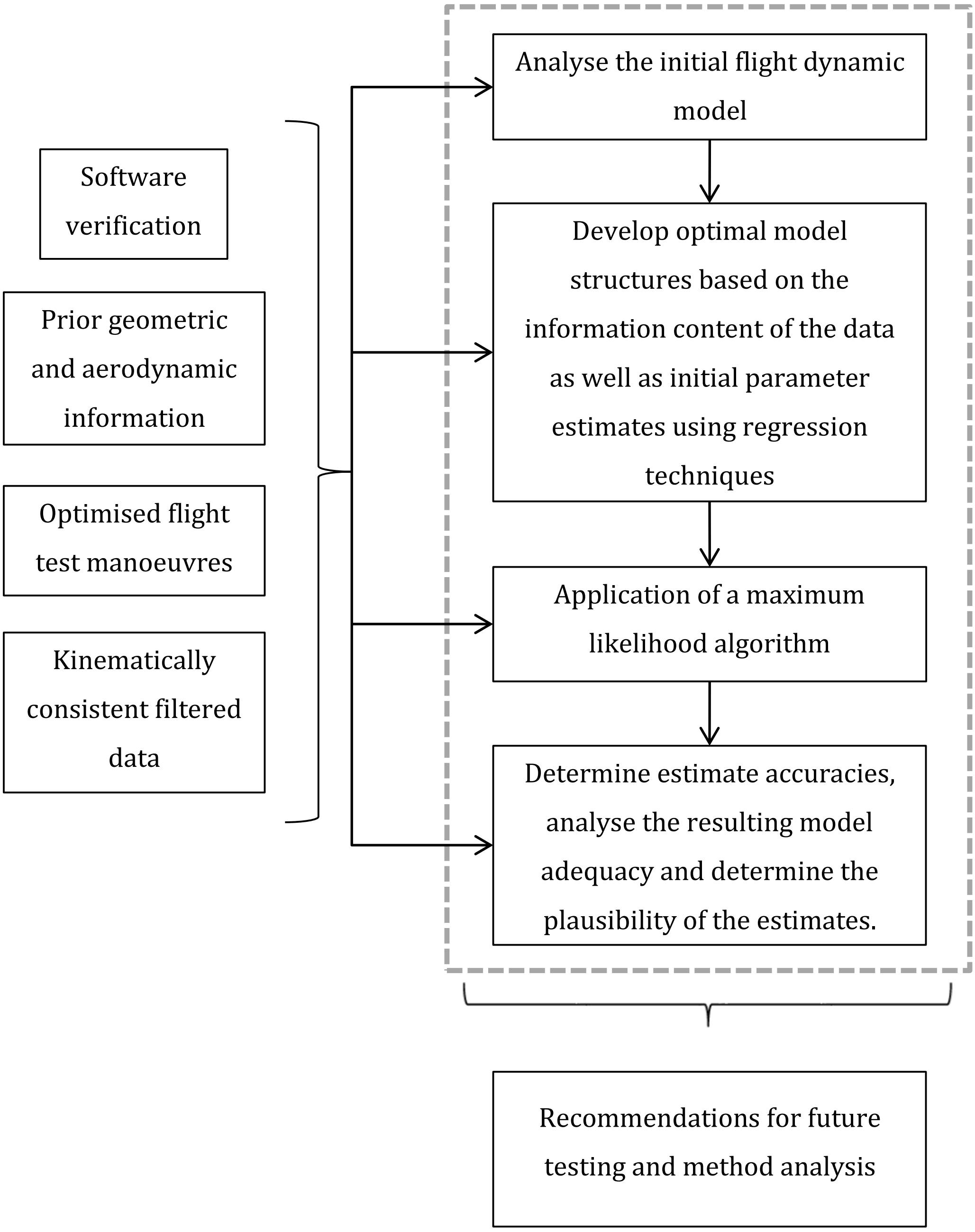

Figure 3-9 Parameter Identification Method within the System Identification Framework

3.4.2 Validity of Linearized Kinematics

Linearized decoupled equations of motion were assumed (based on the low amplitudes of the planned manoeuvres) to maintain a simplistic dynamic model. There was, however, uncertainty with regards to the actual linearity of the UAV responses because of the combination of the UAVs low inertia coupled with larger amplitude responses and higher load factors than expected (simulated data). The approach, driven by force and moment inputs, was then validated based on how representative the linearized model state reconstructions were of the actual system.

The force and moment inputs were derived from the data compatibility linear and angular accelerations (excluding gravitational acceleration) through Eq. 3-14 and 3-15. The angular accelerations used in Eq. 3-15 were derived from the filtered angular rates by application of a numerical central differencing scheme. The resulting body axis forces and moments were a combination of thrust and aerodynamic influences. These were then non-dimensionalized based on the free-stream velocity and density.

$$\begin{aligned}
\sum F_X &= F_{Xthrust} + F_{Xaero} = ma_{X(thrust+aero)} \\
\sum F_Y &= F_{Ythrust} + F_{Yaero} = ma_{Y(thrust+aero)} \\
\sum F_Z &= F_{Zthrust} + F_{Zaero} = ma_{Z(thrust+aero)}
\end{aligned} \qquad 3\text{-}14$$

Where: F_X, F_Y and F_Z are the applied forces (excluding gravity) in the X,Y and Z body axes;

and subscripts Thrust and Aero define the origin of the acceleration or force.

$$\begin{aligned}
L &= I_{xx}\dot{p} - I_{xy}\dot{q} - I_{xz}\dot{r} - r\big(I_{xy}p + I_{yy}q - I_{yz}r\big) + q(-I_{xz}p - I_{yz}q \\
&\qquad + I_{zz}r) \\
M &= -I_{xy}\dot{p} + I_{yy}\dot{q} - I_{yz}\dot{r} + r\big(I_{xx}p - I_{xy}q - I_{xz}r\big) - p(-I_{xz}p + I_{yz}q \\
&\qquad - I_{zz}r) \\
N &= -I_{xz}\dot{p} - I_{yz}\dot{q} + I_{zz}\dot{r} + p\big(-I_{xy}p - I_{yy}q + I_{yz}r\big) - q(I_{xx}p - I_{xy}q \\
&\qquad - I_{xz}r
\end{aligned} \qquad 3\text{-}15$$

Where: L, M and N are the applied moments about the X, Y and Z body axes.

Separate analyses were carried out for the longitudinal and lateral systems due to the decoupled nature of the approximation. To simplify the analysis, the longitudinal analysis was transformed to the stability axis defined in Figure 3-10, demarcated by an S subscript. The relevant forces were transformed to this axis system using Eq. 3-16. The thrust was implicitly accounted for through the augmented lift and drag forces.

$$
\begin{aligned}
C_{Laug} &= -C_{Z(thrust+aero)}cos\alpha + C_{X(thrust+aero)}sin\alpha \\
C_{Daug} &= -C_{X(thrust+aero)}cos\alpha - C_{Z(thrust+aero)}sin\alpha
\end{aligned}
\qquad 3\text{-}16
$$

Where: C_{Laug} and C_{Daug} are the non-dimensional augmented lift and drag force coefficients;

and $C_{Z(thrust+aero)}$ and $C_{X(thrust+aero)}$ are the non-dimensional normal and axial force coefficients due to thrust and aerodynamic forces.

In the current report, the additional subscripts, indicating an augmented coefficient, were used to clarify the difference between the standard definitions of lift and drag, and the modelled forces along the stability axes. The resulting linearized system is given by Eq. 3-17, where the delta symbols represent changes from the reference condition. The parameter definitions for V, α and q are presented in Figure 3-10.

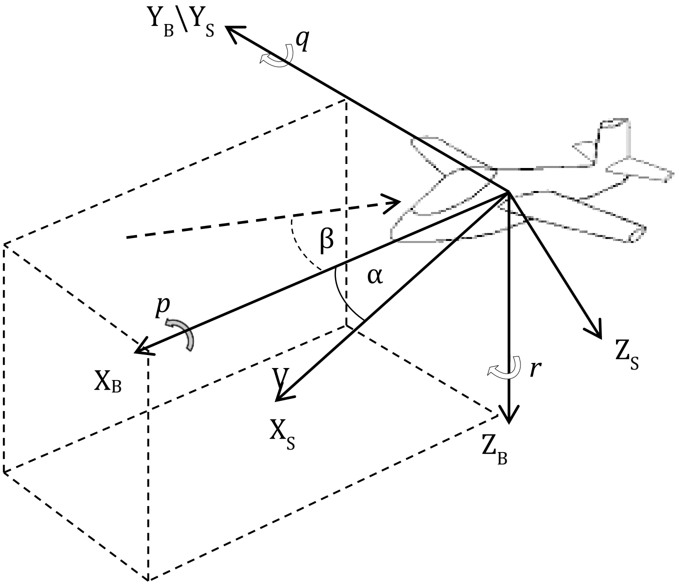

Figure 3-10 Reference Conventions for Flight Dynamic Modelling

$$
\begin{aligned}
\dot{V} &= -\frac{\overline{q_0}S}{m}\Delta C_{Daug} - gcos\gamma_0(\Delta\Theta - \Delta\alpha) + \Delta\dot{V} \\
\dot{\alpha} &= -\frac{\overline{q_0}S}{mV_0}\Delta C_{Laug} + q - \frac{gsin\gamma_0}{V_0}(\Delta\Theta - \Delta\alpha) + \Delta\dot{\alpha} \\
\dot{q} &= \frac{\overline{q_0}S\bar{c}}{I_{yy}}\Delta C_m + \Delta\dot{q} \\
\dot{\Theta} &= q + \Delta\dot{\Theta}
\end{aligned}
\qquad 3\text{-}17
$$

Where: C_D, C_L and C_m are the non-dimensional drag, lift and pitch moment coefficients; and Δ signifies the change of the parameter from the reference condition;

The lateral analysis was performed in the body axis. Positive directions for β, p and r are given in Figure 3-10. The side force and lateral moment coefficients were about the appropriate body axis.

$$\begin{aligned}
\dot{\beta} &= \frac{\overline{q_0}S}{mV_0}C_Y + psin\alpha_0 - rcos\alpha_0 + \frac{gcos\Theta_0}{V_0}\Phi + \Delta\dot{\beta} \\
\dot{p} &= \overline{q_0}Sb\left(\frac{C_l I_{zz}}{I_{xx}I_{zz} - I_{xz}^2} + \frac{C_n I_{xz}}{I_{xx}I_{zz} - I_{xz}^2}\right) + \Delta\dot{p} \\
\dot{r} &= \overline{q_0}Sb\left(\frac{C_n I_{xx}}{I_{xx}I_{zz} - I_{xz}^2} + \frac{C_l I_{xz}}{I_{xx}I_{zz} - I_{xz}^2}\right) + \Delta\dot{r} \\
\dot{\Phi} &= p + rtan\Theta_0 + \Delta\dot{\Phi} \\
\dot{\Psi} &= rsec\Theta_0 + \Delta\dot{\Psi}
\end{aligned} \qquad \text{3-18}$$

Where: C_l, C_n and C_Y are the non-dimensional roll moment, yaw moment and side force coefficients;

Bias parameters were included in the analysis for both the initial state vector and in the integration of states. These were introduced to avoid departures due to respective errors in the prescribed initial state vector and drift errors due to the linearization. The output error method was implemented to estimate these parameters and to reconstruct the state histories. The unknown parameter vectors for the lateral and longitudinal dynamics are given by Eq. 3-19 and Eq. 3-20, respectively.

$$\Theta_{lateral} = [\Delta\beta_0, \Delta p_0, \Delta r_0, \Delta\Phi_0, \Delta\Psi_0, \Delta\dot{\beta}, \Delta\dot{p}, \Delta\dot{r}, \Delta\dot{\Phi}, \Delta\dot{\Psi}] \qquad \text{3-19}$$

$$\Theta_{longitudinal} = [\Delta V_0, \Delta\alpha_0, \Delta q_0, \Delta\Theta_0, \Delta\dot{V}, \Delta\dot{\alpha}, \Delta\dot{q}, \Delta\dot{\Theta}] \qquad \text{3-20}$$

The resulting simulated outputs were compared to the measured outputs and evaluated regarding the model fit and Theil's inequality coefficients discussed in Sec. 2.5.

3.4.3 Parameter Identification Implementation

The parameter identification method, as described in Figure 3-9, encompassed the analysis of the existing model, the prediction of new optimal model structures, and the actual aerodynamic parameter estimation via the least squares and maximum likelihood algorithms based on the theory detailed in Sec. 2.2. Because of the iterative nature of the parameter identification procedure, model structures of varying parameterization were necessary before deriving a suitable result compatible with the manoeuvre set.

The datasets that were used in the analyses were four longitudinal multistep manoeuvres (i.e. 3-2-1-1 and 1-1-2-3 elevator excitations) and two lateral manoeuvres (i.e. bank to bank and rudder doublet combinations). The push-over pull-up and steady sideslip manoeuvres were not considered in this analysis due to large departures from the reference condition. Large departures from a reference condition would require a more complex non-linear model structures and a larger flight dataset to estimate an adequate model. As specified in Sec. 1.3, the objectives of the dissertation were to analyse the identification procedures from the perspective of implementation rather than to fully characterise the airframe. The simpler longitudinal multi-step and lateral control inputs provided adequate responses with sufficient information content to meet this requirement.

The quality of the initial flight dynamic model was analysed before the implementation of the aerodynamic model identification algorithm. This model was also used in JSBSim for the manoeuvre design process as described in 3.2.4. The analysis involved the comparison of reconstructed flight data with the measured results obtained through the flight tests. The linearized dynamic systems were used with a Runge-Kutta integration scheme and the initial aerodynamic model. This process was essentially the application of the first iteration of the output error method (refer to Sec. 2.2.3 for details) as implemented in Sec 3.4.2 but with the forces and moments determined through the aerodynamic model instead. At this stage, the initial state vector and the integration bias parameters (Eqs. 3-19 and 3-20) were already known. The results were ultimately used as the benchmark to the expected model developments via the continuation of the parameter identification procedure. Due to non-linear dependencies, the velocity propagation could not adequately be achieved through the linearized dynamics proposed in Sec. 3.4.2. The integration of the velocity was then excluded from this analysis with its time history being substituted by the measured values at each time increment. This allowed for the continued use of the linearized system to achieve the remaining states. The force and moment model structures and values are presented in Table 3-4. The residuals were checked for whiteness, goodness of fit and predictive qualities in terms of the Theil's inequality coefficient, variance proportion, and covariance proportion as described in Sec. 2.5.

After the analysis of the existing aerodynamic model, new aerodynamic models were estimated. The various parameter identification algorithms described in Sec. 2.2 were utilised in order of increasing complexity. By maintaining the linearized decoupled dynamics, model structures based on the requirements of the flight test data were established via the stepwise regression algorithm and the orthogonal regressor technique described in Sec. 2.2.2. The postulated regressor pool consisted of the aircraft state and control perturbations given by Eq. 3-21.

$$regressor\ set = \left[\alpha, \beta, \frac{\Delta V}{V_0}, \frac{pb}{2V}, \frac{q\bar{c}}{2V}, \frac{rb}{2V}, \delta_e, \delta_a, \delta_r, \delta_T\right] \tag{3-21}$$

Once the force and moment models were adequately estimated, an output error analysis was carried out, again using the linearized decoupled equations of motion. Because the actual control surface deflections were not measured, an assumed lag (i.e. constant time delay) model was imposed on the step inputs. The lag parameter was included in the parameter vector to be estimated. The analysis and estimation of the axial force, C_{Daug}, linked to the velocity propagation, was also eliminated from this stage of the algorithm. Once the parameter estimations were determined, the results were validated in terms of plausibility, residual whiteness and the goodness-of-fit criterion.

The logical progression from this stage of analysis was to move on to force and moment models inclusive of the available static wind tunnel data and the non-linear dynamic equations. The generic model used for this analysis assumed that the wind tunnel data could be linearly related to the entire model via the structure given by Eq. 3-22. A superposition of the individual force and moment components was postulated based on flight test data depicting small amplitude responses about a single reference condition.

The resulting generic structure was made up of three components i.e. the static wind tunnel data, the dynamic influences, and the additional static properties accounting for power effects that were not described by the wind tunnel data (i.e. wind tunnel delta).

$$C_i = f_{i,1}(\alpha, \beta, \delta_c)_{WT} + f_{i,2}\left(\frac{\Delta V}{V}, \frac{pb}{2V}, \frac{q\bar{c}}{2V}, \frac{rb}{2V}\right)_{dynamic} + f_{i,3}(\alpha, \beta, \delta_c)_{WTdelta} \qquad 3\text{-}22$$

Where: $i = C_L, C_Y, C_D, C_l, C_m$ or C_n;

and $\delta_c = \delta_e, \delta_a, \delta_r$ or δ_T; and

subscripts WT and WTdelta represent wind tunnel derived parameters and wind tunnel deltas respectively, while dynamic represents the dynamic

An example of the complete linear aerodynamic model structure using the formulation in Eq. 3-2 is given in Eq. 3-23 for the lift coefficient. A similar process of linear model structure build-up was also applied to the remaining longitudinal and lateral force and moment coefficients.

$$\Delta C_L = (C_{L\alpha}\Delta\alpha + C_{L\delta e}\Delta\delta_e)_{WT} + (C_{L\alpha}\Delta\alpha + C_{L\delta e}\Delta\delta_e)_{WTdelta} + C_{Lq}\frac{q\bar{c}}{2V} \qquad 3\text{-}23$$

This new model structure was then implemented in a further output error simulation. The full non-linear six degrees of freedom equations of motion were utilised to further increase the accuracy of the estimation process. To maintain the system simplicity, the longitudinal and lateral equations remained decoupled. This was achieved by using measured off-axis states where necessary. This method was described by Klein and Morelli (2006) as an adequate method to employ when the non-linearity of the system must be kept while decoupling the solution process. The disadvantage of using measured aircraft states instead of using the integrated states is that the measurement errors are propagated within the time history of the dependent states.

For all the manoeuvres analysed, the validation procedures involved testing the residuals for whiteness, determining the goodness-of-fit parameter value, and determining the Theil's inequality coefficients as described by Jategaonkar (2006) and in Sec. 2.5. The plausibility of the resulting models was based on a comparison of the aerodynamic derivative signs and magnitudes with conventional stable aircraft aerodynamic derivatives.

3.4.4 Section Synopsis

By maintaining a structured implementation method, a progressive analysis of the parameter identification algorithm was possible. The use of kinematic linearization allowed for the simplification of the model identification by decoupling the lateral and longitudinal dynamic analyses. The validation of using the linearized equations was analysed based on the dataset acquired from flight testing. Furthermore, an analysis of the initial aerodynamic model was implemented to create a benchmark to which further models were compared. Finally, the parameter identification algorithms were implemented, with the inclusion of the static wind tunnel data, to achieve the estimated aerodynamic model. The plausibility of results at each step was based on comprehensive residual analyses (refer to Sec. 2.5), while the final model was compared to historic stability and control data by measures of relative magnitudes.

3.5 ANALYSIS OF THE SYSTEM IDENTIFICATION IMPLEMENTATIONS

3.5.1 Introduction

The analysis of the implementations and methodologies described in the previous subsections consisted of the culmination of the restrictions encountered and the algorithm constraints based on the UAV system characteristics as well as the efficacy of the proposed solution modifications. The steps given in Figure 3-11 shows the method employed in determining the viability of each of the systems identification procedures. The following sub-sections describe the steps of the assessment method for each system identification module.

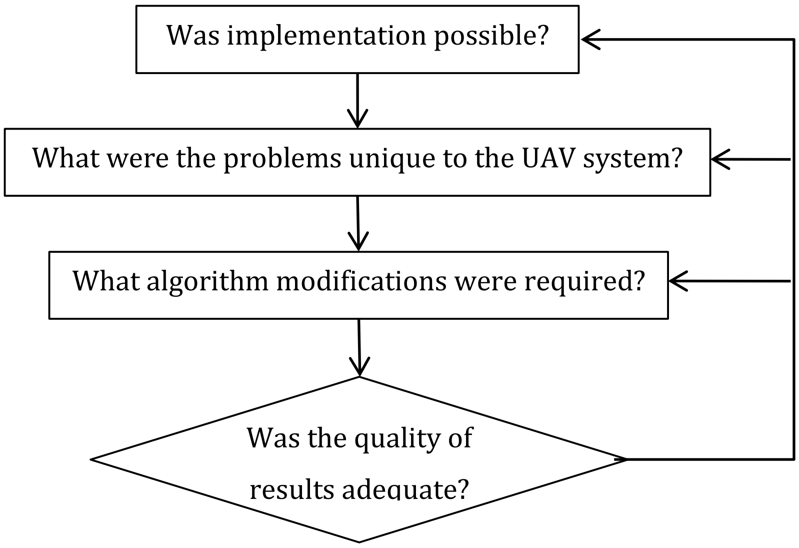

Figure 3-11 Assessment Questions for Determining the Viability of Systems Identification Algorithms

3.5.2 Flight Test Planning and Manoeuvre Implementations

The flight test was assessed in terms of whether all planned manoeuvres were carried out successfully. As noted in Sec. 3.2.6, these procedures were included in the manoeuvre verification procedure. Additional assessments were made based on a more qualitative analysis of the implementation of the flight plan. As described in Sec. 3.2, the autonomous navigation and stability control loops were disabled for the duration of the flight test. This differed from the systems identification applications to UAV's as discussed in Sec. 2.8 where the flight control systems were significant components of successfully implementing the flight tests. These additional assessments of the manoeuvres were based on the adequacy of the combination of remote piloting and ground station information in achieving the required reference conditions and the communication involved when the FCS predefined manoeuvres were triggered.

Implementation errors were evident in the longitudinal multi-step control inputs and the lateral rudder doublet inputs. The impact of these errors was analysed by comparing the power spectral densities of the designed input against the implemented input. The small control input errors were expected to yield insignificant reductions in the designed bandwidth, hence still providing adequate excitation.

An assessment of the practicality of the flight test procedures was achieved by combining the verification procedures described in Sec. 3.2.6 and the qualitative analysis of the manoeuvre implementation procedures.

3.5.3 Data Compatibility Procedures

In most systems identification analyses performed on manned or unmanned aircraft (refer to Chapter 2 for a list of references), extensive instrumentation systems were installed to obtain as much response data as possible from flight tests. The Modular UAV was equipped only with basic navigational sensors, detailed in Sec. 3.2.3, and, therefore, some critical states required for aerodynamic modelling had to be estimated via a data reconstruction algorithm.

As noted through the implementation method of the data compatibility algorithm, a significant objective was to reconstruct plausible angle of attack and sideslip time histories for each manoeuvre, based on an assumption of steady wind. The assessment of the validity of the reconstructed angle of attack and angle of sideslip was qualitative and based on realistic responses given the manoeuvre sets that were analysed. The validity of the assumption of a constant wind vector, however, was based on the assessment of the statistical variation of the estimated wind vector for all manoeuvres. Any significant effects of excluding scale factor and time lag parameters for each instrument measurement (refer to Eq. 2-29) would have been evident in the reconstruction due to the coupled nature of the utilised equations of motion. The Euler angles estimated via the onboard Kalman filter were excluded from the observation vector of the system because these were not direct measurements and could have influenced the data compatibility solution procedure. The plausibility of the reconstructed system was however validated by comparing the reconstructed Euler angles to the onboard estimated Euler angles.

The optimal filter described in Sec. 2.6 was utilised to determine the sensor measurement noise variances. The use of this method was validated through application to simulated data as described in Sec. 3.3.3. The initial validation process consisted of a residual analysis and a comparison of the estimated variance to the actual variance. The residual analysis was included to determine whether any systematic response was filtered from the dataset. An identical residual analysis was employed when the filter was applied to the actual flight data. The second step of validation as described in Sec. 3.3.3 involved assessing the effect of these estimated measurement variances when used within the IEKF algorithm. The IEKF algorithm was set up to estimate measurement biases on the simulated sensor data. The algorithm was implemented using both the correct measurement variances and the variances estimated via the optimal filter.

Due to the data compatibility problems experienced when the actual flight data was analysed (due to erroneous magnetometer measurements), a third simulated analysis was implemented. This was based on inflating the true variances by a factor of 10, thus simulating a significant error in the measurement variance inputs to the IEKF algorithm.

During application of the data reconstruction algorithm on the flight test data, it was evident that the magnetometer measurements were significant sources of error within the state reconstruction analysis. This source of error was attributed to the use of an approximated reference magnetic field vector generated from a pre-flight calibration or other undefined sources of magnetic interference. A third simulated data analysis was then carried out to simulate a large error in the measurement error estimations used in the IEKF. True variances were inflated by a factor of 10 and the effects this had on IEKF results was analysed.

Based on the positive results of the third validation test, the magnetometer measurement variances were adjusted to represent a much larger variance. The input measurement variances were simultaneously reduced due to the higher degree of confidence in the inputs. These modifications reduced the sensitivity of the IEFK algorithm to magnetometer systematic errors. The continued inclusion of the magnetometer measurement was because the overall trends available were useful for correcting for gyroscope drifting. The iterative specifications of the inflation factors were based on analysing the reconstructed input measurements (i.e. the accelerometer and angular rate gyroscope measurements) via a residual analysis. Gaussian residuals were an indication of the validity of the data reconstruction algorithm. A similar residual analysis was implemented on the observation parameters.

Much of the data reconstruction evaluation was based on residual analyses of the measurements. By analysing the problems encountered during this step of the systems identification algorithm, additional instrumentation requirements and pre-flight calibration procedures were assessed for future flight tests.

3.5.4 Parameter Identification

The parameter identification requirement was to derive a more realistic model for the test UAV based on applying increasingly complex modelling techniques. Because the flight testing programme was limited to a single 30-minute flight of small amplitude manoeuvres, about a cruise condition, an emphasis was placed on a linearized small perturbation model. The application of the parameter identification module was, however, an exploratory task to determine the extent of identification possible with the limited data available. The various implementation steps were described in Sec. 3.4.

Due to the strong dependence of the parameter identification module on both the flight test results and the data reconstruction, it provided a platform to further assess whether these respective modules were adequately implemented. The relevant performance criteria were mentioned in the theoretical review, Sec. 2.2. For the regression analyses, these included standard deviations, a comprehensive residual analysis and data co-linearity checks. The Cramer-Rao bounds, residual analyses, goodness-of-fit parameter, and the Theil's inequality coefficients were important for the output error assessments. The final validity check was based on a comparison of the estimated stability and control coefficients to other aerodynamically stable aircraft.

3.5.5 Section Synopsis

A detailed approach to the assessment of the adopted methodologies was described. The necessary modifications to the generic algorithms were discussed along with the specifications of the qualitative and quantitative performance criteria for each module of the process.

3.6 CHAPTER SYNOPSIS

The preceding sub-sections discussed the implementation of the method summarised in Figure 3-1. By following this high-level algorithm, it was implicitly possible to determine the capabilities of the standard application of the theory developed in Chapter 2 as well as to generate various modifications necessary for the continuation of the model identification algorithm.

The flight testing method involved designing an adequate set of manoeuvres given the limited flight time, an uncertain initial aerodynamic model, limited instrumentation, and FCS capabilities. The resulting flight test plan relied primarily on integrating remote piloting, predefined FCS control inputs, and telemetry monitored at the ground station. Due to the limited flight time, traditional manoeuvres were implemented, thereby generating adequate information content with expected safe responses.

The data compatibility process involved the implementation of the IEKF algorithm in combination with an optimal filter. A significant objective of the process was to determine whether the necessary set of dynamically consistent aircraft states could be achieved given the instrumentation available. This included the reconstruction of the angle of attack and sideslip, and implicitly, the wind vector.

The parameter identification implementation based on the theoretical algorithms detailed in Sec. 2.2 was presented. The validity of utilising linearized decoupled kinematic systems was of significance due to the expected non-linearity of small UAV dynamics. The remaining process followed the standard algorithms for model structure development and finally parameter estimation using the output error method.

Lastly, the assessment criteria adopted to determine the validity, performance and hence viability of the systems identification algorithm applied to the test UAV was described. These criteria provided the backdrop to the presentation and analysis.

4 RESULTS AND DISCUSSION

4.1 INTRODUCTION

This results chapter presents the data required to determine the viability of offline systems identification using low-cost instrumentation. The chapter is divided into three sections. The first describes the flight test procedures and presents the qualitative manoeuvre analyses. The second section presents the data compatibility results, where the quantitative analyses of the manoeuvres, instrumentation, and environmental assumptions are considered. The third section presents the model structure development and the parameter identification results.

4.2 FLIGHT TESTING

4.2.1 Introduction

The analysis of the flight test was based on two significant criteria. These consisted of the correct implementation of manoeuvres and an assessment of flight test procedures regarding practicality and efficacy. Separate manoeuvre sets were created based on the three objectives listed below:

- Atmospheric data generation
- Steady state data generation for static aerodynamic model parameters
- Dynamic data generation

The following sub-sections present the flight test data as well as the assessments for each manoeuvre set.

4.2.2 Atmospheric Data

The atmospheric evaluation included measurements of air temperature, the QNH reference sea level pressure, and the implementation of manoeuvres that were designed to facilitate the estimation of the wind vector. The resulting atmospheric data is presented in Table 4-1.

Air temperature measurements at the ground station remained at 19.0°C $\pm$ 0.5°C throughout the flight test. The QNH value representative of the reference sea level pressure was 102.6 kPa and 102.4 kPa at the start and the end of the flight test respectively. Given the short test period, approximately constant temperature (to within the resolution available), and the small change in QNH reference pressure, a steady environment could be approximated in the system identification analysis procedures. The air pressure was determined from standard atmosphere tables using the temperature and QNH measurements. The air density was then calculated from the corresponding temperature and pressure.

Table 4-1 Atmospheric Data Obtained During Flight Test

Measurement Timeline	QNH [kPa] (Reference Pressure)	Altitude [m] (ASL)	Temperature [°C]	Pressure [kPa]	Density [kg/m^3]
Initial	102.60	1400	19.0	86.73	1.03
		1600	17.7*	84.60	1.01
Final	102.40	1400	19.0	86.55	1.03
		1600	17.7*	84.43	1.01

*Derived from the ISA table

The temperature, pressure, and indicated airspeed were used to evaluate the true airspeed according to Eq. 4-1. Eq. 4-1 is only applicable if the airflow corrections between indicated airspeed and a calibrated measurement are minimal (i.e.$V_{CAS} \cong V_{IAS}$) and if the compressibility effects can be considered negligible (i.e.$V_{CAS} \cong V_{EAS}$). The former requirement was considered adequate due to the positioning of the pitot probe away from prop-wash effects and relatively far ahead of the wing leading edge. The only correction was made based on the relative position of the pitot away from the centre of gravity and the kinematics of the manoeuvres. The effect of the latter assumption based on compressibility effects were also considered minimal due to the test flight condition Mach number being less than 0.1. Given the assumed applicability of Eq. 4-1, an uncertainty for the derived true airspeed was then required because of its significance in both the data compatibility and parameter estimation routines.

$$V_{TAS} = f(V_{IAS}, T, P) = V_{CAS}\sqrt{\rho_0}\sqrt{\frac{RT}{P}} = V_{IAS}\sqrt{\frac{\rho_0}{\rho}} \qquad 4\text{-}1$$

Where: V_{TAS} and V_{IAS} are the true airspeed and indicated airspeed respectively;

ρ_0 is the reference density, 1.23 kg/m^3;
R is the universal gas constant for air;
T is the temperature in Kelvin;
and P is the static pressure in Pascals.

The true airspeed uncertainty was evaluated by Eq. 4-2 that accounts for resolution uncertainties determined through Eq. 4-3. Measurement cross-correlations between temperature, pressure, and indicated airspeed were neglected.

$$\bar{u}_{VTAS} = \sqrt{\left(\frac{\partial V_{TAS}}{\partial V_{IAS}}\right)^2 (\bar{u}_{IAS})^2 + \left(\frac{\partial V_{TAS}}{\partial T}\right)^2 (\bar{u}_T)^2 + \left(\frac{\partial V_{TAS}}{\partial P}\right)^2 (\bar{u}_P)^2} \qquad 4\text{-}2$$

Where: $\bar{u}_{VTAS}$, $\bar{u}_{IAS}$, $\bar{u}_T$, $\bar{u}_P$ are the uncertainty for the true airspeed, and mean uncertainties for indicated airspeed, temperature, and pressure respectively;
$\frac{\partial V_{TAS}}{\partial x}$ were the sensitivities based on the respective parameters, *x*: V_{IAS}, P, and T.

$$\bar{u}_{measurement} = \frac{0.5(res)}{\sqrt{3}} \qquad 4\text{-}3$$

Where: *res* is the measurement resolution.

Two representative cases for the uncertainty analysis were evaluated:

1. Only uncertainties based on instrument resolution were applied.
2. The uncertainties of temperature and pressure were artificially inflated to approximate large uncertainties due to QNH altitude differences (environmental differences) and human error applied to temperature measurements.

The second case was thought to yield a more realistic approximation to the respective uncertainties. The resulting uncertainty of the true airspeed for both cases are given in Table 4-2, where the corresponding sensitivity parameters of Eq. 4-2 were evaluated for a cruise condition at 22m/s and at an altitude of 1600m ASL (Above Sea Level).

Table 4-2 Uncertainty Results for True Airspeed Evaluations

Case	$\bar{u}_{VTAS}$ [m/s]	$(res)\ \bar{u}_{VIAS}$ [m/s]	$(res)\ \bar{u}_{T}$ [°C]	$(res)\ \bar{u}_{P}$ [kPa]
1	0.11	(0.01) 0.00	(0.1) 0.03	(0.01) 0.00
2	0.34	(0.01) 0.00	(0.5) 0.14	(0.10) 0.03

The uncertainty presented in Table 4-2 has a direct influence on the estimation of the wind vector within the data compatibility procedure. This dependence is discussed in Sec. 4.2.5. Given the cruise airspeed of the UAV of 22m/s, the results presented in Table 4-2 are respectively equivalent to a 0.50% and a 1.55% relative uncertainty. As would be expected, the impact of true airspeed uncertainty would increase as the cruise speed decreases. A generic conclusion on the adequacy of this measurement system, for system identification on this class of UAV, cannot be made because of the direct relation to the particular flight characteristics (i.e. Operational speed regimes).

The next objective of the atmospheric analysis was to perform two remotely piloted box manoeuvres. These manoeuvres were designed to generate enough information content within the data to estimate a mean wind vector. The design criteria for this manoeuvre stipulated a rectangular flight path at a constant height of 200m and nominal indicated cruise airspeed of 22m/s. The unconditioned telemetry data for the first box manoeuvre is shown in Figure 4-1. The figure includes the three control effectors on the left as well as the three significant dynamic response parameters for the box manoeuvre (i.e. height, airspeed, and position) on the right. The linear trend lines are shown in Figure 4-1(d) and (e) were derived from least squares fitting routines. Each segment of the manoeuvre is demarcated by a vertical line in Figure 4-1(d). Identical time axes are used in Figure 4-1(a)-(e) to assist in comparisons between the parameters. Arrows are used in Figure 4-1(f) to denote the anti-clockwise flight path on a horizontal plane.

Table 4-3 Statistical Properties for the Least Squares Linear Fitting of the Height and Velocity Measurements from the First Box Manoeuvre

Statistics	Height [m]	Velocity (Indicated) [m/s]
mean	180.9	21.1
std. deviation	25.8	1.6
range	94.3	9.4
min	141.7	16.0
max	236.0	25.4

Table 4-3 includes the relevant statistical data for the two trend lines. Particular attention should be drawn to the velocity and height standard deviations and the range of each parameter. The height measurement range of 94.3m meant that the effect of wind shear had to be considered a possible influence on the estimation of a mean wind velocity vector. The velocity measurement yielded a standard deviation and measurement range of 1.6m/s and 9.4m/s respectively. This magnitude of velocity variation combined with the irregular flight path (shown in Figure 4-1(f)) negated the possibility of easily approximating a mean wind velocity vector through algebraic vector summations. The more complex dynamic relationships required to determine the wind velocity vector were included in the two-step IEKF data compatibility analysis (Sec. 3.3.4).

The least squares trends for altitude and velocity also indicated an overall decrease in mechanical energy during the manoeuvre. A mean rate of descent of 0.5m/s combined with a deceleration of 0.02m/s^2 indicated inadequate trimming of the UAV during the various segments of the manoeuvre. Further evidence of inadequate trimming can be extracted from Figure 4-1(a), (b), and (c), each presenting the significant control inputs by the remote pilot throughout the manoeuvre. The linear and angular accelerations generated by the continuous control inputs meant that the objective of steady trimmed flight segments of the box manoeuvre was not achieved.

Telemetry data with similar characteristics was generated for the second box manoeuvre and is presented in Appendix F. The flight height was significantly below the test height. This led to a notably different wind vector estimated via the data compatibility process as will be presented and discussed in Sec. 4.2.5.

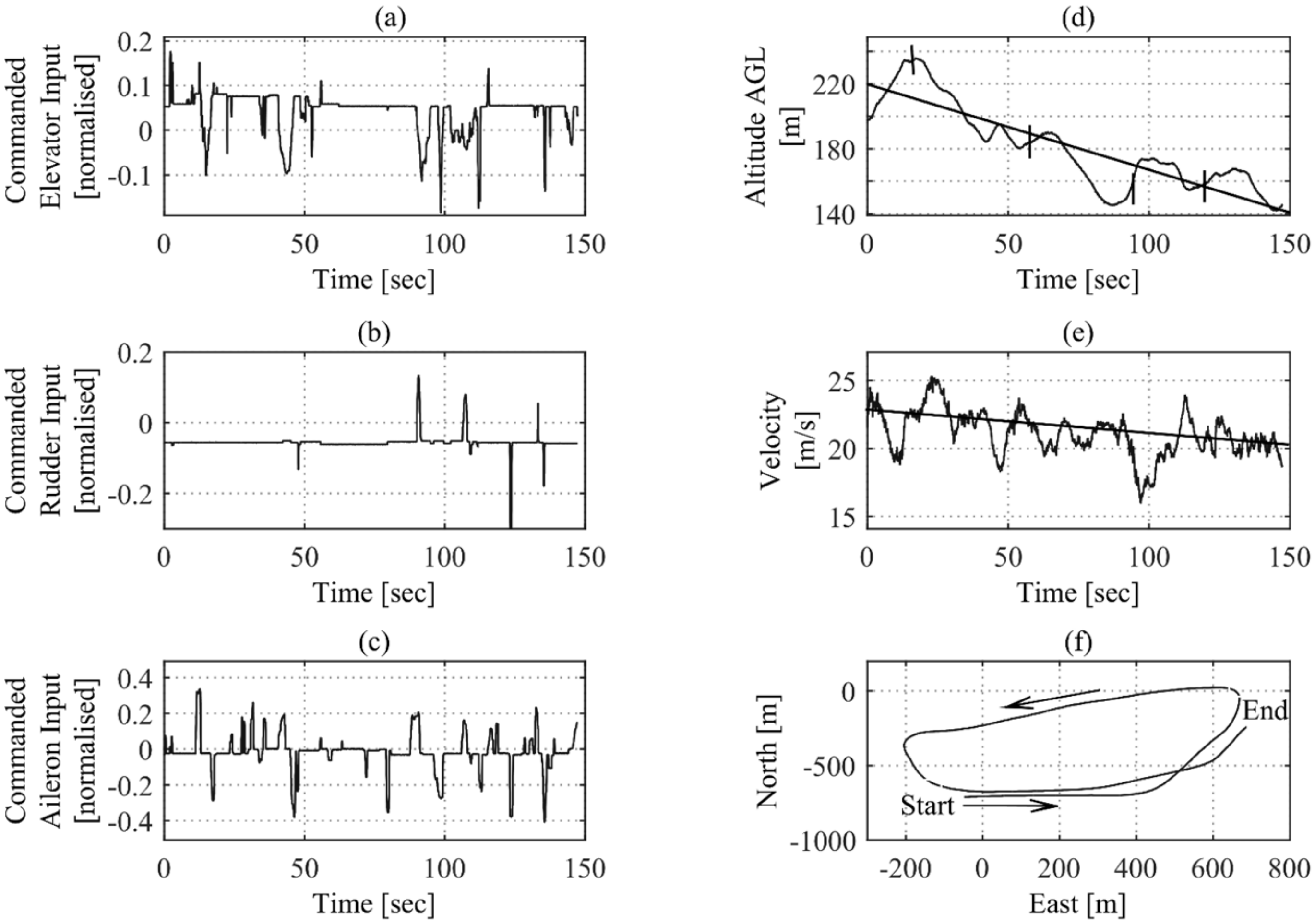

Figure 4-1 Initial Box Manoeuvre Flight Data for a Nominally Constant V_{IAS} = 22 m/s

Telemetry was streamed to the ground station and indicated airspeed was sporadically communicated to the remote human pilot during the manoeuvres (see Figure 3-7 for operational setup). Through the manoeuvre results discussed above, it was evident that the reference frame for remotely piloted flight hindered the ability to perform accurate manoeuvres. The lack of significant visual cues also contributed to the inability to maintain the box manoeuvre shape and to adequately hold altitude. A waypoint navigation system to achieve adequate rectangular flight paths and a trimming autopilot to attain steady flight about the desired condition is strongly recommended for future systems identification flight testing. In the absence of a navigation system, a continuous audio cue of relevant state information should be given to the remote pilot to improve situational awareness.

Consideration of the above shortfalls related to accurate data generation led to strong requirements for an adapted flight test approach and, in particular, the results pointed out the significant disadvantage brought about by the lack of a navigation system. The impact of higher accuracy temperature and pressure measurements was also presented and may warrant the use of on-board sensors dependent on the speed regimes being modelled.

4.2.3 Steady State Data

The requirements for the steady state manoeuvre set were to obtain adequate data to estimate the steady state coefficients of an aerodynamic model. A quasi-steady flight was to be achieved with minimal transient oscillations of aircraft dynamic states. Due to the simplistic linear aerodynamic model objective and method, detailed in Sec. 1.3 and Sec. 3.2.2 respectively, large departures from the reference flight condition were to be avoided. The two proposed manoeuvres were steady push-over pull-ups and steady sideslips.

The aircraft response to the first steady push-over pull-up manoeuvre is presented in Figure 4-2, providing the important parameters that define the success of the manoeuvre. The input to the system and the resulting body-axis accelerations (excluding gravitational acceleration component and where the Z-axis convention is positive down) are given in Figure 4-2 (a), (b) and (c) respectively, whilst the kinematic state data is given in (d), (e), and (f). A predefined automatic elevator sinusoidal command was utilised at a frequency of 0.1Hz and amplitude of $\pm 3°$ about the trim deflection. The combination of the large elevator command and the long period of implementation led to the stalling of the aircraft during the second push-over pull-up (refer to Appendix F), which prompted pilot intervention seen as the large elevator command at the end of the manoeuvre.

Figure 4-2 (e) and (f) show an approximately linear initial rate of change as illustrated by the solid trend line. This rate of change had described inadequate trimming of the aircraft before the manoeuvre was implemented. The significant differences between the initial and end conditions were characteristic of a high energy manoeuvre. Both push-over pull-up manoeuvres were characterised by large pitch rates, significant velocity (+6 and -11m/s) and altitude variations (-50m), and high load factors (greater than +2g). The above-mentioned factors deviated from the standard small perturbation assumptions made for linearized dynamic modelling applicability. The data analyses of such non-linear manoeuvres were beyond the scope of this dissertation.

The manoeuvre specification was a result of a simulated response test using the initial aerodynamic model. The error in the push-over pull-up manoeuvre was thus a specification error based on an inadequate initial model. This error signified the importance of an adequate initial flight dynamic model for manoeuvre design tasks.

It is recommended that either a significantly lower frequency specification or a lower amplitude input be used in future systems identification tests. A lower frequency specification would require a longer manoeuvre period resulting in flight across the boundaries of the designated test airspace. A reduction in the amplitude would be the only adjustable parameter available to meet the manoeuvre objective given the system limitations.

The coordinated steady heading sideslip was the second type of steady state manoeuvre performed. This manoeuvre was implemented to generate data on the lateral coupling of the aircraft flight dynamics. The success criterion was to maintain different magnitudes of sideslip while maintaining a heading. Effective lateral trimming of the aircraft, via roll control authority was required and was undertaken via the remotely piloted commands. The rudder step inputs were also implemented by remote piloting rather than a flight control system function. The telemetry data for the manoeuvre is presented in Figure 4-3, where the lateral control inputs and the lateral acceleration are given on the left and the aircraft states on the right.

The rudder inputs shown in Figure 4-3 (b) indicate that the required rudder steps of 3°, 7° and 15° were successfully implemented and the approximately constant headings for each rudder deflection are given in Figure F-11. A trimmed kinematic state accompanying each deflection was, however, not achieved. Figure 4-3 (a) shows the continuously changing aileron correction required to achieve a constant heading. The large roll and yaw rates between $\pm 20\ {}^{\circ}/s$ shown in Figure 4-3 (d) and (e) were also an indications of inadequate trimming.

The failure to achieve both steady state manoeuvre types in terms of meeting the planned quasi-steady conditions demonstrated the difficulties in performing accurate steady systems identification manoeuvres through remote piloting. Pilot over-corrections due to the lack of sufficient visual cues were one of the main contributing factors to this failure. Once again the advantage of a complete flight control system in the UAV system identification process was highlighted. Adequate trimming controllers should be used to attain the steady trimmed states required at specified flight test conditions. Sufficiently accurate initial flight dynamic models are also required for manoeuvre design allowing for an accurate predictive environment for departure limitations. The analyses of these steady manoeuvres were beyond the scope of this dissertation due to high dynamic nature of the manoeuvres and the departures from the modelled flight condition. It should be noted that there was no evidence of a mathematical or instrumentation restriction to estimating the required steady state aerodynamic parameters from these datasets, however, a non-linear, coupled dynamic model would be required to adequately model the dynamic behaviour of the aircraft. Increasing the number of unknown model parameters via the non-linear modelling, would yield a significant decrease in the statistical accuracy of individual model parameters because of the limited datasets available.

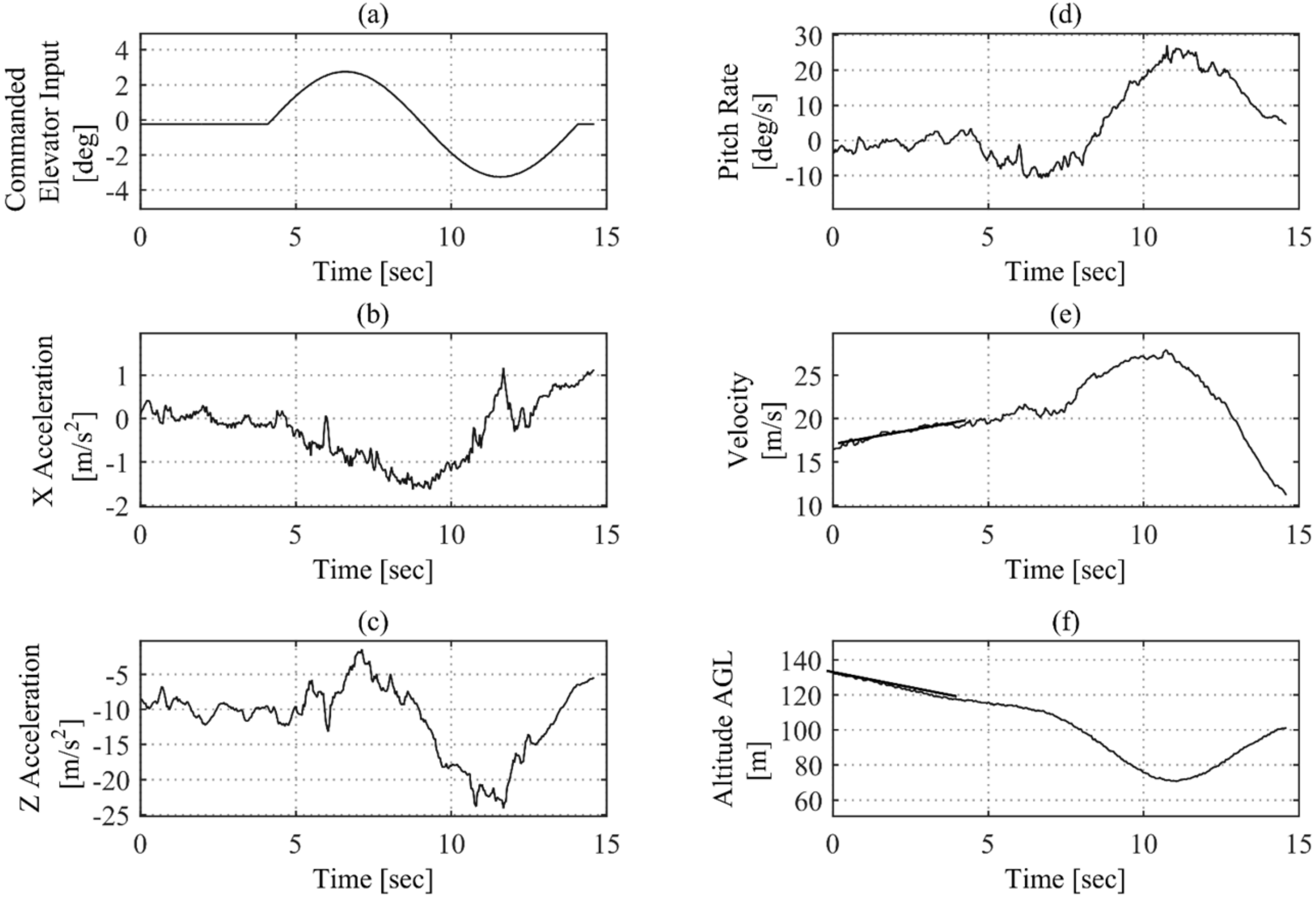

Figure 4-2 Initial Quazi-Steady Push-over Pullup Manoeuvre at Intended Nominal Speed of 22 m/s

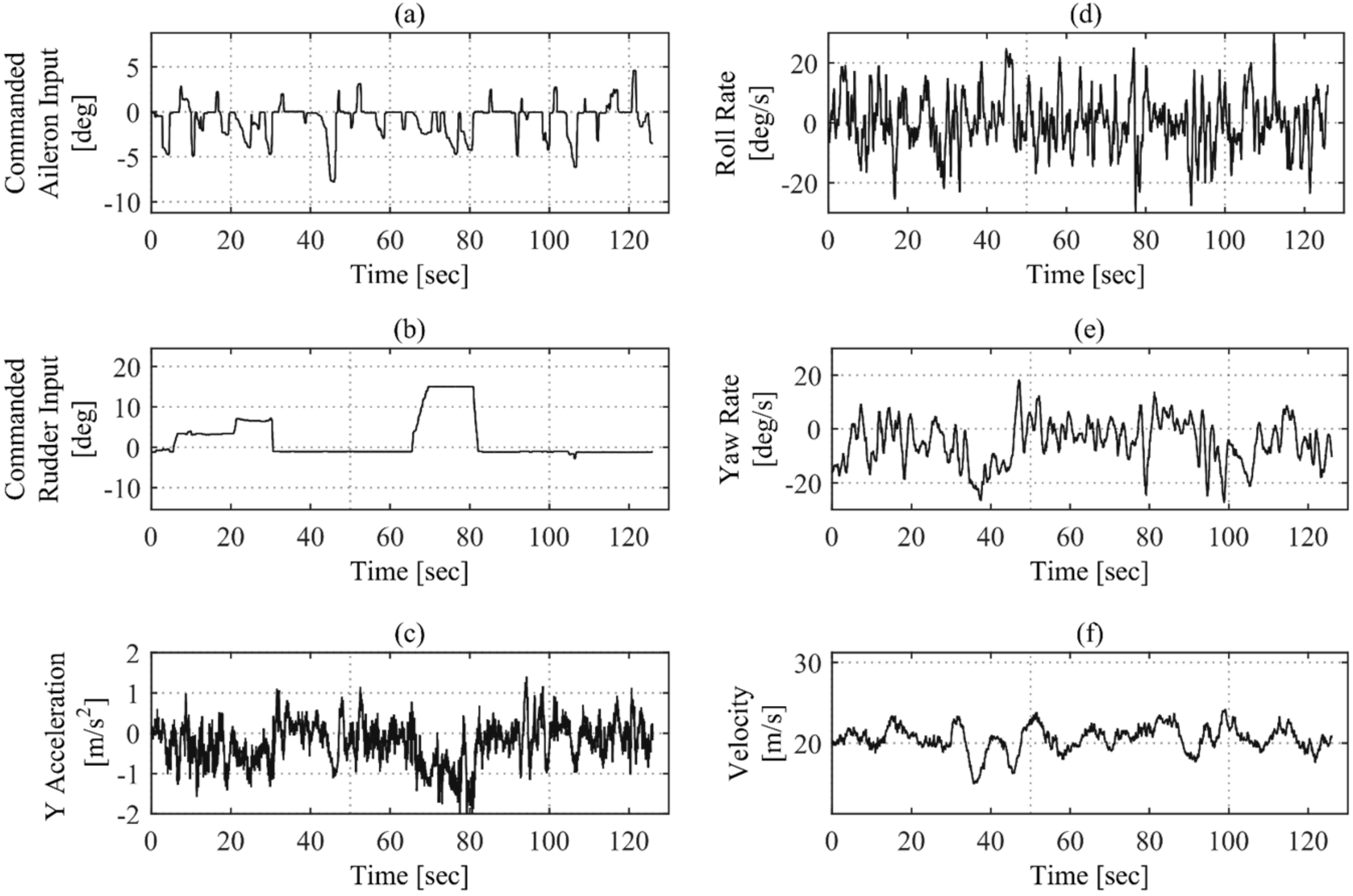

Figure 4-3 Coordinated Steady Sideslip Flight Data

4.2.4 Dynamic Data

The implementation of the manoeuvres associated with the dynamic data generation was described in Sec. 3.2.2 and Sec. 3.2.5. The manoeuvres consisted of 3-2-1-1 or 1-1-2-3 elevator deflection sets to excite the longitudinal short period mode as well as a combination of bank-to-bank and rudder doublets to excite the Dutch-roll mode and generate information on the lateral coupling.

Four 3-2-1-1 (or 1-1-2-3) manoeuvres were implemented via predefined control commands. Telemetry from one of these manoeuvres is presented in Figure 4-4. The parameters important to a longitudinal, linearized model are provided. The elevator control input and the X and Z body axis accelerations (excluding gravitational contributions) are presented in Figure 4-4 (a)-(c). Figure 4-4 (a) shows the 3-2-1-1 elevator command starting with a positive 4° deflection. The pitch rate indicated airspeed, and height represents the important longitudinal states in a linearized model and are presented in Figure 4-4 (d)-(f). The remaining 3-2-1-1 and 1-1-2-3 longitudinal manoeuvres are presented in Appendix F, where the deviations from the trimmed conditions vary in magnitude.

The predefined manoeuvre, implemented through a limited control system function, was implemented after a trimming procedure via full remote control. Adequate trimming of the aircraft was achieved with approximately constant airspeed and altitude, and a near zero pitch rate. The velocity telemetry for all four longitudinal manoeuvres (Appendix F) shows that the nominal indicated airspeed was consistently lower than the specified 22 m/s thus introducing some error into the model development stages. Figure 4-4 (a) shows a small positive X-acceleration. This acceleration bias magnitude is less than 0.5 m/s^2, however, leading to a minor rate of change of the initial velocity measured. The aircraft returned to a steady trimmed condition noted by an approximately zero pitch angular velocity and constant airspeed and altitude. The final loss in altitude was approximately 5 m due to mechanical energy losses through the manoeuvre. Similar trends for the aircraft responses were evident for the remaining longitudinal manoeuvres, although larger changes in altitude were evident (approximately 20 m). Given the conservative pressure uncertainty determined in Sec. 4.2.2, presented in Table 4-2, and the ISA change in pressure for a 20m height difference at the given atmospheric conditions (approximately 0.2 kPa), the change in the initial and final conditions was significant. This change in reference condition was taken into account when correcting the indicated airspeed to true airspeed. The change was deemed small enough not to warrant an additional linearized model at a new reference condition.

The oscillations that occur as a result of the longitudinal excitation are evident by the small amplitude overshoots of the Z-acceleration and pitch rate measurements. The signal to noise ratio based on the oscillation amplitude was not favourable. Of particular importance to the small amplitude, excitation was an implementation error regarding the 3-2-1-1 time step parameter. The Δt step time for the 3-2-1-1 manoeuvres was 0.44s rather than the designed 0.36s (i.e. a 16.4 % target-frequency error). The impact of the error is graphically presented in Figure 4-5 for the 1-1-2-3 case where the spectral density of both the implemented and the designed manoeuvres are presented. The effect of the frequency difference led to a shift in the power spectral density of the input towards the lower frequency band. The shaded area indicates the effective frequency band reduction (spanning approximately 0.3 Hz). Given the erroneous input frequency band, the calculated longitudinal short period frequency of 0.834 Hz (refer to Sec. 3.2.5) still remained inside the excitation band. It should also be noted that the power spectral densities shown in Figure 4-5 were generated from the time histories of the commanded control inputs, ignoring any control surface response time. Accounting for this would further shift the input spectral density band towards lower frequencies further reducing the significance of the command error.

The above-mentioned command error does cause a reduction to the available natural frequency error margin. An error margin is required to accommodate differences between the natural frequency derived from the initial aircraft model and that of the actual aircraft. For the current case shown in Figure 4-5, a reduced error margin would be significant if the true short period natural frequency of the aircraft was closer to or above 1 Hz. The combination of the implementation error, and initial model errors were deemed contributing factors to the small oscillatory nature of the aircraft response.

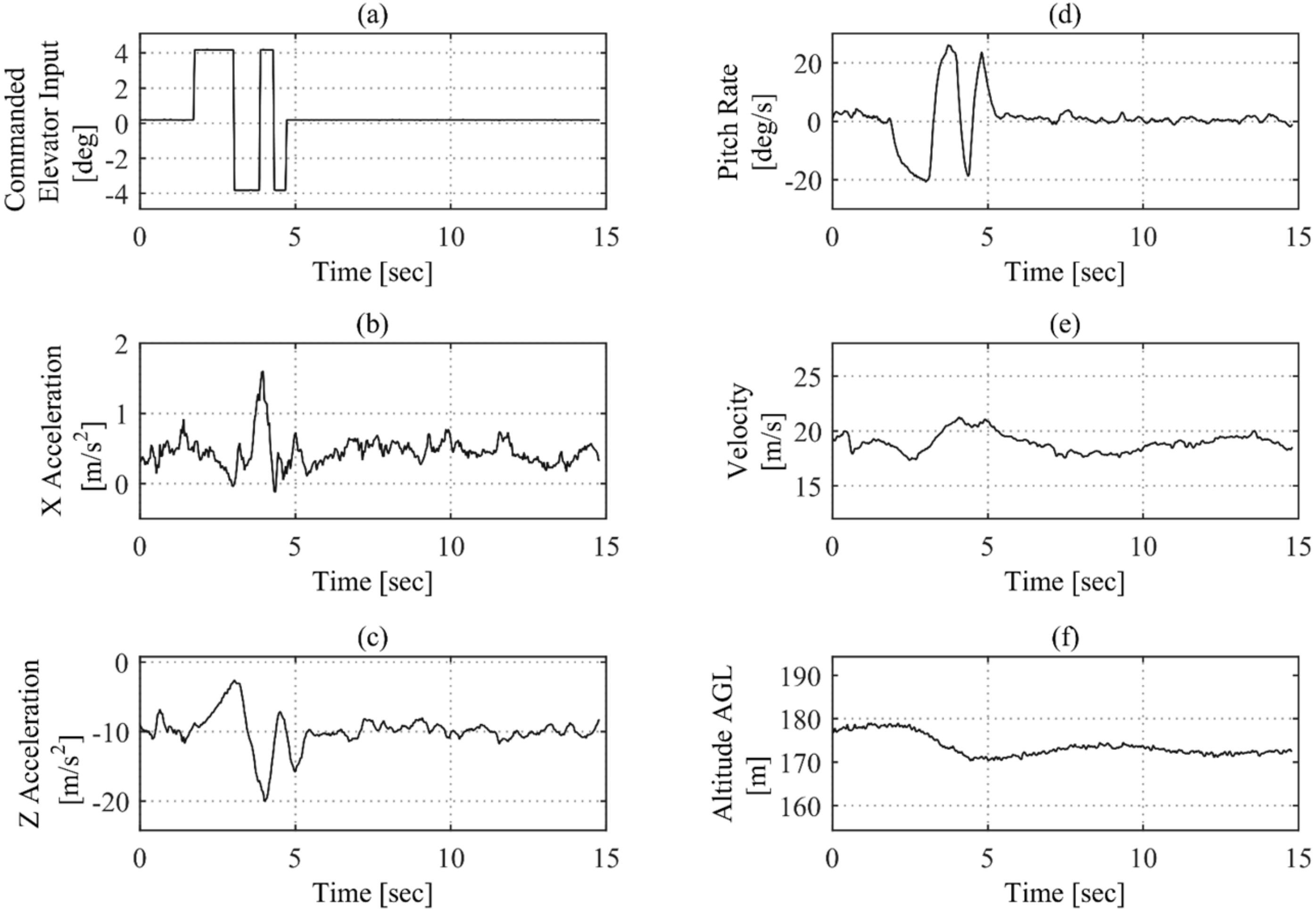

Figure 4-4 Longitudinal Excitation: 3-2-1-1 Elevator Command – Flight Data

When the actual longitudinal responses were compared to the simulated responses presented in Sec. 3.2.5, it was evident that a significant discrepancy existed. The actual responses were significantly more stable than the simulated responses (Figure 3-5). In particular, the phugoid mode damping was much higher in the actual aircraft as demonstrated by the low-frequency oscillations in Figure 4-4 (e) and (f) following the excitation. These comparisons further signified the inadequacies of the initial flight dynamic model and justified the selection of simpler more robust control input designs. A further, quantitative analysis of the level of excitation will be provided in Sec. 4.4, with particular attention given to longitudinal parameter identification requirements.

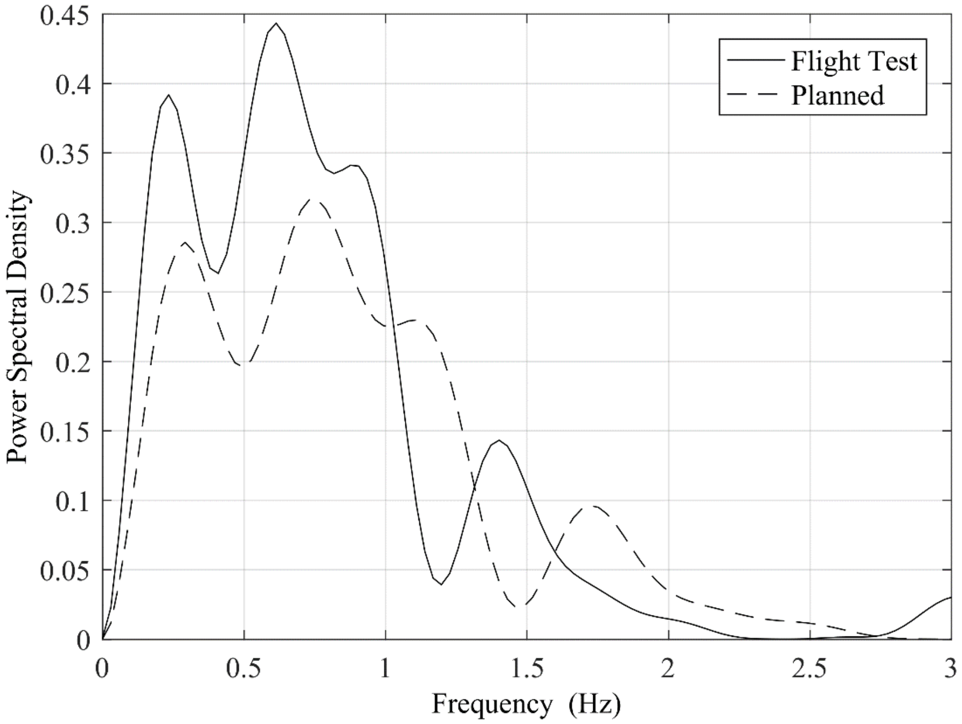

Figure 4-5 Spectral Density Difference between Planned and Achieved Control Input

Dutch-roll was the second dynamic mode that was excited. This was achieved via an optimised rudder doublet. These doublets were implemented following a bank-to-bank roll manoeuvre. The combination was achieved via both remote pilot commands and predefined FCS control commands.

The telemetry data from the dutch-roll manoeuvre is given in Figure 4-6. Subplots (a) and (b) represent the lateral control inputs, where the aileron command is implemented by remote piloting and the rudder input is a predefined FCS function. The sequential combination of the inputs was successful and the correct doublet amplitudes (±12°) were implemented. The manoeuvre was implemented at a well-trimmed flight condition with approximately zero angular rates and a constant airspeed at the start of the manoeuvre (i.e. approximately 2.5 sec). A slight decrease in altitude was registered in Figure 4-6 (c) but at a rate of climb magnitudes below 1m/s. The remaining aircraft responses are given in Figure 4-6 (c)-(f) and include the height, roll rate, yaw rate, and indicated airspeed respectively. The significant damped oscillatory responses of the roll rate and yaw rate should be noted and are indicative of a dutch-roll mode. The system returns to a steady state at a flight condition of lower altitude and significantly lower airspeed due to mechanical energy losses. As described in Sec. 3.2.2 the rudder doublet was performed immediately after the bank to bank manoeuvre to maximise the dynamic response. This sequential manoeuvre resulted in the actual dutch roll response at a slightly different flight condition (+7m/s) than planned as noted by the altitude and airspeed during the rudder command period. It is recommended that the dutch roll manoeuvre be a separate manoeuvre in future tests to avoid errors in initial flight conditions. Similar results were obtained for the repeated dutch-roll manoeuvre and are presented in Appendix F.

The above discussions of the lateral and longitudinal modal excitations and responses justified the choice of the simple optimised inputs. Complex optimised control inputs involving detailed harmonic analyses were not considered because of the level of uncertainty of the initial flight dynamic model. Adequate steady trimmed states were achieved before all excitations. The target velocity and reference altitude conditions were, however, often not met. A higher degree of control from an automated system is recommended to achieve required reference conditions in future flight tests.

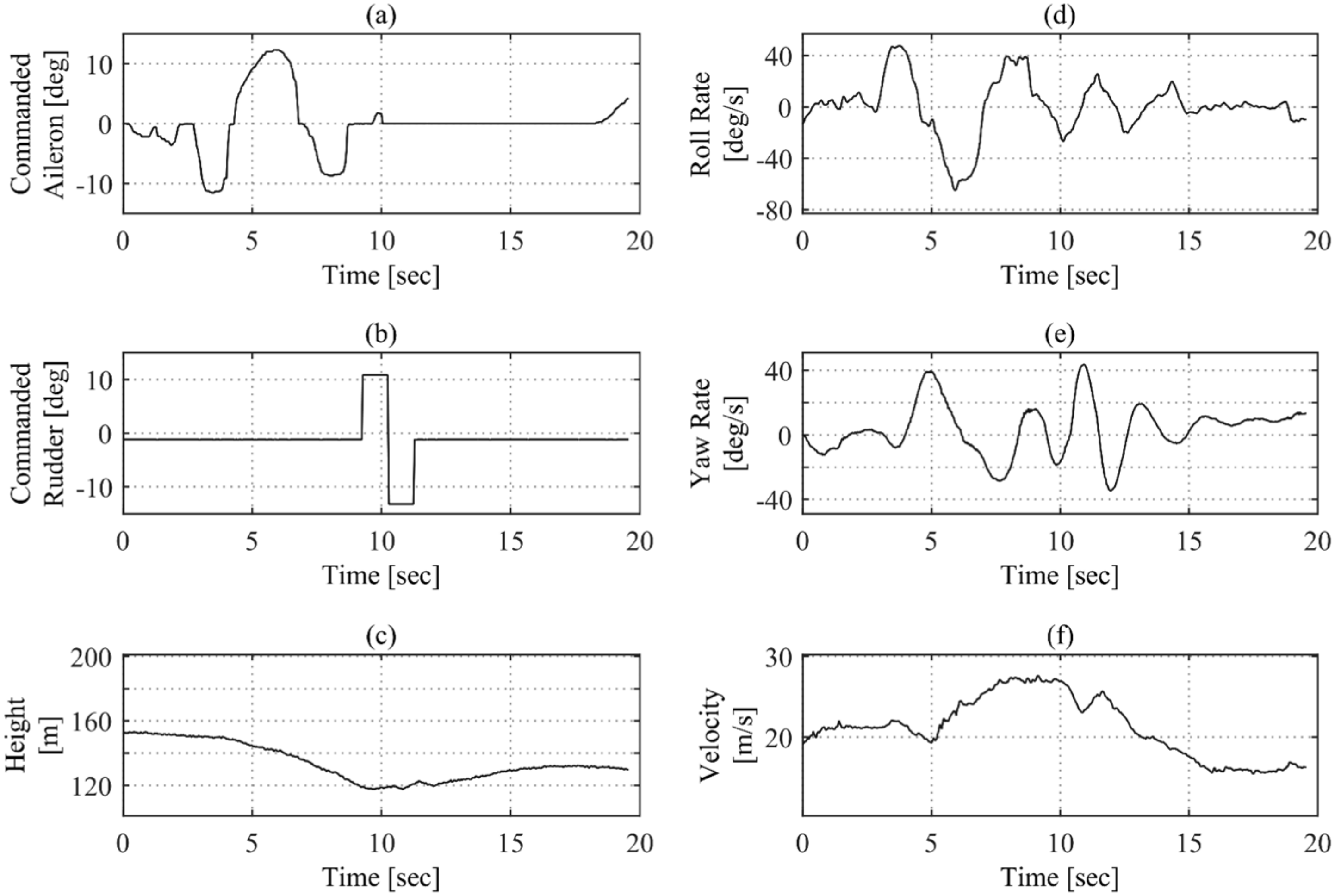

Figure 4-6 Bank to Bank and Rudder Doublet Combination – Flight Data

4.2.5 Conclusions

The previous subsections detailed the data obtained during the flight test and discussed the adequacy of the excitations, measurements, and implementation procedures. Emphasis was placed on qualitative criteria with a clear objective of assessing the practicality of the proposed flight test techniques.

Regarding the atmospheric data, the importance of an onboard air temperature sensor and a static pressure port is emphasised based on the potential errors introduced to the density estimations and by inference the derived true airspeed or Reynolds number. By reviewing the implementation of the box manoeuvres, it was clear that the success of the manoeuvre was significantly influenced by the pilot in the loop. This was attributed to the remote pilot's reference frame being disconnected from the actual dynamics of the UAV. The problem arising from different reference frames is unlike manned flight where the pilot has a significantly increased situational awareness due to the 'first-person-feel' of the dynamics of the aircraft as well as visual cues such as the horizon. The introduction of reliable autonomous navigational control laws would greatly enhance the success of these manoeuvres removing the line of sight dependencies and associated difficulties experienced by remote piloting. If remote piloting is deemed the only available option, continuous audio cues detailing specific measurements (e.g. Velocity measurements) or additional visual cues such as tethered balloons demarcating specific heights should be considered. This being noted, the required circuit was performed, both at the start and at the end of the flight test, providing flight data with 360° heading information required for an approximation of an average wind vector through the data compatibility process.

The analysis of the steady state manoeuvres showed a failure to meet the requirements of quasi-steady flight. These failures highlighted the importance of an adequate initial flight dynamic model for effective manoeuvre design.

The final manoeuvre set dealt with the excitation of the lateral and longitudinal short period modes. Of particular importance within this analysis was the value of the predefined control input capability. The ability allowed for manoeuvres with a high level of repeatability to be implemented and enhanced the potential to achieve the desired excitations in accordance with the specified manoeuvre designs. The shift in the frequency band due to erroneous manoeuver specifications before flight testing was also analysed. It was concluded that the resulting frequency band was still sufficient to excite the natural frequency of the aircraft rigid body modes. The available error band for adequate excitation was, nonetheless, reduced. The significant excitation of the Dutch-roll mode also justified the use of simple, robust manoeuvre inputs when notable uncertainties exist in the initial flight dynamic model.

From the previous analyses, it was evident that varying degrees of success were possible through the flight test plan and implementation procedures. These successes were largely influenced by adequate communication between the ground station and pilot as well as the difficulties of performing accurate manoeuvres through remote piloting. Human factors were significant influences to the success of the flight test method.

The current section dealt with the qualitative aspects of the flight testing and whether the flight test techniques yielded accurate implementations of manoeuvres. The following section deals with the conditioning of the measured flight data and the reconstruction of particular aircraft states (i.e. Angles of attack and sideslip) according to the requirements of the parameter identification techniques.

4.3 DATA COMPATIBILITY AND STATE RECONSTRUCTION

4.3.1 Introduction

The necessity of a data compatibility and state reconstruction algorithm within the systems identification process was discussed in Sec. 2.4 and Sec. 3.3. The objective of the data compatibility procedure was two-fold. The first was to approximate time histories of the angles of attack and sideslip for the flight test manoeuvres. The second was to reconstruct a dynamically consistent dataset from the various sensor measurements. The IEKF algorithm was selected, requiring realistic estimates of the measurement covariance matrices (defined in Sec. 2.4) for optimal performance of the algorithm. The optimal filter method was selected to aid in the estimation of these covariances from flight data. A simulated study on the applicability of this filter was also carried out with detailed results presented in Appendix E.2 and summarised in Sec. 4.3.2. Once this was achieved, the modified data compatibility method was implemented using the actual flight test data. The results of the data compatibility and state reconstruction, detailed in the following subsections, were analysed based on the procedures described in Sec. 3.5.3.

4.3.2 Optimal Filtering for Measurement Noise Variance Estimation

The use of the optimal filtering technique to estimate the instrument measurement covariance matrix was suggested by Morelli (1995) and Klein and Morelli (2006). In the current report, the adequacy of the technique was analysed via simulated data as described in Sec 3.3.3. The first step involved validating the adequacy of using the optimal filter in estimating typical IMU (inertial measurement unit) measurement error variances. The second step involved analysing the preliminary performance of the IEKF based on using the derived measurement variances. An analysis of the validation is provided in Appendix E.2

The validation results of the first step showed that the filtering technique required a high signal to noise ratios (much greater than one) to obtain good approximations to the actual measurement variances. The measurement variances were also underestimated for all parameters. This underestimation of the measurement variances was expected as noise within the lower frequency bands cannot be differentiated from the signal using the current technique. The ability to estimate the variances, to within realistic representations of the true measurement variances, was significantly dependent on the estimation of the filter parameters, in particular, the C_n evaluation (refer to Eq. 2-48). The reliance of the estimated variances on the performance of the curve fitting process of the postulated cubed root trend led to various degrees of error between individual measurements.

The following step of validation of the method involved determining the impact of the potential measurement variance error on the IEKF algorithm. The impact was based on the relative increase in the predicted parameter accuracies (i.e. the instrumentation biases) between IEKF runs using the estimated measurement variances and the true measurement variances respectively. An additional run was carried out with the measurement variances increased by a factor of 10 to simulate larger variance errors.

The baseline test (i.e. no measurement variance error) was used to benchmark the IEKF algorithm. Residual analyses of the output state vector of the baseline case displayed Gaussian characteristics with autocorrelation functions approximating impulse functions with a 95% confidence interval and near-linear cumulative probability functions. These residual characteristics indicated that systematic errors were negligible for the reconstruction of the output states of the manoeuvre. The following two validation test case results were compared with the baseline test results. Bar chart representations of the relative estimated parameter errors showed good correlation (Figure E-1 and Figure E-2) between the baseline case and the second case (i.e. the case using the derived measurement variance matrix). The third case that utilised the inflated measurement variances (overestimated measurement variances) showed significant decreases in the accuracies of the IEKF parameter predictions. The dramatic decreases in accuracy stress the sensitivity of the IEKF algorithm to the predicted measurement variances.

It would thus be advisable practice to determine the correct measurement variances via controlled laboratory testing to avoid any potentially significant errors based on the estimation of the measurement variances. However, if laboratory testing is not a viable option, the cautious application of the optimal filter in deriving the measurement variances could lead to negligible reductions in the IEKF performance.

4.3.3 Data Compatibility and State Reconstruction of Experimental Results

The absence of an angle of attack sensor within the instrument set meant that data reconstruction procedures were required to determine the angle of attack and angle of sideslip time histories for each flight test manoeuvre. These variables were needed to effectively use the parameter estimation algorithms for traditional aerodynamic model parameter estimations. These procedures were also necessary to construct a kinematically consistent set of data (i.e. the removal of biases, scale factors, and time lags) from the raw measurements. The conventional data reconstruction methods were described in Sec. 2.4. The unique characteristics of the actual UAV flight test measurement set, however, led to a required modification of the conventional data reconstruction method. The modifications are described in Sec. 3.3.4 and by the flowchart in Figure 3-8.

The first step of the modified algorithm involved the estimation of the measurement error covariance matrix through the use of the optimal filtering technique as discussed in Sec. 4.3.2 for the simulated data analysis. The flight test datasets belonging to the box manoeuvres were used for this analysis because of the statistical advantages offered by the pseudo steady state vector and the lengthy datasets. A sample of the results from the optimal filtering of the Z-acceleration is provided in Figure 4-7 to Figure 4-9. Similar resulting trends were achieved for the remaining measurements and are provided in Appendix G.2.

Figure 4-7 presents the magnitudes of the coefficients for the Fourier sine series transformation. The selection of the coefficient peak threshold values (as described by the filtering method in Sec. 2.6) was based on the relative decrease in value of the adjacent coefficient peaks. Once the peak threshold was identified, the previous peak, as well as the following three coefficient peaks (i.e. five effective data points), were used in the least squares fitting routine of the signal model. The noise model was fitted to an average of the remaining peaks following the peak threshold value.

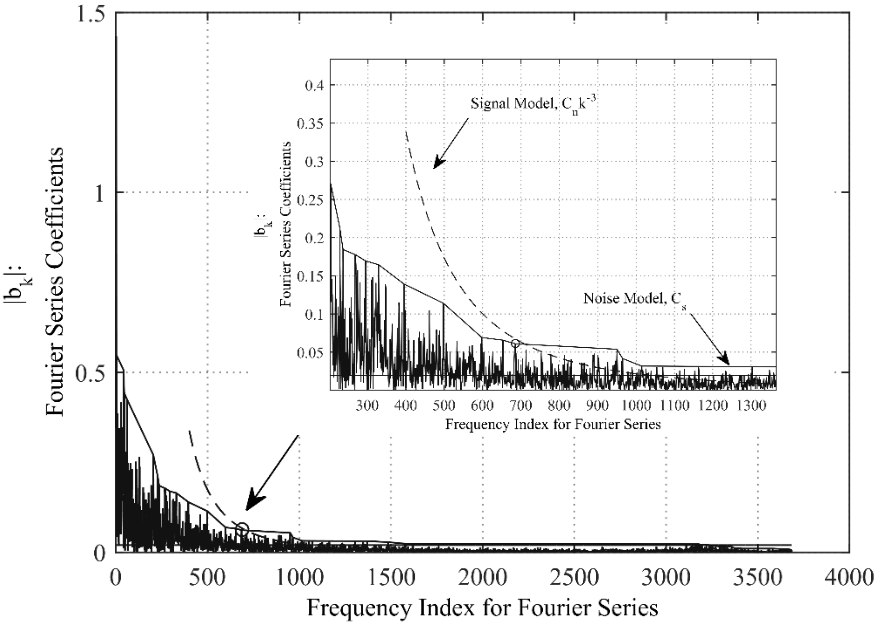

Figure 4-7 Fourier Sine Series Transformation – Optimal Filter

The residual and autocorrelation function resulting from the optimal filtering is given in Figure 4-8 and Figure 4-9. No deterministic trend in the residuals was evident and the autocorrelation as a function of lag indices (unequal to zero) was within the estimated standard deviations of the residuals. These filtering results indicated consistency with the white noise approximations for the actual measurement noise thus reducing the possibility of systematic errors being introduced by the filtering process.

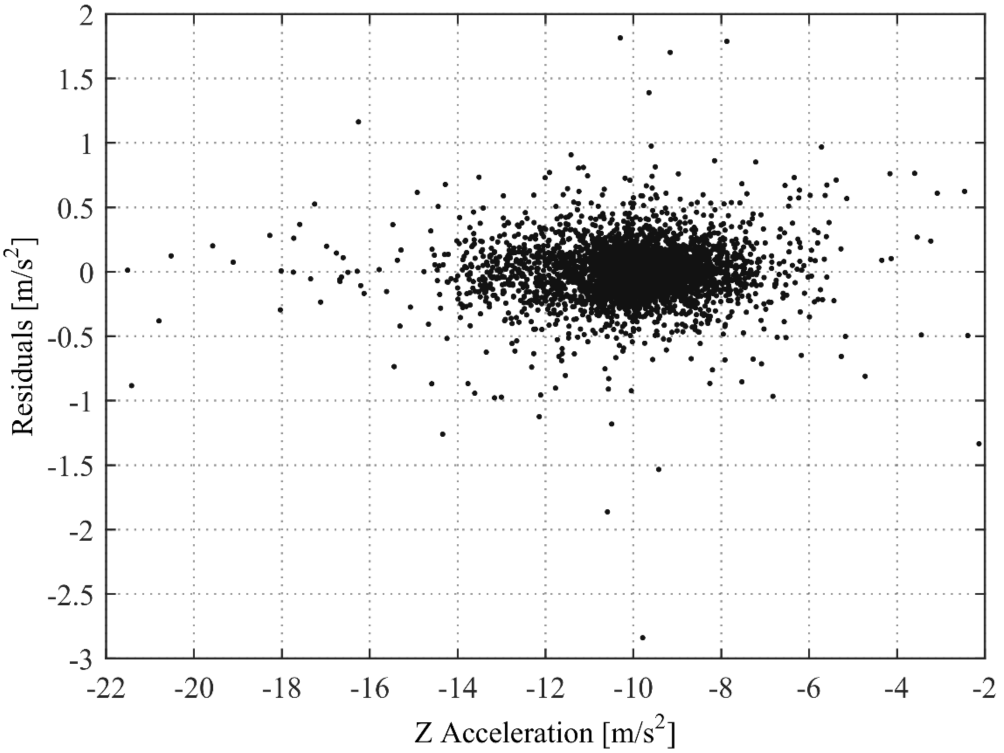

Figure 4-8 Z-Acceleration Residuals – First Box Manoeuvre

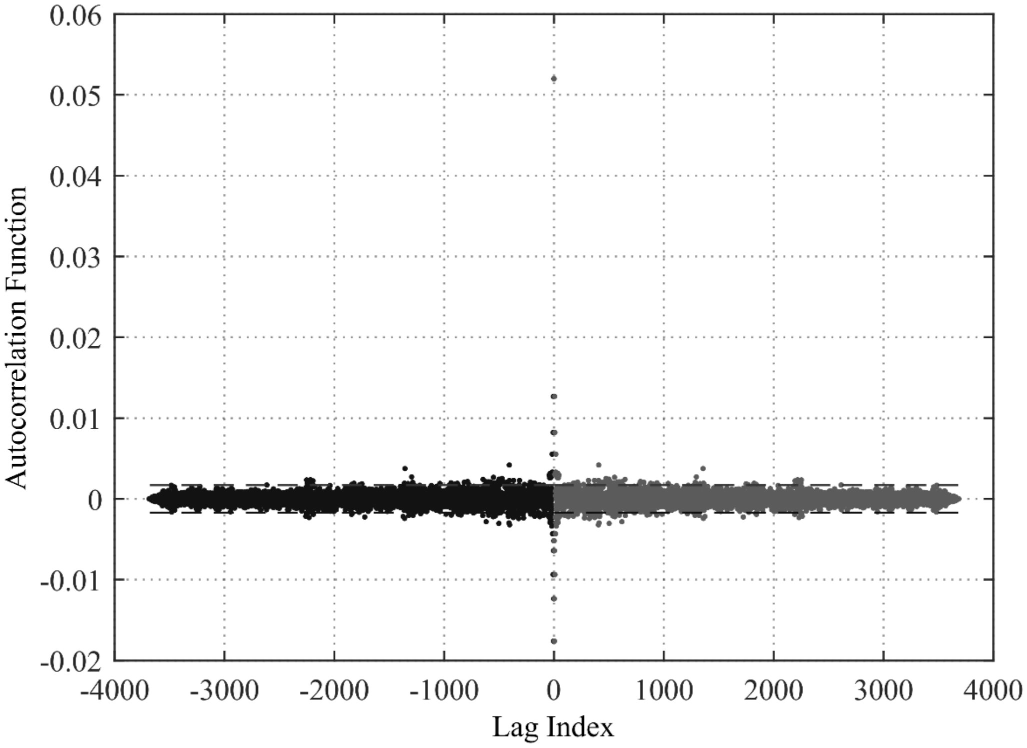

Figure 4-9 Autocorrelation Function for Z-Acceleration Residuals – First Box Manoeuvre

The final estimated measurement covariance matrix achieved via the optimal filtering algorithm is provided in Appendix G.4.

Following the estimations of the instrument measurement variances and the corrections for positional compatibility with the centre of gravity (as required by the modelling technique), the next step involved the application of the IEKF algorithm to estimate the average wind vector components and consequently the approximated angles of attack and sideslip. The first manoeuvres to be analysed were the box manoeuvres due to the high level of directional variation. The process, as previously mentioned, was iterative due to the level of uncertainties in the IEKF solution parameters (i.e. the measurement covariance matrix). The measurement residuals at the end of each iterative step were analysed based on the level of adherence to white noise characteristics. This residual analysis gave a good indication of the existence of systematic errors that may have been introduced by the IEKF algorithm.

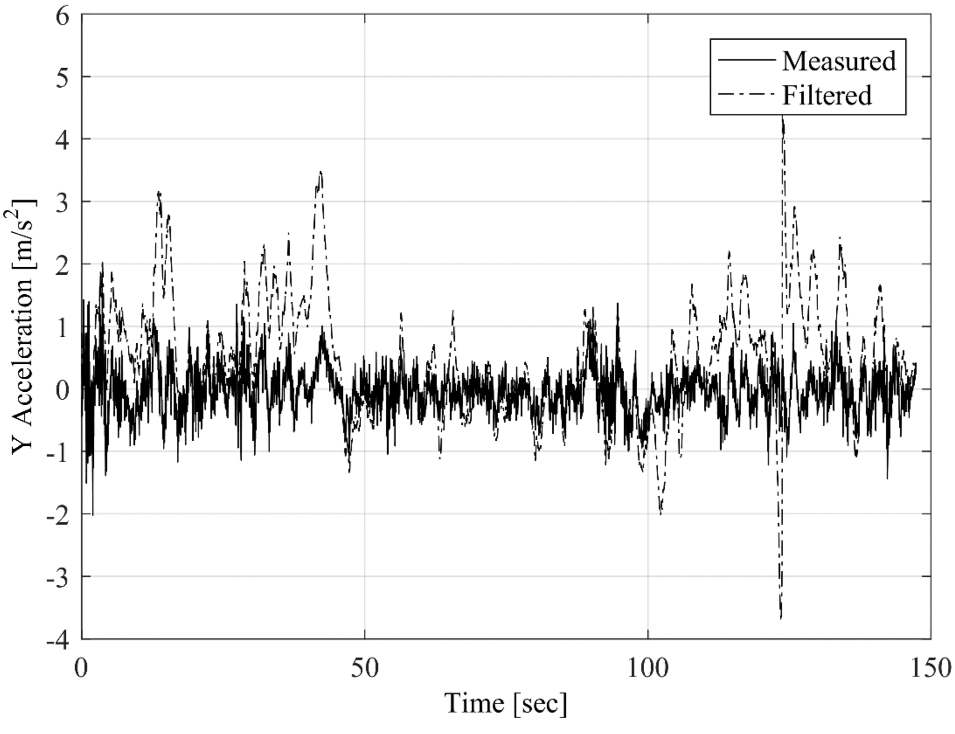

Figure 4-10 Sample of Initial Reconstruction of the Y-Acceleration

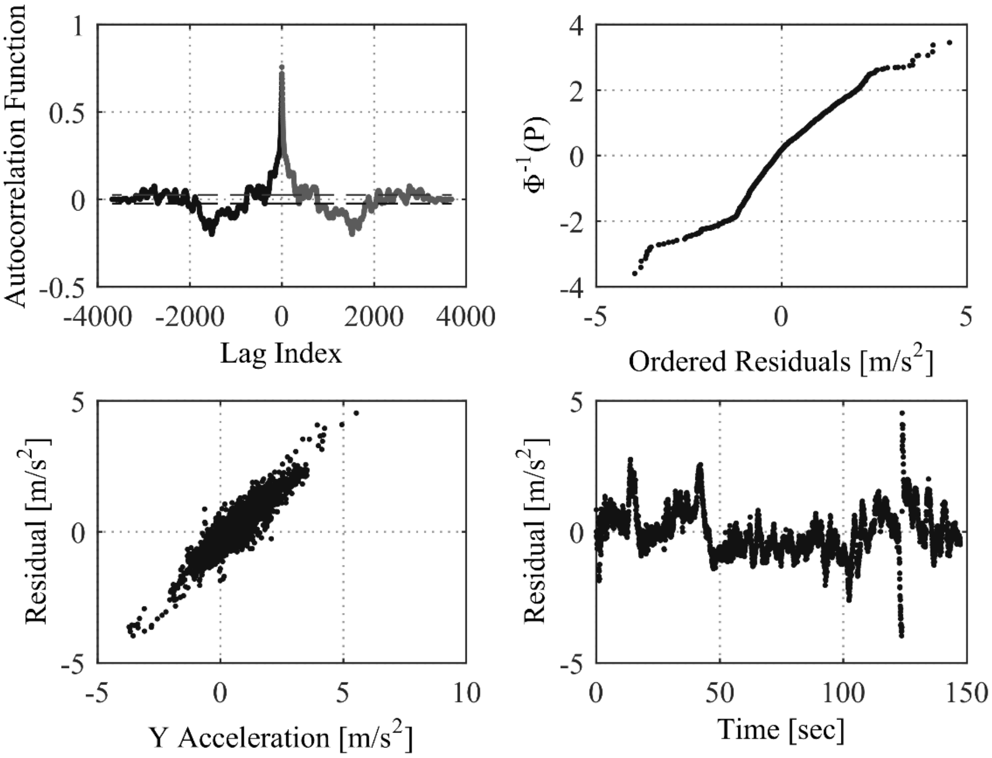

Figure 4-11 Sample of Initial Residual Analysis for the Y-Acceleration

The initial iteration used the estimated measurement error covariance matrix, initial zero magnitude wind vectors, and zero magnitude instrument biases. The corresponding, initial residual results of the accelerometer and rate gyroscope measurements were characterised by poor correlations to white noise approximations and unrealistic angles of attack and sideslip. An example of the initial result for the reconstructed Y-acceleration is given in Figure 4-10 along with the residual analysis in Figure 4-11. Ideal white noise characteristics would yield an autocorrelation function resembling an impulse function within a 95% tolerance level, a linear function representing the inverse of the cumulative probability density, and no functional dependence of residuals on the measurement magnitudes or with time. The presented results in Figure 4-10 and Figure 4-11 are representative of the observed initial trends of the remaining measurements that are given in Appendix G.2.

The initial systematic errors were based on inaccuracies in the Euler angle estimations. The dynamic model used to propagate the Euler angles in a time series used the combination of the three axis magnetometer and the three rate gyroscope flight test measurements. It was hypothesised that the systematic errors seen in the data were due to the uncalibrated reference magnetic field. In order to relax the IEKF algorithm dependence on the magnetometer measurements the associated measurement error variances were inflated significantly to account for small systematic errors as well as the estimated measurement noise. Additionally, a more stable solution was also achieved by simultaneously decreasing the expected measurement error variances of the accelerometers and angular rate gyroscopes. These correction factors, given in Table 4-4, in conjunction with iteratively adjusting the initial augmented state vector yielded results that were more plausible, consisting of Gaussian-like residuals and realistic angles of attack and sideslip. The final residual analysis for the Y-acceleration example is given in Figure 4-12. Similar improvements in the residual characteristics were observed for the remaining measurements (refer to Appendix G.2).

Table 4-4 Measurement Variance Correction Factors

Measurement	Variance Multiplier
X Acceleration	0.1
Y Acceleration	0.01
Z Acceleration	0.01
Roll Rate	0.01
Pitch Rate	0.01
Yaw Rate	0.01
Magnetometer X	10000
Magnetometer Y	1000
Magnetometer Z	10000

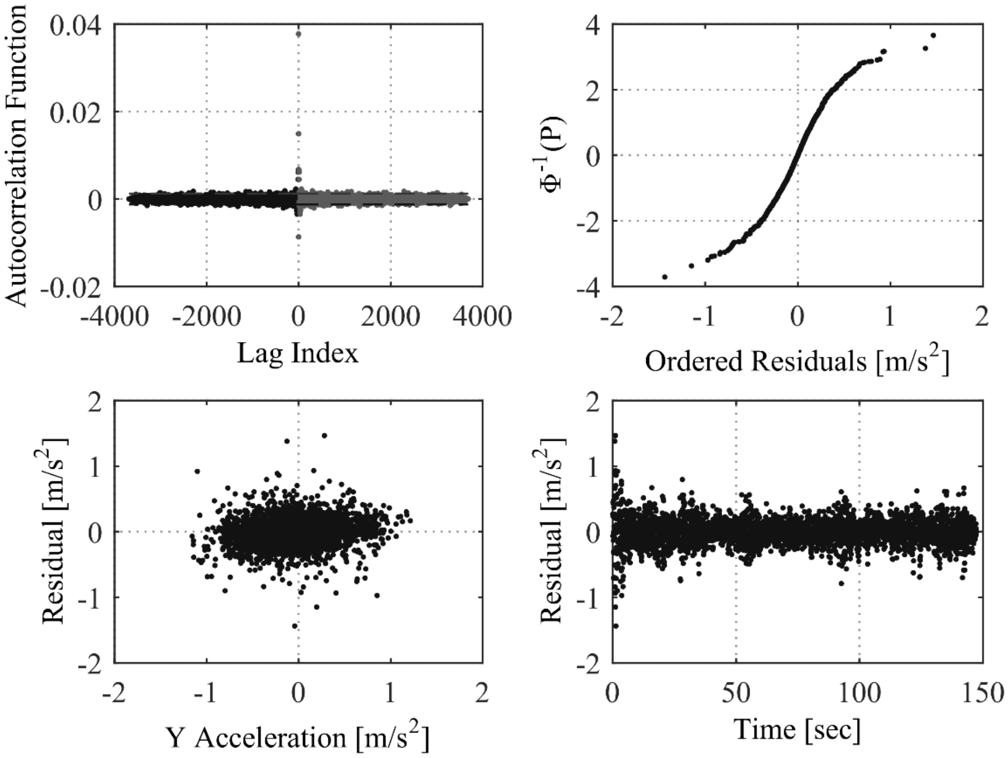

Figure 4-12 Final Residual Analysis for the Y-Acceleration Measurement

The IMU measurement biases associated with the iterative process of state reconstructions (refer to Figure 3-8) are shown in Figure 4-13 and Figure 4-14 and are plotted against the flight test time. These biases represent the RMS differences between the reconstructed IMU measurements and the corresponding raw measurements for each manoeuvre of the flight test. The variations of the biases throughout the flight test were initially postulated to be representative of instrumentation drift parameters per manoeuvre. However, the indeterminate time dependency evident in Figure 4-13 and Figure 4-14 did not support the notion of near-continuous, identifiable, drift characteristics of IMU sensors. The estimated IMU biases were products of both the systematic modelling errors within the IEKF algorithm as well as the unaccounted measurement drift errors. These estimated bias parameters could not be considered solely physically realistic parameters (i.e. sensor drift) but were maintained in the IEKF algorithm as accumulative corrective factors within the dynamic model. Additionally, the bias estimations yielded comparable magnitudes for both accelerometer and gyroscope measurements across the three principal axes, thus increasing the statistical confidence in the estimates.

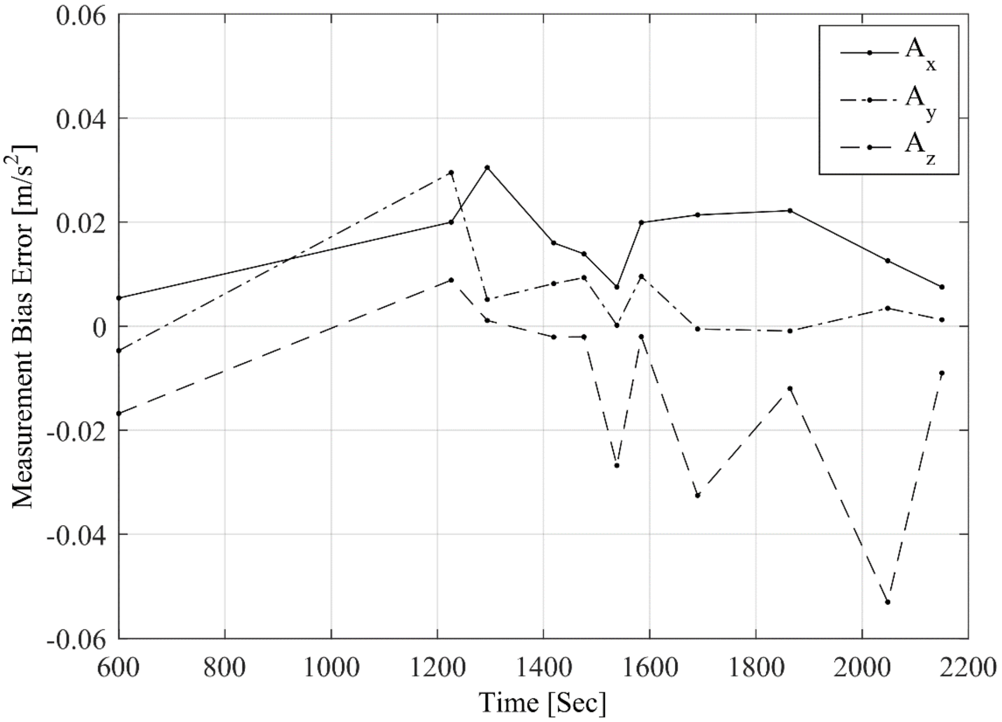

Figure 4-13 Estimated Accelerometer Biases for System Identification Manoeuvre Set

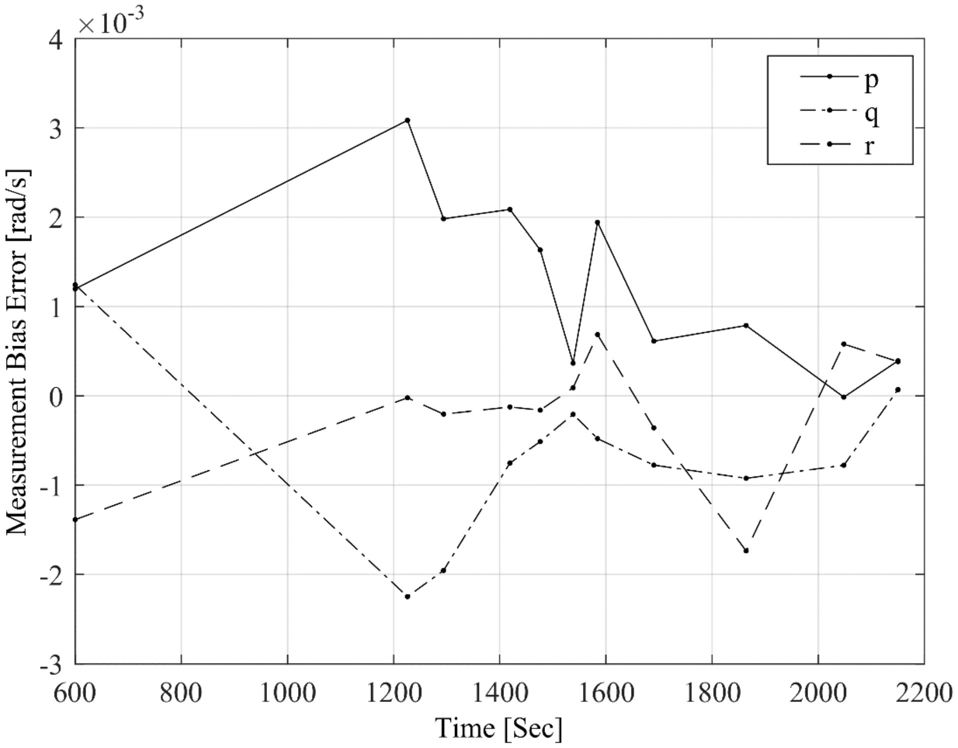

Figure 4-14 Estimated Angular Rate Gyroscope Biases for System Identification Manoeuvre Set

The modified magnetometer measurement variances in the IEKF initialization were noted in the large magnetometer standard deviations presented in Figure 4-15. The difference in the dynamically consistent magnetometer reading (i.e. IEKF filtered data) and the measured reading can be attributed to the poor accuracy of the magnetometer, a poor selection of the magnetometer reference values, or a misalignment of the magnetometer with the body axis of the aircraft. These proposed influences were not verified and should be studied further if the magnetometer is to be used in future flight test programmes. The magnetometer readings were maintained within the data compatibility algorithm as the trends between the measured and estimated flight parameters correlated to an extent (see Figure 4-15) and added additional angular position information that increased the accuracy of the bias estimations of the angular rate gyroscopes as described above.

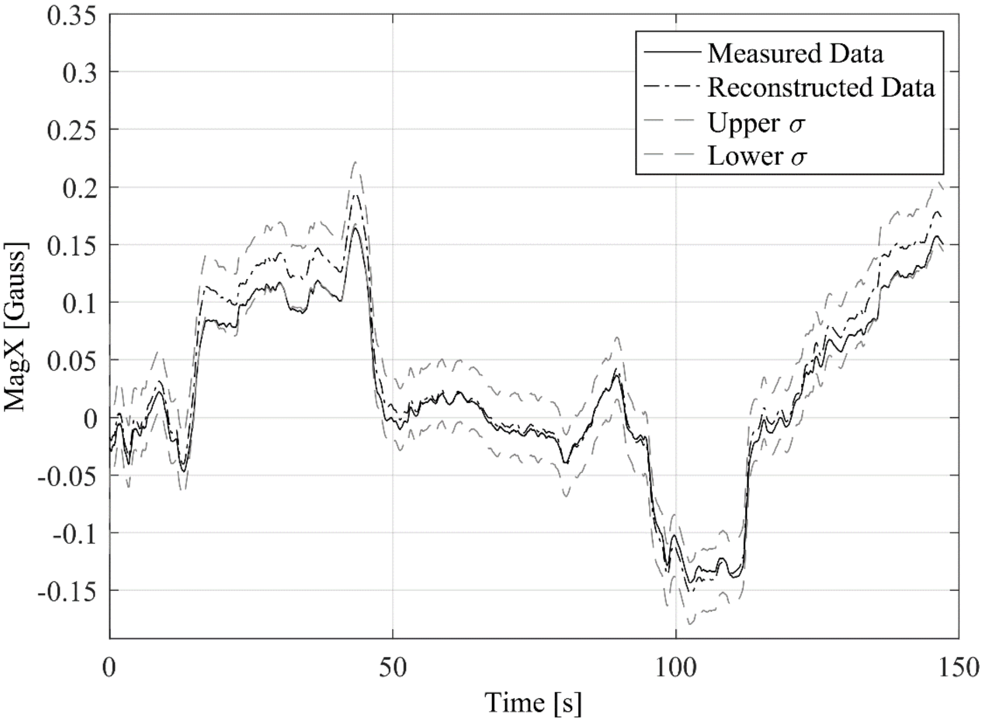

Figure 4-15 Magnetometer Measurement Reconstruction using the IEKF Algorithm

The final wind vector estimates along with the pitot tube measurement corrections are provided in Table 4-5 and Table 4-6. The exclusion of the vertical wind vector component made little impact on the residual nature of the filtered accelerations and observation measurements (i.e. GPS measurements) and led to a better-conditioned solution with realistic results for the lateral-plane wind vector components. For a more detailed and higher accuracy analysis, the angle of attack and sideslip sensors would need to be utilised. By including an angle of attack and sideslip angle sensors, the assumption of a constant wind vector may also be dropped thereby eliminating an additional source of uncertainty.

Table 4-5 Wind Vector Results: Box Manoeuvres

Manoeuvre:	W_X [m/s] (σ^2)	W_Y [m/s] (σ^2)	ΔV_{pitot} [m/s] (σ^2)
Box 1	-1.664 (9.61 x10^{-6})	6.167 (6.76 x10^{-6})	0.894 (5.29 x10^{-6})
Box 2	-2.939 (21.16 x10^{-6})	6.141 (11.56 x10^{-6})	1.206 (12.25 x10^{-6})

Table 4-6 Wind Vector Results: Dynamic Manoeuvres

Manoeuvre:	W_X [m/s] (σ^2)	W_Y [m/s] (σ^2)	ΔV_{pitot} [m/s] (σ^2)
Push-over Pull-up 1	-2.203 (84.64 x10^{-6})	5.779 (67.24 x10^{-6})	0.702 (57.76 x10^{-6})
Push-over Pull-up 2	-1.436 (88.36 x10^{-6})	5.094 (67.24 x10^{-6})	0.490 (56.25 x10^{-6})
3-2-1-1 +4deg. Elevator	-1.574 (81.00 x10^{-6})	5.839 (73.96 x10^{-6})	0.950 (67.24 x10^{-6})
3-2-1-1 -4deg. Elevator	-1.562 (82.81 x10^{-6})	5.819 (65.61 x10^{-6})	0.967 (59.29 x10^{-6})
1-1-2-3 +6deg. Elevator	-1.728 (77.44 x10^{-6})	6.398 (70.56 x10^{-6})	0.634 (60.84 x10^{-6})
1-1-2-3 -6deg. Elevator	-1.566 (9.61 x10^{-6})	6.335 (9.00 x10^{-6})	0.607 (9.00 x10^{-6})
Bank-to-bank,Rud Doublet	-1.689 (7.84 x10^{-6})	6.507 (88.36 x10^{-6})	1.085 (9.00 x10^{-6})
Steady Heading Sideslip	-2.551 (6.25 x10^{-6})	5.902 (86.49 x10^{-6})	1.447 (7.29 x10^{-6})
Mean:	-1.826	5.967	0.889
Variance (σ^2) :	0.377	0.427	0.306

It can be seen from Table 4-6 that the mean values obtained for the wind velocities from the IEKF analyses correlated well with the estimates from the initial and final box manoeuvres. The small variances show that the assumption of a relatively constant wind vector throughout the flight testing was plausible. The bias and the high variance of the pitot tube velocity measurement can partially be attributed to the fact that the modelling error due to the absence of the vertical wind component and errors in the true airspeed measurements (due to the pitot tube misalignments with the airflow and density errors) were combined with the random measurement error in the implemented instrument model.

Regarding re-constructability of the system, a check based on the rank of the Grammian matrix as described in Sec. 3.3.4 using Eq. 3-12 was carried out after the algorithm was applied. The rank of the Grammian matrix equalled the number of states in the augmented state matrix and thus represented a full rank matrix. Hence, the system was re-constructible given the information available.

4.3.4 Conclusions

The data compatibility research method was carried out through a systematic approach yielding information about the performance of the algorithm. This approach consisted of simulated analyses as well as the application of the implementation method, defined in Sec. 3.3.4, to the actual flight datasets. The applicability of the optimal filtering technique, the practical application of the IEKF algorithm, and the estimation of a steady wind vector assumption were explored.

The applicability of the optimal filter as an aid to estimate the measurement error covariance matrix was first analysed through a simulated environment. It was observed that the quality of the estimated measurements variances was significantly influenced by the evaluation of the filter parameters. The results indicated large relative errors for measurements with low signal to noise ratios. The application of the estimated measurement noise variances within the IEKF solution process yielded parameter estimation solutions that were comparable to the IEKF results using the true variances. A significant increase in error was evident when measurement covariance matrix was considerably inflated. The estimation of the measurement noise characteristics should be avoided when possible, being replaced by true measurement noise estimation via controlled laboratory tests. The estimation method used was nevertheless adequate for preliminary stable IEKF filtering and estimation results.

The practical application of the method described by Figure 3-8 was then analysed. The iterative nature of the method proved successful in maintaining the conditioning of the IEKF algorithm while adapting the algorithm parameters through post-iteration residual analyses of measurements. The initial application of the data compatibility algorithm yielded unrealistic filtered solutions with evidence of large systematic errors. The errors were found to be due to the magnetometer measurements. The influence of the magnetometer errors was alleviated by significantly increasing the estimated measurement variance. This variance inflation led to a well-conditioned data compatibility process. Instrumentation biases were also estimated and accounted for any systematic dynamic model error or measurement errors. The estimated wind vectors for all manoeuvres showed consistency with the assumption of a steady wind vector with mean values correlating to the box manoeuvres. Deviations from the mean estimation were also due to changing reference altitudes. The final angles of attack and sideslip were considered realistic with angles within the expected ranges for small perturbation manoeuvres about the trimmed condition.

It was thus possible to achieve a dynamically consistent set of filtered data using the available measurement quality. Approximations of the angles of attack and sideslip were also achievable; however, the level of uncertainty of the angles could not be validated without additional sensors onboard the aircraft.

4.4 PARAMETER IDENTIFICATION

4.4.1 Introduction

The objective of the parameter identification process was to determine whether a representative linear aerodynamic model could be derived based on the available flight test parameters and the low quality of the measurements. Due to the sequential method, the parameter identification module also served as a performance measure for the preceding system identification modules. As mentioned in Sec. 3.4, the parameter identification step was broken down into smaller objectives sequentially increasing in complexity. The analyses followed the method presented in Figure 3-9. The following sub-sections explore the validity of the linearized model assumption and detail the parameter identification results.

4.4.2 Linearization Assessment

A step before the parameter identification procedure involved validating the use of the decoupled linearized equations of motion to propagate the aircraft states in a computational environment for the Modular UAV. This was carried out to ensure that the mathematical model preserved the kinematics of the system before using the model within the parameter estimation routine.

An output error estimation routine was implemented within the kinematic state propagation procedure. As detailed in Sec. 3.4.2, the estimator was initially used to determine corrections to the initial state conditions and any measurement correction factors such as drift (refer to Eq. 3-17 and Eq. 3-18). The forcing terms in the dynamic model consisted of the forces and moments derived from the measured linear and angular accelerations. Since a linearized system was being analysed, perturbations in the forces and moments were used. The perturbations were relative to the approximately trimmed initial forces and moments for each manoeuvre. The longitudinal and lateral dynamics were also decoupled as described in Sec. 3.4.2 and analysed independently. The linearization simplifications were expected to yield a degree of systematic error and model mismatch as the coupling between lateral and longitudinal axes was removed. The resulting simulated dynamics were compared to the flight test measurements and evaluated by Theil's coefficient criteria to identify the extent of the systematic error. These validation criteria and their respective characteristics are detailed in Sec. 2.5.

The Theil's inequality coefficient, U_i, is a scaled representation of the standard deviations of the residual between the simulated responses and the actual measurements. Based on a general rule-of-thumb, an adequate model would yield a Theil's inequality coefficient close to zero, with an acceptable maximum of between 0.25 and 0.3 (Jategaonkar, 2006). The Theil's covariance parameter, U_i^C, must be as close as possible to unity, indicating negligible systematic errors. Theil's coefficients with the above characteristics serve as good indicators of acceptable candidate models.

The Theil's inequality coefficients for the lateral responses for each lateral manoeuvre analysed is presented in Figure 4-16. All U_i values for the lateral manoeuvres were below the recommended 0.3 indicative of an acceptable model match over the specified manoeuvre period. The low Theil's covariance parameters, U_i^C, given in Figure 4-17, however, indicate that the linearized model may contain systematic errors. Systematic errors may not be immediately evident over a single specified time period if the variance of the residuals between the model and measurements are within acceptable bounds (i.e. Theil's inequality less than 0.3), but do influence the predictive properties of the model. The most significant evidence of the systematic error was found in the reconstructed time history (Figure 4-18) of the roll angle for both lateral manoeuvres correlating to the respective low Theil's covariance. The time history in Figure 4-18 includes the processed measured data and the upper and lower bounds of the linearized model (each one standard deviation above and below the mean). The presented bounds, in this case, were only an indication of the quality of the model fit to the particular manoeuvre. In order to quantify the actual standard deviation and uncertainty propagation (related to the predictive nature of the model) it is recommended to perform further validation using further flight data not used in the model estimation procedure. The peak roll angle mismatches between 2 and 5 seconds and slight phase shifts seen between 6 and 12 seconds of elapsed manoeuvre time can be seen in Figure 4-18. In the absence of further flight test data, this qualitative assessment of the time histories was the only indication of the level of degradation in the model fit when linearizing and decoupling the lateral and longitudinal dynamics of the UAV. A more comprehensive analysis of the predictive quality of the model can be accomplished as more flight test data becomes available in future flight test programmes of the UAV. For the analysis of the current limited datasets, the linearized approximations for the lateral states were still considered statistically viable based on the low Theil's inequalities coefficients (i.e. good model fit to measured available data).

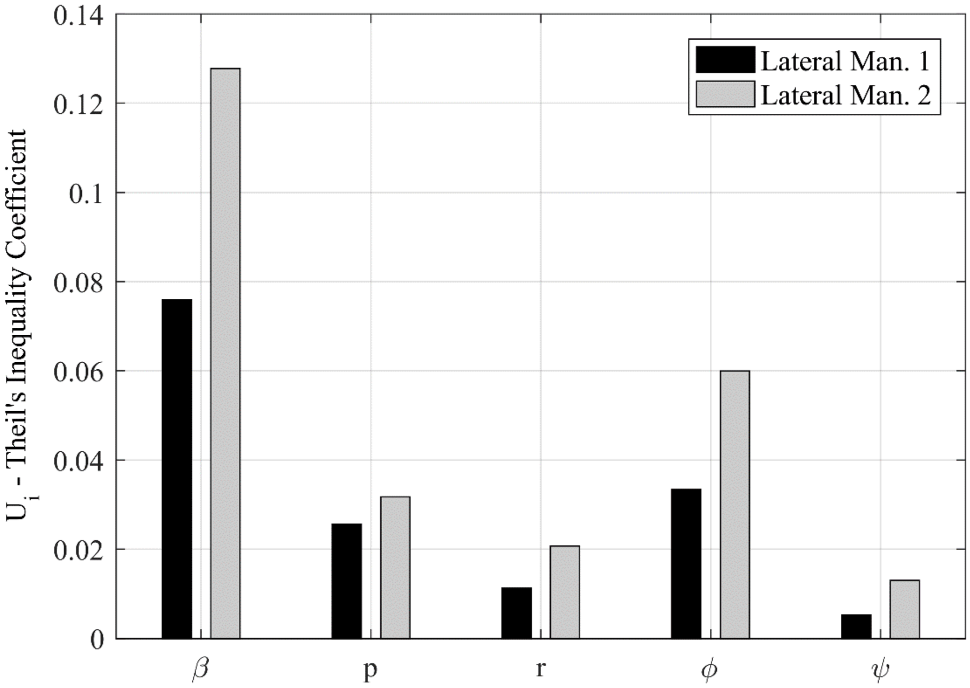

Figure 4-16 Theil's Inequality: Linearized Lateral Dynamic Model Assessment

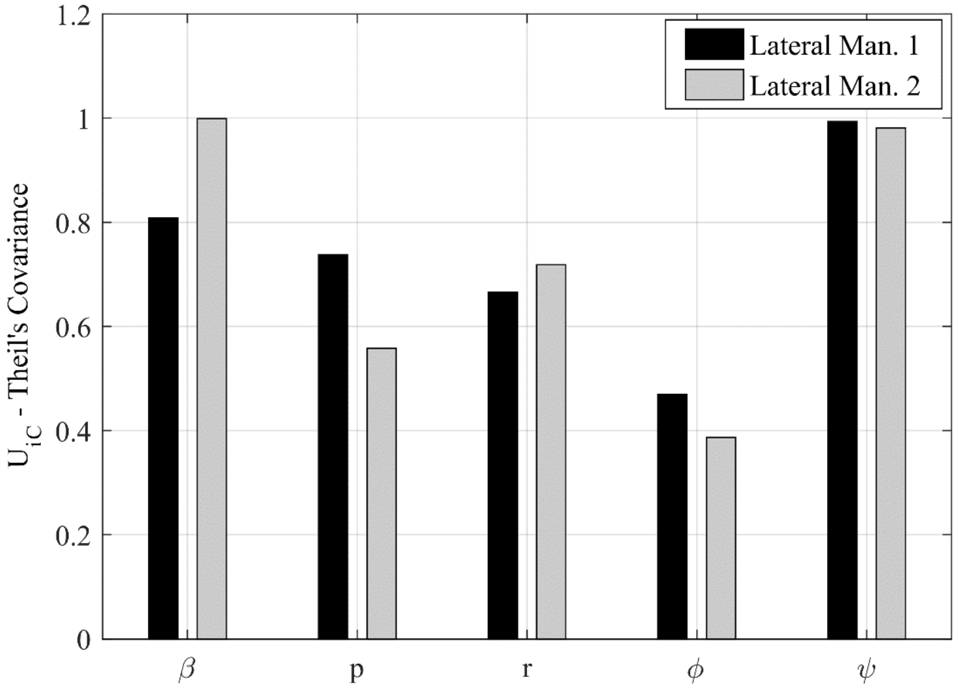

Figure 4-17 Theil's Covariance Parameter: Linearized Lateral Dynamic Model Assessment

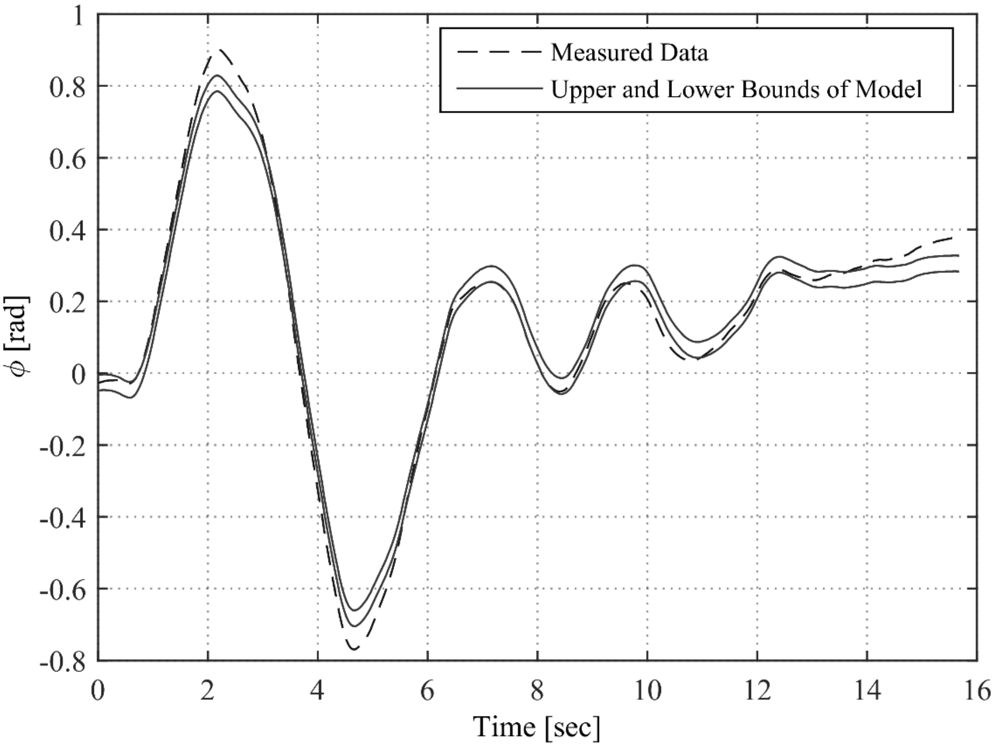

Figure 4-18 Linearized Lateral Dynamic Model: Euler Roll Angle (Lateral Man. 1)

The next validation step was to analyse the linearized longitudinal characteristics. The resulting Theil's inequality and Theil's covariance properties are presented in Figure 4-19 and Figure 4-20 respectively. All four longitudinal multistep flight test manoeuvers were analysed. The legend naming convention employed in Figure 4-19 and Figure 4-20 was used to differentiate the multistep manoeuvres by the elevator deflection magnitudes and directions of the first step. All four longitudinal aircraft states met the statistical criteria, based on the Theil's coefficients, for all analysed multistep manoeuvres.

Linearization of the dynamic model was deemed adequate for the lateral and longitudinal dynamics for the limited datasets. The adequacy of the linearization was based on the Theil's covariance and inequality coefficients. As noted above, any indication of systematic error (e.g. Euler roll angles) was further assessed via a qualitative assessment of the time history of the linearized output compared to the processed measured data.

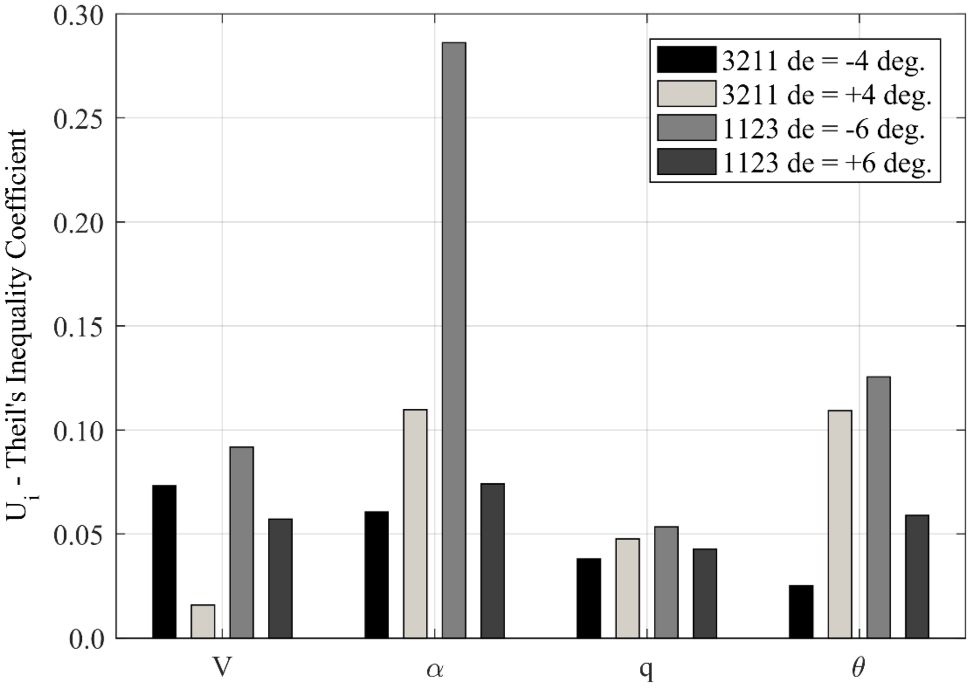

Figure 4-19 Theil's Inequality: Linearized Longitudinal Dynamic Model Assessment

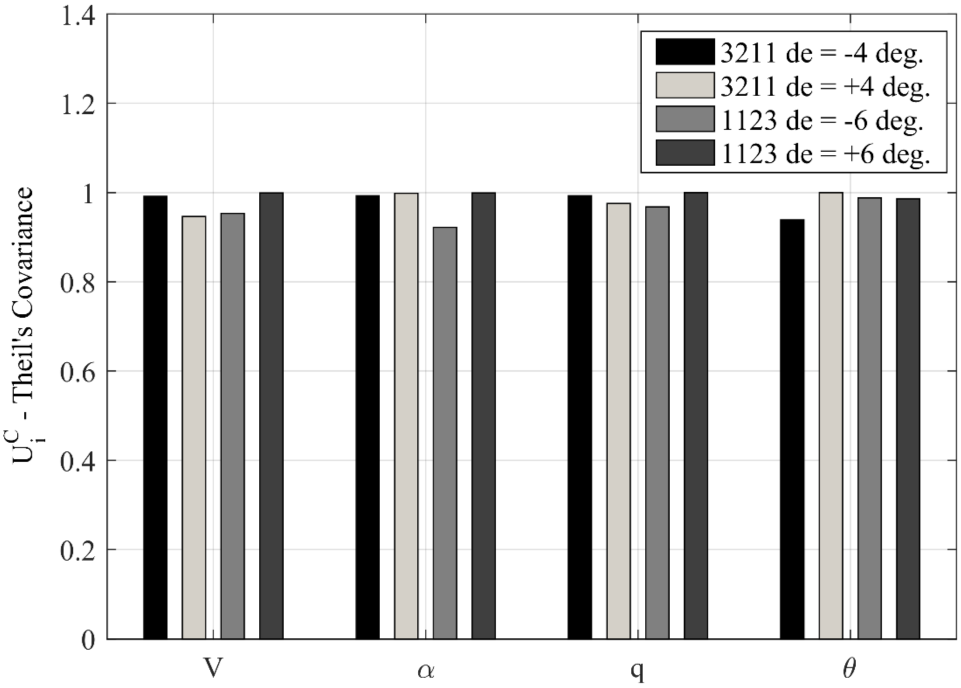

Figure 4-20 Theil's Covariance Parameter: Linearized Longitudinal Dynamic Model Assessment

4.4.3 Analysis of Initial Flight Dynamic Model

The next step was to benchmark the initial flight dynamic model. The reason for this as described in Sec. 3.4.3 was to establish a reference point from which improvements to the aerodynamic model could be compared. The linearized equations of motion for each manoeuvre were adopted. An indication of the adequacy of the simplified equations of motion was determined in Sec. 4.4.2. The resulting accuracies of the aircraft states based on the initial aerodynamic model are given in Figure 4-21 and Figure 4-22 for longitudinal manoeuvers and in Figure 4-23 and Figure 4-24 for lateral manoeuvres. Velocity was excluded from the current longitudinal analysis because of the strong dependence on a representative power model. The initial axial force model did not contain any power dependency as only power-off data was available. An adequate fidelity thrust model was beyond the scope of the current study. The total number of longitudinal states was thus limited to three parameters i.e. α, q, θ. Similar to the linearization validation presented in Sec. 4.4.2, the two lateral manoeuvres and four longitudinal multistep manoeuvres were analysed.

The respective comparisons for the longitudinal and lateral manoeuvres (Figure 4-21 to Figure 4-24) demonstrated the high Theil's inequality coefficients indicative of a poorly characterised aerodynamic model. In particular, the Theil's inequalities for the lateral states were high (close to or above the acceptable maximum of 0.3) across both available manoeuvres. The exception was the heading, which yielded an acceptable Theil's inequality but poor Theil's covariance, indicative of systematic errors. The remaining Theil's covariance proportions for both lateral and longitudinal manoeuvres also indicated possible systematic errors, equating to initial aerodynamic model errors and low predictive qualities. There was significant potential for the improvement of the aerodynamic model.

As a representation of the quality of the a priori models, the time histories of the state vectors for two of the flight test manoeuvres (i.e. one lateral and one longitudinal manoeuvre) are shown in Figure 4-25 and Figure 4-26. The roll rate and yaw rate presented in Figure 4-26 showed significant differences between the modelled and the actual damping and damped frequencies. There were shortfalls due to the required model bias parameters (seen in the pitch rate bias in Figure 4-25). Bias parameters in the linearized models are required to account for any drift of the raw measurements (used as input data) or to correct the initial conditions. The effect of the absence of the bias parameter is most notable in the gradient differences in the pitch angle time history (Figure 4-25).

The current section indicated the inadequacies of the initial mode and highlighted the type of corrections that are required through parameter identification estimates. It was clear that the estimates of state initial conditions were vital for a linearized system.

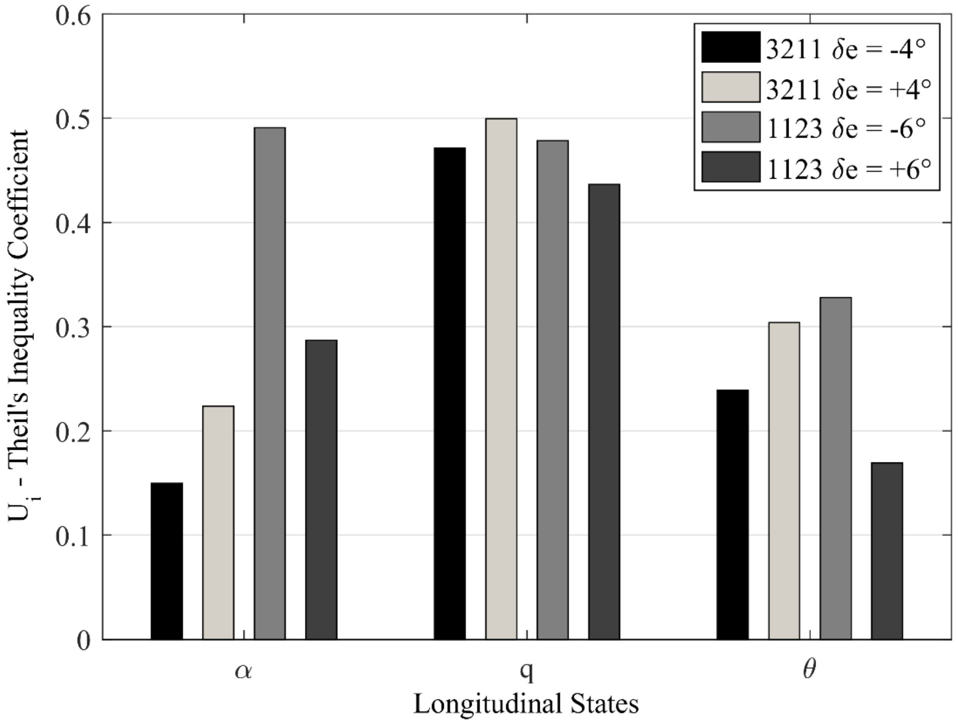

Figure 4-21 Theil's Inequality Coefficients of Initial Longitudinal Responses

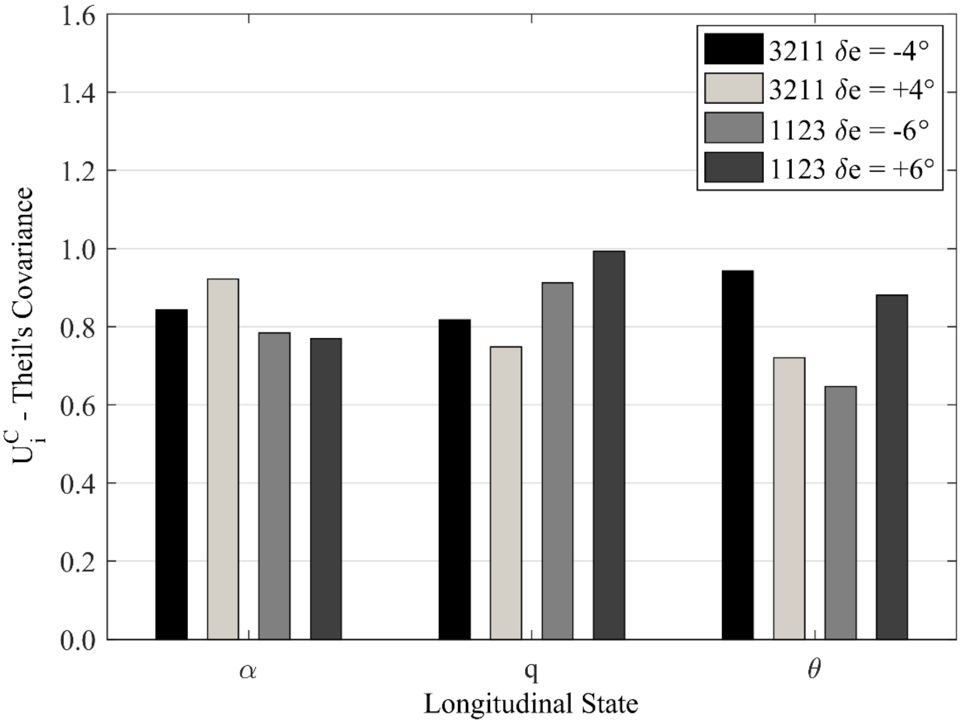

Figure 4-22 Theil's Covariance of Initial Model Longitudinal Reponses

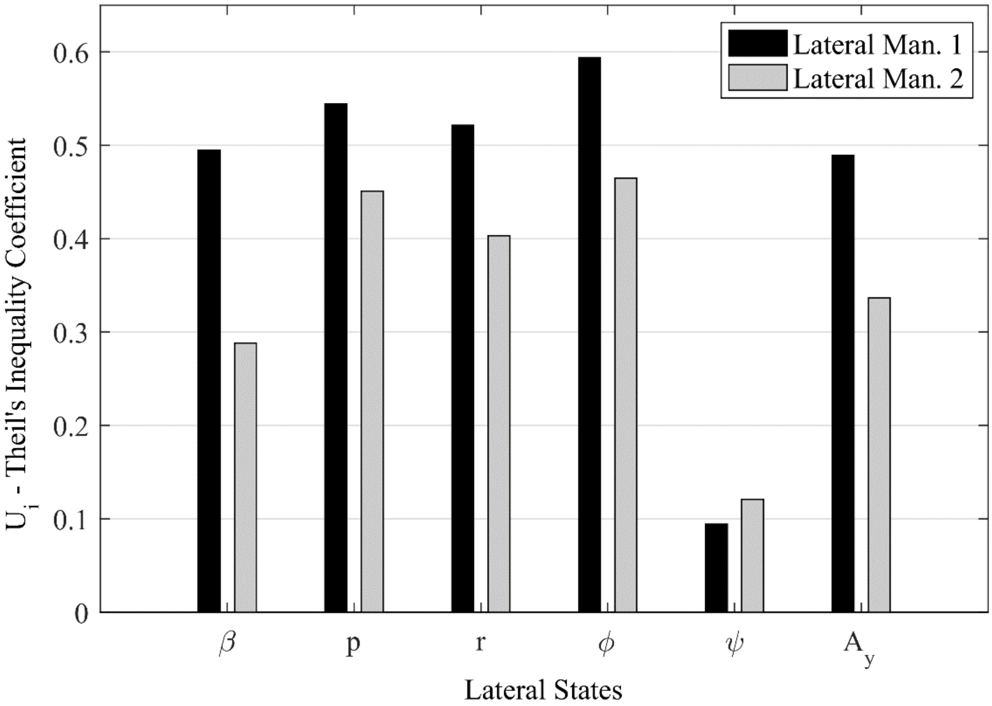

Figure 4-23 Theil's Inequality Coefficient of Initial Model Lateral Responses

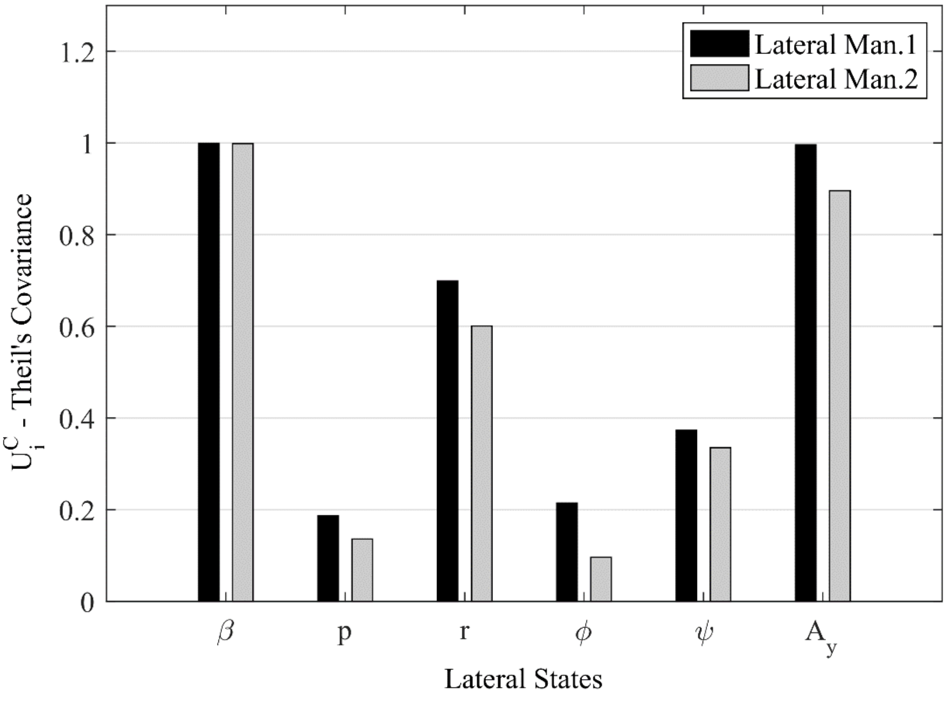

Figure 4-24 Theil's Covariance of Initial Model Lateral Reponses

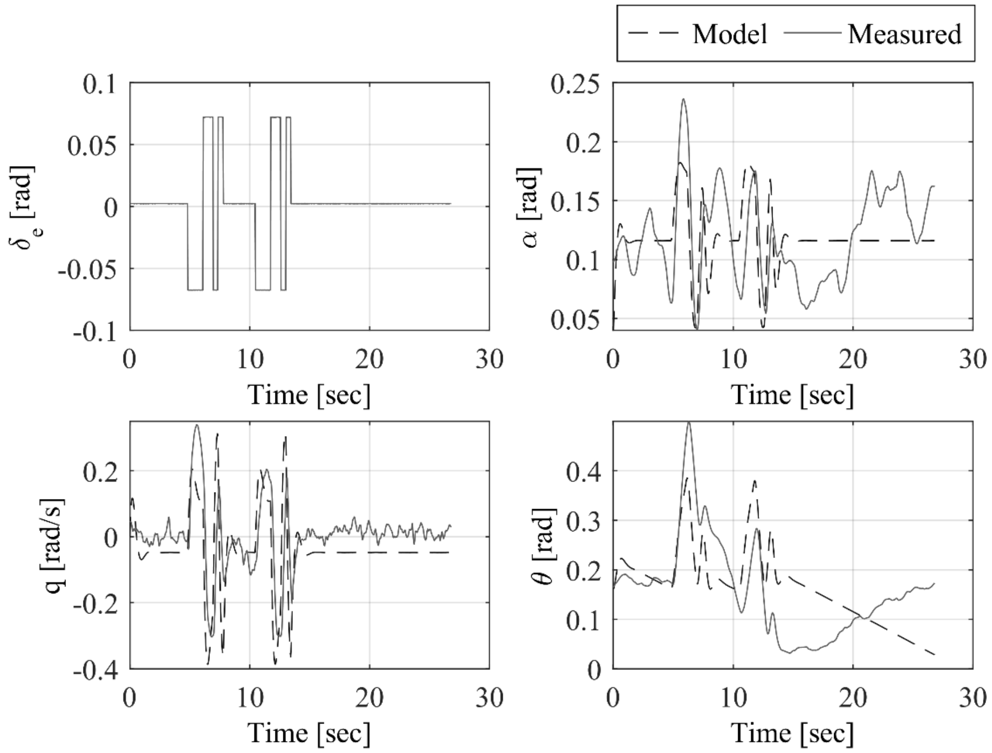

Figure 4-25 Comparison between Modelled and Measured Longitudinal States

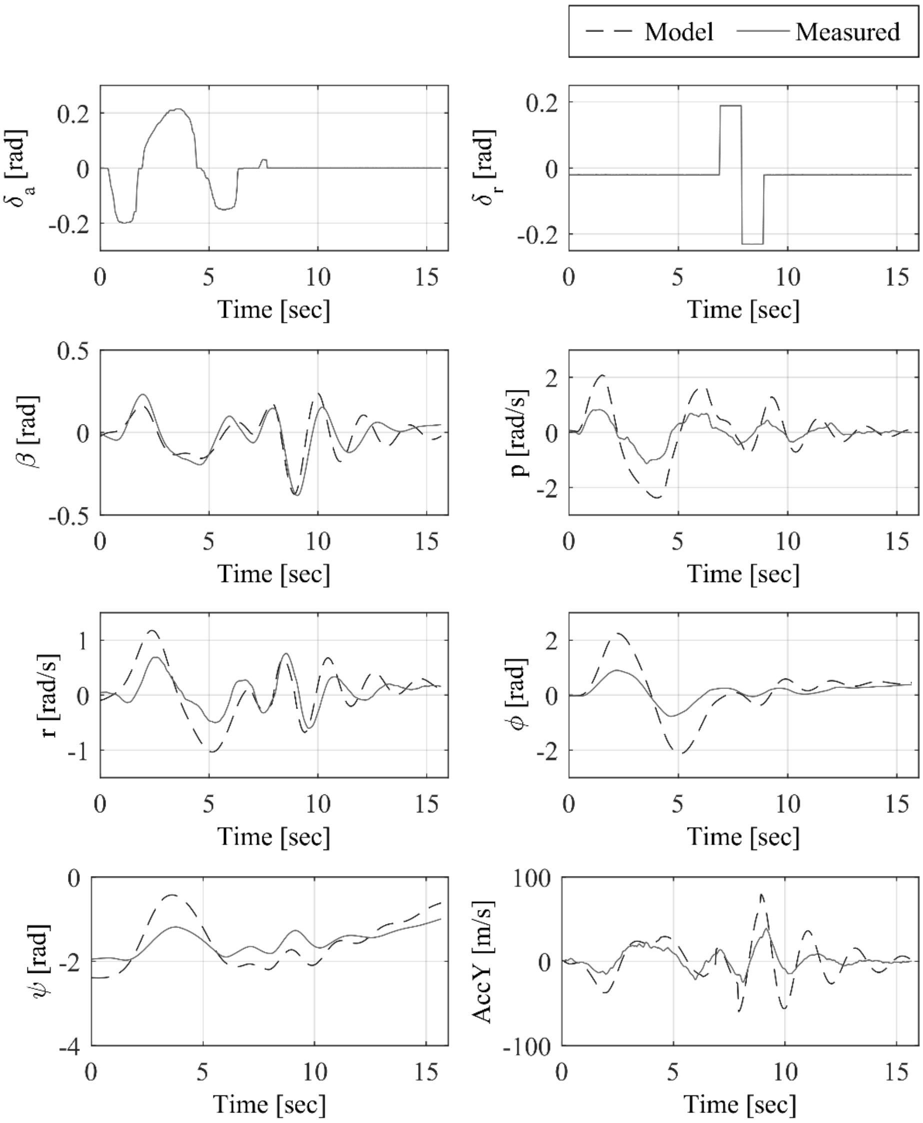

Figure 4-26 Comparison between Modelled and Measured Lateral States

4.4.4 Parameter Identification: Linear Regression

The following step in the parameter identification method was to develop adequate linear aerodynamic model structures for the lateral and longitudinal manoeuvres about a single cruise flight condition as described in Sec. 2.2.1 and Sec. 2.2.2. The initial pool of regressors for the linear aerodynamic model consisted of all first order, perturbed aircraft states. This pool was further reduced by applying the stepwise regression technique (refer to Sec. 2.2.2). A final reduction of model regressors and an initial estimate of the model parameters were determined via the orthogonal regressor technique.

The lateral force and moment structures were based on the data recorded for the two lateral manoeuvres. As stated in Sec. 3.4.3, these consisted of a combination of a sequential bank-to-bank roll and a rudder doublet. An example of the regression results for the side force coefficient model structure is given in Table 4-7. The remaining force and moment coefficient regression analyses are provided in Appendix H.1. Table 4-7 contains the key parameter significance variables: the t_0-statistics[1] and the relative error margin. Furthermore, three parameters indicating model quality were generated (i.e. the coefficient of determination (R^2), the standard deviation of the model (σ), and the condition number). The correlation coefficients were also evaluated to gauge the potential existence of significant regressor collinearity. The definitions and significance of the model quality parameters are provided in Sec. 2.2.1.

The side force coefficient (C_Y) stepwise regression analysis yielded model structures for both lateral manoeuvres that consisted of high coefficients of determination (i.e. Greater than 90%), condition numbers under 100 and comparable standard deviations between the two manoeuvres. The estimated C_Y model structures presented in Table 4-7 for lateral manoeuvre 1 and 2 partially differed by the inclusion of the angle of attack. The final model structure was composed of the parameters that were common to both structures (i.e. Common model regressors) as well as the inclusion of the angle of attack. The angle of attack was included due to its aerodynamic significance and the associated t_0-statistic for lateral manoeuvre 2. These selected model parameters then served as the regressor pool for the orthogonal regressor technique (Refer to Appendix D.1 for details on the technique). The final model structure is given by Eq. 4-4.

$$C_Y = C_{Y_0} + C_{Y_\alpha}\alpha + C_{Y_\beta}\beta + C_{Y_V}\left(\frac{\Delta V}{V_0}\right) + C_{Y_{\hat{p}}}\left(\frac{pb}{V_0}\right) + C_{Y_{\delta a}}\delta_a + C_{Y_{\delta r}}\delta_r \qquad 4\text{-}4$$

The model fit achieved for the first manoeuvre, corresponding to the 94.86 % coefficient of determination, is given in Figure 4-27. A notable model-based concern was the lack of adequate control surface dynamics modelling, evident by the sharp step in the predicted dataset at approximately eight seconds. The adverse effects of not accounting for this control lag were minimal based on the matching achieved on the

---

[1] The t_0-statistic is a representative parameter of the contribution of the regressor to the final model. It is calculated as the square of the F_0-statistic described in Sec. 2.2.2.

transient oscillation. The absence of the control surface lag must, however, be acknowledged because of the inherent introduction of higher frequencies into the model. The lag error signifies the importance of recording the actual control deflections rather than utilising the commanded inputs, especially when: aerodynamic loads are higher; control surfaces have increased inertias about the hinge line, or actuators have slower response times. These errors potentially introduce phase shifts in the modelled output responses due to differences in the excitation frequency bands. Since a time domain analysis is based on minimising the error between data points at comparative times, any lags have a direct adverse impact on the identified model. The error would be akin to comparing two frequency responses based on different frequency excitations.

A similar process was followed for the rolling moment and yawing moment models. The yawing moment coefficient model, much like the side force coefficient model, yielded good model matches with comparable standard deviations between the different manoeuvres. The rolling moment matches were poor as noted by the model fit presented in Figure 4-28 for the first lateral manoeuvre. This was attributed to the noise introduced when numerical differentiation procedures were used on the noisy roll rate signal in order to evaluate the angular acceleration required in the roll moment derivation.

Table 4-7 Stepwise Regression Results – C_Y – Lateral Manoeuvre 1

	Lateral Man. 1		Lateral Man. 2	
Regressors	t_0	(σ/θ^*) [%]	t_0	(σ/θ^*) [%]
α	-	-	13.98	7.1
β	72.29	1.4	75.68	1.3
$\Delta V/V_0$	6.89	14.5	10.82	9.2
$pb/2V_0$	10.29	9.7	10.16	9.8
$\delta_{aileron}$	20.08	4.9	20.50	4.9
δ_{rudder}	13.95	7.2	15.43	6.5
R^2 [%]	94.8		95.9	
σ	0.01		0.01	
Condition No.	13.5		25.0	

Table 4-8 Correlation Coefficients [Key: Man1 (Man2)]

	α	β	$\Delta V/V_0$	$pb/2V_0$	$\delta_{aileron}$	δ_{rudder}
α	1	-	-	-	-	-
β	(-0.22)	1	-	-	-	-
$\Delta V/V_0$	(-0.63)	0.25 (0.22)	1	-	-	-
$pb/2V_0$	(0.21)	0.03 (-0.24)	0.07 (-0.32)	1	-	-
$\delta_{aileron}$	(0.31)	0.16 (-0.09)	0.12 (-0.34)	0.85 (0.88)	1	-
δ_{rudder}	(0.07)	-0.17 (-0.14)	-0.09 (-0.08)	0.07 (0.10)	0.03 (0.08)	1

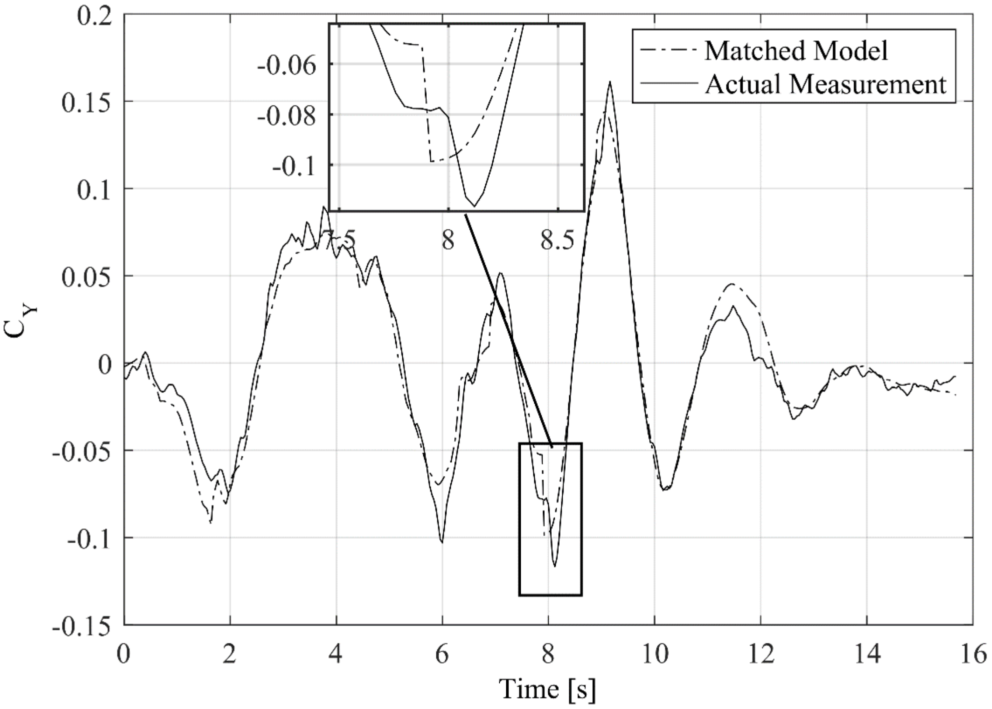

Figure 4-27 Linear Regression: C_Y Result – Model versus Measurement

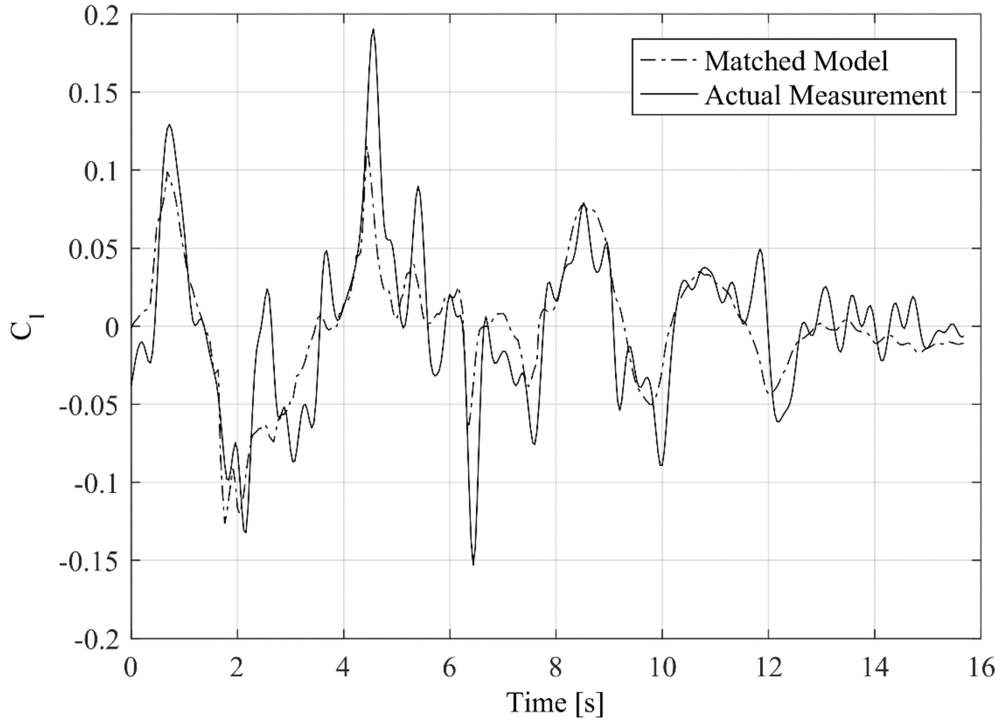

Figure 4-28 Linear Regression: C_l Result – Model versus Measurement

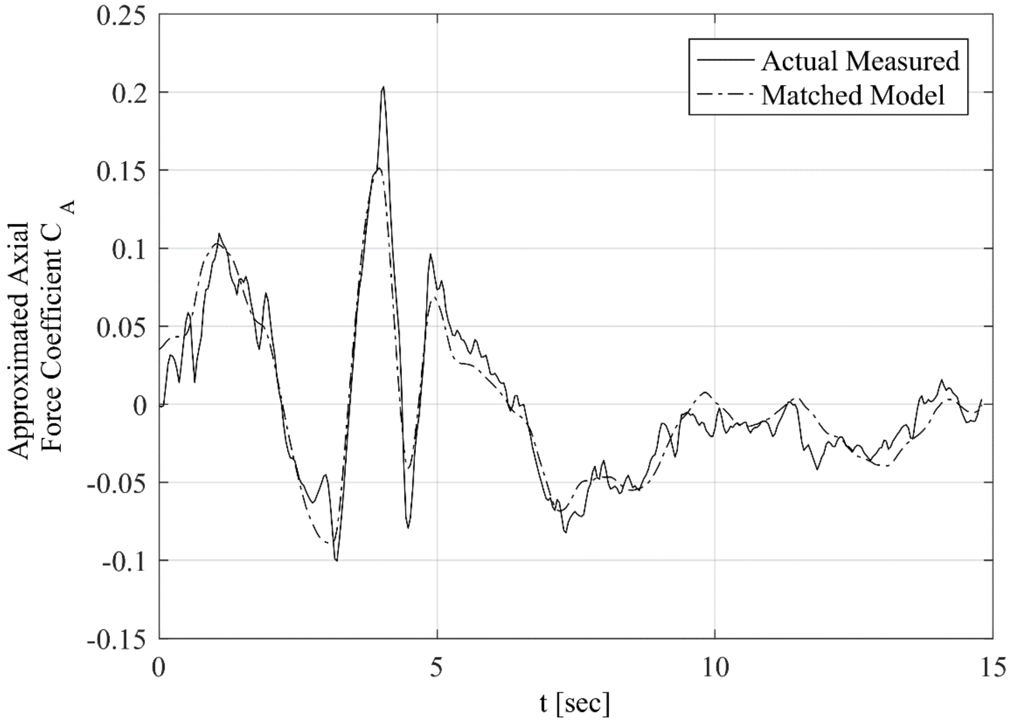

Figure 4-29 Linear Regression: C_A Result – Model versus Measurement

The longitudinal force moment model structures were then analysed using a similar process to that of the lateral models. The calculated axial force coefficient was a combination of the drag, lift, and thrust force. The thrust force was not independent as an adequate power model was not available. The thrust force and the drag were also assumed to be approximately parallel throughout the manoeuvre to simplify the analysis. This force combination also led to a reduction in the physical meaning of the parameters of the traditional linear aerodynamic drag model. The variation of thrust at a constant throttle setting was considered negligible as long as small excursions in the angle of attack were evident and approximately constant airspeeds were met across the longitudinal test manoeuvres. The resulting model structure and initial parameter estimates showed a good match (i.e. a coefficient of determination of 91.97 %) to the measured data as seen in the presentation of the result for one of the longitudinal manoeuvres in Figure 4-29. The resulting simplified final model structure and non-physical axial force derivatives used in this analysis signified the importance of a prior power model to correctly model the drag of the aircraft. A good thrust model would allow for the possibility of more robust aerodynamic models, models that have physical meaning, and models that are not limited to a specific manoeuvre. The limitation of the current model structure is noted by the variance of the final regression estimates for all four longitudinal manoeuvres. This variation in parameter estimates combined with the good model fit per manoeuvre was evidence of the uniqueness of the model to specific flight manoeuvres. This uniqueness implied a low model predictive capability.

The stepwise regression procedure yielded excellent model fits but did not yield plausible estimate results for the dynamic model parameters: $C_{L_{\dot{\alpha}}}$ and C_{L_q}. This was due to the approximately linear relationship between the rate of change of angle of attack and the pitch rate as seen by Eq. 4-5 when lateral states are negligible. This relationship is the reason for the excellent model fit and the high t_0-statistics associated with these parameters (see Table 4-9 for an example regression analysis result for one longitudinal manoeuvre) yielding a regression model strongly dependent on the kinematic correlations rather than on aerodynamic model approximations. The effect was also noted in the moment coefficient parameters associated with the rate of change of angle of attack and pitch rate. Unrealistic parameter estimates were achieved even though good model matches were evident. The initial dynamic coefficients for the lift and moment coefficient models used within the output error method were thus based on the initial data rather than preliminary regression estimates.

$$\begin{aligned} \dot{\alpha} &= -\frac{\bar{q}S}{mVcos\beta}C_L + q + \frac{g}{Vcos\beta}(cos\theta cos\phi cos\alpha + sin\theta sin\alpha) \\ &\qquad - tan\beta(pcos\alpha + rsin\alpha) \qquad \text{4-5} \\ \dot{\alpha} &\approx -\frac{\bar{q}S}{mVcos\beta}C_L + q + k \end{aligned}$$

Highly correlated parameters lead to significant identification problems and large uncertainties when using linear models as described by Jategaonkar (2006). High parameter correlations make it difficult to differentiate between the contributions of the parameters to the model. Jategaonkar (2006) describes the various strategies that are used to remedy this correlation. Application of these strategies required further flight testing and further aircraft specification data that were not available at the time of testing and analysis. One method was to apply a significant elevator doublet while the aircraft is rolled to angles greater than 50°. This method would require a coupled non-linear model, where the applicability of the linearity approximations is reduced due to the larger lateral dependencies. Another method advised was to analyse the lift coefficient regarding two contributions i.e. the separation of the wing and tail contributions to lift.

Table 4-9 Stepwise Regression Results - C_L - (3-2-1-1)

<table>
<tr><td colspan="6">C_L – 3-2-1-1: ±4° Elevator Deflection</td></tr>
<tr><td>Regressor</td><td>θ^*</td><td>σ</td><td>θ</td><td>t_0</td><td>$100(\sigma/\theta^*)$</td></tr>
<tr><td>$pb/2V_0$</td><td>-0.09</td><td>0.004</td><td>-1.84</td><td>22.54</td><td>4.42</td></tr>
<tr><td>$q\bar{c}/2V_0$</td><td>1.31</td><td>0.005</td><td>187.81</td><td>257.35</td><td>0.39</td></tr>
<tr><td>$\alpha\bar{c}/2V_0$</td><td>-0.98</td><td>0.005</td><td>-193.87</td><td>190.53</td><td>0.52</td></tr>
<tr><td colspan="6">* Standardised parameter</td></tr>
<tr><td>R^2 [%]</td><td>99.77</td><td colspan="4" rowspan="3">$C_L = C_{L_0} + C_{L_\alpha}\alpha + C_{L_{\hat{p}}}\frac{pb}{2V_0} + C_{L_{\hat{q}}}\frac{qb}{2V_0} + C_{L_{\dot{\alpha}}}\frac{\dot{\alpha}b}{2V_0}$</td></tr>
<tr><td>σ</td><td>0.004</td></tr>
<tr><td>Condition No.</td><td>5.25</td></tr>
</table>

Given the data shortfalls discussed earlier in this section, it should be noted that the modelling technique yielded suitable and consistent model structures and parameter estimates per manoeuvre. Further data is required to determine the predictive qualities of the models.

4.4.5 Parameter Identification: Maximum Likelihood

The initial step of the implementation of the output error estimation algorithms was also based on linear decoupled systems. The use of these linear decoupled systems was validated in Sec. 4.4.2. The second step of output error model development was based on the non-linear equations of motion (see Sec. 3.4.3 for method). This step included the power-off wind tunnel data represented as b-splines within the algorithms for efficient lookup. The corrected state data from the data compatibility process were used as inputs in the state propagation models when required (i.e. for off-axis states) within either of the decoupled analyses (i.e. Longitudinal or lateral). Additionally, the velocity equation was removed from the main longitudinal analysis. The axial force model associated with the velocity propagation was estimated separately and also included measured airspeed as an input state. This longitudinal model separation increased the conditioning of the algorithm, yielding a plausible solution when the alternative full coupled system was found to be divergent. This second step of output error model development, using the non-linear equations of motion supplemented by wind tunnel data, was further divided into two estimation approaches. The first approach only estimated the dynamic parameters. The wind tunnel delta parameters were held constant at zero. The second approach was based on estimating the full complement of parameters from the required model structure (see Eq. 3-22). A comparison was then made between the three output error results and against the initial aerodynamic model.

The comparative results of the three output error solutions are given in Figure 4-30. From the Theil's inequality coefficient comparisons for both lateral manoeuvres, a correlation between the increase of this parameter and the complexity of the estimation process was noted. The linearized model was found to yield the lowest Theil's inequality coefficient across all lateral states. In addition, the Theil's inequality coefficient was below the recommended maximum of 0.3 for all lateral states. All Theil's inequality coefficients were below the a priori model reflecting an increase in the quality (i.e. decrease in error) of the lateral model fit. The fit quality decreased as the complexity of the models increased. The full non-linear model with all unknown parameters estimated was found to yield the largest error across the three output error approaches. The significance of achieving better accuracy using a minimalistic model was evident and correlated to the principle of parsimony[2].

The analysis of the systematic errors using the Theil's variance and covariance parameters provided an initial indication of the predictive qualities of the estimated model. Due to the limited set of data available, however, conclusions regarding the predictive nature remain subjective. As more data becomes available, the predictive qualities of the models can be assessed through thorough validation. The Theil's variances shown in Figure 4-30 show that the side force or lateral acceleration model has higher systematic errors than the a priori model. The strong aerodynamic dependence of side force on the sideslip angle is reflected in the increased systematic error on the sideslip state model. Further directional testing would help to improve upon the side force parameter estimates. The lateral manoeuvres analysed contained little dynamic dependence on the sideslip angle causing the noted model deficiencies. The remaining lateral and directional states showed lower indications of systematic error through reduced Theil's variances. As with the Theil's inequality coefficient, the possible systematic errors for the linear dynamic lateral model were consistently low.

The lateral model results (i.e. Figure 4-30) showed that the analysis based on the linearized equations of motion and without the wind tunnel data was consistently more accurate than the approach utilising wind tunnel data and non-linear equations of motion. An improvement on the initial lateral model fits was made with all three output error estimates. It should also be noted that although improved model fits were possible with the current parameter identification technique, more data is required to reduce the possible systematic errors. This is attributed to the statistical nature of the maximum likelihood parameter estimation technique.

The higher accuracies of the linearized approach over the two non-linear approaches may also be attributed to a possible error in wind tunnel data for the first non-linear approach and a significant increase in unknown parameters for the second non-linear approach. The wind tunnel data did not account for power effects and the aerodynamic influence of the landing gear. Lateral dynamic sensitivities to power-plant effects may

---

[2] The principle of parsimony, as described by Jategaonkar (2006) states that a model should only be as complex as required and that any additional increases in complexity adversely affects the parameter estimate accuracies.

be significant given the twin-propeller configuration, where each propeller is a lateral distance from the centre of gravity of the UAV and rotation is in the same sense. The higher accuracy of the linear model was counter-intuitive but highlighted the importance of using valid simplifications to achieve a higher accuracy predictive model.

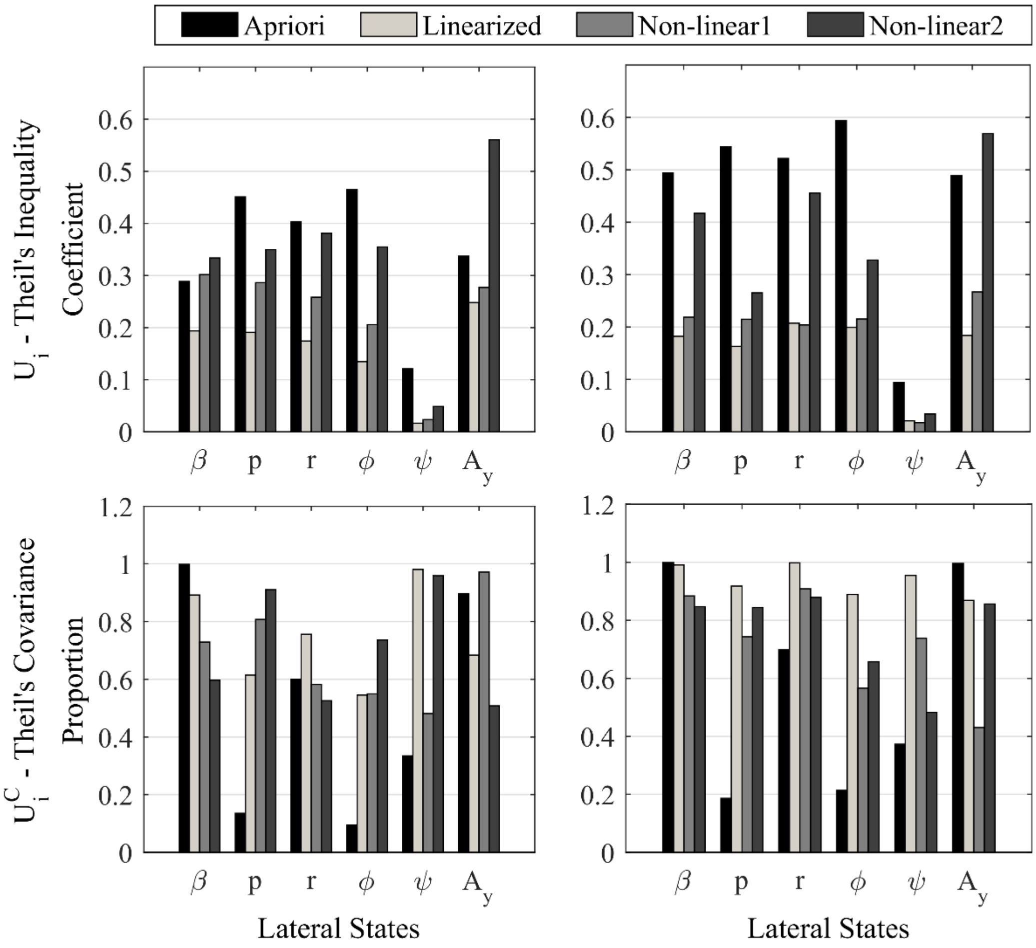

Figure 4-30 Output Error Method Lateral Results – Theil's Coefficients

The final parameter estimate results of the linearized model are given in Table 4-10 while the model time histories for the lateral manoeuvres are presented in Figure 4-31 with respect to the lateral and directional flight test inputs. The control lag was estimated to approximately one time step. However, the large standard deviation of the lag rendered the estimated value void of any physical significance. The accuracy of this time lag may only lead to useful estimates when sampling rates are increased and control surfaces dynamics are considered. Figure 4-31 reflects the Theil's coefficients and variances noted in Figure 4-30 for the linearized approach. Peak amplitudes were well captured and phase shifts were limited in all lateral time histories. The relative standard deviations are provided in the third column of Table 4-10. It should be noted that only three parameters (i.e.C_{Y_β}, C_{n_β}, and $C_{n_{\delta r}}$) were estimated to within a relative standard deviation of 10%. Given the good model fit, the low accuracies indicate the poor confidence of the predictive nature of the selected model. The parameter accuracies improve as more information is introduced into the parameter estimation process through additional flight data. The selected lateral manoeuvres were not sufficient to reduce correlation between the control inputs and output responses used within the model structure. Data obtained from additional focussed manoeuvres would reduce the correlation and increase the accuracies of the parameters. The influence of additional flight data to the parameter accuracies were beyond the scope of the current study and objectives.

In the absence of additional flight test data, confidence levels were also judged based on a parameter plausibility check. Plausibility checks given in Table H-21 were based on comparing the estimated parameters to average force and moment coefficient values for stable, conventional aircraft configurations which may be found in references such as Roskam (1979). With the exception of $C_{Y_{\hat{p}}}$ and $C_{Y_{\delta a}}$ the parameter estimates obtained from the output error methods were plausible and correlated well in terms of magnitude and direction.

It can be concluded that the parameter estimation approach taken for the lateral flight dynamics model was successfully implemented. A plausible model was achieved that correlated well to the measured data, however, further flight data is required to improve the parameter accuracies and predictive characteristics of the models.

Table 4-10 Output Error Parameter Results - Lateral, Linearized Dynamics

Parameter	Initial Model	OE Estimate	$100 * (\sigma/\theta)$
C_{Y_α}	0.133	0.033	275.15
C_{Y_β}	-0.598	-0.522	5.35
$C_{Y_{\hat{p}}}$	0.473	0.601	59.06
$C_{Y_{\delta a}}$	0.359	0.352	32.93
$C_{Y_{\delta r}}$	0.158	0.188	16.09
C_{l_β}	-0.023	-0.027	24.68
$C_{l_{\hat{p}}}$	-0.131	-0.363	31.04
$C_{l_{\dot{\beta}}}$	-0.078	-0.016	513.92
$C_{l_{\delta a}}$	-0.093	-0.139	25.22
C_{l_r}	0.033	0.052	137.98
C_{n_β}	0.064	0.066	6.36
$C_{n_{\hat{p}}}$	0.014	0.002	3519.30
$C_{n_{\hat{r}}}$	-0.171	-0.209	38.95
$C_{n_{\dot{\beta}}}$	-0.156	-0.087	90.18
$C_{n_{\delta a}}$	0.011	0.025	95.19
$C_{n_{\delta r}}$	-0.042	-0.055	8.14
τ	0.000	0.034	130.89

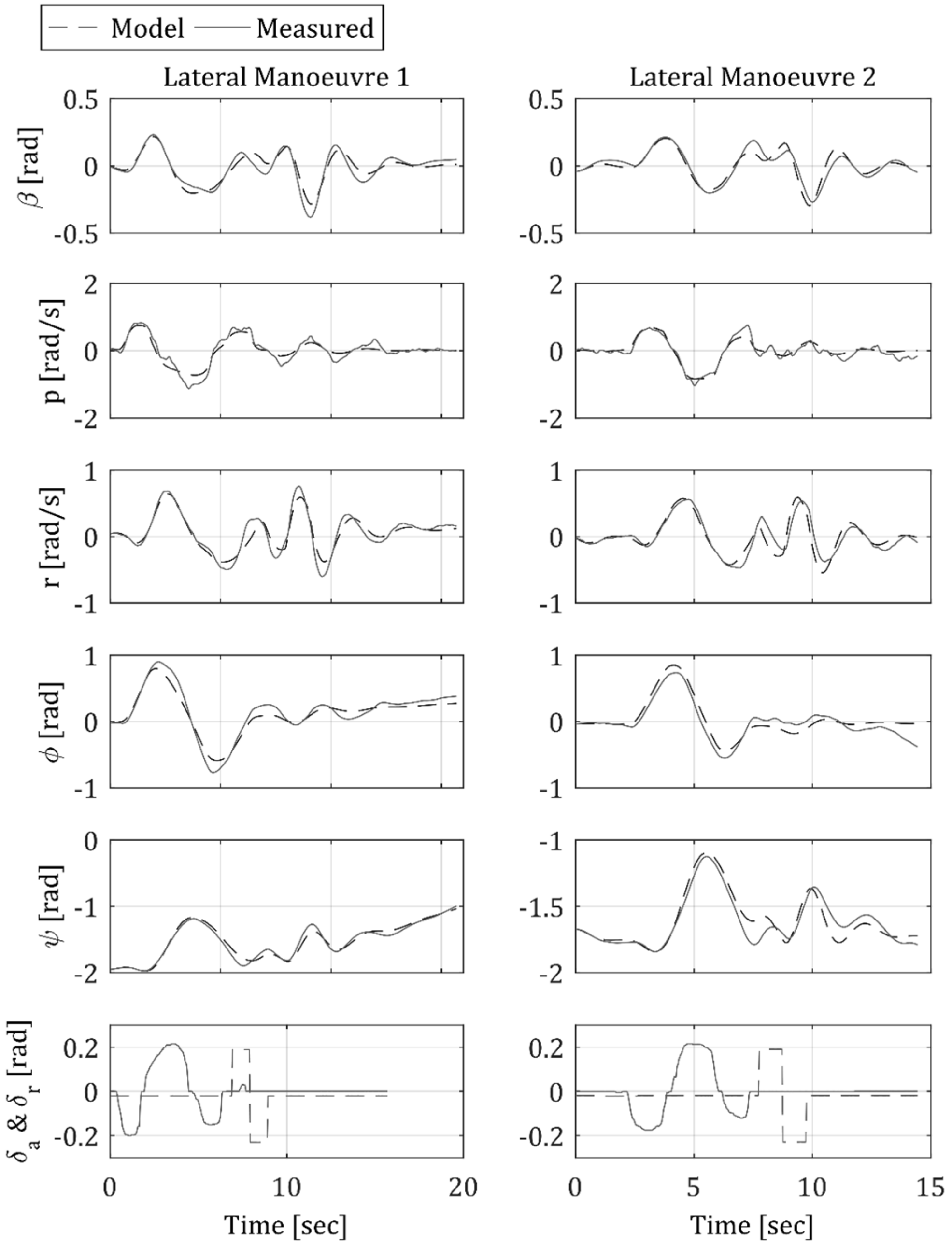

Figure 4-31 Output Error Model Results - Lateral, Linearized, Decoupled Dynamics – Time Histories

As mentioned previously, the axial force model estimation routine was separated from the analysis of the lift and pitching moment identification. The two manoeuvres used for the longitudinal model analyses contained the least lateral influences of the four available longitudinal manoeuvres. The lift and pitching moment models were estimated first. Divergent output error solutions occurred when the pitch damping coefficients were included in the parameter estimation vector for the linearized dynamic analysis. As a result of the divergence, the pitch damping coefficients were kept constant at the initial model values and the algorithm was used to determine estimates of the static coefficients only. This was due to the high correlation between the pitch rate and the rate of change of angle of attack. Although damping coefficients were excluded from the estimation process, the static longitudinal parameters were estimated with good accuracy within 15% relative standard deviation as presented in Table 4-11. The relative standard deviation of lift coefficient derivative with respect to roll rate was high at 42.63% and can be attributed to insufficient roll excitation within the longitudinal manoeuvre. The corresponding time histories are presented in Appendix H.2.

Table 4-11 Output Error Results - Longitudinal, Linearized, Decoupled Dynamics

Parameter	Initial Model	Final Analysis	$100\times\left(\frac{\sigma}{\theta}\right)$
C_{L_α}	4.987	4.344	9.56
C_{L_V}	0	0.778	14.75
$C_{L_{\hat{p}}}$	0	1.728	42.63
$C_{L_{\hat{q}}}$	4.639	-	-
$C_{L_{\dot{\alpha}}}$	1.372	-	-
C_{m_α}	-1.218	-0.357	13.65
$C_{m_{\hat{q}}}$	-17.421	-	-
$C_{m_{\dot{\alpha}}}$	-1.687	-	-
$C_{m_{\delta e}}$	-1.377	-0.977	3.16
τ	0	-	-

Estimation of the full set of parameters using the longitudinal non-linear equations of motion and wind tunnel data also led to a divergent parameter estimation solution. The final approach used the non-linear equations of motion, wind tunnel data and a parameter estimation vector only including the moment derivatives C_{m_q} and C_{m_α}. Non-physical results were again achieved for both non-linear runs. The combination of the linear model structure (see Eq. 3-22) and the information within the longitudinal flight data available was not adequate to estimate the lift and pitching moment dynamic coefficients via the output error method as noted by the divergent (non-solution) results. As with the linear regression analyses, additional flight test methods to decouple the dynamic parameters of the linear models would have to be implemented in order to achieve realistic aerodynamic model estimates.

As mentioned above, the axial force model was estimated using a separate output error simulation. The solution procedure only utilised the non-linear equations of motion because the linearized system was not a valid assumption for accurate velocity propagation given the level of noise inherent to the state measurements (refer to Sec. 4.4.2). The wind tunnel data was also excluded from this analysis because the dataset did not include thrust effects. Resulting velocity matches using the estimated axial force model was good with low relative standard deviations (i.e. below 15%) determined for the parameter set (refer to Table 4-12). It is important to re-iterate that these models were unique to each manoeuvre and throttle settings. Further testing and an adequate power model would be required to accurately model the axial force. The corresponding time histories are presented in Appendix H.2.

Table 4-12 Output Error Parameter Results – Axial Force, Non-linear Dynamics

Parameter	Initial	Final Analysis	$100\times\left(\frac{\sigma}{\theta}\right)$
C_{A_α}	0.577	0.722	10.52
C_{A_V}	0.365	0.525	2.77

The longitudinal model parameter identification routine showed significant limitations to estimation when parameter correlations were high. These limitations again highlight the importance of uncorrelated information content in the flight test data to achieve adequate parameter identification.

4.4.6 Conclusions

The parameter identification algorithm was applied through multiple implementation methods of varying complexities. These ranged from linearized models about the initial conditions of each manoeuvre to non-linear kinematic modelling involving the use of the static, power-off wind tunnel data.

The first step in the estimation method involved the validation of the linearization assumptions due to the larger amplitudes experienced during flight testing when compared to simulated amplitudes. The linearized model responses were assessed against Theil's inequality coefficients and covariance proportions to quantify the accuracy and the level of systematic errors. The linearized lateral dynamic model yielded good correlations to the measured state reconstructions with resulting Theil's inequality coefficients under the recommended 0.3 threshold. The good model fit was also reflected through a qualitative time history comparison. The Theil's covariance assessment, however, showed that there may exist systematic errors within the model for the particular manoeuvre of interest. The assessment of the nature of these possible systematic errors required further flight testing and was beyond the scope of this study. The next step was to validate the longitudinal linearization. All longitudinal state models yielded outputs below the recommended Theil's inequality coefficient of 0.3. The measured velocity data was thus used in the state propagation equations in subsequent parameter identification routines within this research. The remaining longitudinal linearized models (i.e. angle of attack and pitch rate) were valid, yielding good fits to the measured data.

The next step involved the benchmarking of the initial aerodynamic model. Both longitudinal and lateral manoeuvres were reconstructed using the initial model and compared to the measured data. The velocity state model was excluded as an adequate power model was not available and was beyond the scope of the current study. Theil's inequality coefficients and Theil's covariances were used to assess the model results. Apart from the heading, all states were close to or above the Theil's inequality recommended threshold of 0.3. Further to this, significant biases were noted within the time history comparisons of the model output and the measured responses. There was potential for significant improvement in the model parameters through the current parameter identification techniques.

The regression techniques were separated by lateral and longitudinal analyses. The lateral models structures and corresponding parameter estimates yielded good model fits for the side force coefficients and yaw moment coefficients; however the rolling moment models were poor. This was attributed to the noisy reconstructed roll moment dependent on the numerical differentiation of the angular roll rate. The exclusion of control lags was observed to be negligible, where the modelled responses did not contain any significant phase shifts. Regarding the longitudinal results, the modelling procedures were significantly influenced by the correlation between the rate of change of the angles of attack and the pitch rate. This yielded non-physical models based on the implicit kinematic relationship rather than aerodynamic force approximations. The process of stepwise regression yielded adequate models given the model fit achieved for lateral and longitudinal models. The various flight test and modelling techniques required to overcome these correlations were also detailed.

The maximum likelihood applications were more complex and required a significant amount of simplifications before stable, plausible solutions were achieved. Decoupling of the lateral and longitudinal states were required for both linear and non-linear solutions. This reduced the estimation overhead of the technique, constraining the algorithm and yielding convergent solutions. It was observed that the use of the linearized model and equations of motion led to the highest accuracy estimation results. The absence of both a thrust model and aerodynamic power effects on wind tunnel data reduced the accuracy of the initial model. This reinforced the modelling rule-of-thumb to maintain reduced complexity throughout the system identification process.

The data quality obtained via the data compatibility procedure, however, led to good results being achieved for the lateral model estimations based on the Theil's criteria. The validity of the reconstructed angle of sideslip was inherent to the plausible lateral stability derivatives that were achieved. The effect of low sampling rates and inaccuracies of control lags were observed to have had negligible influence on the comparatively low-frequency modes that were excited and modelled. This is in line with conclusions made by Morelli (1993) in which the absence of control lags had minimal effects on the control inputs for the manoeuvre design techniques. The significance of modelling control surface delays, however, should be accounted for when dealing with higher aerodynamic loads or higher control surface excitation frequencies.

4.5 NOTES ON THE VALIDATION PROCEDURES

Validation and accuracy judgements for both data compatibility and parameter estimation procedures were based on the following criteria recommended by Jategaonkar (2006):

- Residual Whiteness
- Goodness of fit
- Theil’s Inequality Coefficient
- Plausibility

It was found that the checks for residual whiteness were more significant in the data compatibility procedure than the parameter identification step. The check for residual whiteness in the data compatibility step helped to determine any irregularities within the filtering process and was an instrumental tool in determining the magnetometer inaccuracies. It was also used to confirm the adequacy of the Gaussian noise assumptions placed on the raw measurements.

The goodness of fit parameter and the Theil's inequality parameters were significant in the output error parameter identification procedures because it allowed for comparisons between different models in a quantitative manner. The improvements in the estimated lateral models over the apriori models were evidenced by the improvements in these parameters.

Regarding plausibility of the estimated values of the aerodynamic parameters, the parameters were compared with recorded stability and control data for a few conventional layout, stable aircraft found in Roskam (1979). This was possible due to the use of non-dimensional coefficients and the fact that stability and control derivatives were being analysed at this stage of system identification. Low accuracy apriori dynamic data was also available and thus used as a ballpark estimate for the likely value of the estimated results. The availability of wind tunnel data made this type of checks possible for the static derivatives as well.

The predictive qualities of the estimated models, usually achieved by matching the model output to an unanalysed set of data, was not estimated due to the amount of data available. Further testing would be required to gain further valid datasets adhering to the flight conditions that were analysed. Also, because repeatability of flight manoeuvres is, in general, low, conventional validation tests, such as those performed on wind tunnel analyses, are not possible.

4.6 MODELLING ERRORS

Various assumptions were made during the analysis procedures that may have been sources of error for the identification procedures. However, these assumptions were necessary in arriving at adequate force and moment models with the limited data available. The significant assumptions, along with the assumed effects will be discussed in this section.

Atmospheric assumptions were made, whereby turbulence was assumed to be negligible. A constant wind vector for each manoeuvre was also assumed. These factors directly influenced the eventual results of the reconstructed angle of attack and angle of sideslip time histories. The effect of any errors at the reconstruction phase was propagated through to the stepwise regression and output error analyses where the flow angles were used as regressors or measured output data respectively. These errors cannot be significantly reduced without independent measurements of the flow angles. These errors were, however, minimised via the iterated extended Kalman filter where the dynamics of the system was adhered to while filtering.

The next assumption was based on the relationship between the aircraft inertial characteristics and the expected dynamics of the aircraft. The moments of inertia values were based on a component-wise build-up rather than experimental testing. Also it was assumed that the aircraft mass properties were symmetrical about the X-Z plane therefore, the I_{yz} and I_{xy} values were assumed to be zero. The moments of inertia of the propellers were also considered negligible due to the negligible mass and relatively small propeller diameter. Errors in these properties would directly affect the evaluation of the moments acting on the aircraft and, therefore, the estimation procedures. Significant phase shifts will also occur if the inertial properties are significantly erroneous. The symmetry assumptions, however, are common practice and care was taken to accurately perform the component-wise build-up of the inertial properties. Adverse gyroscopic effects of the propeller were also deemed negligible if angular rates were low as in the manoeuvres performed.

Control deflection assumptions were also made, where the control surfaces were assumed to react instantaneously to the commands. This assumption was due to the measurements of commanded inputs and not control surface deflections. To alleviate some of the introduced error, provision was made for a constant lag term for each control surface. The effect of air-loads on the control surfaces was also not accounted for. The discrepancy that arose out of this assumption directly affected the modelling process. The extent of the errors introduced by this assumption is a complex evaluation without access to models derived with the actual control deflections available. Hence, phase shifts in the resulting models were a likely possibility but found to be negligible as the resulting model time histories reflected minimal phase errors.

Another significant assumption was that the aerodynamic forces and moments can be modelled by a linear combination of the instantaneous values of the aircraft state at any point in time. The aerodynamic loads depend on the time histories of the aircraft states as well. The instantaneous assumption is usually accepted practice when quasi-steady conditions are evident and small perturbation manoeuvres are carried out. The linear modelling is also based on the assumption of attached flow. This was deemed plausible since low angles of attack were evident in the analysed manoeuvres.

From the above discussion, it is evident that many sources of error did exist. Because this parameter identification procedure was the first iteration of the systems identification process, it would serve as a benchmark for further testing when the Modular UAV is fitted with a complete instrumentation set geared toward global aerodynamic modelling. The exact extent to which the modelling was affected by the above assumptions would then be evident via a comparison with results obtained from further analyses.

5 CONCLUSIONS

5.1 PARAMETER IDENTIFICATION

Parameter identification techniques were applied to the estimation of linear force and moment models for a single flight condition (i.e. cruise at 22 m/s) of an unmanned aerial vehicle. Linear regression was utilised to construct the model structures as well as the initial set of parameter estimates to be used in the maximum likelihood algorithm. Data compatibility procedures using an iterated extended Kalman filter with a global smoother were also applied to reconstruct the angles of attack and sideslip. The conclusions described in this section were based on the performance of these algorithms in conjunction with the flight test programme limitations based on the flowchart process presented in Figure 3-11.

Regarding the parameter estimation procedures, the regression analyses for the lateral manoeuvres yielded good model fits for the side force coefficient and yaw moment coefficient based on high coefficients of determination and regressor correlation estimations less than 90%. However, the roll moment coefficient matching was less accurate due to the numerical differentiation process of the measured roll rate and uncertain inertial data when deriving the moment time history. The effects of excluding the control time lags were also observed to yield negligible phase shifts after the modelled transient responses correlated with the measured values for the yaw moment and side force (refer to Sec. 4.4.4, and Figure 4-27). In order to reduce uncertainty with regards to control surface response and to reduce the total number of unknowns, it is recommended to experimentally determine the control response times from ground testing using control steps and frequency sweeps.

The requirement for a thrust model was noted during the longitudinal model regression analyses. The analyses were reduced to determining an approximate axial force while assuming a constant thrust vector that was parallel to the drag vector but in opposite directions. This limitation restricted the identification of an adequate drag model and thus also limited the predictive capabilities of the resultant aerodynamic model. It is highly recommended that an adequate thrust model be developed prior to further flight testing. The lift force and the pitch moment parameter estimations were also problematic due to the high correlations between the pitch rate and rate of change of angle of attack. To overcome these correlations, the model structures would have to be adapted to account for a component-wise build-up of the lift and pitch moment, through differentiating between body, wing, and tail contributions. Another suggested method would involve further flight testing, where different flight test manoeuvres would be required introducing large lateral perturbations to decouple the approximate linearity described by Eq. 4-5.

The next step involved the application of the maximum likelihood technique. Various techniques had to be implemented to attain stable convergent parameter estimation solutions. The separation of the longitudinal and lateral equations of motion, while still maintaining the non-linearity of the dynamics, increased the conditioning of the output error solution process and led to convergence. It was also determined that the linearized decoupled equations of motion were valid and thus implemented yielding satisfactory results for the lateral models (refer to Figure 4-31). The parameter identification results obtained using the linearized decoupled equations were of comparatively higher accuracy than results achieved through the combination of non-linear equations of motion and unknown deltas on wind tunnel data. This was attributed to the wind tunnel data not accounting for the fixed landing gear effects and power effects. The longitudinal analyses through both regression and maximum likelihood techniques did not yield any plausible aerodynamic models. As previously mentioned, this was due to the strong correlation between the longitudinal damping terms, $C_{L_{\dot{\alpha}}}$ and C_{L_q}. Therefore, both regression analyses based on time independent linear force and moment model construction and maximum likelihood based on kinematic (time dependent) analyses were affected significantly by the high parameter correlations within the linear stability and control longitudinal model structures, particularly when lateral influences were minimal.

Parameter correlation was noted as having a significant influence on the parameter estimates and estimation procedures (refer to Sec. 4.4.5 and Table 4-11). To reduce these correlations, particular emphasis should be placed on generating uncorrelated data as far as possible. In certain instances such as the longitudinal damping terms, the manoeuvres required to generate uncorrelated states may be beyond the cleared envelope. In these cases, it would be beneficial to estimate one of the correlated terms via alternate means (e.g. $C_{L_{\dot{\alpha}}}$). Subsequently the estimation can be carried out for the

combined term (e.g. $C_{L_q} \approx C_{L_q} + C_{L_{\dot{\alpha}}}$) and then decomposed based on the ratio of the matched combined parameter with the unmatched single parameter.
Additionally, constant time lags were introduced to the control inputs of the maximum likelihood method to model the lag between the control commands and the actual control surface responses. Results were obtained for the lateral manoeuvres and yielded values approximately equal to the sample period (i.e. approximately 0.04s as per Table 4-10). To improve on these estimates, the sampling rate would have to be increased to obtain dynamic state data within the transient control surface response.

Due to the failure of the longitudinal modelling procedures, only the lateral estimated models were validated against historic stability and control derivatives for conventional configuration aircraft. This was not an ideal validation procedure since any insight on the predictive qualities of the identified models was limited. Ideally, as mentioned in Jategaonkar (2006) and Klein and Morelli (2006) additional datasets, not used in the identification procedure, should be used in comparative analyses with the modelled responses to determine the predictive quality of the models.

From the lateral results, it was concluded that the identification of adequate parameter estimates was possible given the quality and extent of the information available on a low-cost UAV equipped with basic navigational instrumentation. Various additional techniques, however, would have to be applied. Particular attention should be given to the characterization of the longitudinal dynamics, to carry out effective parameter identification analyses. Additional wind tunnel testing was also suggested to determine the power effects of the propellers on the aerodynamics. Accurate inertial data should be attained via experimental testing such as swing testing with the aircraft configuration to be used. Accurate propulsion models should be created so that the drag models (for longitudinal models) and gyroscopic loads (for coupled lateral state modelling) may be effectively estimated. These additional sources of data would provide a significant increase in the quality of aerodynamic models achievable.

5.2 DATA COMPATIBILITY

In terms of data requirements, the application of the data compatibility check was also a vital component in the parameter identification algorithm. An iterated extended Kalman filter with a global smoother was used to reconstruct the flow angles and the constant wind vector that was assumed. An iterative solution procedure was applied accounting for the drift biases of the accelerometers and angular rates gyroscopes via the analysis of residual means. This was a valid implementation procedure since the drift biases were assumed to be small and thus, the impact on the stability of the algorithm was minimal (refer to Sec.4.3.3, Figure 4-13 and Figure 4-14). Larger biases (thus larger systematic errors), would lead to dynamic divergences of the state time histories and thus, the implementation procedure would be invalid. The acceleration and angular rate residual analyses involving residual plots versus time, the autocorrelation function, and residual cumulative probability plots provided valuable insight into the validity of the solution at the end of each iteration. These analyses assumed that the accelerometer and angular rate gyroscopes were free of systematic errors due to installation errors and thus only measurement errors were expected. This assumption was mainly attributed to the limited set of instrumentation available on board the UAV. The success of this implementation procedure was based on the good correlation between the estimated Euler angles and the onboard pre-calibrated Euler angle estimations.

The application of an optimal filtering technique in determining the measurement covariance matrices through the resultant residuals was also deemed successful through simulations and was a necessary component in the implementation of the Kalman filter algorithm. The ability to estimate the measurement error covariance matrices was shown to depend on the estimation of the filter parameters (refer to Sec. 4.3.2) and was therefore not the ideal estimation procedure; hence, precedence should be given to instrument characterization through controlled laboratory calibration tests. Upon application of the estimated measurement error covariance matrices on the flight data, it was found that the variance of the magnetometers had to be increased significantly (see Table 4-4) due to probable systematic errors. This problem was not attributed to the failure of the optimal filter technique since the error was not due to a misrepresentation of the white measurement noise but rather due to systematic errors based on uncertain magnetic field reference values.

Final results from the data compatibility algorithm for all manoeuvres yielded consistent wind vector estimations, in conjunction with good residual qualities and realistic estimations of angles of attack and sideslip. As presented in Table 4-5 and Table 4-6, the estimated wind vector for the dynamic manoeuvres correlated well with the estimated vector obtained from the analyses of the first box manoeuvre. Due to significantly differing reference altitudes between the first and second box manoeuvres, a notable difference between the estimated wind vectors was evident. The residual analyses of the accelerations and the angular rates showed correlations with white noise characteristics, with the autocorrelations resembling impulse functions (with a specified standard deviation tolerance). The systematic errors introduced by the assumption of a constant wind vector were considered negligible.

It was determined that appropriate data reconstruction analyses could be achieved with the navigational instrumentation on board the UAV. A dynamically consistent set of data was thus possible, reducing the systematic errors within the parameter identification procedures. Success of the estimated lateral models provided confidence in the estimated sideslip time histories. However, to eliminate the uncertainties involved in the data reconstruction and thus parameter identification procedures, angle of attack and sideslip sensors would have to be installed on to the UAV. This would also eliminate the assumption of constant wind vectors and provide enough information to include the accelerometer and rate gyroscope bias estimations within an IEKF algorithm solution.

5.3 FLIGHT TESTING FOR AERODYNAMIC PARAMETER IDENTIFICATION

Regarding the flight test analyses, preliminary observations found that significant variations in reference flight conditions between manoeuvres were evident. This was attributed to the fact that the manoeuvres were piloted from a ground station with a line of sight visual references only. This is in contrast to piloted flight of full-scale aircraft where the pilot has adequate real-time information available to him and a better frame of reference to carry out the manoeuvres effectively. It was recommended that the automatic navigational and stability control systems should be used for future flight tests (similar to the procedures applied by Suk et al. (2003)) so that the error introduced by the man in the loop may be removed and to effectively decouple longitudinal and lateral responses. Alternatively, a real-time calculated index of merit of the trim can be determined from the telemetry and provided to the pilot prior to the manoeuvre. It should, however, be noted that the magnitude of the differences in flight conditions experienced are generally negligible in the low speed, low altitude regimes (incompressible conditions) under which the tests were conducted.

Lateral manoeuvres were, however, carried out successfully with enough information being recorded for effective parameter identification under the required objective set. The successful combination of the R/C pilot and predefined control inputs for the sequential bank-to-bank roll and rudder doublet proved that if required, the manoeuvres may be implemented correctly provided that the manoeuvre is well coordinated by the ground station. The importance of the predefined inputs is also noted through the successful applications of the 3-2-1-1 manoeuvres (refer to Appendix F) where lateral control influences were eliminated thus reducing lateral state perturbations.

The failure to achieve adequate steady state data through the push-over pull-up manoeuvres and steady sideslip manoeuvres also indicated the importance of utilising an adequate initial flight dynamic model in the manoeuvre optimization procedures. Poor initial models decrease the probability of a successful manoeuvre providing the information content required. On the same note, the application of simple manoeuvres such as control doublets, and 3-2-1-1 manoeuvres rather than complex multi-steps or optimised harmonic inputs also proved valuable when poor initial models did exist. The increased margin for error, due to the large frequency bandwidth that these manoeuvres provide (see Figure 4-5), allowed for the successful excitation of the oscillatory modes of the UAV.

Due to the short flight test period, repeated manoeuvres required for validation purposes were limited. Therefore, extended flight test programmes would be required to obtain adequate information for complex parameter identification tasks and to increase the predictive qualities of the identified models. Obtaining adequate validation data is vital to quantify the statistical properties of the model with accuracy.

5.4 CONCLUDING REMARKS

Concerning the parameter identification research questions presented in Figure 3-11, and the main objective detailed in Sec. 1.3, the implementation of the parameter identification algorithms in achieving plausible simplified aerodynamic models was possible given the basic navigational instrumentation. However, the process did involve modifications to the parameter estimation and data compatibility algorithms to achieve stable solutions. To maximise the potential of the techniques, additions to the testing technique and instrumentation set need to be implemented. In terms of flight testing, the man-in-the-loop should be eliminated particularly if adequate navigational and stability control systems are available. Additionally, significant increases in model quality may be achieved through the installation of angles of attack and sideslip sensors, establishing an accurate thrust model, accurately characterising the inertia and mass properties of the airframe, and adequately characterizing the instrument variances through detailed calibrations.

6 REFERENCES

Babister A.W., 1961, Aircraft Stability and Control, Division 6: Flight Testing Volume I, Pergamon Press.

Batterson J.G., 1981, Estimation of Airplane Stability and Control Derivatives from Large Amplitude Longitudinal Maneuvers, NASA TM 83185, NASA.

Berndt J.S. and JSBSim Development Team, 2010, JSBSim An Opensource, Platform-Independent Flight Dynamics Model in C++, JSBSim Reference Manual, [Available at: http://jsbsim.sourceforge.net/documentation.html], [Accessed: 22 February 2016].

Berndt J.S. and JSBSim Development Team, JSBSim - Open source flight dynamic model in C++, Ver. 1.0, [Available at: https://sourceforge.net/projects/jsbsim/files/JSBSim_Source/], [Accessed: 22 February 2016].

Blackwell J. and Feik R.A., 1990, Identification of Time Delays in Flight Measurements, Journal of Guidance, Control and Dynamics, Vol. 14 (No. 1), pp. 132-139.

Broughton B.A., 2008, Blended Wing Body Project, Council for Scientific and Industrial Research, South Africa, Project Proposal

Chumalee S., Whidborne J.F., 2010, Unmanned Aerial Vehicle Aerodynamic Model Identification from a Racetrack Manoeuvre, Proceedings of the Institution of Mechanical Engineers, Part G: Journal of Aerospace Engineering, Vol. 224 (no. 7), pp. 831-842.

Cook M.V., 2007, Flight Dynamics Principles, 2nd Edition, Elsevier Ltd.

Dorobantu A., Murch A., Mettler B., and Balas G., 2013, System Identification for Small, Low-Cost, Fixed-Wing Unmanned Aircraft, Journal of Aircraft, Vol. 50 (No.4), pp. 1117-1130

Duke E.L., Antoniewicz R.F., and Krambeer K.D., 1988, Derivation and Definition of a Linear Aircraft Model, NASA Reference Publication 1207, NASA, Scientific and Technical Information Division.

Etkin B., 1959, Dynamics of Flight - Stability and Control, New York, John Wiley & Sons.

Greenberg H., 1951, A Survey of Methods for Determining Stability Parameters of an Airplane from Dynamic Flight Measurements, NACA TN 2340.

Iliff K.W., 1987, Aircraft Parameter Estimation - AIAA Dryden Lecture in Research for 1987, NASA TM 88281, NASA Ames Research Center.

Iliff K.W., 1989, Parameter Estimation for Flight Vehicles, Journal of Guidance, Control and Dynamics, Vol. 12 (No. 5), pp. 609-622.

Jategaonkar R.V., 2006, Flight Vehicle System Identification - A Time Domain Method, Reston, Virginia, Progress in Astronautics and Aeronautics, American Institute of Aeronautics and Astronautics.

Jategaonkar R.V., 2006, FVSysID, Flight Vehicle System Identification – Support Software, Progress in Astronautics and Aeronautics, American Institute of Aeronautics and Astronautics, [Conditional Availability at: http://arc.aiaa.org/doi/book/10.2514/4.866852], [Accessed: 22 February 2016].

Jonkers H.L., 1976, Application of the Kalman Filter to Flight Path Reconstruction from Flight Test Data Including Estimation of Instrumental Bias Error Corrections, Report VTH-162, Department of Aerospace Engineering, Delft University of Technology.

Klein V. and Batterson J.G., 1983, Determination of Airplane Model Structure from Flight Data Using Splines and Stepwise Regression, NASA TP 2126, NASA, Scientific and Technical Information Division.

Klein V., 1989, Estimation of Aircraft Aerodynamic Parameters from Flight Data, Progress in Aerospace Sciences, Vol. 26 (No. 1), pp. 1-77.

Klein V., Batterson J.G., and Murphy P.C., 1981, Determination of Airplane Model Structure from Flight Data by Using Modified Stepwise Regression, NASA TP 1916, NASA, Scientific and Technical Information Division.

Klein V. and Morelli E.A., 2006, Aircraft System Identification - Theory and Practice, Reston, Virginia, Progress in Astronautics and Aeronautics, American Institute of Aeronautics and Astronautics.

Maine R.E. and Iliff K.W., 1985, Identification of Dynamic Systems, Theory and Formulation, NASA RP 1138, NASA, Scientific and Technical Information Division.

Maine R.E., Iliff K.W., 1986, Application of Parameter Estimation to Aircraft Stability and Control - The Output Error Approach, NASA RP 1168, NASA Ames Research Center, Scientific and Technical Information Division.

Mathworks®, 2008, Matlab® R2008b, [Available at: http://www.mathworks.com/products/], [Accessed: 22 February 2016].

Morelli E.A., 1993, Practical Input Optimization for Aircraft Parameter Estimation Experiments, NASA CR 191462, NASA Langely Research Center.

Morelli E.A., and Klein V., 1995, Determining the Accuracy of Aerodynamic Model Parameters Estimated from Flight Test Data, AIAA 95-3499, AIAA Atmospheric Flight Mechanics Conference, AIAA.

Morelli E.A., and Klein V., 2005, Application of System Identification to Aircraft at NASA Langley Research Center, Journal of Aircraft, Vol. 42 (No. 1), pp. 12-25.

Morelli E.A., 2006, SIDPAC2.0, Aircraft System Identification – Theory and Practice – Support Software, [Conditional Availability at: https://www.aiaa.org/books/].

Morelli E.A., 1995, Estimating Noise Characteristics from Flight Test Data Using Optimal Fourier Smoothing, Journal of Aircraft, Vol. 32 (No. 4), pp. 689-695.

Morelli E.A., 1995, Global Nonlinear Aerodynamic Modeling Using Multivariate Orthogonal Functions, Journal of Aircraft, Vol. 32 (No. 2), pp. 270-277.

Morelli E.A., 1999, Flight Test of Optimal Inputs and Comparison with Conventional Inputs. Journal of Aircraft, Vol. 36 (No. 2), pp. 389-397.
Mulder J.A., Chu Q.P., Sridhar J.K., Breeman J.H., and Laban M., 1999, Non-linear Aircraft Flight Path Reconstruction Review and New Advances, Progress in Aerospace Sciences, Pergamon, Vol. 35, pp. 673-726.

Mulder J.A., Sridhar J.K. and Breeman J.H., 1994, Identification of Dynamic Systems - Applications to Aircraft, Part2: Nonlinear Analysis and Manoeuvre Design, AGARD-AG-300 Vol.3 Part 2, AGARD.

Neeland H., Arda M., Morgan D., Shirinzadeh, 2007, Autonomous Unmanned Aerial Vehicle, Department of Mechanical and Aerospace Engineering, Monash University, Australia.

Rajamurthy M.S., 1985, DO 28D1: Aircraft parameter Identification, TMSE 8501.

Roache P.J., 1998, Verification of Codes and Calculations, AIAA Journal, Vol. 36 (no. 5), AIAA.

Roskam J., 1979, Airplane Flight Dynamics and Automatic Flight Controls – Part 1, Roskam Aviation and Engineering Corporation, Appendix C5, pp. 625-633

Suk J., Lee Y., Kim S., Koo H., Kim J., 2003, System Identification and Stability Evaluation of an Unmanned Aerial Vehicle from Automated Flight Tests, KSME International Journal, Vol. 17 (no.5), pp.654-667.

Tobak M., Chapman G.T., and Schiff L.B., 1984, Mathematical Modeling of the Aerodynamic Characteristics in Flight Dynamics, NASA TM 85880, NASA Ames Research Center.

Wang K.C., and Iliff K.W., 2004, Retrospective and Recent Examples of Aircraft Parameter Identification at NASA Dryden Flight Research Center, Journal of Aircraft, Vol. 41 (no. 4), pp.752.

A. NON-LINEAR DYNAMIC EQUATIONS

The equations of motion that were utilised in the current research may be found in Klein and Morelli (2006) and assumed a rigid body dynamic system. The earth rotation was excluded, thus forming the inertial frame of reference. A flat-earth model was also assumed. The mass of the aircraft was constant, with inertial symmetry about the X-Z aircraft body-plane. Thrust was also assumed to act through the centre of gravity along the X body-axis. The resulting force and moment equations are given below:

$$\begin{aligned} m(\dot{u} + qw - rv) + mg sin\theta &= F_X \\ m(\dot{v} + ru - pw) - mg cos\theta sin\phi &= F_Y \\ m(\dot{w} + pv - qu) - mg cos\theta cos\phi &= F_Z \end{aligned} \qquad \text{A-1}$$

Where: m is the aircraft mass;

g is the gravitational acceleration constant at 9.81 m/s^2;

u, v and w are the velocity components in the X,Y, and Z body axes respectively;

$p, q$and r are the angular velocities about the X,Y, and Z body axes respectively;

ϕ, θ and ψ are the Euler angles between the body axes and the inertial axes;

and F_X, F_Y and F_Z are the liner external force components acting on the airframe in the X,Y, and Z body axes.

$$\begin{aligned} \dot{p}I_X - \dot{r}I_{XZ} + qr(I_z - I_Y) - qpI_{XZ} &= M_X \\ \dot{q}I_Y + pr(I_X - I_Z) + (p^2 - r^2)I_{XZ} &= M_Y \\ \dot{r}I_Z - \dot{p}I_{XZ} + pq(I_Y - I_X) + qrI_{XZ} &= M_Z \end{aligned} \qquad \text{A-2}$$

Where: I is the moment of inertia about the specified body-axis denoted by the subscript;

and M_X, M_Y and M_Z are the moments applied about the respective body axes.

By removing the thrust force and the moments generated by the propellers and non-dimensionalizing about a reference condition the forces and moments are given by:

$$\begin{aligned} F_X &= \bar{q}SC_X + T \\ F_Y &= \bar{q}SC_Y \\ F_Z &= \bar{q}SC_Z \end{aligned} \qquad \text{A-3}$$

and,

$$
\begin{aligned}
M_X &= \bar{q}SbC_l \\
M_Y &= \bar{q}S\bar{c}C_m + I_p\Omega_p r \qquad \text{A-4} \\
M_Z &= \bar{q}SbC_n - I_p\Omega_p q
\end{aligned}
$$

Where: $\bar{q}$ is the dynamic pressure at the reference condition;

S is the reference wing area;

b is the wing span;

$\bar{c}$ is the mean aerodynamic chord;

Ω is the rotational speed of the propellers;

T is the thrust;

and C_X, C_Y, C_Z, C_l, C_m, and C_n are the corresponding non-dimensional linear force and moment coefficients about the three orthogonal body axes.

The rotational kinematic relationships linking the Euler angle rates to the body axis angular rates were determined by:

$$
\begin{aligned}
\dot{\phi} &= p + tan\theta(qsin\phi + rcos\phi) \\
\dot{\theta} &= qcos\phi - rsin\phi \qquad \text{A-5} \\
\dot{\psi} &= sec\theta(qsin\phi + rcos\phi)
\end{aligned}
$$

Whilst the navigational equations representing the system velocity components in the inertial frame were evaluated by:

$$
\begin{aligned}
\dot{x} &= u(cos\psi cos\theta) + v(cos\psi sin\theta sin\phi - sin\psi sin\phi) \\
&\quad + w(cos\psi sin\theta cos\phi + sin\psi sin\phi) \\
\dot{y} &= u(sin\psi cos\theta) + v(sin\psi sin\theta sin\phi + cos\psi cos\phi) \qquad \text{A-6} \\
&\quad + w(sin\psi sin\theta cos\phi - cos\psi sin\phi) \\
\dot{h} &= u(sin\theta) - \mathrm{v}(cos\theta sin\phi) - \mathrm{w}(cos\theta cos\phi)
\end{aligned}
$$

B. ADDITIONAL MAXIMUM LIKELIHOOD PROPERTIES

B.1 CONVERGENCE CRITERIA

The convergence criteria utilised for the maximum likelihood method was based on a few common parameters and is also described in Sec. 2.2.3. These were the magnitude of parameter update; the relative change in the cost function; the absolute change in the cost function gradient; and the relative change of the diagonal elements of the error covariance matrix. The inequality criteria quoted by Klein and Morelli (2006) have been accepted as yielding reliable results. They are as follows:

$$\frac{\|\theta_k - \theta_{k-1}\|}{\|\theta_{k-1}\|} < 0.001 \tag{B-1}$$

Where: $\theta_k$is the parameter vector at the k-th iteration of the Gauss-Newton iteration scheme.

This represented the percentage change of the magnitudes of current iterative parameter vector to the previous estimate being less than 0.1%.

The next criteria dealt with the change in the cost function being less than 0.1% of the magnitude of the previous value of the cost function. The third criteria allowed for convergence when the magnitude of the change in the diagonal elements of the R matrix reach values below 5% of the previous values. Lastly, a value of the cost gradient, for each unknown parameter, of below 0.05 is required for convergence.

$$\left|\frac{J(\theta_k) - J(\theta_{k-1})}{J(\theta_{k-1})}\right| < 0.001 \tag{B-2}$$

Where: $J(\theta_k)$ is the cost function corresponding to the k-th parameter vector estimation.

$$\left|\frac{(r_{jj})_k - (r_{jj})_{k-1}}{(r_{jj})_{k-1}}\right| < 0.05, \forall j, j = 1,2,\dots,n_o \tag{B-3}$$

Where: $\left(r_{jj}\right)_k$ is the j-th diagonal element of the measurement covariance matrix at the k-th iteration of the maximum likelihood method.

$$\left|\left(\frac{\partial J(\theta)}{\partial \theta_j}\right)_{\theta=\theta_k}\right| < 0.05, \forall j, j = 1,2, \dots, n_p \qquad \text{B-4}$$

Where: $\left(\frac{\partial J(\theta)}{\partial \theta_j}\right)$ is the partial derivative of the cost function with regard to the j-th parameter.

B.2 EVALUATION OF THE SENSITIVITY MATRIX

As noted by Klein and Morelli (2006) and Jategaonkar (2006), the sensitivity matrix generated at each new value of θ can be calculated by two different methods: an analytical approach or a numerical approach. According to the authors, the numerical approach lends itself to being less complicated when a non-linear system is being analysed. This method of determining the sensitivities of the output equations to the system parameters involves the evaluation of the partial derivative $\frac{\partial y}{\partial \theta_j}$ by a numerical approximation based on either forward numerical differencing or central numerical differencing. The central differencing technique was determined to be more accurate. It involves perturbing each parameter individually while all others remain constant and computing the model output at each perturbation. The central differencing scheme deals with perturbations in either direction of the current parameter estimate. It is defined by the gradient calculated between the two perturbed outputs.

$$\frac{\partial y}{\partial \theta_j} = \frac{y\left(\theta_0 + \delta\theta_j\right) - y\left(\theta_0 - \delta\theta_j\right)}{2\left|\delta\theta_j\right|} \qquad \text{B-5}$$

Where: $\delta\theta_j$ represents the perturbation of the j-th parameter.

Different values quoted range from $0.01\theta_j$recommended by Klein and Morelli (2006) to $10^{-6}\theta_j$ recommended by Jategaonkar (2006).

B.3 NEARLY SINGULAR INFORMATION MATRICES

Although creating a parameter identification model from via the maximum likelihood algorithm can be achieved relatively easily, various computational problems may arise. These computational problems lead to divergence of the iterative procedure or erroneous results. A sizable concern is given to nearly singular information matrices, M. If the information matrix is nearly singular, its inversion has two main detrimental effects on the algorithm. The first is a divergent cost function and the second is large parameter step sizes within the Gauss-Newton optimisation scheme. According to Klein and Morelli (2006) the three techniques commonly used to accommodate the nearly singular information matrix are the rank deficient method; the Levenberg-Marquardt method; and the Bayes-like method.

The Levenberg-Marquardt method involves an additional positive definite matrix being added to the information matrix to improve the condition of the information matrix actually used. The positive definite matrix that is added usually comprises of a positive scalar multiple of the identity matrix. Therefore, the Levenberg-Marquardt method requires an augmentation of the entire information matrix as well as the determination of the scalar multiplier for each iteration of the Gauss-Newton optimisation.

The Bayes-like method on the other hand modifies the cost function by imposing prior information on the parameters. This in turn modifies the information matrix calculated during the Gauss-Newton optimisation which reduces the chance of ill-conditioning by filling in the lack of information content that would have led to a nearly singular matrix. A more in depth explanation of this method is given in Klein and Morelli (2006).

The last technique, as stated above is the rank deficient method. This technique is based on singular value decomposition of a matrix. The matrix of singular values (Usually a diagonal matrix) is calculated at each iterative step of the Gauss-Newton optimisation. A ratio of each singular value to the largest singular value is calculated. When the ratio falls below a predetermined criterion indicating ill-conditioning, then the inverse of the element associated with the low singular value is replaced by zero (Klein and Morelli, 2006). All elements of the singularity matrix corresponding to a ratio greater than the criterion is inverted without any alteration. This allows for a correction to be made only where it is needed and not to the entire information matrix. Hence the information matrix inverse would be determined as described below:

$$\begin{aligned} M &= USV^T \\ M^{-1} &= VS^{-1}U^T \end{aligned} \tag{B-6}$$

Where: U and V are the unitary matrices yielded by the singular value decomposition;
and S is the diagonal singular value matrix.

The rank deficient method is usually preferred over the other two methods due to its relative simplicity. It should be noted that when any of the above methods are utilised to increase the conditioning of the information matrix the estimation process is biased (Klein and Morelli, 2006). This biasing is usually accepted over the potential error that could be introduced via an ill-conditioned information matrix.

C. JSBSIM SIMULATION ENVIRONMENT

C.1 JSBSIM

JSBSim is an open source flight dynamic model. The aircraft models are created in XML format made up of different aircraft components. The vital components of the aircraft model are the mass and inertial models, the aircraft geometry, flight control models, propulsion models, and aerodynamic models. Other optional system models are provided but were not significant in terms of the requirements of the current project.

The forces and moments due to aerodynamic influences are built up as force or moment components about the three axes of the aircraft. Each component along each axis is summed to give a total force or moment contribution about their respective axis. The components are provided as a single variable (representing a stability or control derivative) or in multi-dimensional tables for non-linear aerodynamic models.

A flight control system can also be assembled to provide a defined sequence of control deflections necessary in parameter identification manoeuvre design. These control systems can be, and were, compiled in a separate XML file and called by the main aircraft definition file. This functionality is applicable to all components of the aircraft described above.

The output files compiled by JSBSim can be constructed based on user specified properties. Examples of these properties are the aircraft state information, control surface deflections, aircraft location. Additionally, all the selected properties would be sampled at a user defined frequency throughout the simulation. Therefore, all information relevant to the flight dynamics can potentially be recorded. A full list of the components and attributes can be found in Berndt (2010).

C.2 SIMULATED AIRCRAFT MODEL

The first aircraft model was a linear model based on the aircraft detailed in Roskam (1979). The reference flight condition of the aerodynamic model is given in Table C-1. The corresponding aerodynamic model characteristics are provided in Table C-2. The aerodynamic reference point for the forces and moments was taken as the centre of gravity of the aircraft.

Table C-1 Reference Flight Condition Parameters (Roskam, 1979)

Property	Value	Unit
Altitude	35000	ft
Velocity	876	ft/s
Air Density	0.000739	slugs/ft^3

Table C-2 Stability and Control Derivatives (Roskam, 1979)

Parameter	Value	Parameter	Value
C_{L_0}	0.26	C_{D_0}	0.03
C_{L_α}	3.75	C_{D_α}	0.3
$C_{L_{\dot{\alpha}}}$	0	C_{D_u}	0.27
C_{L_q}	0	$C_{T_{X0}}$	0.03
$C_{L_{\delta e}}$	0.40		
C_{L_u}	0.27		
C_{m_0}	0	C_{Y_β}	-0.68
C_{m_α}	-0.4	C_{Y_p}	0
C_{m_q}	-2.7	C_{Y_r}	0
$C_{m_{\dot{\alpha}}}$	--1.3	$C_{Y_{\delta a}}$	-0.016
$C_{m_{\delta e}}$	-0.58	$C_{Y_{\delta r}}$	0.095
C_{l_β}	-0.08	C_{n_β}	0.125
C_{l_p}	-0.24	C_{n_p}	-0.036
C_{l_r}	0.07	C_{n_r}	-0.27
$C_{l_{\delta a}}$	0.042	$C_{n_{\delta a}}$	-0.001
$C_{l_{\delta r}}$	0.006	$C_{n_{\delta r}}$	-0.066

D. ADDITIONAL LITERATURE

D.1 LEAST SQUARES REGRESSION: ORTHOGONAL REGRESSORS

The orthogonal regressor method is based on generating orthogonal regressors from the initial regressor pool prior to the least squares analysis. Therefore, the first step involves the selection of standard dynamic parameters (i.e. angle of attack, angle of sideslip, roll rate, pitch rate, etc.) as well as control inputs/deflections. This step is common to the standard least squares estimation scheme.

The following step involves the orthogonal regressor matrix generation. As described in Morelli (1995), the orthogonal functions p_j are functions of the original regressor matrix. To make sure all possible polynomial combinations are accounted for, a reference index, k, is allocated to each of these combinations. Each index, k, corresponds to an array containing a set of integers describing the power to which each original regressor is raised. The order of the elements within the arrays corresponds with the order of the original regressor matrix (i.e. the first element in an array corresponds with the first column of the original regressor matrix). For example, if index k=3 corresponds to the array: [1 0 1 2], the resulting kth polynomial combination of the original regressors is:

$$w_k = x_1^{k_1} \otimes x_2^{k_2} \otimes \dots \otimes x_m^{k_m} \qquad \textbf{D-1}$$

$$e.g.\ w_3 = x_1^1 \otimes x_2^0 \otimes x_3^1 \otimes x_4^2 \qquad \textbf{D-2}$$

Where: m is the number of original regressors;

$\otimes$ is the dot product of any two vectors;

w_k is the k-th orthogonal vector;

x is a regressor from the original pool of regressors;

and the order of the k-th set, $\varphi(k)$, is evaluated by the addition of all elements within the k-th set. The order of the above example, Eq. D-2, is $\varphi(3) = 1 + 0 + 1 + 2 = 4$.

All sequential k sets must be ordered according to the polynomial order they relate to (i.e. A second order set should come after a first order set). In other words k=1 must be the set with the lowest polynomial order. This is usually a zeroth order set {0 0 … 0}, accounting for the regressor of ones as in the previous methods described, to accommodate the constant bias term. Therefore p_1 is usually the vector of ones.

The next step involves generating the orthogonal multivariate polynomial functions. Each orthogonal function, p_k, is derived from Eq. D-3.

$$p_k = x_\mu \otimes p_{\tilde{k}} - \sum_j \gamma_k^j p_j \tag{D-3}$$

Where: $\tilde{k}$ is the previous k-th array;

μ is the index of the array that changed;

and γ is a constant.

The previous k-th set is defined as the set from which the current set "evolves from". This means that the previous set should differ by one element to that of the current set and the difference should be equal to positive one. Therefore, for example, if the current k-th set is {1 0 1 2} then a previous set could be {0 0 1 2}. From the definition it is seen that $p_k$is the orthogonal function related to the previous k-th set. Following this, is the index μ representing the element that changed in the k-th array. In the example given above, μ = 1. The variable γ_k^j is calculated via Eq. D-4.

$$\gamma_k^j = \frac{p_j^T \left(x_\mu \otimes p_{\tilde{k}} \right)}{p_j^T p_j} \tag{D-4}$$

The summation in Eq. D-4 is carried out over $j < k$ and only if the *j*th set is a polynomial order equal to, one below or two below the current *k*th set The number of *k* sets limits this process. Increasing the number of *k* sets can be achieved by either adding more regressors to the original regressor matrix or by increasing the limiting polynomial order. As was noted previously, increasing the number of regressors could lead to the prediction capabilities being degraded and as mentioned in Klein and Morelli (2006), the output noise could be modelled. The *k* sets could also be developed by accounting for every possible multivariate polynomial combination (more of a brute force strategy), or by introducing k sets with indices that are most likely to be relevant, thus reducing the chance of creating a model without physical meaning.

Once all potential orthogonal regressors are generated, the most relevant regressors are chosen in a similar manner to that of stepwise regression. Although in this case, only the PSE value is used as a measure of model adequacy. The potential regressors are entered into the model according to the correlation coefficient value, R^2. Hence, the regressor with the highest correlation coefficient value will be entered into the model first. Due to the nature of the PSE criteria, a model is deemed adequate when this criterion reaches a minimum.

In the next step all orthogonal regressors retained in the model would be represented by polynomial functions. This allows for the representation of the orthogonal regressors as functions of the original regressors. As explained in Klein and Morelli (2006), this process introduces little error due to the formulation of the regressors as represented in Eq. D-5. The polynomial structure is given as:

$$p_k = b_{k1}w_1 + b_{k2}w_2 + \cdots + b_{kk}w_k \qquad \textbf{D-5}$$

The process of estimating the coefficients, b_{kk} is carried out via the least squares estimation procedure. The error introduced by polynomial expansion is negligible as reported in Morelli. Once the orthogonal regressors are represented as multivariate polynomials, they are used as regressors in a global model least squares algorithm. The coefficients of the global model are determined via the usual least squares estimation scheme. As a final step, in order to represent the final model as a function of the original regressors, the parameters are grouped according to the original regressors. Therefore a global model is arrived at which is an explicit multivariate polynomial function of the original regressors.

E. ALGORITHM VERIFICATIONS

E.1 INTRODUCTION

The importance of verification and validation of the various functions or algorithms was of paramount importance if a successful parameter identification process was to be achieved. Because all the proposed algorithms were successfully used in practice by various authors, and the fact that the theory base has been rigorously developed (refer to Sec. 2), more emphasis was placed on the verification of the coding rather than on the validation of the theory in the current section. The importance of going through an effective verification process was so that credible comparisons can be made with past and future systems identification analyses and to confidently modify the SIDPAC 2.0 and FVSysID algorithms adding a greater degree of complexity when required.

On the other hand, validation in a systems identification environment is used to describe the predictability of the resultant model against performance criteria using datasets that were not used in the model creation. The main reason for this limited definition of validation is because flight manoeuvres cannot be replicated perfectly in a real environment, and hence repeatability characteristics are generally very low.

The main verification results for the algorithms used are presented in the following sub sections. As described above, an emphasis was placed on the verification of the adapted and new Matlab® scripts created by the author.

E.2 FILTERING FOR MEASUREMENT NOISE VARIANCE ESTIMATIONS

The use of the optimal filtering technique to estimate the instrument measurement covariance matrix was suggested by Morelli (1995) and Klein and Morelli (2006). In the current report, the adequacy of the technique was analysed via simulated data as described in Sec 3.3.3. The first step involved validating the adequacy of using the optimal filter in estimating typical IMU (inertial measurement unit) measurement error variances. The second step involved analysing the preliminary performance of the IEKF based on the respective estimated measurement variances.

Results for the first step of the analysis are given in Table E-1 detailing the imposed noise characteristics on the simulated flight parameters, the estimated results and corresponding errors. The manoeuvre consisted of both longitudinal and lateral control surface excitations. Conservative noise variances were imposed on the data in order to represent a lower quality IMU.

The derived measurement variances were defined as the variances of the residual between the optimally filtered data and the unfiltered data. It was evident that the method relied on good signal to noise ratios. This signal-to-noise dependency is noted in some cases with large relative errors in excess of 40% (i.e. X acceleration) when the signal to noise ratio was much less than one. An important characteristic is that all measurement variances were underestimated (i.e. A conservative estimate). A postulation for the under-estimation of variances was that the cut-off frequency was too high, reducing the optimality of the filter. A high cut-off frequency leads to an increase in the noise band being absorbed into the extracted signal, yielding lower residuals and the under-prediction of the variance.

By analysing the definition of the optimal filter, Eq. 2-48, it is evident that the effective cut-off frequency is dependent on two parameters i.e. C_n and C_s. In the current work, C_n was evaluated as the RMS value of successive peak magnitudes of the Fourier sine series coefficients, $b|k|$, within the higher frequency spectrum of the analysis. Due to the relatively minor changes in peak magnitudes of the sine series coefficients within the higher frequency bands, optimal values for the calculated RMS can be achieved easily. The evaluation of C_s , however, was more sensitive to the least squares fit of the sequential $b|k|$ values near the cut-off frequency band. Even though the global $b|k|$ coefficient trend for the signal follows the postulated cubed root fit, abrupt local changes near the cut-off frequency are possible. This possibility adversely affects the least squares fit of the cubed root function that utilised only local peaks for such a fit. The optimality of the C_s evaluation was more sensitive to the local trends of the peak magnitudes of the Fourier sine series coefficients, hence affecting the effective cut-off frequency. This affected the optimality of the filter and the variances that were determined. The ability of estimating the variances to within realistic representations of the true measurement variances via the optimal filter, was significantly dependent on the estimation of the filter parameters, in particular the C_n evaluation. The reliance of the estimated variances on the performance of the curve fitting process of the postulated cubed root trend led to various degrees of error between individual lateral measurements.

Table E-1 Optimal Filter Effectiveness on Predicting the Measurement Noise on Lateral States and Navigation Parameters given a Lateral Manoeuvre

Parameter	True Noise RMS	True Variance	Estimated Variance	True Signal-to-noise	Estimated Signal-to-noise	Variance Error [%]	Signal-to-noise Error [%]
p [rad/s]	0.010	109.7E-06	93.7E-06	16.56	17.94	-14.54	8.31
q [rad/s]	0.010	109.7E-06	95.9E-06	2.48	2.88	-12.53	16.31
r [rad/s]	0.010	109.7E-06	57.8E-06	3.14	4.53	-47.31	44.15
accel_x [m/s^2]	0.984	0.97	0.95	0.15	1.02	-1.86	560.25
accel_y [m/s^2]	0.984	0.97	0.88	0.95	1.45	-9.03	52.27
accel_z [m/s^2]	0.984	0.97	0.83	32.68	35.36	-14.03	8.22

The following step of the validation of method, involved determining the validity of using the variance estimates, based on the level of error described above, within the data compatibility module. The severity of the potential variance error was determined by comparing the IEKF estimation results for the instrumentation biases using the estimated variance and the true instrument variances respectively. An additional run was carried out with the measurement variances increased by a factor of 10 to simulate large variance errors. Three runs were carried out in total with increasing measurement variance errors.

As described in Sec. 3.3.3, in addition to Gaussian measurement noise, biases were included in the simulated data for accelerations, angular rates, inertial (earth relative) positions, and inertial velocities. The initial bias parameters (a priori data) used in the algorithm were set to zero in all cases. The results of the IEKF estimations are provided in Table E-2. The different measurement covariance test specifications are listed below:

- Test 1: True measurement covariance matrices
- Test 2: Measurement covariance matrix estimated via optimal filter results
- Test 3: Measurement covariance matrix of Test 2 multiplied by 10

Comparative plots of the relative errors and the standard deviations associated with the resultant estimates are provided in Figure E-1 and Figure E-2 respectively.

The baseline test: Test 1, was analysed in terms of the performance of the IEKF algorithm. Therefore, a comprehensive residual analysis on the input measurements (a_x, a_y, a_z, p, q, r) was carried out, thus verifying the Kalman filtering and estimation process. Results of these residual tests are provided in Appendix G.1. It was found that the autocorrelation functions resembled impulse function within a tolerance correlating to a 95% confidence interval. The linearity of the inverse of the cumulative probability functions also signified a correlation to Gaussian noise characteristics thus validating the IEKF measurement error assumptions. These results were indicative of the satisfactory performance of an IEKF filtering procedure.

Table E-2 IEKF Parameter Estimation Results

Parameter Bias	True Bias	Test 1	Test 2	Test 3
Δa_x, [ft/s^2]	0.1	0.1085	0.1172	0.155
Δa_y, [ft/s^2]	0.1	0.0794	0.089	0.1414
Δa_z, [ft/s^2]	0.1	0.1048	0.0867	0.0619
Δp, [rad/s]	0.1	0.0996	0.0996	0.0995
Δq, [rad/s]	0.1	0.1007	0.1007	0.101
Δr, [rad/s]	0.1	0.1002	0.1002	0.1003
Δh, [ft]	5	5.1033	4.4262	1.6496
$\Delta \dot{h}$, [ft/s]	5	5.0935	5.0698	4.7522
ΔN, [ft]	5	4.8236	4.4997	1.8211
$\Delta \dot{N}$, [ft/s]	5	5.0325	5.0114	4.6762
ΔE, [ft]	5	4.7141	4.7585	2.505
$\Delta \dot{E}$, [ft/s]	5	5.0757	5.0789	4.8312

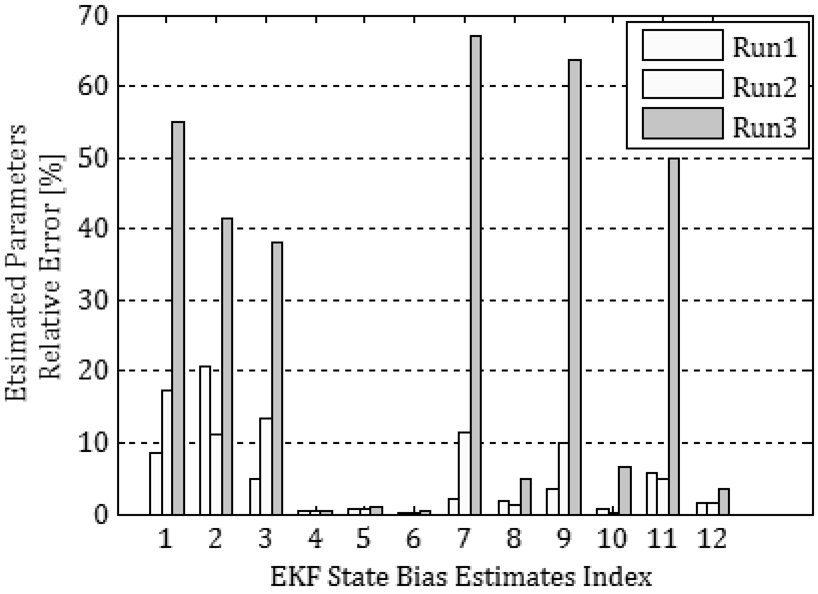

Figure E-1 IEKF Relative Errors of Estimates

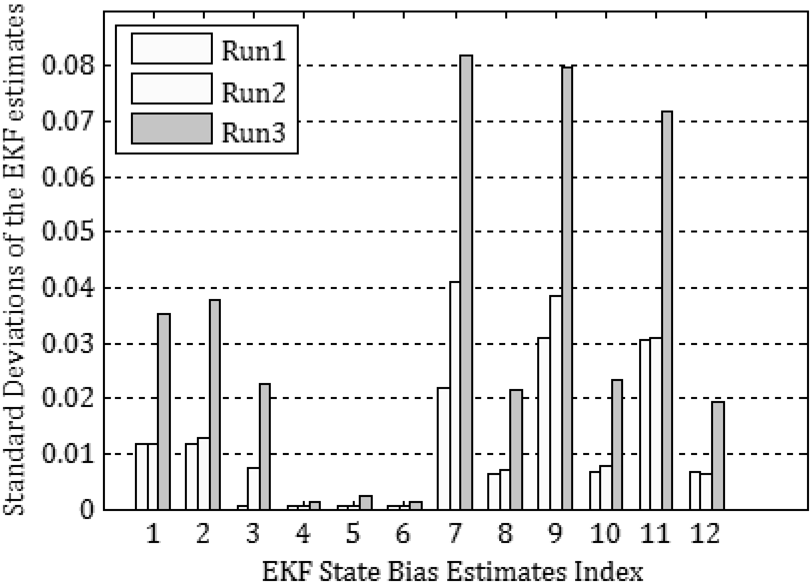

Figure E-2 IEKF Standard Deviations of Estimates

Figure E-1 and Figure E-2 present the trends that were observed through the different IEKF tests on the basis of calculated standard deviations and relative errors. The adverse effects of using the estimated covariances (Test 2) over the true measurement covariances were evident however not as significant as the errors due to large covariance errors. Therefore, if careful application of the optimal filter was carried out, realising the importance of the C_n evaluation, negligible IEKF errors could be achieved, however the sensitivity of the IEKF algorithm to the measurement covariance matrix errors had to be acknowledged.

The reader should also note that the information present in Figure E-1 and Figure E-2 limited the results to relative comparisons between each other and not on absolute values. This was due to the fact that the IEKF bias results were also dependent on the magnitudes (represented by RMS values) of the corresponding measurements as noted in Figure E-3. Because the excitation being analysed was predominantly longitudinal, larger errors in the lateral parameters were evident. Hence, as was expected (refer to estimator properties in Sec. 2.4), the IEKF performance was also significantly dependent on the information content within the dataset.

In conclusion, it would therefore be advisable practice to determine the correct measurement covariances via controlled laboratory testing to avoid any potentially significant errors based on the estimation of the covariances through a filtering process such as the optimal filter. However, if this is not an option, as is the case for the current research, the cautious application of the optimal filter in deriving the measurement covariances could lead to negligible reductions in the IEKF performance. Additionally, the dependence of the parameter estimations on the level of excitation of the measurements should be considered based on preliminary results of Sec. 4.4.

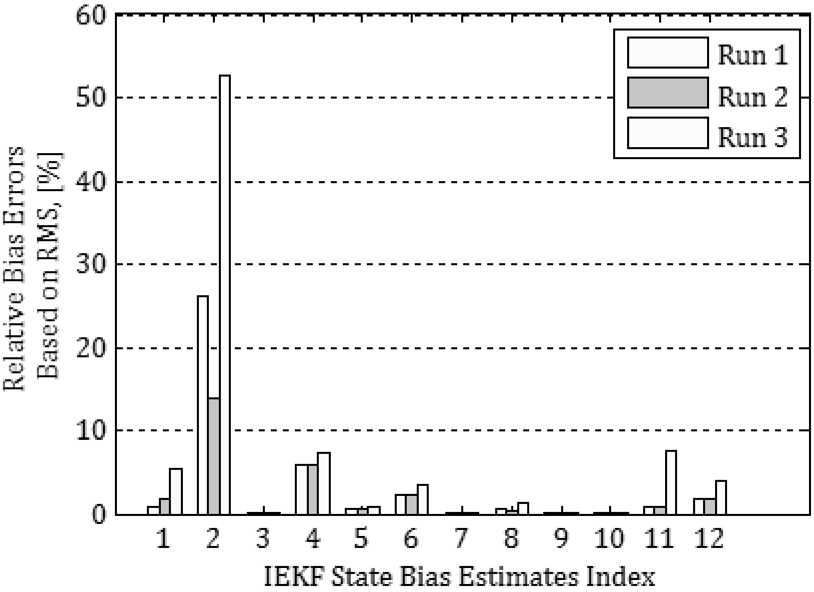

Figure E-3 IEKF Relative Errors based on Measurement RMS

E.3 LEAST SQUARES REGRESSION AND RESIDUAL ANALYSES

The least squares function was verified against the result from Klein and Morelli (2006), where identical datasets were used. The resulting yawing moment model had a coefficient of determination, R^2, value of 0.996 or 99.6%. The model standard deviation was calculated to be 2.25E-4. This result correlated well with the secondary data. Figure E-4 shows the resultant yawing coefficient, C_n , against the measured values.

The estimated parameters were similar to the benchmark case as shown in Table E-3 to Table E-6. Other verification parameters that correlated well with the secondary data were the t_0 statistic, the variances of each parameter as well as the elements of the covariance matrix.

The residuals, autocorrelation function, and the cumulative probability function exhibited the same magnitudes as that of the secondary data and showed the same qualitative characteristics. The standard deviations for each of these parameters using a 95% confidence interval also correlated with the secondary data. Quantitative verification of the residuals was indirectly determined through the corrections of the parameter standard deviations, accounting for coloured residuals. The corrected standard deviations matched those of the secondary data to 2 significant digits.

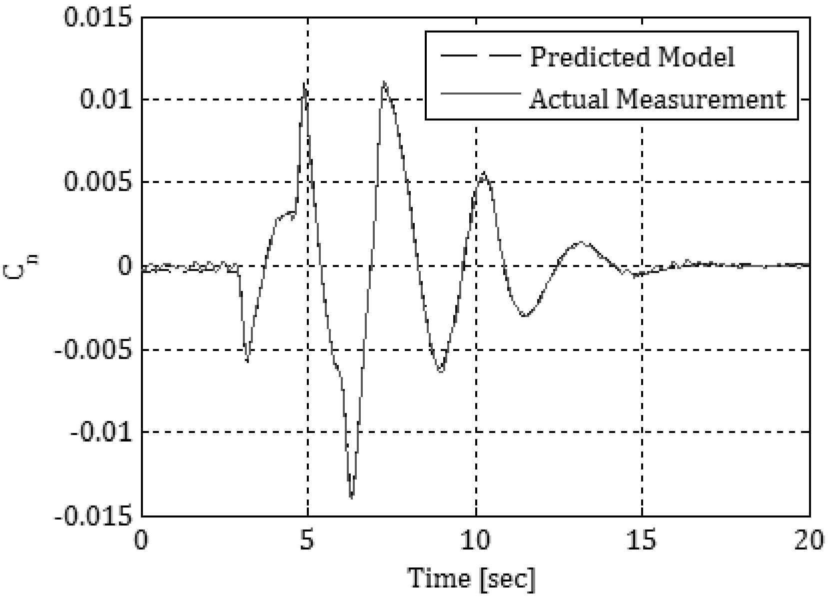

Figure E-4 Comparison of Modelled and Measured Cn

Table E-3 Secondary Data - Estimation Results (Klein and Morelli, 2006)

Table	Estimate	σ	$\lvert t_0 \rvert$	100(s/p)	corrected σ
C_{n_β}	8.54E-02	3.58E-04	238.90	0.40	1.16E-03
C_{n_p}	-5.15E-02	1.43E-03	35.90	2.80	4.01E-03
C_{n_r}	-1.98E-01	1.30E-03	151.80	0.70	3.66E-03
$C_{n_{\delta a}}$	2.34E-03	5.00E-04	4.70	21.40	1.27E-03
$C_{n_{\delta r}}$	-1.31E-01	5.97E-04	218.50	0.50	1.88E-03
C_{n_0}	4.60E-04	7.42E-06	62.00	1.60	2.71E-05
σ	2.25E-04				
R^2	99.6				

Table E-4 Least Squares Regression Function Results – Modified Algorithm

Parameter	Estimated	σ	|t₀|	100(σ/θ)	corrected σ
C_{n_β}	8.54E-02	3.58E-04	238.94	0.42	1.16E-03
C_{n_p}	-5.15E-02	1.43E-03	-35.91	-2.78	4.02E-03
C_{n_r}	-1.98E-01	1.30E-03	-151.81	-0.66	3.68E-03
$C_{n_{\delta a}}$	2.34E-03	5.00E-04	4.67	21.39	1.27E-03
$C_{n_{\delta r}}$	-1.31E-01	5.97E-04	-218.50	-0.46	1.89E-03
C_{n_0}	4.60E-04	7.42E-06	61.97	1.61	2.72E-05
σ	2.25E-04				
R^2	99.622				

Table E-5 Secondary Data – Correlation Coefficients (Klein and Morelli, 2006)

	C_{n_β}	C_{n_p}	C_{n_r}	$C_{n_{\delta a}}$	$C_{n_{\delta r}}$	C_{n_0}
C_{n_β}	1	0.82	0.15	0.67	-0.02	0.03
C_{n_p}	-	1	0.3	0.89	-0.18	-0.02
C_{n_r}	-	-	1	0.29	0.79	-0.21
$C_{n_{\delta a}}$	-	-	-	1	0.16	-0.01
$C_{n_{\delta r}}$	-	-	-	-	1	-0.28
C_{n_0}	-	-	-	-	-	1

Table E-6 Least Squares Regression Function - Correlation Coefficients – Modified Algorithm

	C_{n_β}	C_{n_p}	C_{n_r}	$C_{n_{\delta a}}$	$C_{n_{\delta r}}$	C_{n_0}
C_{n_β}	1.000	0.820	0.154	0.667	-0.018	0.030
C_{n_p}	-	1.000	0.304	0.885	0.177	-0.017
C_{n_r}	-	-	1.000	0.290	0.793	-0.210
$C_{n_{\delta a}}$	-	-	-	1.000	0.158	-0.006
$C_{n_{\delta r}}$	-	-	-	-	1.000	-0.278
C_{n_0}	-	-	-	-	-	1.000

The autocorrelation function and the inverse of the cumulative distribution function were also evaluated. The plotted results were qualitatively similar to that presented in Klein and Morelli (2006).

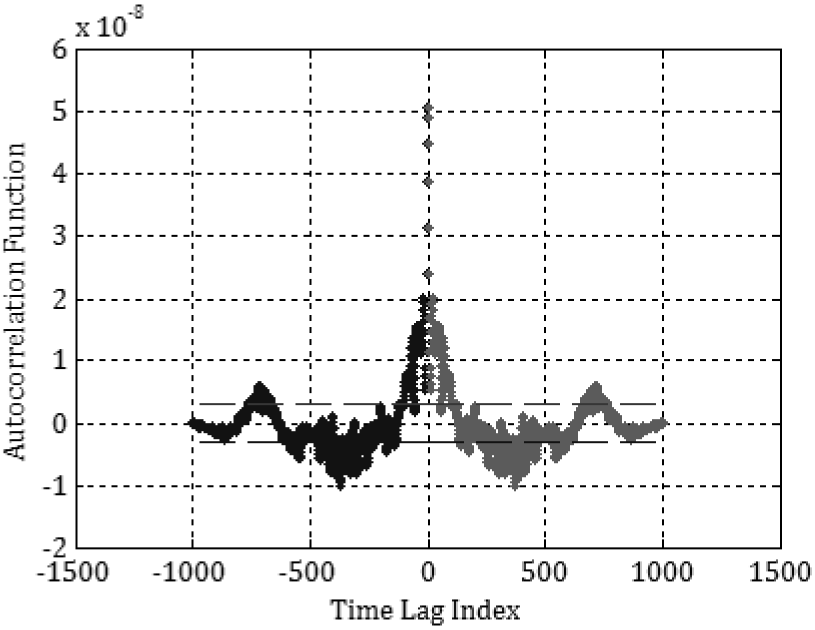

Figure E-5 Autocorrelation Function Verification

Figure E-6 Cumulative Probability Analysis

Because all parameters that were tested correlated well (i.e. identically to at least 2 significant digits), the verification was successful and the least squares function was hence utilised confidently in further programs.

E.4 STEPWISE REGRESSION ANALYSES

The stepwise regression algorithm involved in model structure determination was verified against existing data found in Klein and Morelli (2006) and from the estimates of SIDPAC 2.0. All algorithms used at this stage of verification used secondary data describing a large amplitude longitudinal manoeuvre of a highly manoeuvrable jet aircraft. This regressor data is presented in Figure E-7. The parameters of interest, listed below, were compared with the secondary data at each step of the stepwise regression procedure. This served as verification that the equations utilised were applied correctly.

The parameters compared in the verification process were:

- Aerodynamic parameter estimates
- Partial correlation factors of the regressors
- PSE values
- PRESS values
- F-statistic values of each parameter

All the parameters of interest matched the secondary data at each step of the algorithm, hence verifying the solution process to the degree necessary. The resulting normal force coefficient was found to be:

$$C_Z = C_{Z_0} + C_{Z_\alpha}\alpha + C_{Z_q}q + C_{Z_{\delta e}}\delta e + C_{Z_{\alpha^2}}\alpha^2 \qquad \textbf{E-1}$$

The final model result as compared to the measured value of normal force coefficient is given in Figure E-8. The final model had an R^2 value equal to 99.34% and a standard deviation of 4.18×10^{-2}. The results of the verification process for the 5 progressive steps of the stepwise regression are presented in Table E-7.

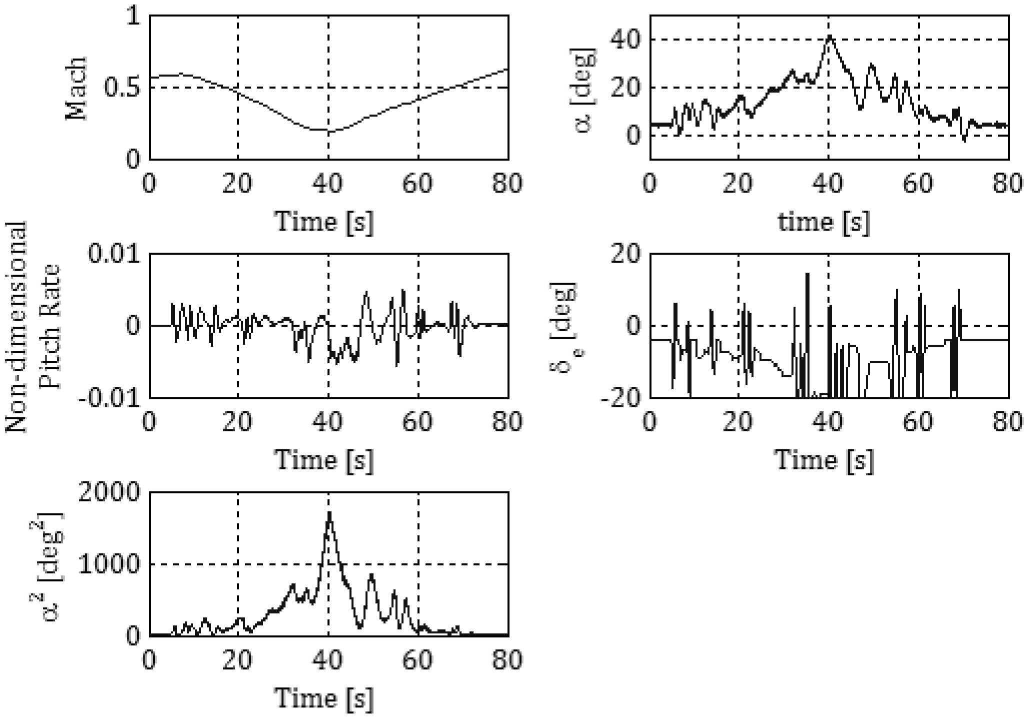

Figure E-7 Verification Regressor Data (Klein and Morelli, 2006)

Table E-7 Stepwise Regression Verification Results

Klein and Morelli (2006) and SIDPAC 2.0				Modified Algorithm		
Step 1						
	Parameter	F0	r	Parameter	F0	r
C_{Z_M}	0	-	0.725	0	-	0.725
C_{Z_α}	0	-	0.973	0	-	0.973
C_{Z_q}	0	-	0.031	0	-	0.031
$C_{Z_{\delta e}}$	0	-	0.166	0	-	0.166
$C_{Z_{\alpha^2}}$	0	-	0.838	0	-	0.838
PRESS	852			852.22		
PSE	0.266			0.26615		
R^2	0			0		
Step 2						
	Parameter	F0	r	Parameter	F0	r
C_{Z_M}	0.00	0.00E+00	0.020	0.00	0.00E+00	0.020
C_{Z_α}	-3.13	1.20E+05	-	-3.13	1.15E+05	0.000

C_{Z_q}	0.00	0.00E+00	0.305	0.00	0.00E+00	0.305
$C_{Z_{\delta e}}$	0.00	0.00E+00	0.114	0.00	0.00E+00	0.114
$C_{Z_{\alpha^2}}$	0.00	0.00E+00	0.306	0.00	0.00E+00	0.306
PRESS	23			23.05		
PSE	0.00735			0.00735		
R^2	97.3			97.3		

Klein and Morelli (2006) and SIDPAC 2.0				Modified Algorithm		
Step 3						
	Parameter	F0	r	Parameter	F0	r
C_{Z_M}	0.00	0.00E+00	0.000	0.00	0.00E+00	0.000
C_{Z_α}	-3.21	1.60E+05	-	-3.21	1.62E+05	0.000
C_{Z_q}	-27.00	1.40E+03	-	-27.02	1.40E+03	0.000
$C_{Z_{\delta e}}$	0.00	0.00E+00	0.322	0.00	0.00E+00	0.322
$C_{Z_{\alpha^2}}$	0.00	0.00E+00	0.303	0.00	0.00E+00	0.303
PRESS	16			16.04		
PSE	0.00524			0.00524		
R^2	98.1			98.12		
Step 4						
	Parameter	F0	r	Parameter	F0	r
C_{Z_M}	0.00	0.00E+00	0.100	0.00	0.00E+00	0.100
C_{Z_α}	-3.35	2.00E+05	-	-3.35	1.96E+05	0.000
C_{Z_q}	-32.30	2.80E+03	-	-32.33	2.82E+03	0.000
$C_{Z_{\delta e}}$	-0.42	1.50E+03	-	-0.42	1.52E+03	0.000
$C_{Z_{\alpha^2}}$	0.00	-	0.485	0.00	0.00E+00	0.485
PRESS	10.9			10.9		
PSE	0.00372			0.00372		
R^2	98.7			98.73		
Step 5						
	Parameter	F0	r	Parameter	F0	r
C_{Z_M}	0.00	-	0.008	0.00	0.00E+00	0.008
C_{Z_α}	-4.17	7.00E+04	-	-4.17	6.98E+04	0.000
C_{Z_q}	-28.10	4.00E+03	-	-28.13	4.01E+03	0.000
$C_{Z_{\delta e}}$	-0.43	3.20E+03	-	-0.43	3.18E+03	0.000
$C_{Z_{\alpha^2}}$	1.34	3.00E+03	-	1.34	3.01E+03	0.000

PRESS	5.6			5.62		
PSE	0.00216			0.00216		
R^2	99.3			99.34		

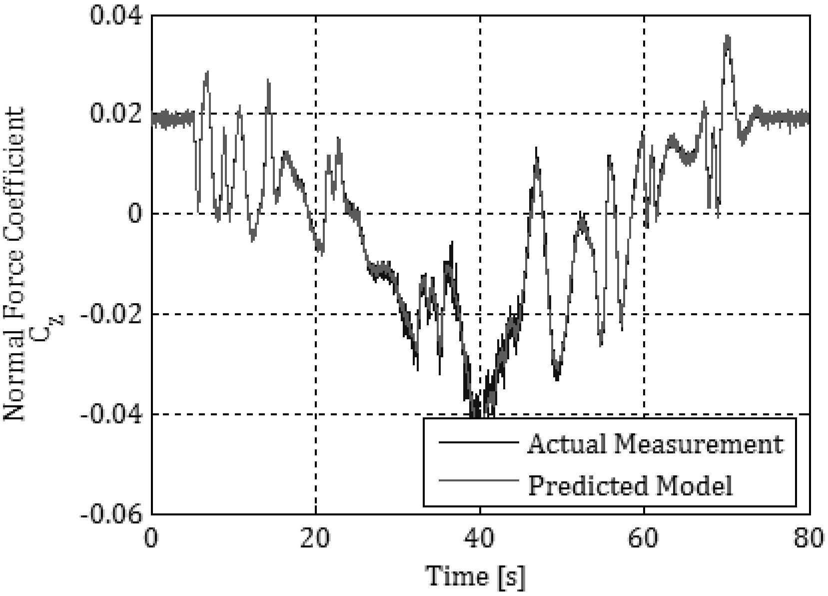

Figure E-8 Stepwise Regression Model Result

E.5 ORTHOGONAL REGRESSOR TECHNIQUE

Also described in Sec. 2.2.1 was the use of orthogonal functions as regressors within the linear regression procedures in order to efficiently develop a model structure using polynomial functions of the aircraft states as candidate regressors. This method was based on the procedure described by Klein and Morelli (2006) and a summary of the algorithm may be found in Appendix D.1. First, second and third order polynomial combinations of the initial pool of regressors were provided for, although higher orders were possible. The final set of regressors used in the algorithm was determined by a combination of the minimum PSE value and the correlation factor of each candidate regressor with the output. The mathematical detail of this method can be found in Morelli (1995). Because no secondary results were available for this algorithm, the verification and validation needed a more rigorous approach. Therefore, the program was divided into different phases and the relevant outputs at each stage were verified as described in this section.

Phase 1: The first phase of verification was used as a check on the polynomial creation process and whether or not the correct polynomial orders were satisfied. This check was successful. An extract from the polynomial indices describing the regressor combinations is given in Table E-8, where the polynomial order limit was set to 2. The column indices represent each regressor while each row contains the possible polynomials.

Phase 2: The next step involved the positive identification of orthogonality between each of the proposed orthogonal regressors that were created from the initial regressor pool. This check was achieved by determining whether the vector dot products between the regressors were equal to zero (indicating orthogonality). This is presented in Table E-9, where all regressors yielded an approximately zero value.

Phase 3: Following this, a check for the correct selection order of relevant regressors based on the partial correlation coefficients was carried out. Because the regressors were orthogonal the partial correlation coefficient would not change as regressors are added into the model. Thus they were prioritized from the highest to lowest partial correlation coefficient for possible selection. The three partial correlation functions shown in Table E-10 correspond to the orthogonalisation of the initial pool of regressors using the first order orthogonal least squares analysis.

Table E-8 Database of Possible Polynomial Combinations

	Regressor Indices:		
	1	2	3
Possible combinations:	0	0	0
	1	0	0
	0	1	0
	0	0	1
	2	0	0
	1	1	0
	1	0	1
	0	2	0
	0	1	1
	0	0	2

Table E-9 Check for Orthogonality

	Regressors	
Dot product	i	j
0.256 E-13	1	2
0.599 E-13	1	3
0.0006 E-13	1	4
-0.041 E-13	2	3
0.0004 E-13	2	4
0.0005 E-13	3	4

Table E-10 Partial Correlation Prioritization Verification

Regressor Selection Order	Partial Correlation, R [%]
Bias value regressor	-
1	72.52
2	24.84
3	0.77

Phase 4: The next two verification steps (i.e. the verification of the polynomial conversion of the orthogonal functions and the final model) used the following initial regressor set for the establishment of a non-dimensional normal force coefficient model for the large amplitude manoeuvre described by the data in Figure E-7: $C_Z = f\left(\alpha, \frac{q\bar{c}}{2V_0}, \delta e, M\right)$.

For computational simplification, the selected orthogonal regressors were fitted by polynomial functions as described by Morelli (1995). The curve fitting analysis was done via the least squares algorithm. The first four resultant matches between the orthogonal function and the polynomial fit, for the particular verification example, are shown in Figure E-9.

The final step involved the validation of the final model. The non-linear model created for the non-dimensional normal force coefficient is shown in Figure E-10. The orthogonal regressor parameter set, the parameter variances, as well as the coefficient of determination are shown in Table E-11. The model parameters in terms of the initial regressor set are given in Table E-12. The qualitative residual analyses are shown in Figure E-11 to Figure E-13.

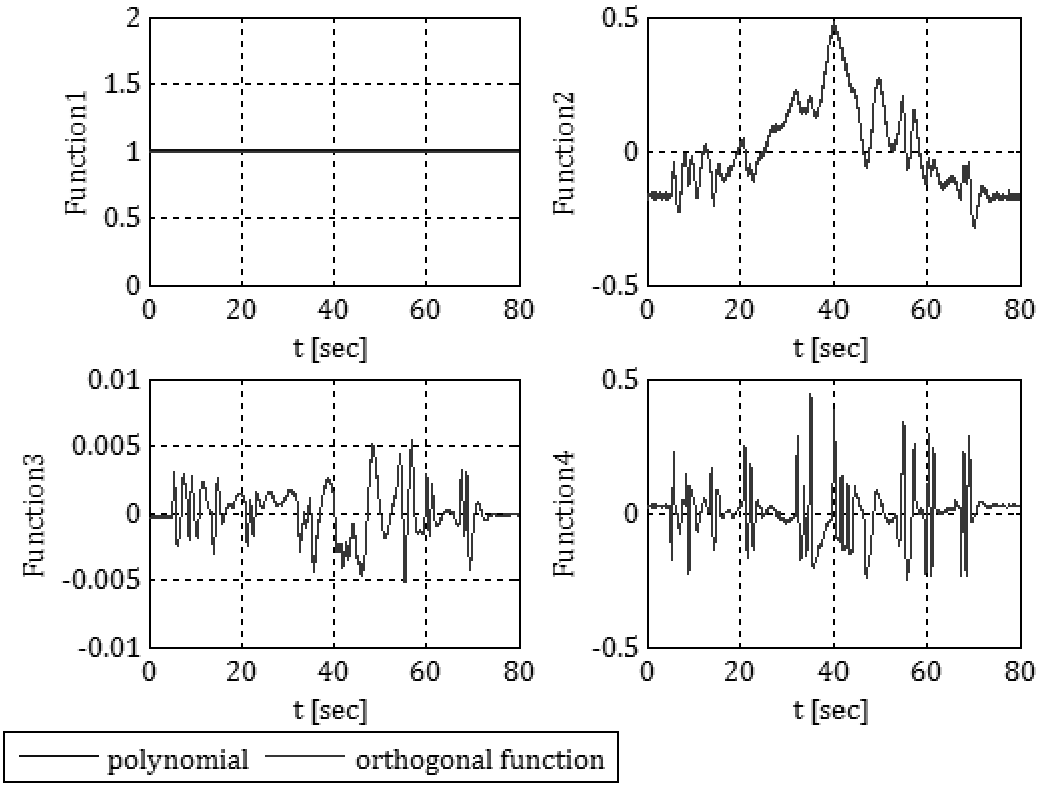

Figure E-9 Polynomial Curve Fitting of Orthogonal Regressors

The final model structure was determined to be:

$$C_Z = C_Z = C_{Z_0} + C_{Z_\alpha}\alpha + C_{Z_q}\frac{q\bar{c}}{2V} + C_{Z_{\delta e}}\delta e + C_{Z_{\alpha^2}}\alpha^2 + C_{Z_M}M \qquad \textbf{E-2}$$

The model structure achieved via orthogonal regressors matched the model structure proposed by Klein and Morelli (2006) for the same data set using ordinary stepwise regression. The advantage of using the orthogonal function least squares method is that prior knowledge of any required polynomial functions of the state variables greater than the first degree does not need to be known. Therefore, only the individual first order aircraft states are required in the initial regressor set.

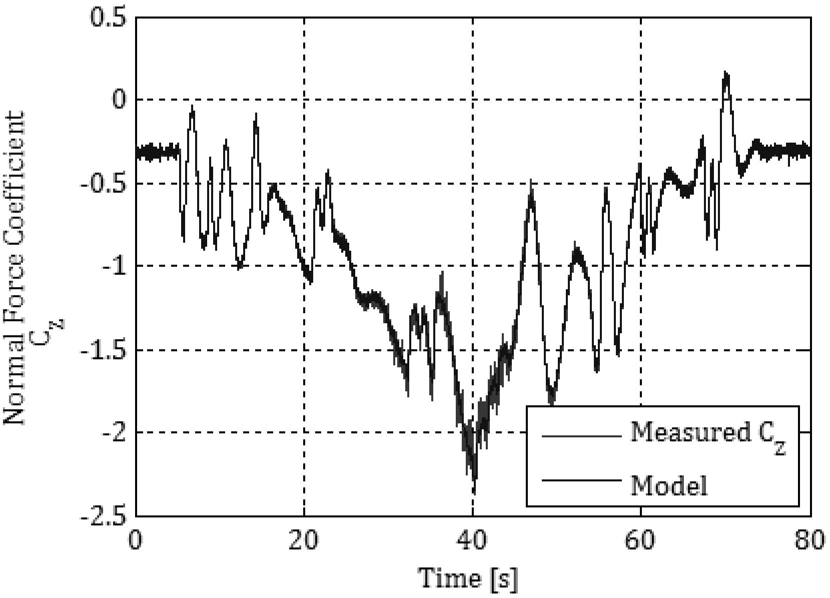

Figure E-10 Resultant Model using Orthogonal Regressors

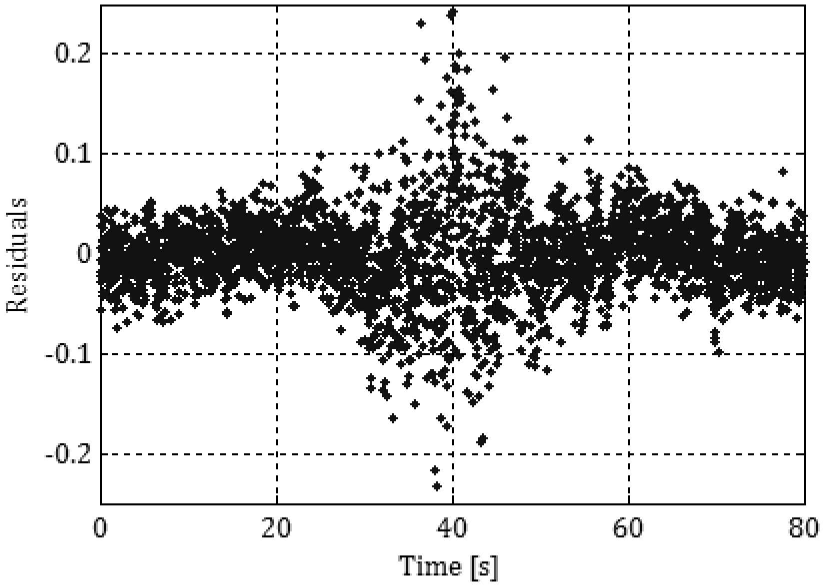

Figure E-11 Residuals of C_Z Model

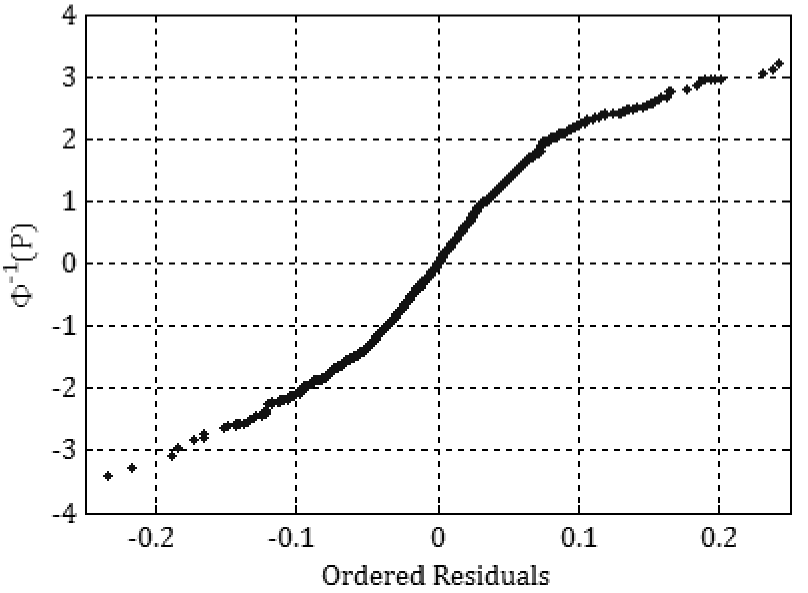

Figure E-12 Residual Analysis - Ordered Residuals

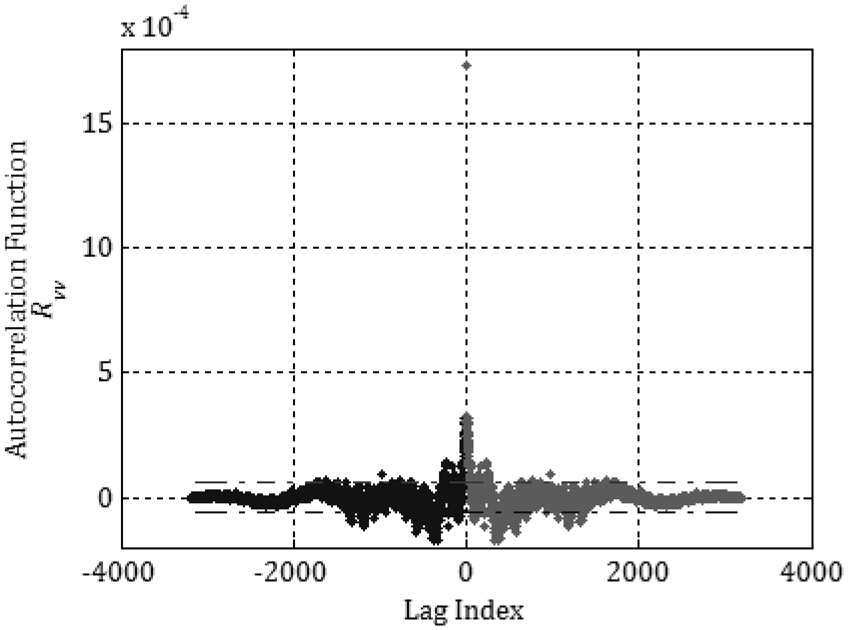

Figure E-13 Residual Analysis - Autocorrelation Function

Table E-11 Parameter Results for Orthogonal Regressors

Orthogonal Regressors	Linear Multipliers (Parameters)	Variance	Partial Correlation, r_{jz}
Function 1	-0.8710	0.0000	-
Function 2	-3.1272	0.0002	0.9730
Function 3	-27.0177	1.1448	0.0082
Function 4	-0.4165	0.0001	0.0060
Function 5	1.2950	0.0078	0.0050
Function 6	0.3243	0.0015	0.0013
Final Model	R^2 = 99.35%, σ = 0.0014		

Table E-12 Parameter Estimates after Conversion to the Initial Regressors

Parameters	Parameter	Variance
C_{Z0}	-0.323	0.0000
$C_{Z\alpha}$	-3.906	0.0033
$C_{Z\hat{q}}$	-29.183	1.6451
$C_{Z\delta e}$	-0.453	0.0003
C_{ZM}	0.072	0.0018
$C_{Z\alpha^2}$	1.295	0.0078

The validity of using orthogonal regressors in a least squares procedure in order to reduce parameter variances was then examined after the algorithm verification process. The data collinearity assessment for the ordinary least squares analysis using standardised regressors are presented in Table E-13 to Table E-15. A summary of the parameters and variances (corrected for coloured residuals) estimated via both methods (i.e. Standard stepwise regression and orthogonal regressors) are shown in Table E-16.

The results shown in Table E-16 show that there may be slight to moderate collinearity effects (i.e. 100 < (condition number = 115.375) < 1000) on parameter estimates, especially with regard to the angle of attack regressor. The correlation functions are all less than 0.9, although the correlation between α and α^2 is adequately high (i.e.

0.895). The variance inflation factors also show elevated values for the α and α^2 regressors. The variance proportions for the angle of attack regressor are all greater than 0.5 showing that some correlation dependencies may occur during estimation. The final comparison of estimates from an ordinary least squares procedure and by a method using orthogonal functions show that no major differences in parameter variances occur between the two methods, except for the bias coefficient. This analysis may be inconclusive in the sense that the regressor correlations were not strong enough to cause any detrimental effects on the ordinary least squares method. Another contributing factor could be that the suggested quantitative correlation assessment threshold values were conservative, leading to a conservative overall assessment of the collinearity. Both these arguments contribute to the proposition that the regressor correlations were too slight to cause detrimental effects for this particular model estimation.

Table E-13 Assessment of Collinearity – Correlation Matrix

	α	$q\bar{c}/2V$	δe	M	α^2
α	1.000	-0.313	-0.158	0.667	-0.895
$q\bar{c}/2V$	-	1.000	0.361	-0.421	0.300
δe	-	-	1.000	-0.447	0.130
M	-	-	-	1.000	-0.367
α^2	-	-	-	-	1.000

Table E-14 Assessment of Collinearity – Variance Proportions

		Variance Proportion				
Eigen value	Condition Index	α	$q\bar{c}/2V$	δe	M	α^2
3.183	1.000	1.197	-0.165	-0.039	-0.003	0.010
1.065	2.989	0.676	0.306	0.007	0.000	0.011
0.545	5.841	1.443	1.287	-1.150	-0.484	-0.097
0.179	17.774	0.818	0.258	-0.299	0.245	-0.021
0.028	115.375	0.971	0.013	0.022	0.000	-0.006

Table E-15 Assessment of Collinearity - Variance Inflation Factors and t_0-Statistics

Parameter	$\lvert t_0 \rvert$	VIF
α	194.220	21.724
$q\bar{c}/2V$	59.867	1.419
δe	52.987	1.676
M	5.138	6.417
α^2	49.356	13.679

Table E-16 Collinearity Effect on Parameter Variances

	Ordinary Regressors		Orthogonal Regressors	
Parameter	Estimate	Variance	Estimate	Variance
C_{Z_0}	-0.459	0.0105	-0.323	0.0001
C_{Z_α}	-4.094	0.0049	-3.906	0.0033
$C_{Z_{\bar{q}}}$	-29.183	1.2006	-29.183	1.6451
$C_{Z_{\delta e}}$	-0.453	0.0003	-0.453	0.0003
C_{Z_M}	0.072	0.0018	0.072	0.0018
$C_{Z_{\alpha^2}}$	1.295	0.0078	1.295	0.0078

E.6 MAXIMUM LIKELIHOOD VERIFICATION

The maximum likelihood method was verified by comparing the results evaluated via SIDPAC 2.0 and the final modified algorithm using data from a lateral manoeuvre of a full scale aircraft. The solution algorithms (i.e. the Newton-Raphson minimization scheme, the sensitivity calculations, and the stopping criteria) remained unchanged and described by the inequality conditions presented in Appendix B.1. The difference between the two algorithms lay in the dynamic equations and how they were integrated. The SIDPAC 2.0 solution method used a second order Runge-Kutta integration scheme using linearized equations of motion whilst a fourth order Runge-Kutta integration scheme was utilised in the modified function based on a six degree of freedom system. The initial state vector was equated to the initial values of the measured state vector rather than an average of the first few data points because the measurement noise was minimal. The initial values for the parameter estimates required by the modified Newton-Raphson algorithm were taken from the values obtained using the linear least squares algorithm. Table E-17 shows the parameter estimation results from the modified function as well as the results from a SIDPAC 2.0 estimation routine.

Table E-17 Verification Results for the Maximum Likelihood Algorithm

	Modified Maximum Likelihood Function		SIDPAC2.0 Maximum Likelihood Function	
Parameter	Estimate	Variance	Estimate	Variance
C_{Y_β}	-0.8898	8.938E-06	-0.8646	7.986E-06
C_{Y_r}	1.1048	2.730E-04	0.9331	2.788E-04
$C_{Y_{\delta r}}$	0.3556	5.837E-05	0.3800	6.494E-05
C_{l_β}	-0.1235	2.980E-07	-0.1196	3.624E-07
C_{l_p}	-0.5890	4.978E-06	-0.5859	6.707E-06
C_{l_r}	0.2229	2.792E-06	0.1889	3.311E-06
$C_{l_{\delta a}}$	-0.2301	5.773E-07	-0.2282	8.324E-07
$C_{l_{\delta r}}$	0.0415	4.126E-07	0.0422	5.547E-07
C_{n_β}	0.0867	9.016E-08	0.0864	4.626E-08
C_{n_p}	-0.0750	1.908E-06	-0.0644	9.712E-07
C_{n_r}	-0.2283	5.973E-07	-0.1906	3.915E-07
$C_{n_{\delta a}}$	-0.0051	2.886E-07	-0.0030	1.32E-07
$C_{n_{\delta r}}$	-0.1307	1.430E-07	-0.1355	7.33E-08

The measured output vector as well as the resulting model output vector are shown in Figure E-14. As can be seen in Figure E-14, a good correlation was attained between the estimated parameters and the output vector variances obtained with SIDPAC 2.0 and the modified algorithm.

Table E-18 Verification of Output Variances

Output Variable	Modified ML Function Output Variance	SIDPAC2.0 Output Variance
β	5.7325E-06	4.0519E-06
p	9.3727E-06	1.5666E-05
r	3.3723E-05	4.8901E-06
ϕ	1.6506E-05	2.4394E-05
A_Y	3.9120E-05	4.7003E-05

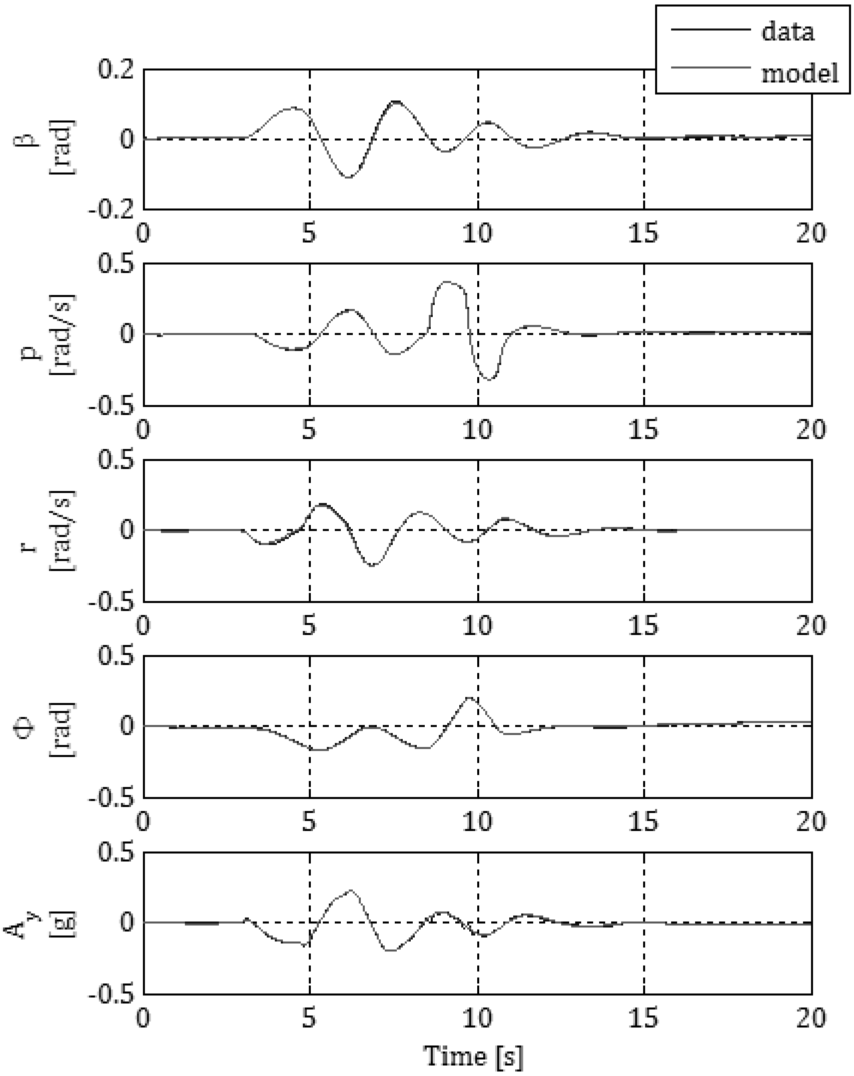

Figure E-14 Maximum Likelihood Model Fit

F. FLIGHT TEST MANOEUVRES

The planned flight test manoeuvres as described in Sec. 3.2 were accomplished. A summary of the manoeuvres is given below.

Box Manoeuvres. Two box manoeuvres were performed by the pilot via R/C controls. Thus there was no control system influence. As according to the test plan one box manoeuvre was performed at the beginning of the test schedule and one at the end of the test. Constant speed and heading was difficult to achieve via manual flight due to wind effects and the pilot's reference point (i.e. on the ground as oppose to the pilot being in the aircraft frame of reference). As can be seen in Figure F-1, a non-negligible variation in altitude and velocity occurred. Ideally, these should have been approximately constant.

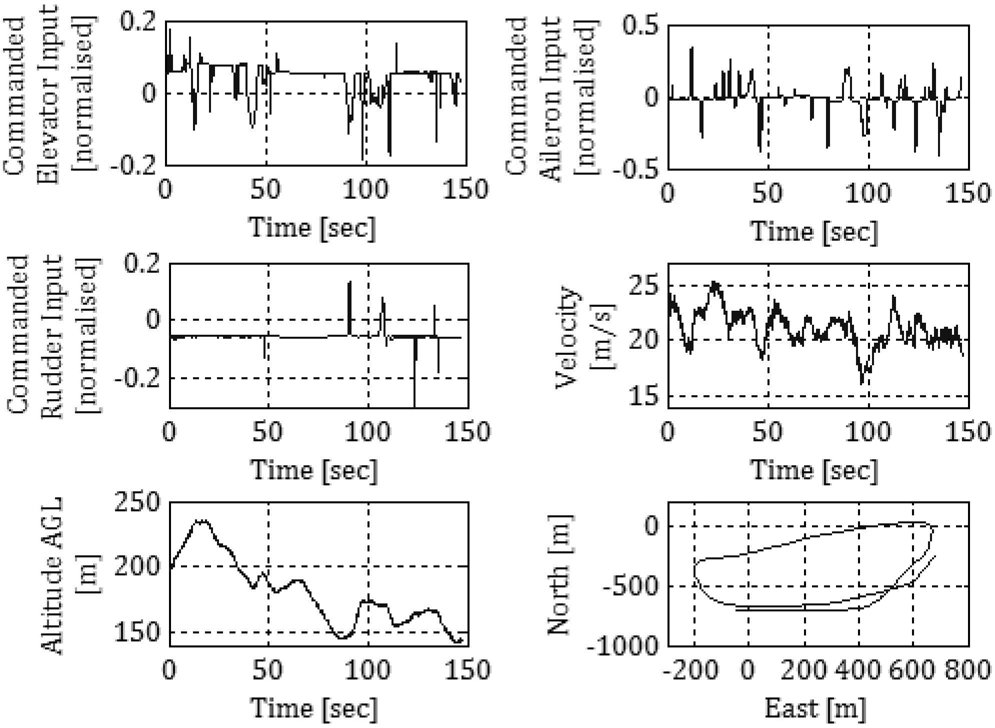

Figure F-1 First Box Manoeuvre

Push-over Pull-up. (Amplitude: +3deg elevator, Frequency: 0.1Hz). Two push-over pull-up manoeuvres were implemented via autonomous controls. The initial trim conditions of 22m/s and 18m/s respectively were successfully reached via piloted R/C controls. Stalling of the aircraft occurred at the end of the second manoeuvre, which prompted a pilot intervention, seen in Figure F-3 as the additional large elevator input. The relatively high load factors (>2g) and pitch rates meant that quasi-steady conditions were not achieved successfully. Also noted was that a return to the trimmed conditions at the end of the manoeuvres was not achieved in either test. This factor had a direct impact on the invalidity of utilising the linearized aerodynamic models for analysis of this manoeuvre.

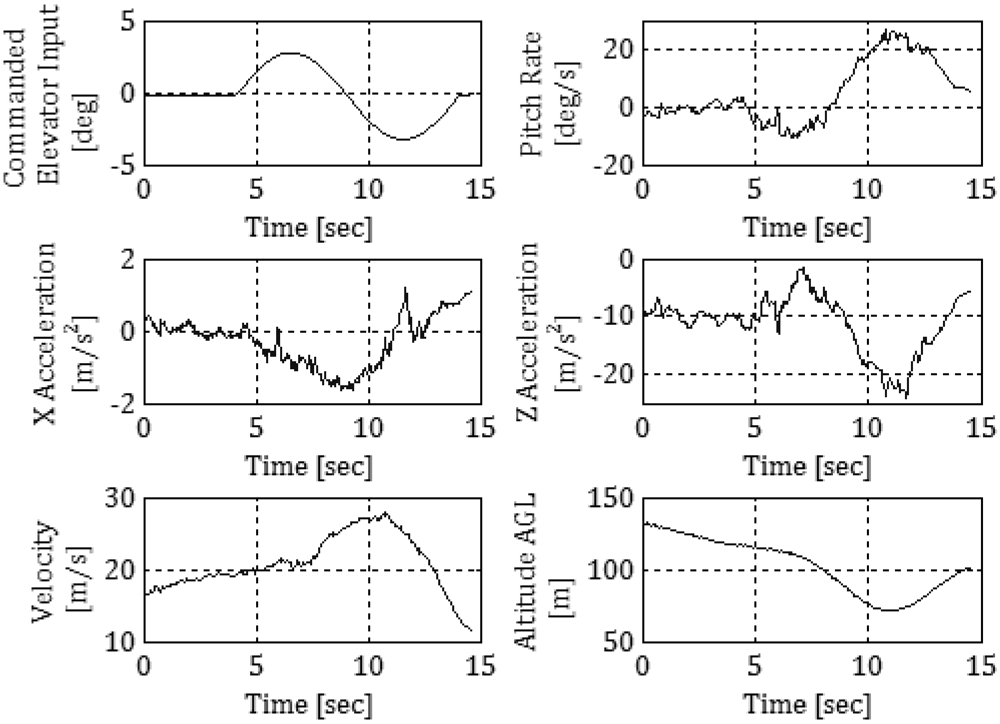

Figure F-2 First Push-over Pull-up Manoeuvre

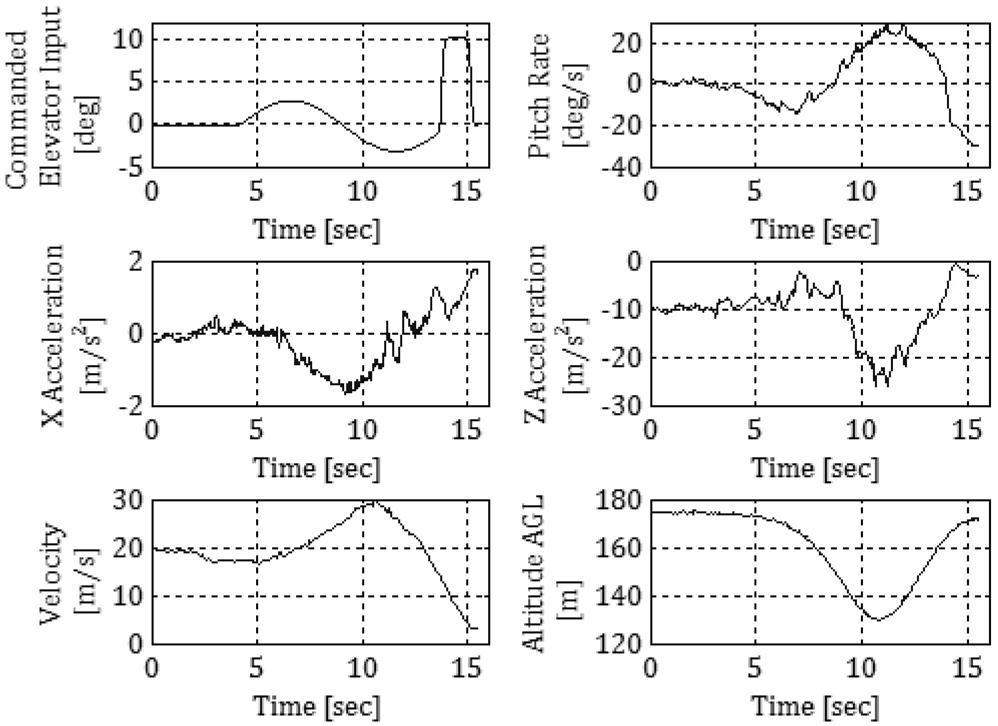

Figure F-3 Second Push-over Pull-up Manoeuvre

3-2-1-1 and 1-1-2-3 Elevator. (Amplitudes: 4 and 6deg, Δt_{3211}: 0.43sec). Significant short period oscillations were only evident in the 3-2-1-1 input where the first elevator step was positive. The poor excitation apparent in the remaining manoeuvres may have been due to the heavy longitudinal damping characteristics of the aircraft or the excitation frequency may have been erroneous. Because prior aerodynamic information for the airframe might not have described the dynamics adequately enough for an effective 3-2-1-1 design, a frequency sweep would have been more appropriate. However, due to airspace restrictions, significant frequency sweep periods would have been unachievable.

The multi-steps that were performed are described below:

(3-2-1-1; Positive; 4deg; actual Δt_{3211}=0.43sec; planned Δt_{3211}=0.36sec).

(1-1-2-3; Positive; 6deg; actual Δt_{3211}=0.43sec; planned Δt_{3211}=0.36sec).

(3-2-1-1; Negative; 4deg; actual Δt_{3211}=0.43sec; planned Δt_{3211}=0.36sec; 2 Consecutive).

(1-1-2-3; Negative; 6deg; actual Δt_{3211}=0.43sec; planned Δt_{3211}=0.36sec; 2 Consecutive).

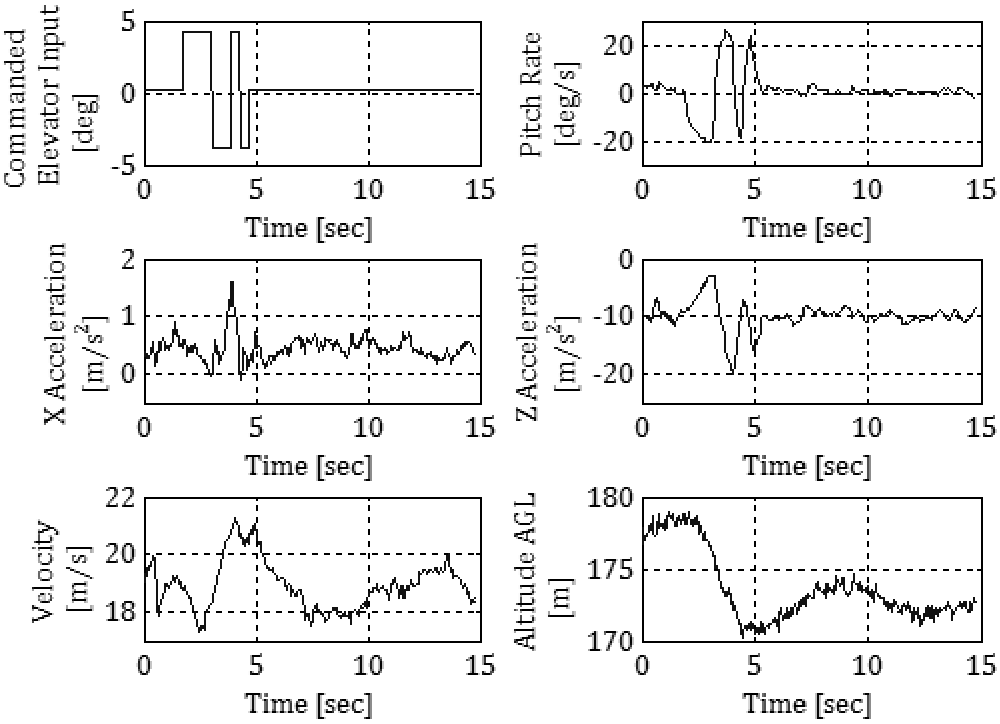

Figure F-4 3-2-1-1 Elevator Manoeuvre (+4deg)

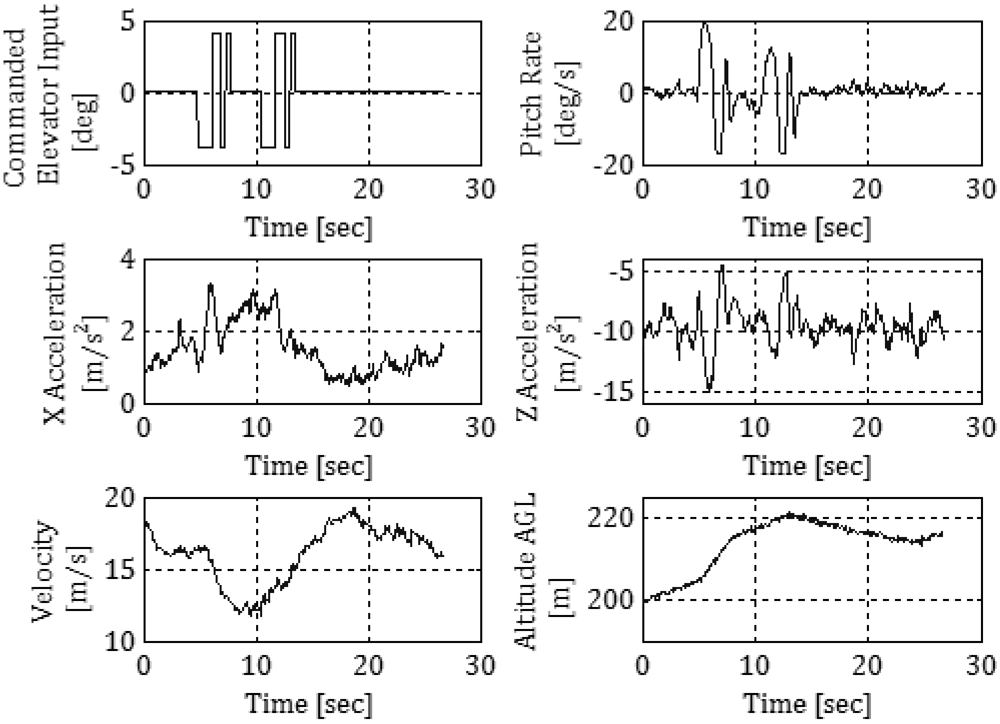

Figure F-5 3-2-1-1 Elevator Manoeuvre (-4deg)

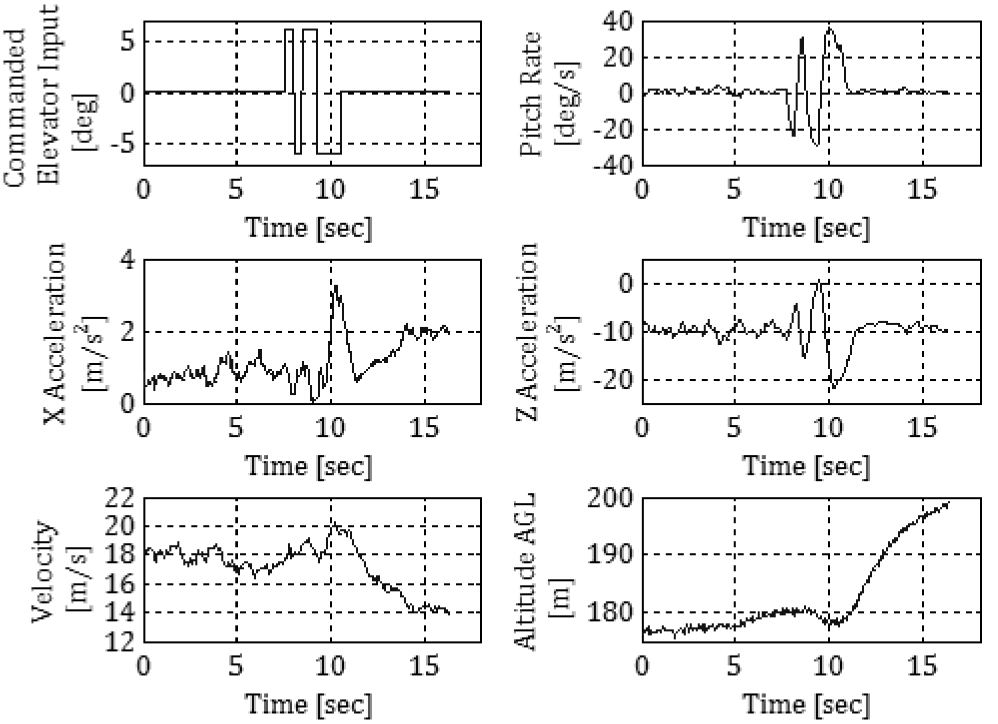

Figure F-6 1-1-2-3 Elevator Manoeuvre (+6deg)

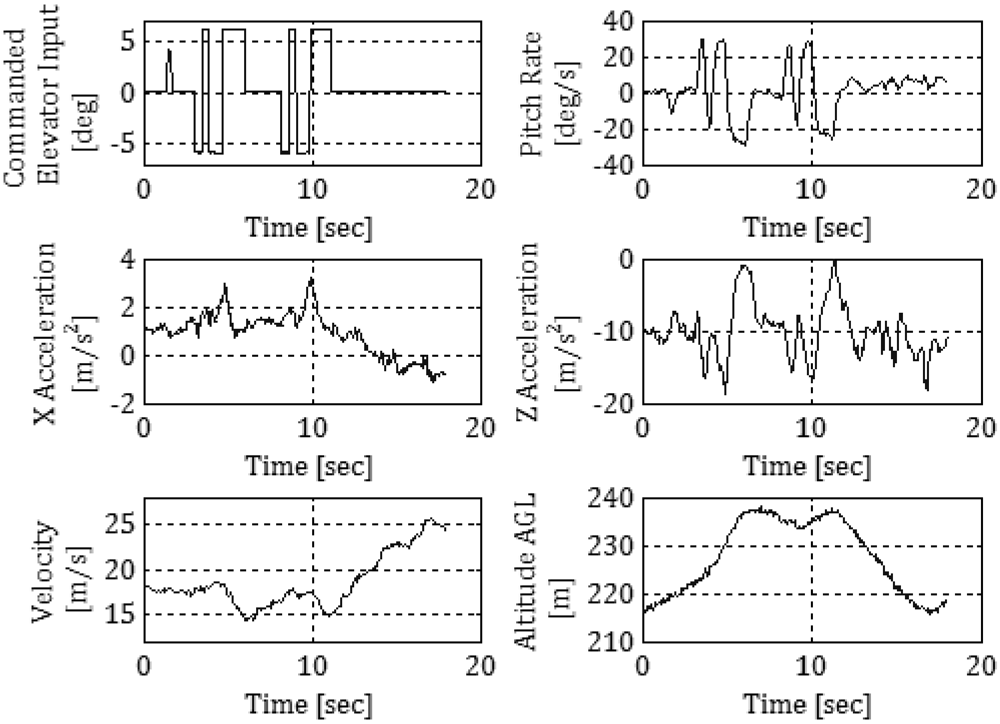

Figure F-7 1-1-2-3 Elevator Manoeuvre (-6deg)

From Figure F-4 to Figure F-7 it was evident that the initial conditions differed from the planned initial conditions. However a consistent initial velocity of 18m/s was achieved for the 1-1-2-3 manoeuvres. The initial altitudes between all four manoeuvres also differed from each other. A noted factor is that due to implementation errors the final target excitation frequency was 0.698Hz instead of the planned 0.833Hz, yielding a 16.21% error. The differences between the planned and executed manoeuvres were due to specification errors prior to programming the automated commands. Due to the large frequency band of the 3-2-1-1 manoeuvre, this resulting error was deemed negligible.

<u>Bank to Bank and Dutch Roll Excitation</u>. (Amplitude: Rudder: ± 12deg. Δt_{rudder}: 1sec. and Aileron: ± 10deg Pilot Input). The planned bank to bank and Dutch roll excitation manoeuvres were carried out sequentially. This was done due to the limited flight time available. The rudder doublet Δt_{rudder} was set to one second instead of the required 0.83 seconds due to an implementation error. As can be seen from Figure F-8 and Figure F-9, this did not have a significantly detrimental effect on the outcome as the Dutch roll mode was adequately excited.

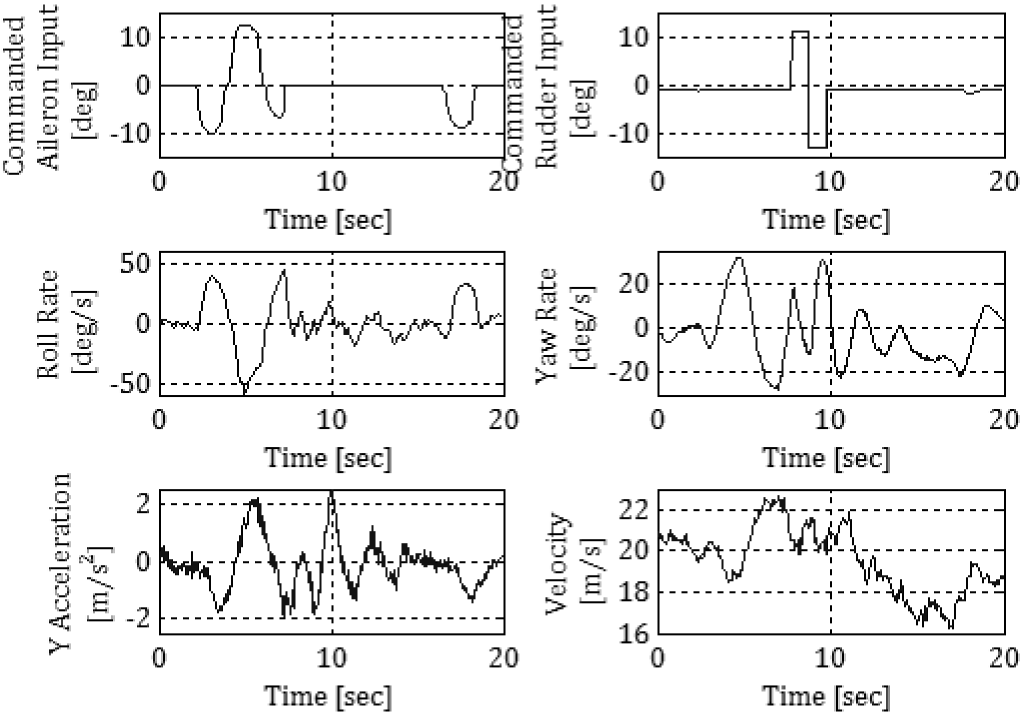

Figure F-8 Bank to bank and Dutch Roll Excitation 1

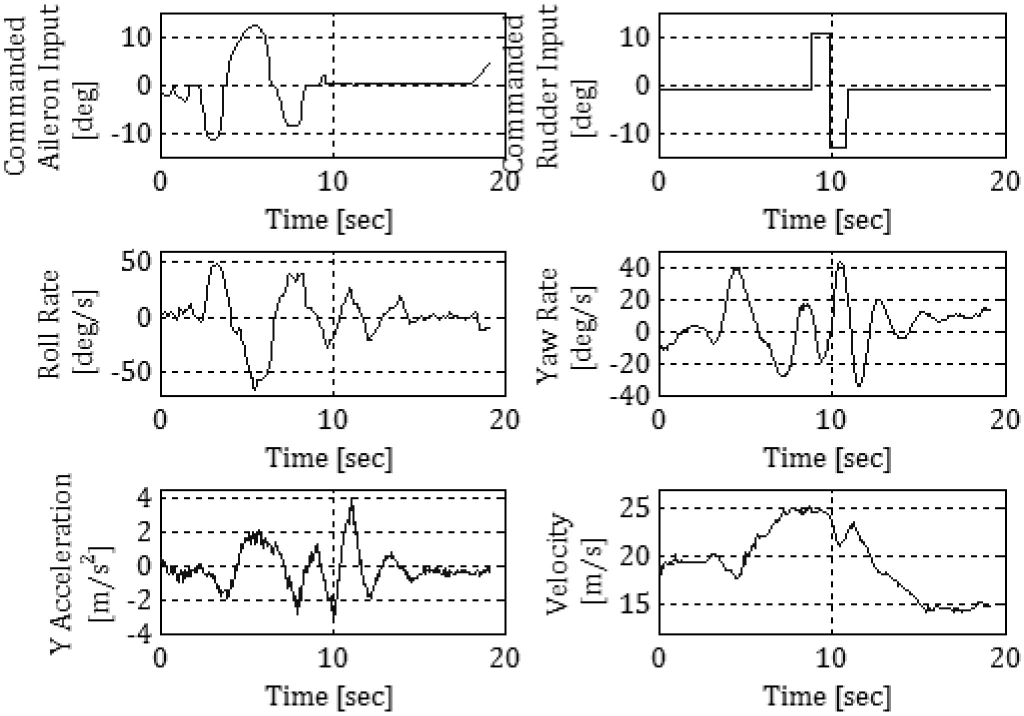

Figure F-9 Bank to bank and Dutch Roll Excitation 2

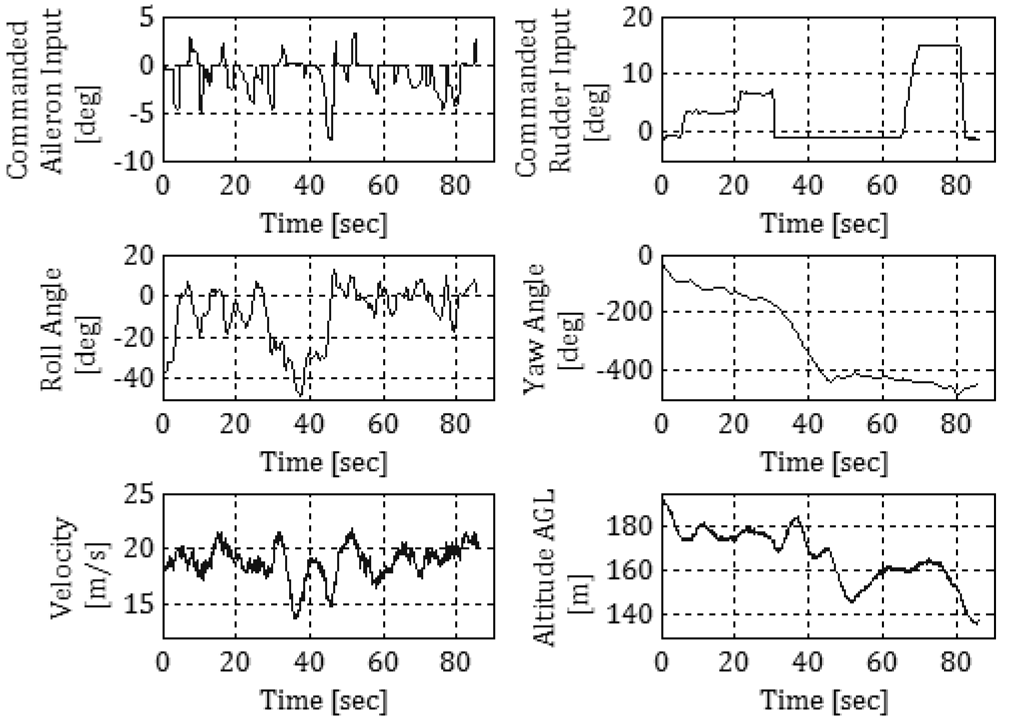

Figure F-10 Steady Heading Sideslip Manoeuvre

Sideslip. (Amplitude: Rudder: +14 deg.). Aileron adjustments were used to keep the aircraft trimmed via the R/C controls. As can be seen in Figure F-10, three different rudder deflections were implemented. Each rudder deflection resulted in a steady yaw angle and approximately constant velocity and altitude. The yaw and roll angle time histories shown in Figure F-10 were evaluated via the on-board estimator that utilised a real time Kalman filtering algorithm programmed into the control system.

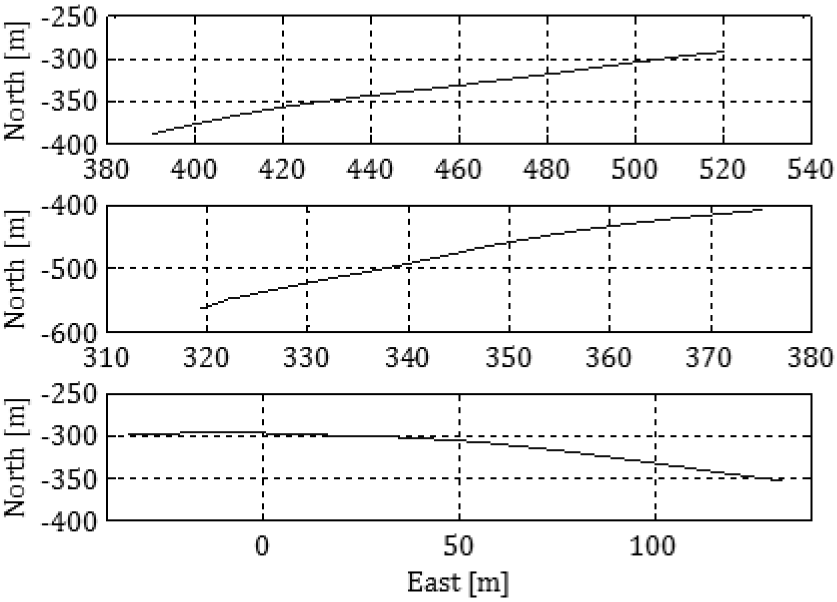

Figure F-11 Steady Heading Sideslip – Constant Heading Representation

G. DATA COMPATIBILITY RESULTS

G.1 VERIFICATION ANALYSES RESULTS

The data reconstruction residual analysis results for the first Kalman filter validation run (i.e. the correct instrument variance parameters were used) will be presented in this section. The analysis made use of visual characteristics of the autocorrelation functions, the inverse of the cumulative probability function, the residual versus the measurement, and the residual as a function of time. Performance weightings were based on the resemblance of the autocorrelation function to an impulse function given a determined tolerance based on the 95% confidence interval, and the approximation of the inverse of the cumulative probability function to a linear function. Additionally, the residual versus the measurement and the residual versus time elapsed should resemble a random scatter of data points. Any functional characteristics that were found within the residual results were an indication that systematic errors occurred within the Kalman filtering procedure. The iterated extended Kalman filter and global smoother results for the input variables are given in Figure G-1 to Figure G-6.

.

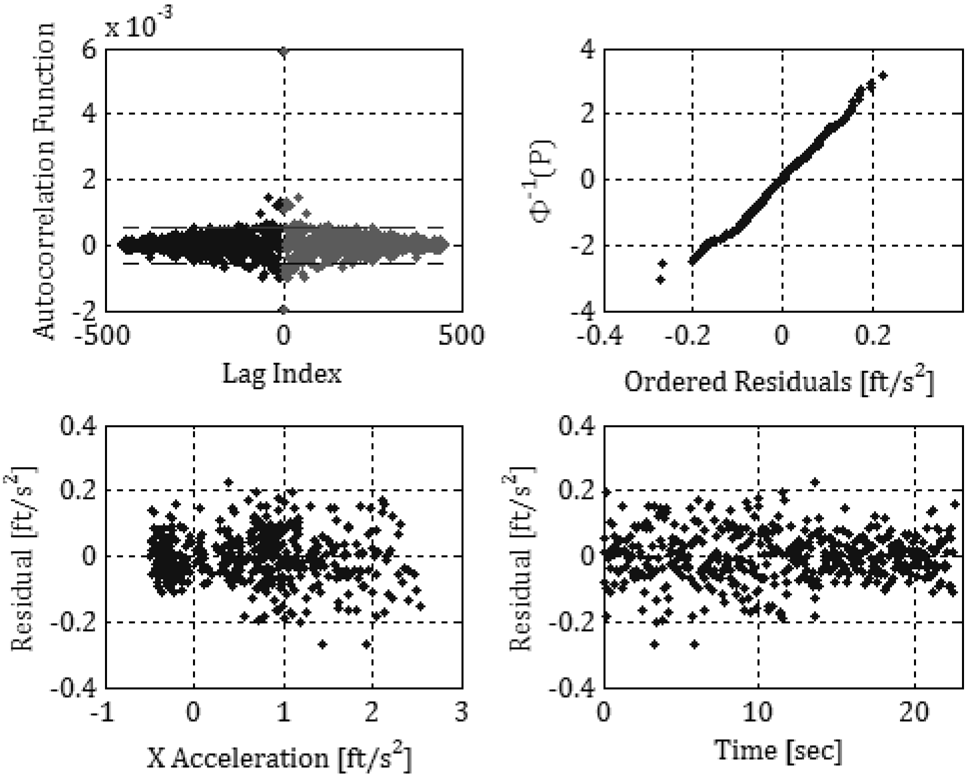

Figure G-1 IEKF Residual Analysis - Run 1 - X Acceleration

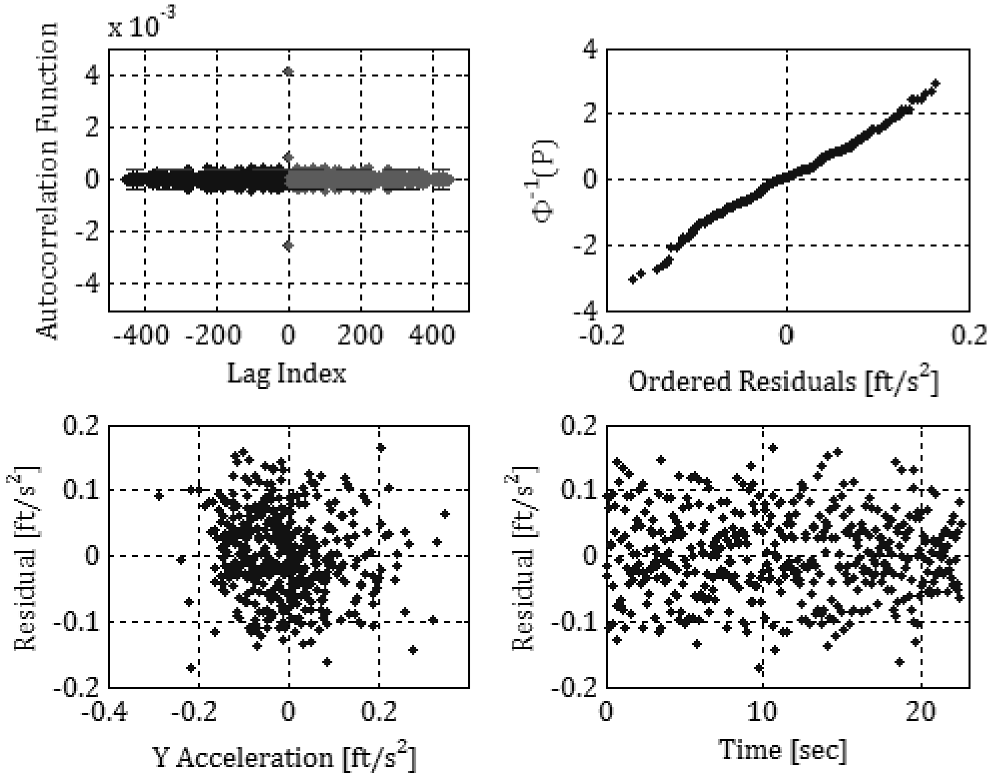

Figure G-2 IEKF Residual Analysis - Run 1 - Y Acceleration

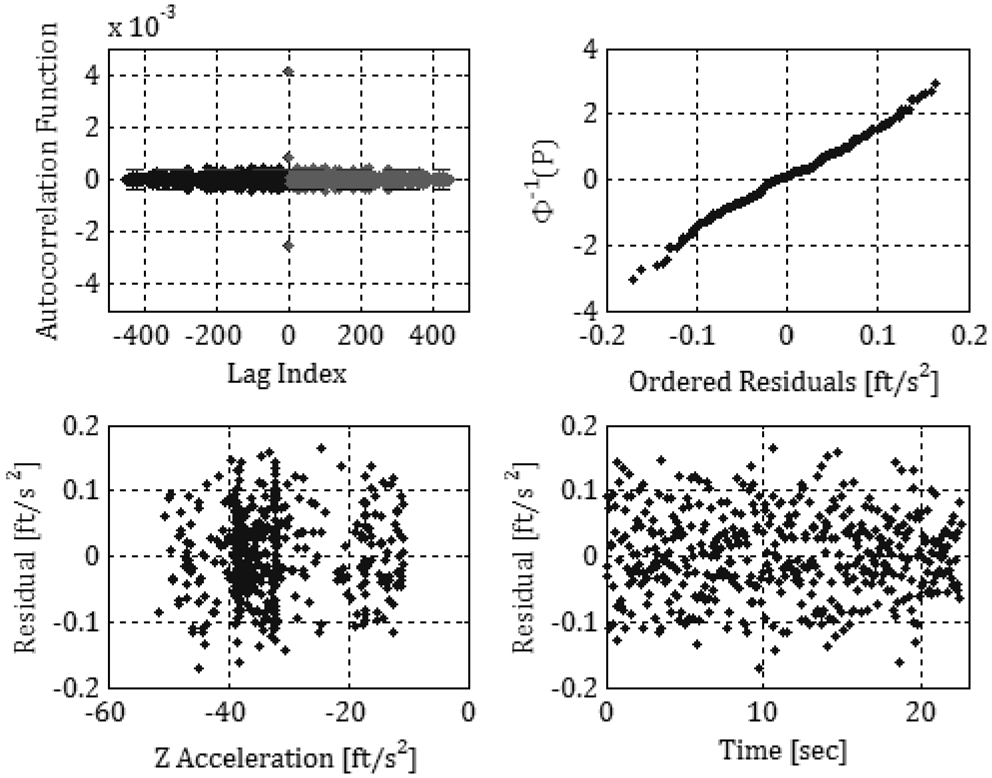

Figure G-3 IEKF Residual Analysis - Run 1 - Z Acceleration

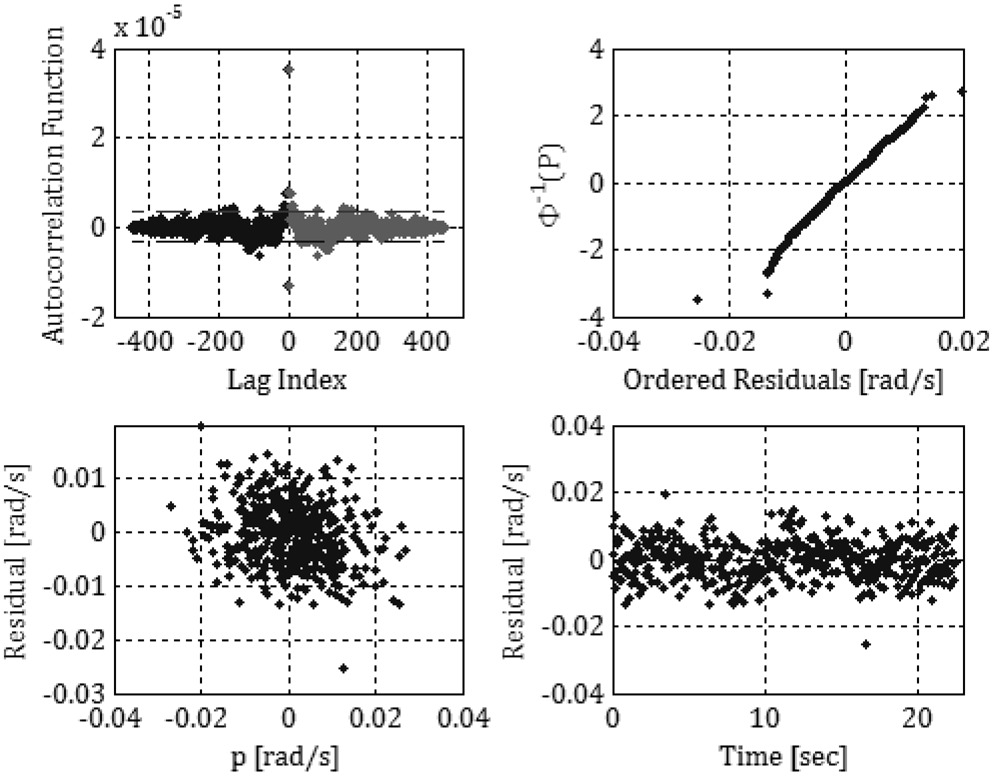

Figure G-4 IEKF Residual Analysis - Run 1 - Roll Rate, p

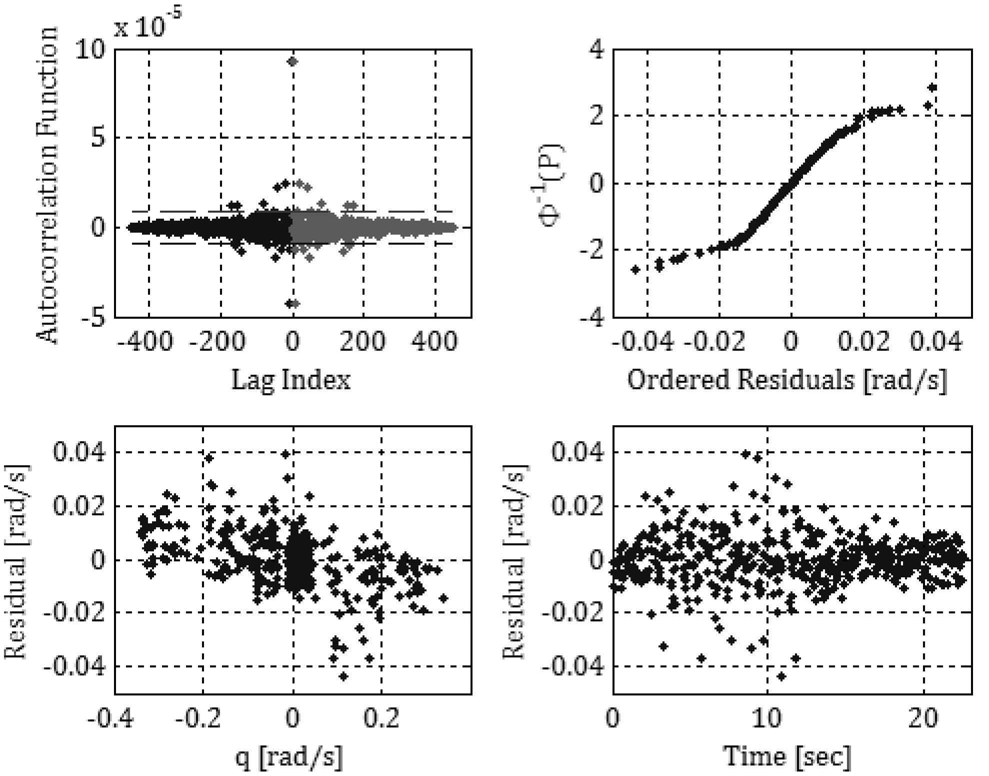

Figure G-5 IEKF Residual Analysis - Run 1 - Pitch Rate, q

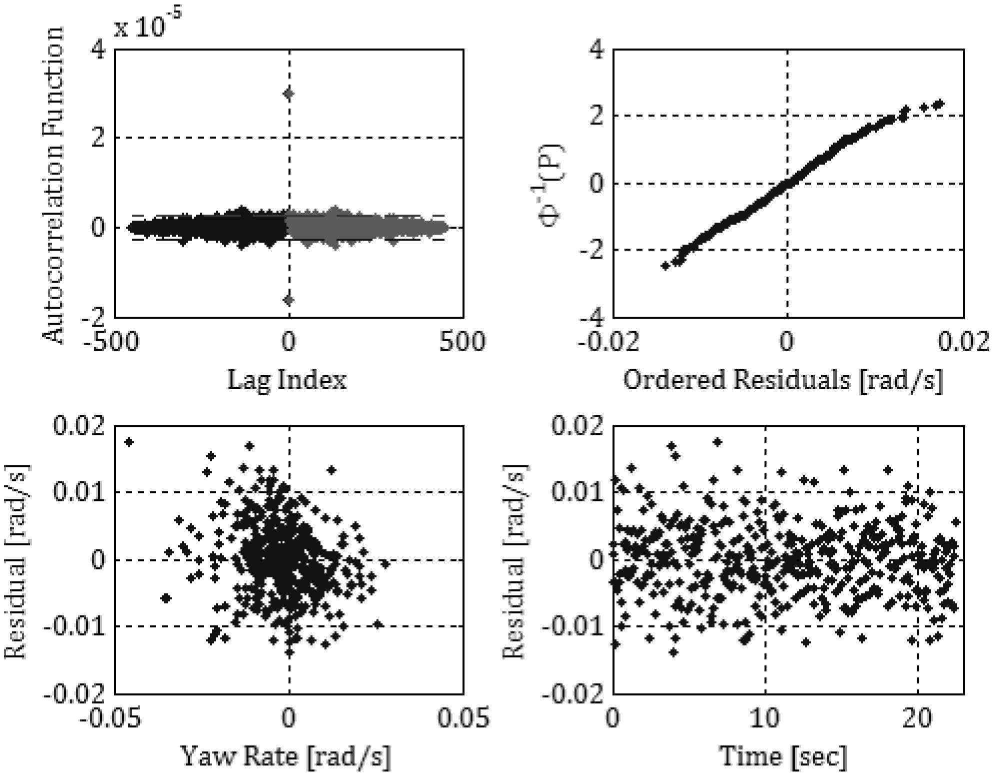

Figure G-6 IEKF Residual Analysis - Run 1 - Yaw Rate, r

The results from the input measurements, in Figure G-1 to Figure G-6, clearly showed strong Gaussian characteristics which was an indication that the Kalman filter operated adequately in filtering the imposed Gaussian noise on the simulated data. These qualitative characteristics, along with the correlation between the estimated biases and the imposed biases formed part of an adequate argument for the correct verification of the Kalman filter function bearing in mind the requirements of the current research hypothesis.

G.2 COMPARISONS OF THE ITERATIVE IMPROVEMENTS OF THE DATA COMPATIBILITY ALGORITHM (BOX MANOEUVRE 1)

This section presents the comparisons of the reconstructed input measurements for the first and final iterations of the data compatibility algorithm as well as the corresponding residual analyses. The improvement in all of the measurements was clearly evident.

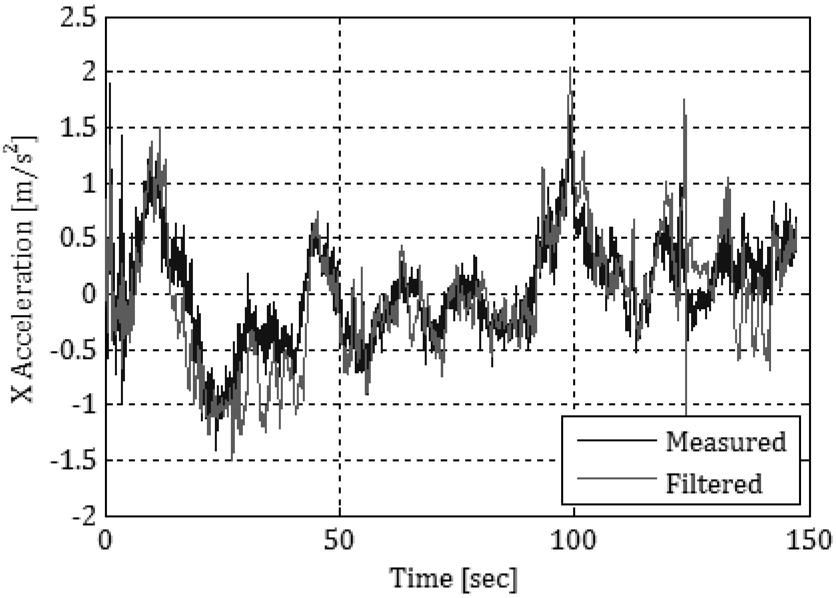

Figure G-7 Initial IEKF Result – X Acceleration

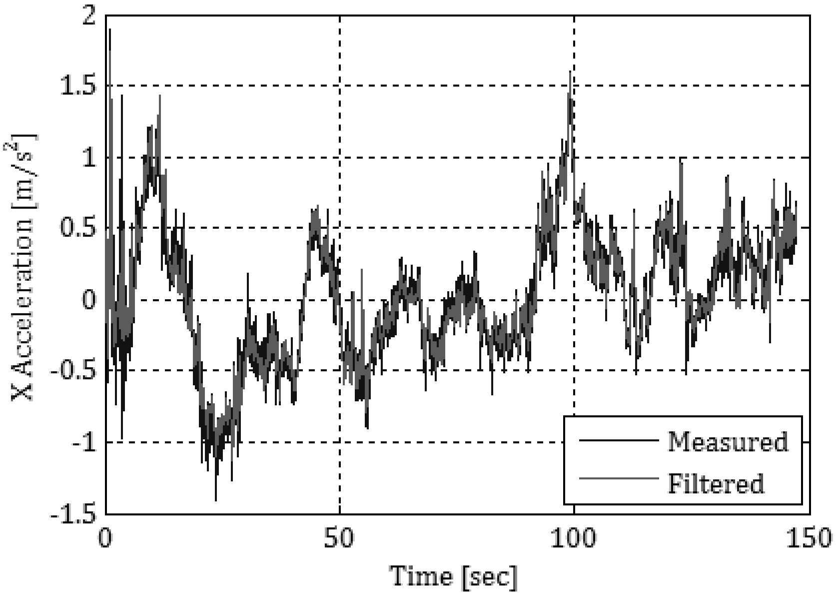

Figure G-8 Final IEKF Result – X Acceleration

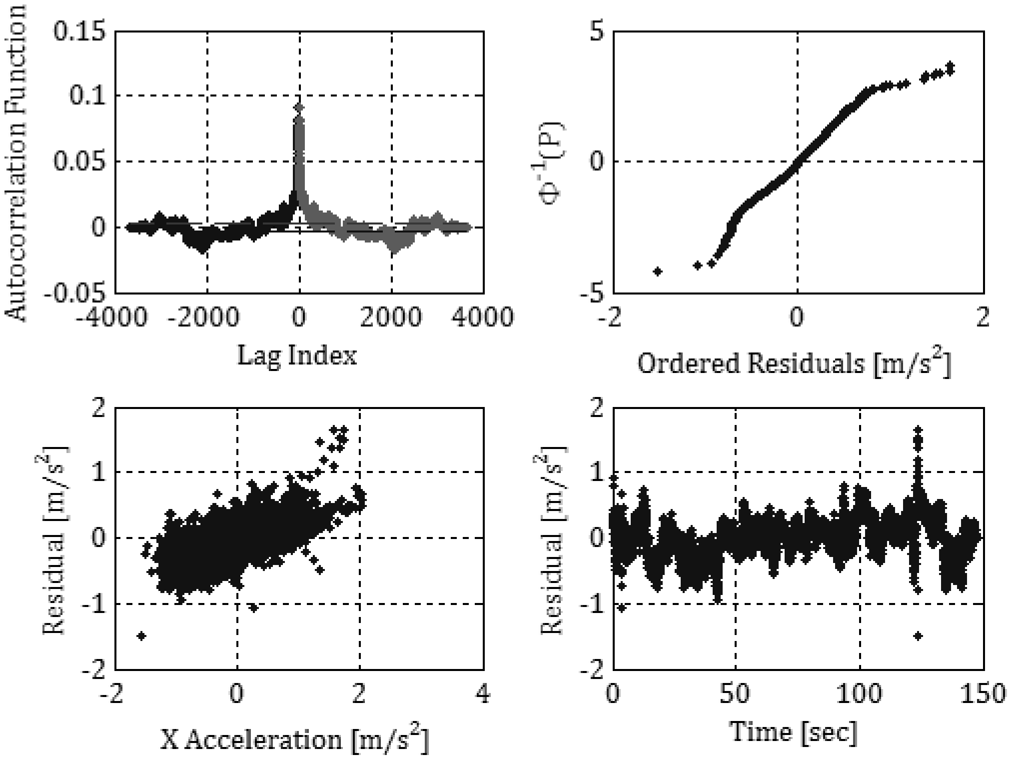

Figure G-9 Initial IEKF Residual Analysis – X Acceleration

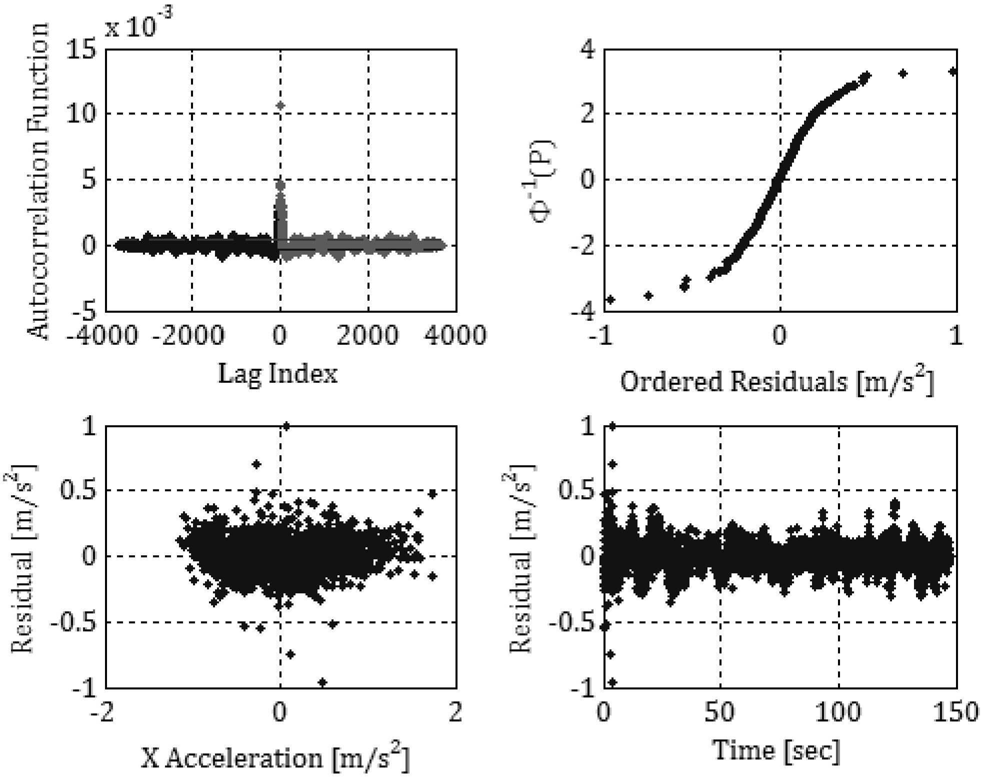

Figure G-10 Final IEKF Residual Analysis – X Acceleration

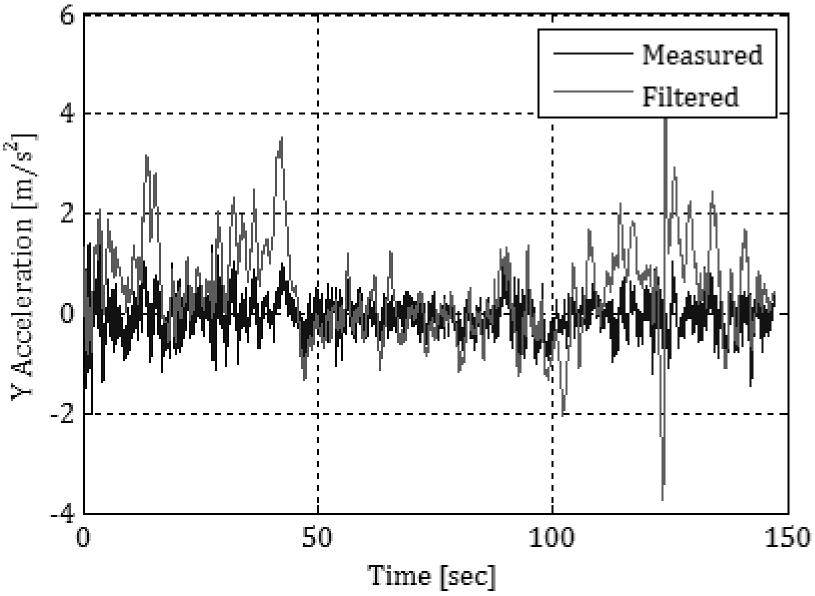

Figure G-11 Initial IEKF Result – Y Acceleration

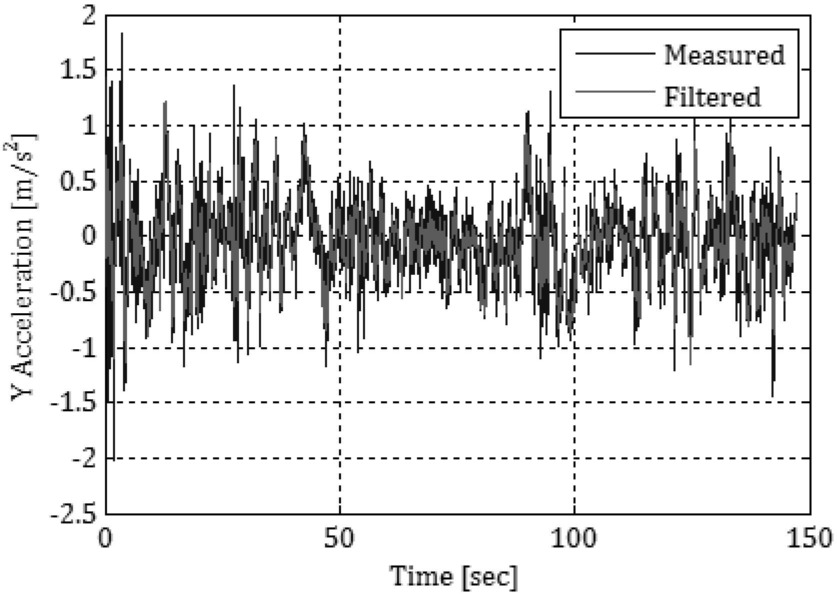

Figure G-12 Final IEKF Result – Y Acceleration

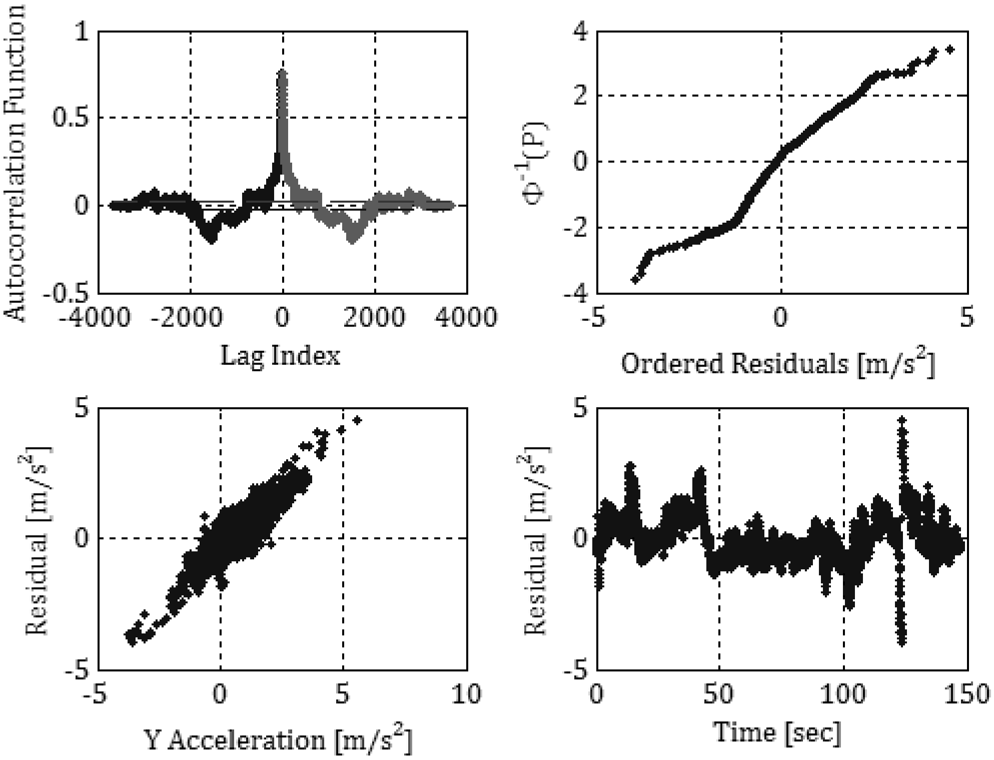

Figure G-13 Initial IEKF Residual Analysis – Y Acceleration

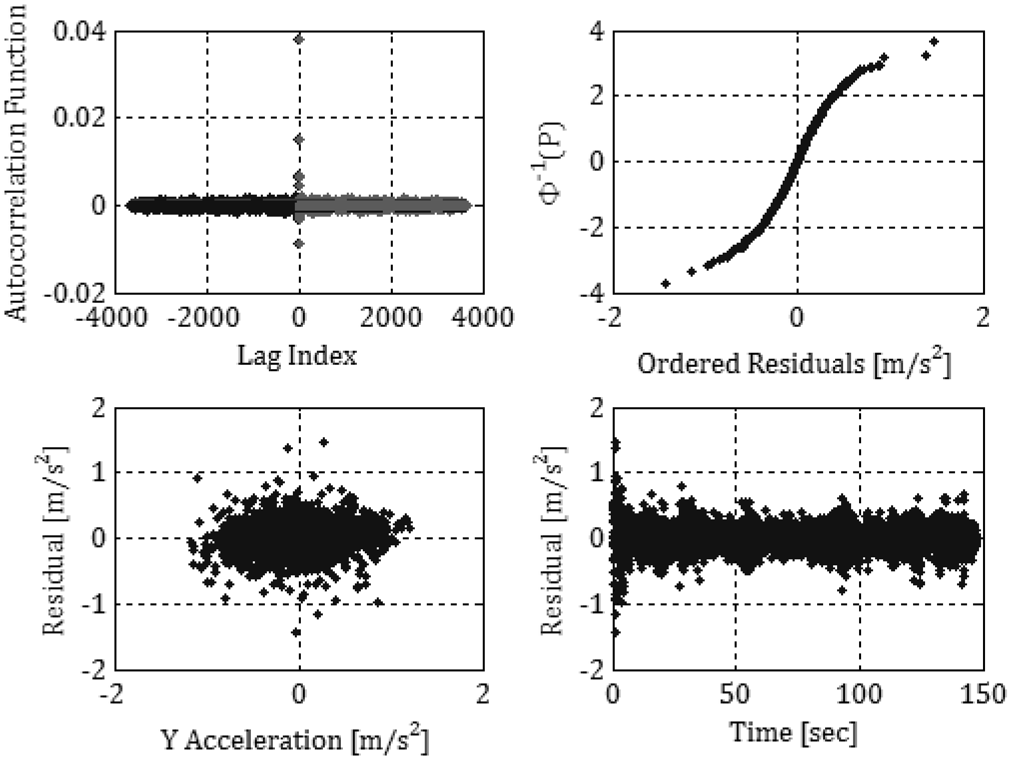

Figure G-14 Final IEKF Residual Analysis – Y Acceleration

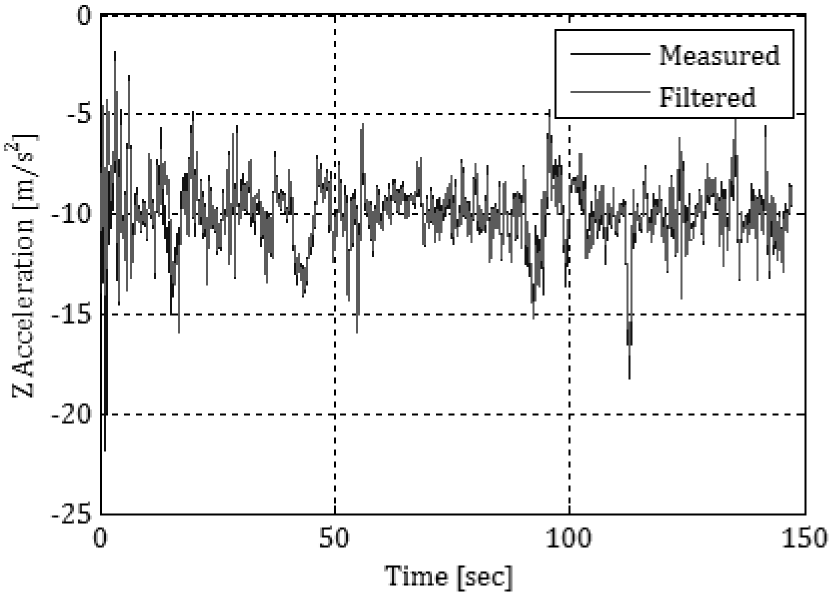

Figure G-15 Initial IEKF Result – Z Acceleration

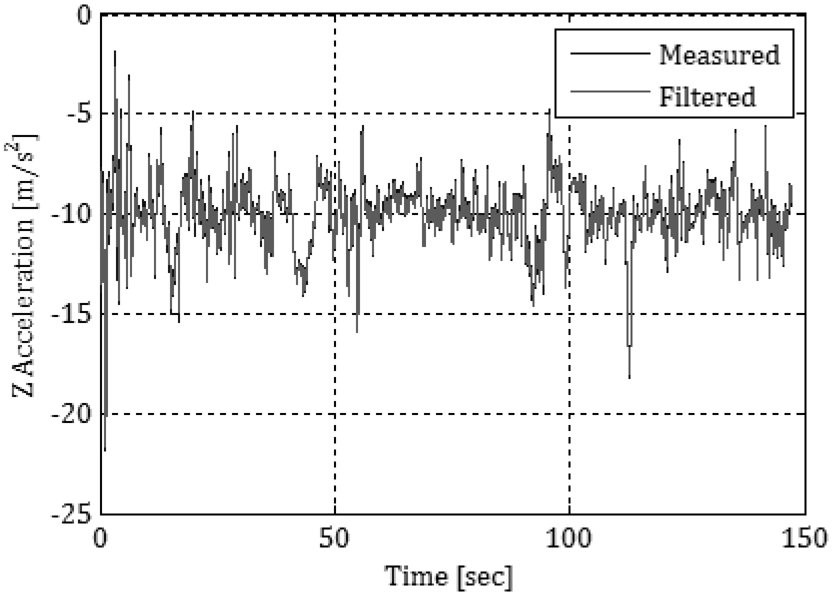

Figure G-16 Final IEKF Result – Z Acceleration

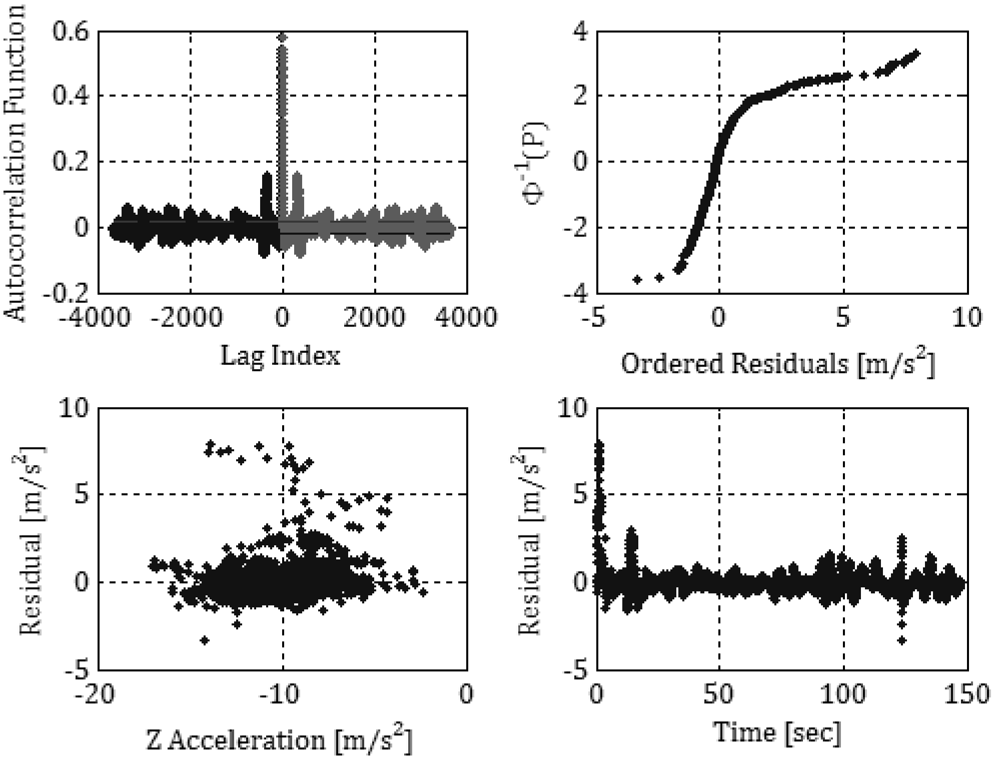

Figure G-17 Initial IEKF Residual Analysis – Z Acceleration

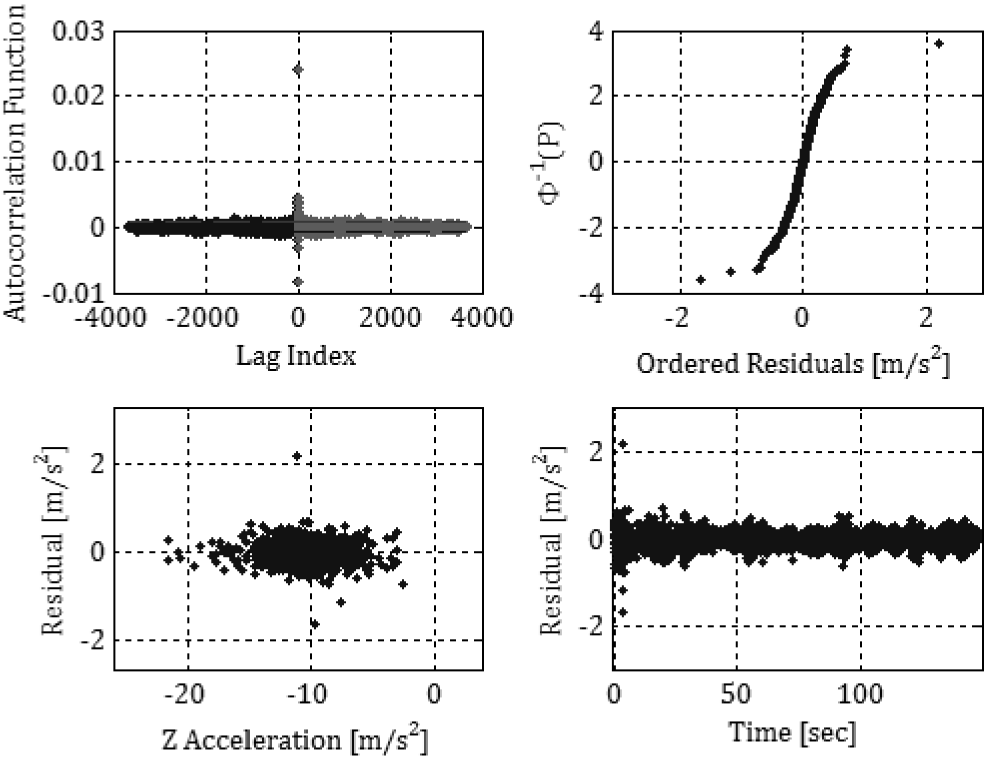

Figure G-18 Final EKF Residual Analysis – Z Acceleration

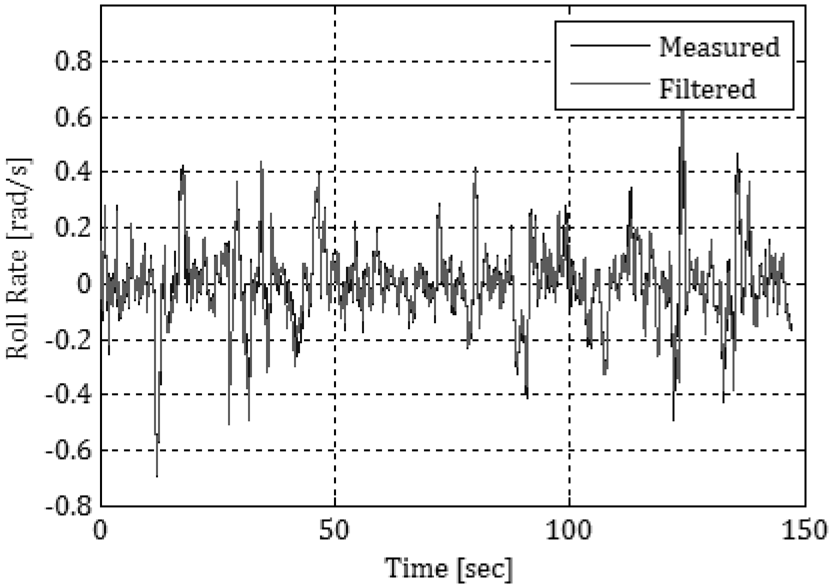

Figure G-19 Initial IEKF Result – Roll Rate

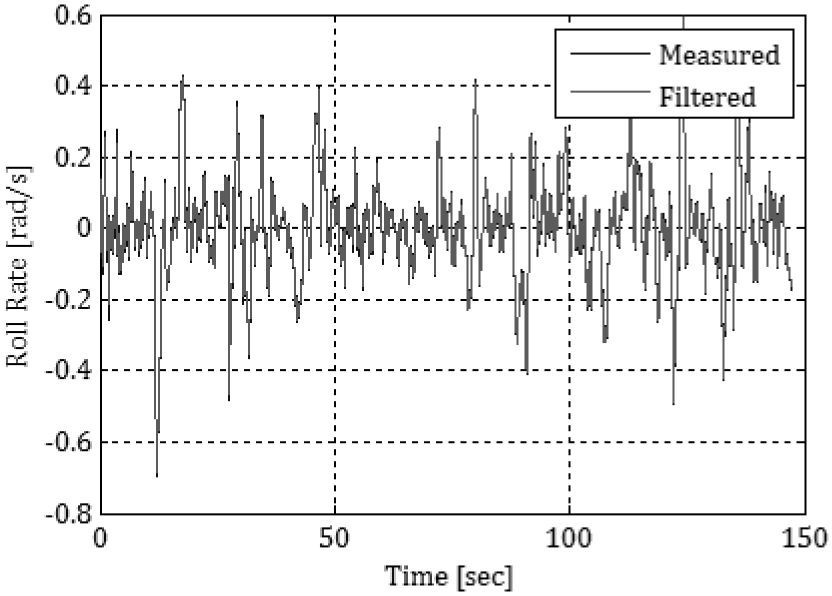

Figure G-20 Final IEKF Result – Roll Rate

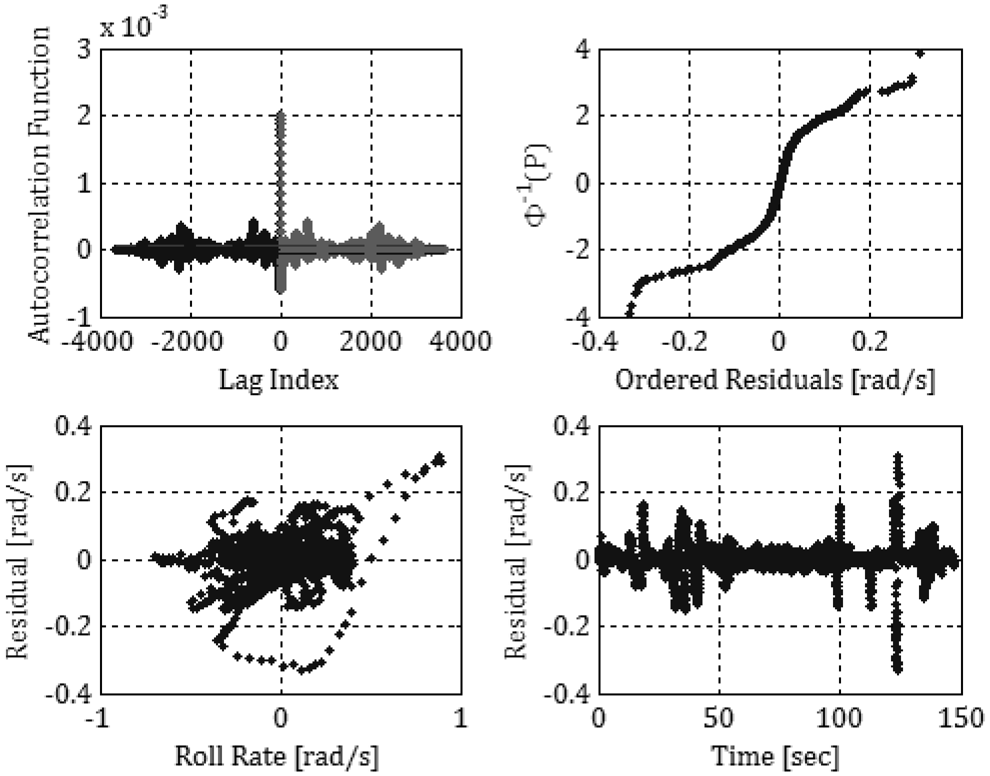

Figure G-21 Initial IEKF Residual Analysis – Roll Rate

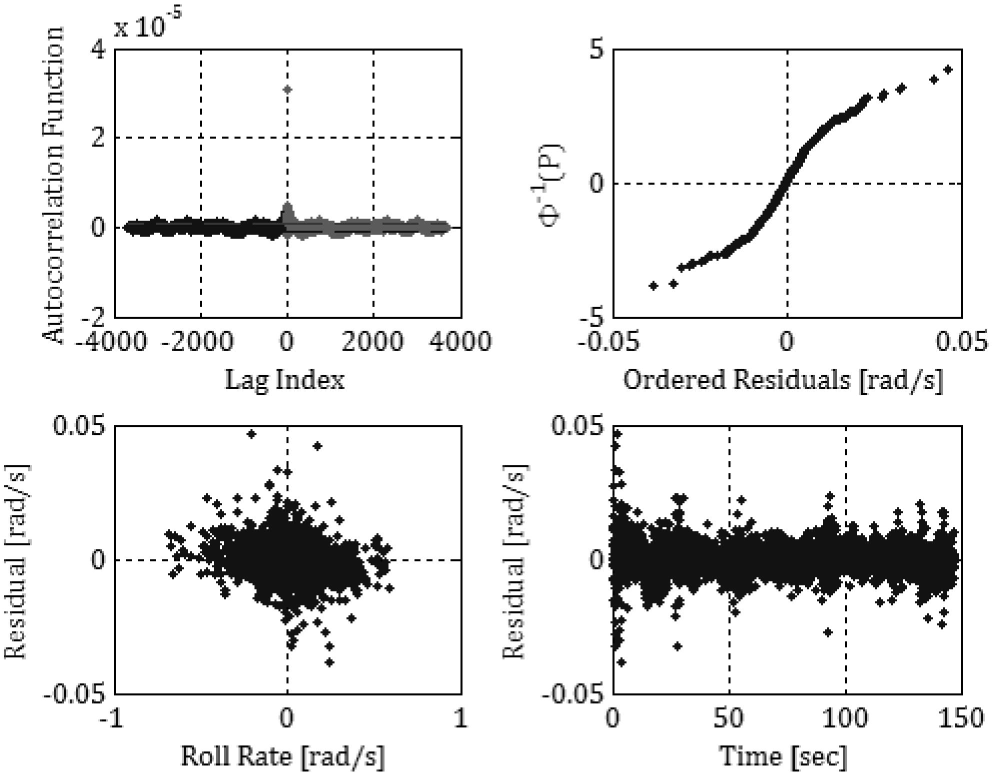

Figure G-22 Final IEKF Residual Analysis – Roll Rate

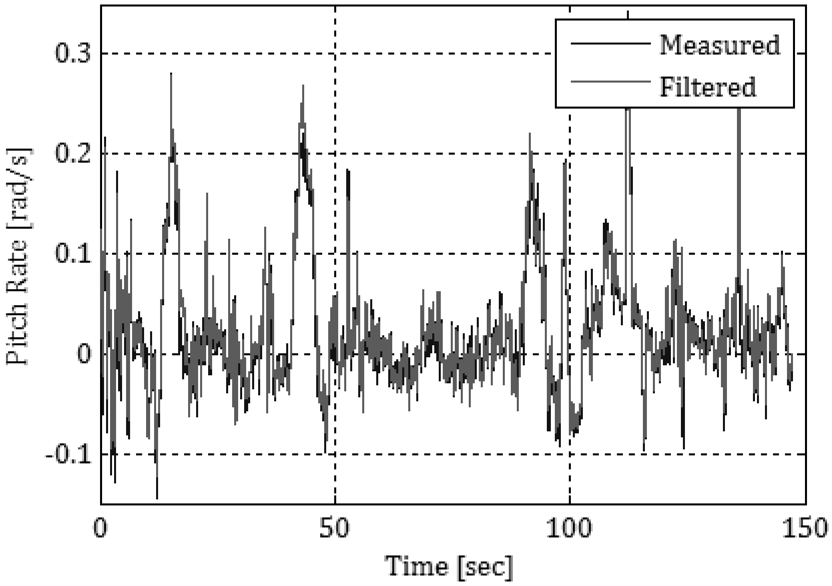

Figure G-23 Initial IEKF Result – Pitch Rate

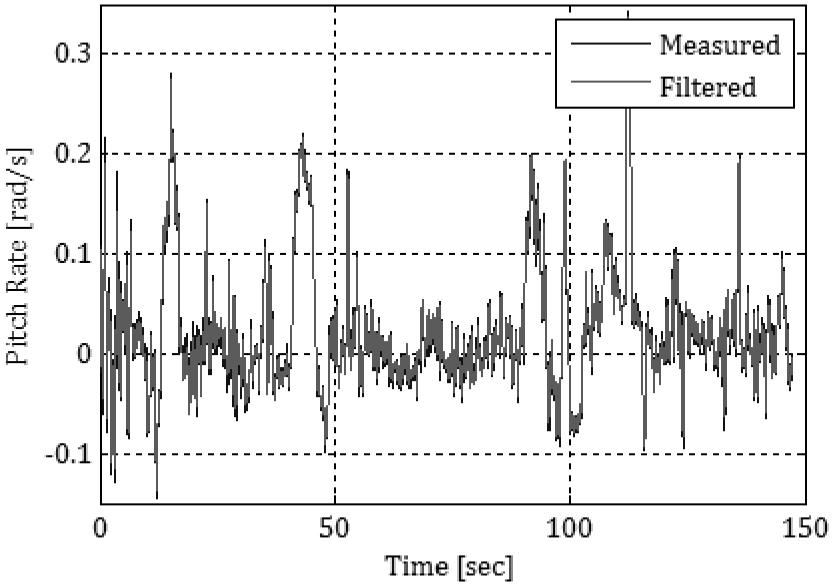

Figure G-24 Final IEKF Result – Pitch Rate

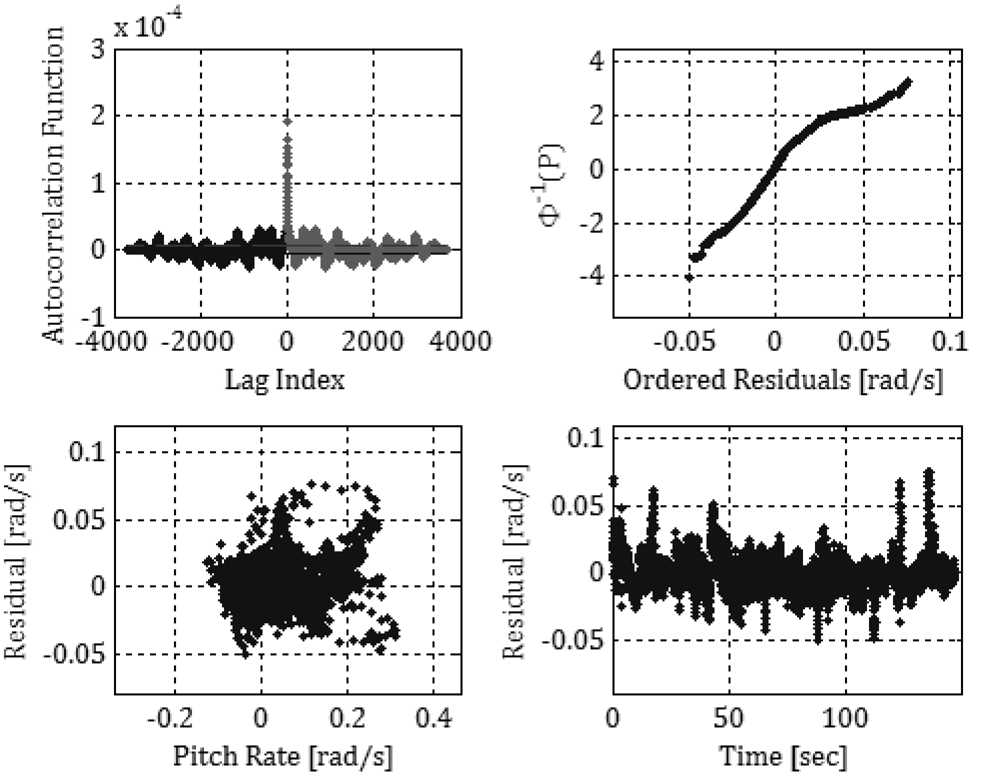

Figure G-25 Initial IEKF Residual Analysis – Pitch Rate

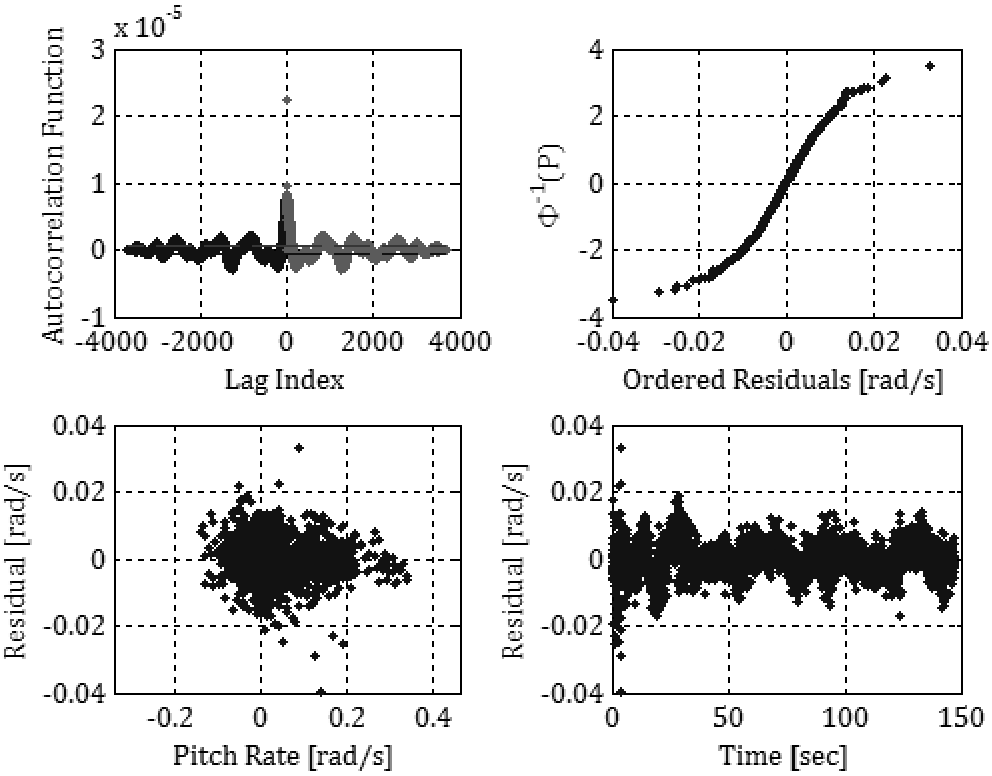

Figure G-26 Final IEKF Residual Analysis – Pitch Rate

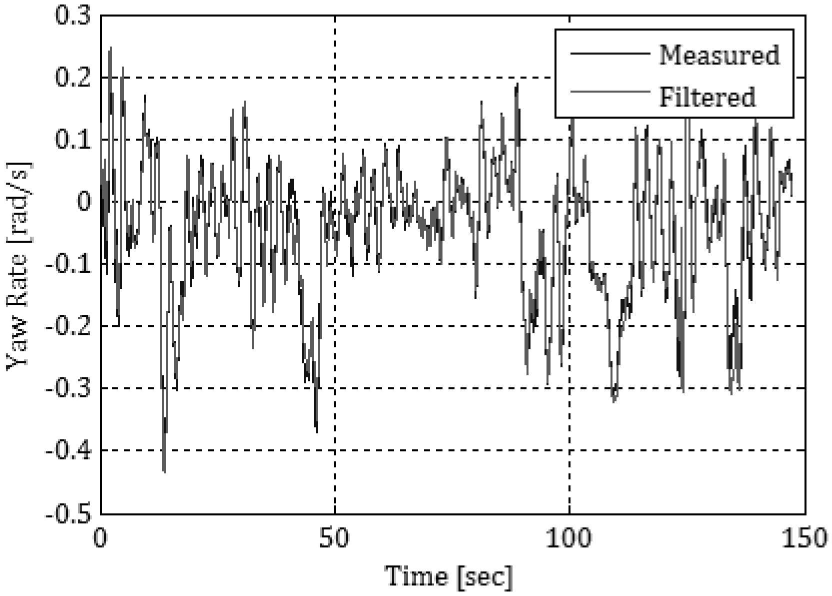

Figure G-27 Initial IEKF Result – Yaw Rate

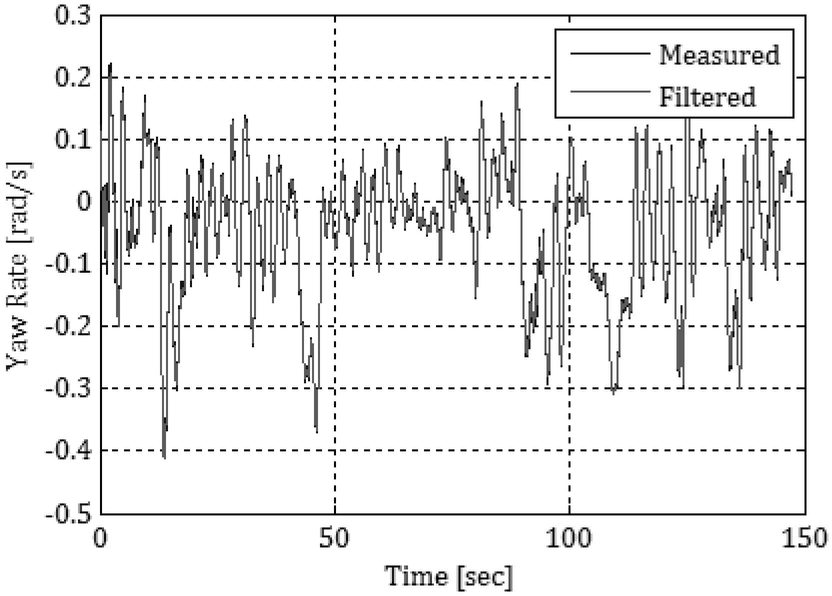

Figure G-28 Final IEKF Result – Yaw Rate

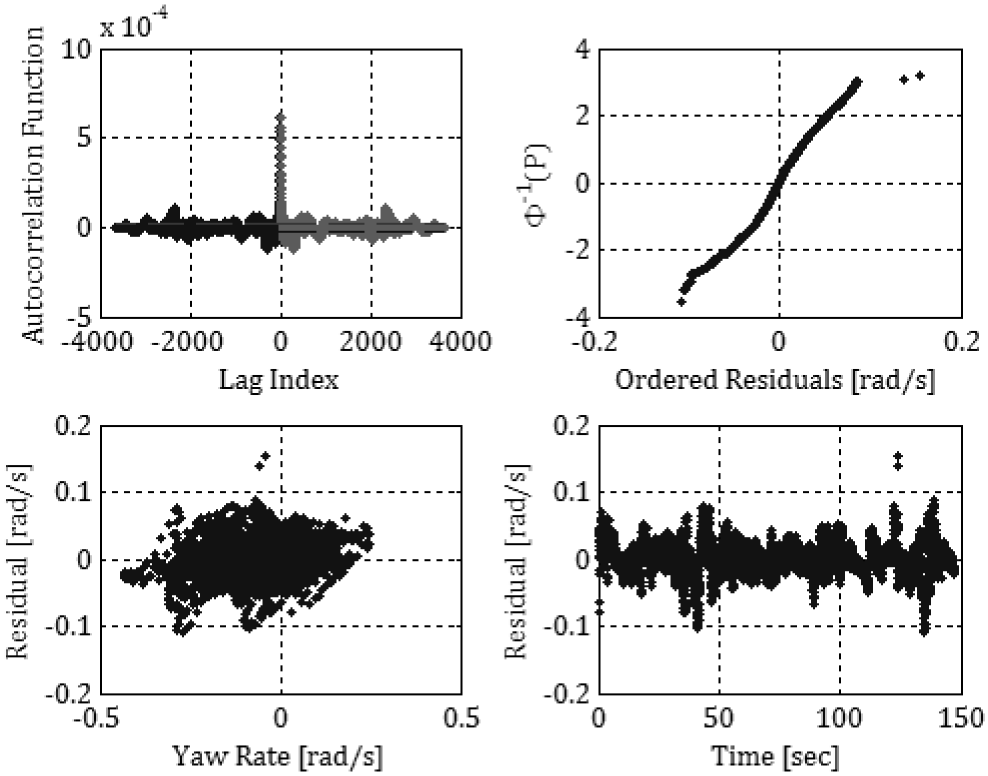

Figure G-29 Initial IEKF Residual Analysis – Yaw Rate

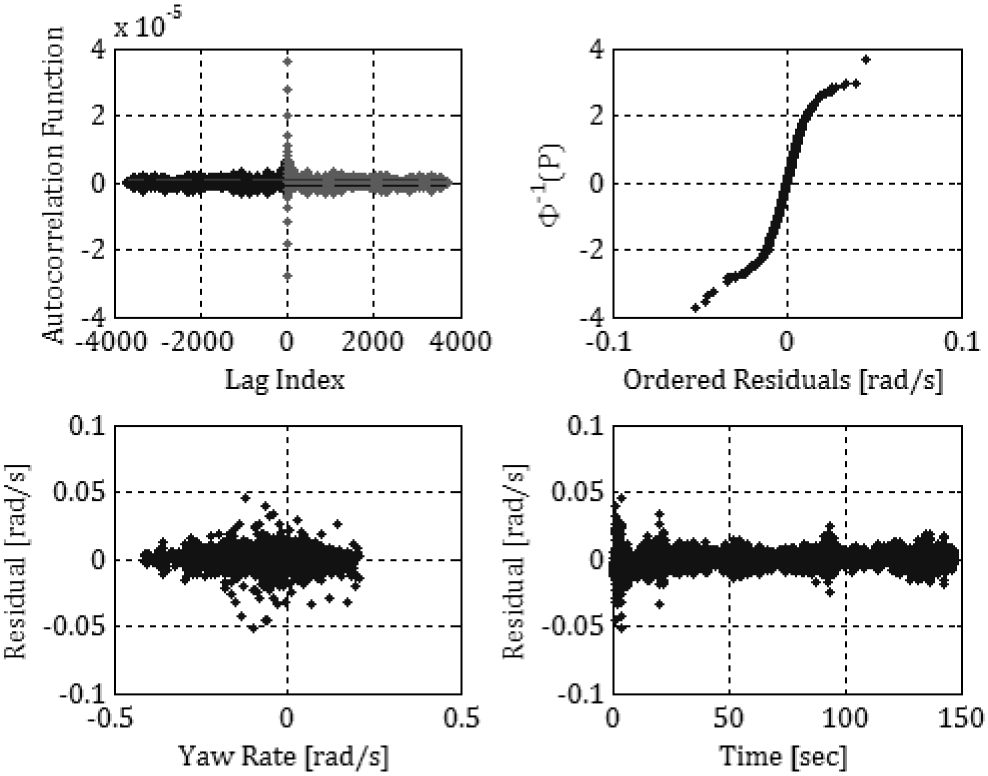

Figure G-30 Final IEKF Residual Analysis – Yaw Rate

G.3 EULER ANGLE COMPARISONS

A comparison was made between the Euler angles estimated via the iterated extended Kalman filter (offline analysis) and the Euler angles estimated via the on-board real-time Kalman filter. The results are presented in Figure G-31 to Figure G-38. The Euler angles were then used to reconstruct the angular rate data obtained via the rate gyroscopes for each manoeuvre. The resulting angular rate residuals from both the estimators are given in Figure G-39 to Figure G-41 for the first box manoeuvre. As can be seen, a bias difference existed between the Euler angle estimates. The residual analysis, on the other hand, yielded plausible Gaussian characteristics for both estimators. The quality of the residuals led to an indefinite conclusion as to which method was more accurate. An additional level of uncertainty was inherent in the on-board Kalman filter algorithm results because the algorithm was not available for analysis and verification. Nevertheless, the correlation between the two independent methods that did exist, in terms of rates of change and plausibility criteria, aids in the argument of a successful use of the algorithms on the measured Modular UAV datasets.

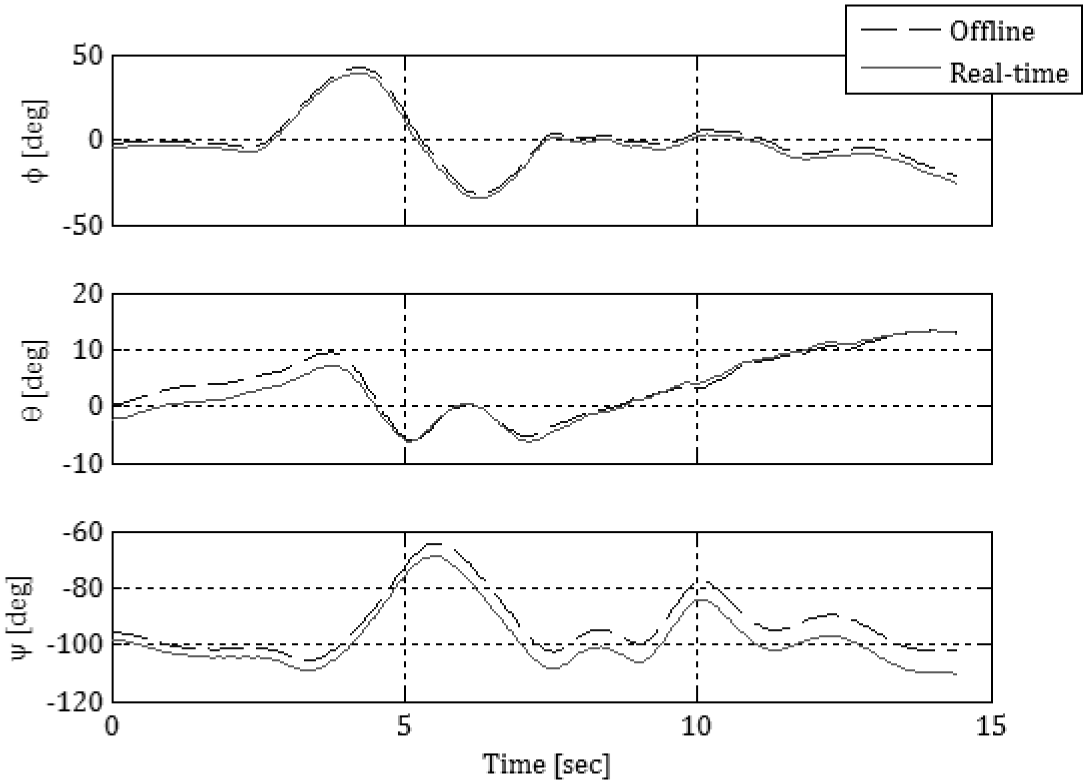

Figure G-31 Euler Comparison - Lateral Manoeuvre 1

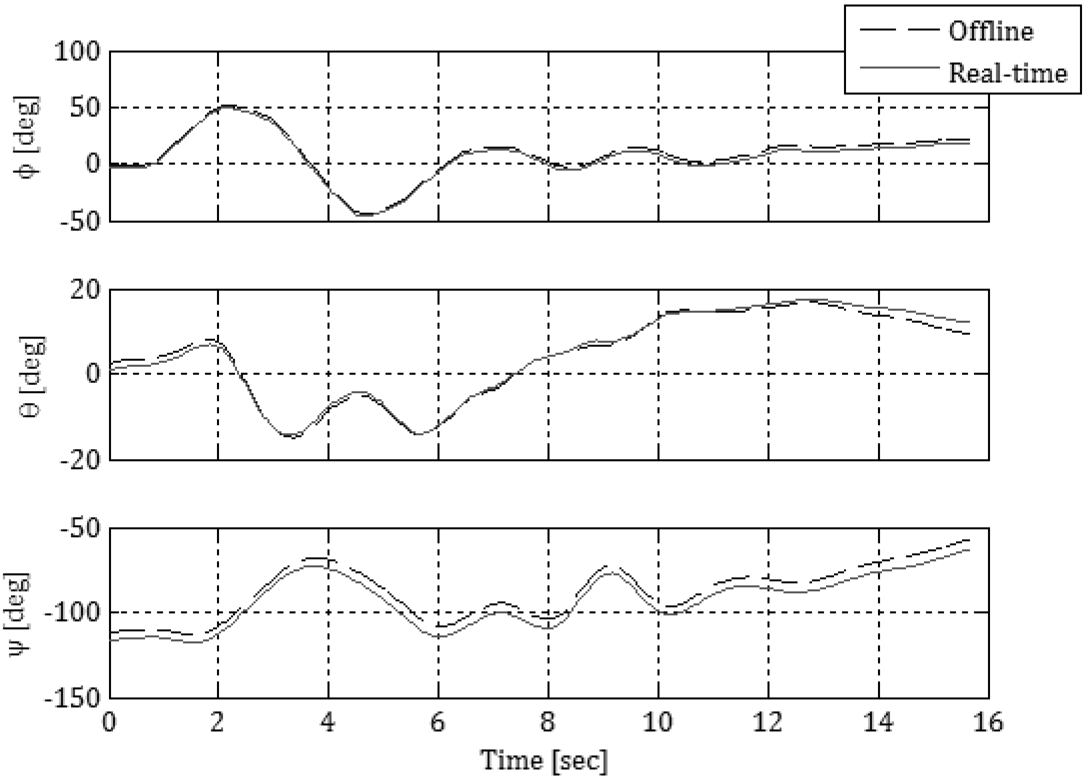

Figure G-32 Euler Comparison - Lateral Manoeuvre 2

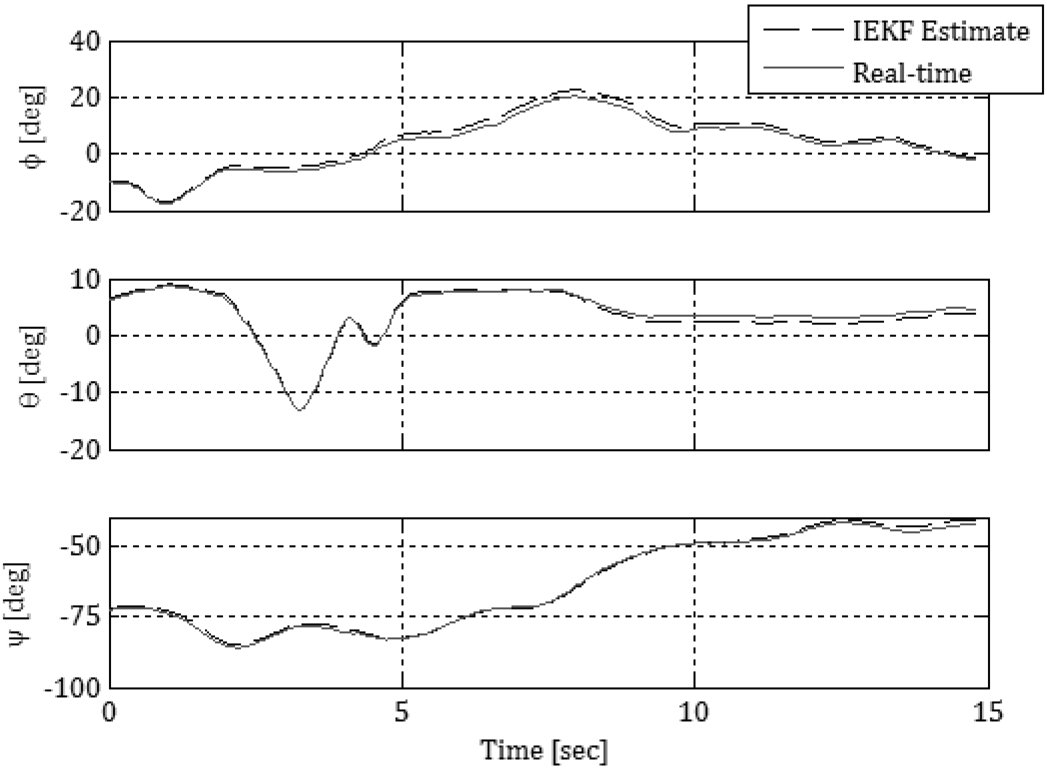

Figure G-33 Euler Comparison - Longitudinal Manoeuvre (3211p4)

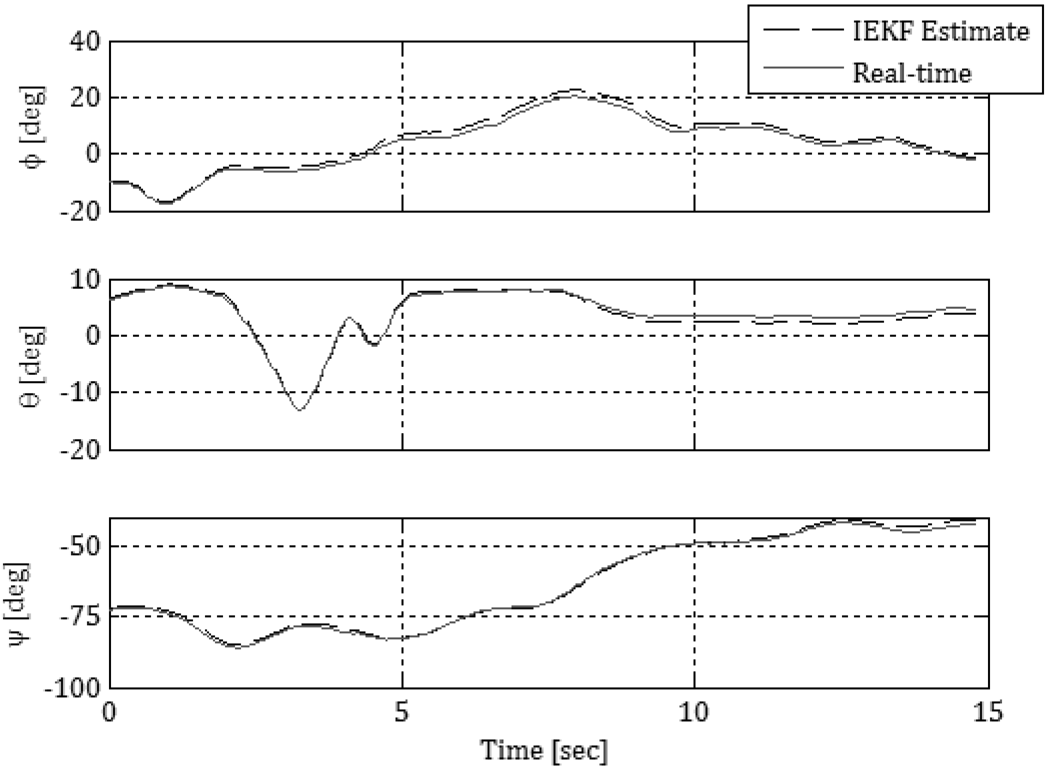

Figure G-34 Euler Angles Comparison - Longitudinal Manoeuvre (3211n4)

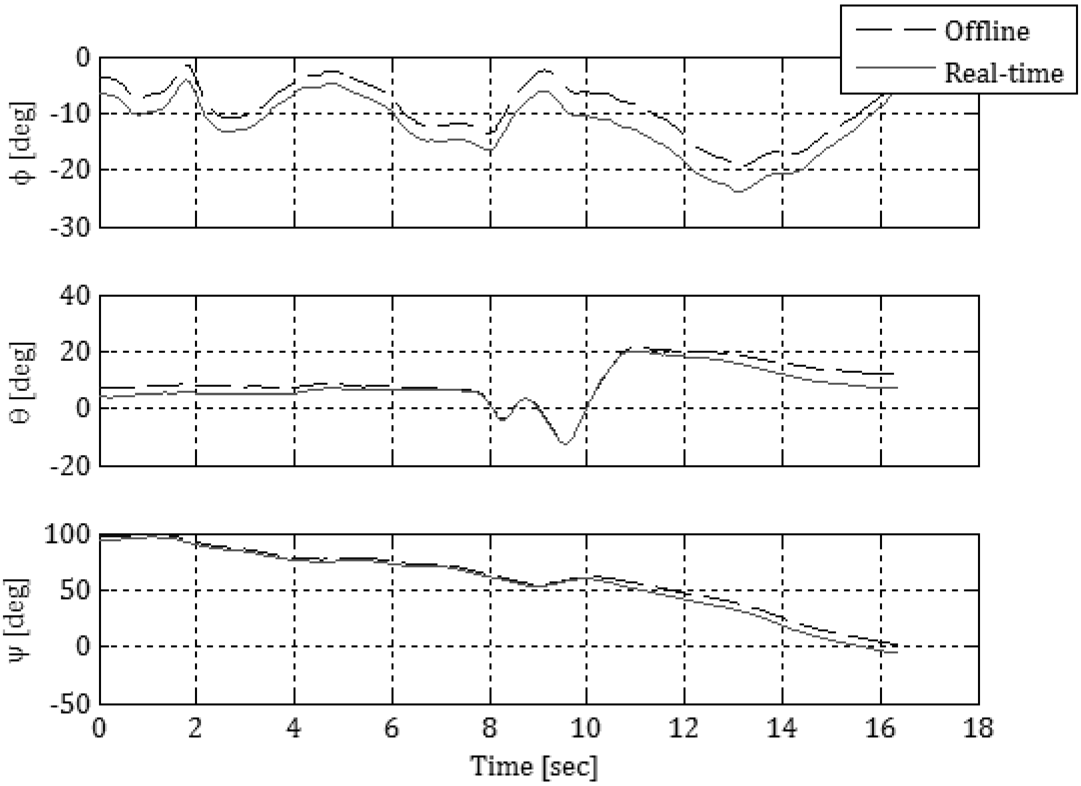

Figure G-35 Euler Angles Comparison - Longitudinal Manoeuvre (1123p6)

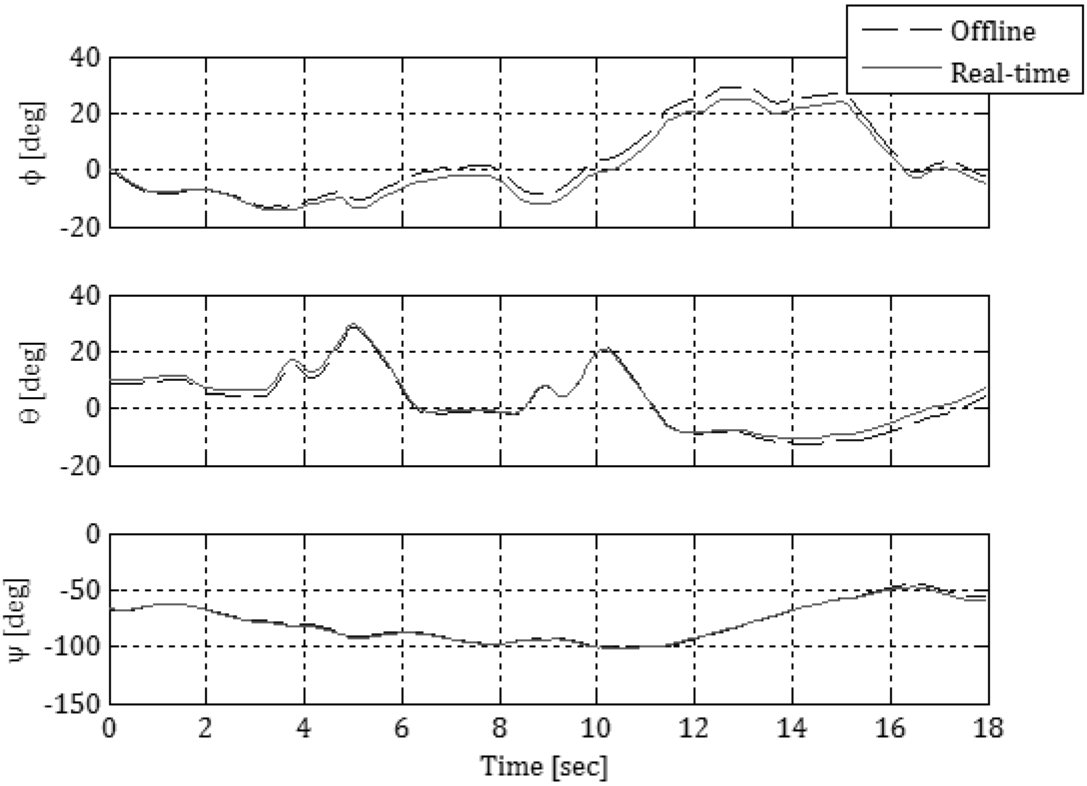

Figure G-36 Euler Angles Comparisons - Longitudinal Manoeuvre (1123n6)

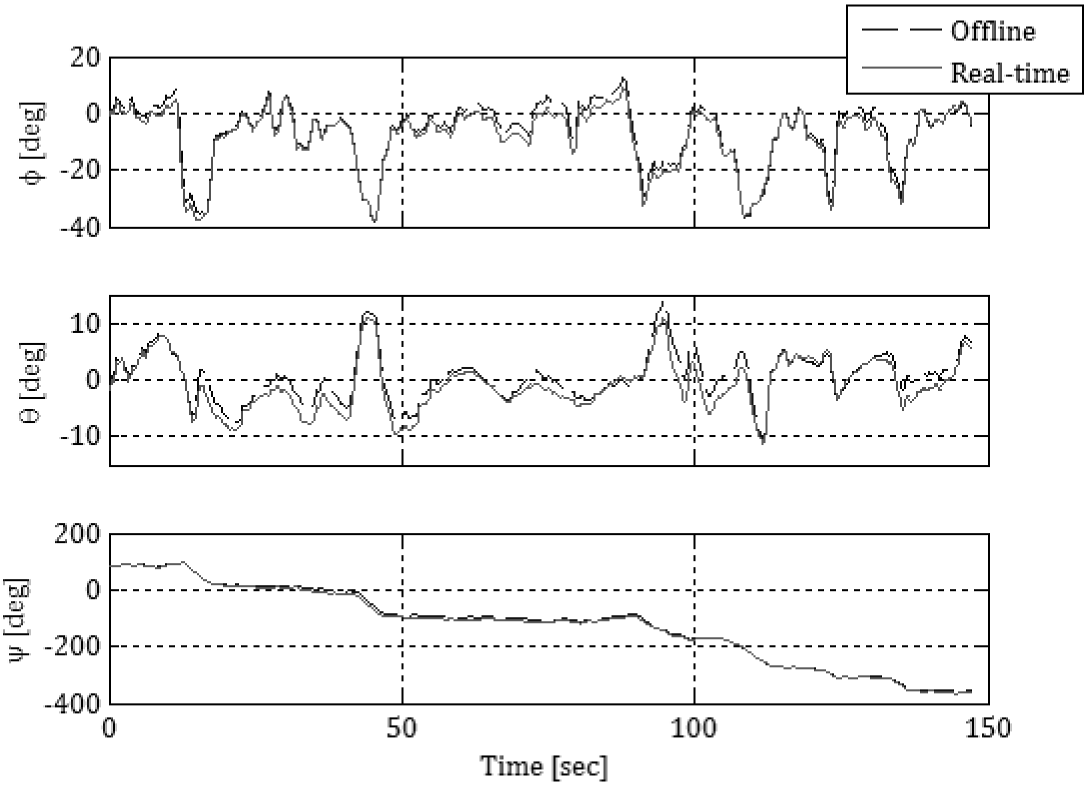

Figure G-37 Euler Angles Comparisons – Box Manoeuvre 1

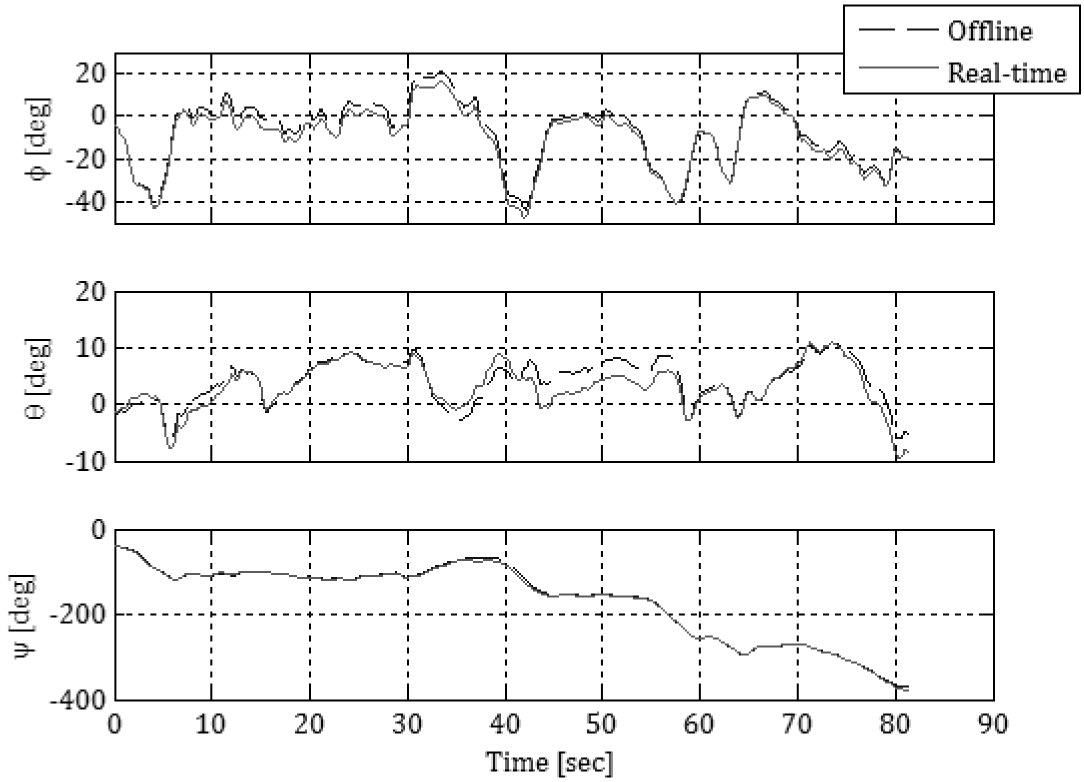

Figure G-38 Euler Angles Comparisons - Box Manoeuver 2

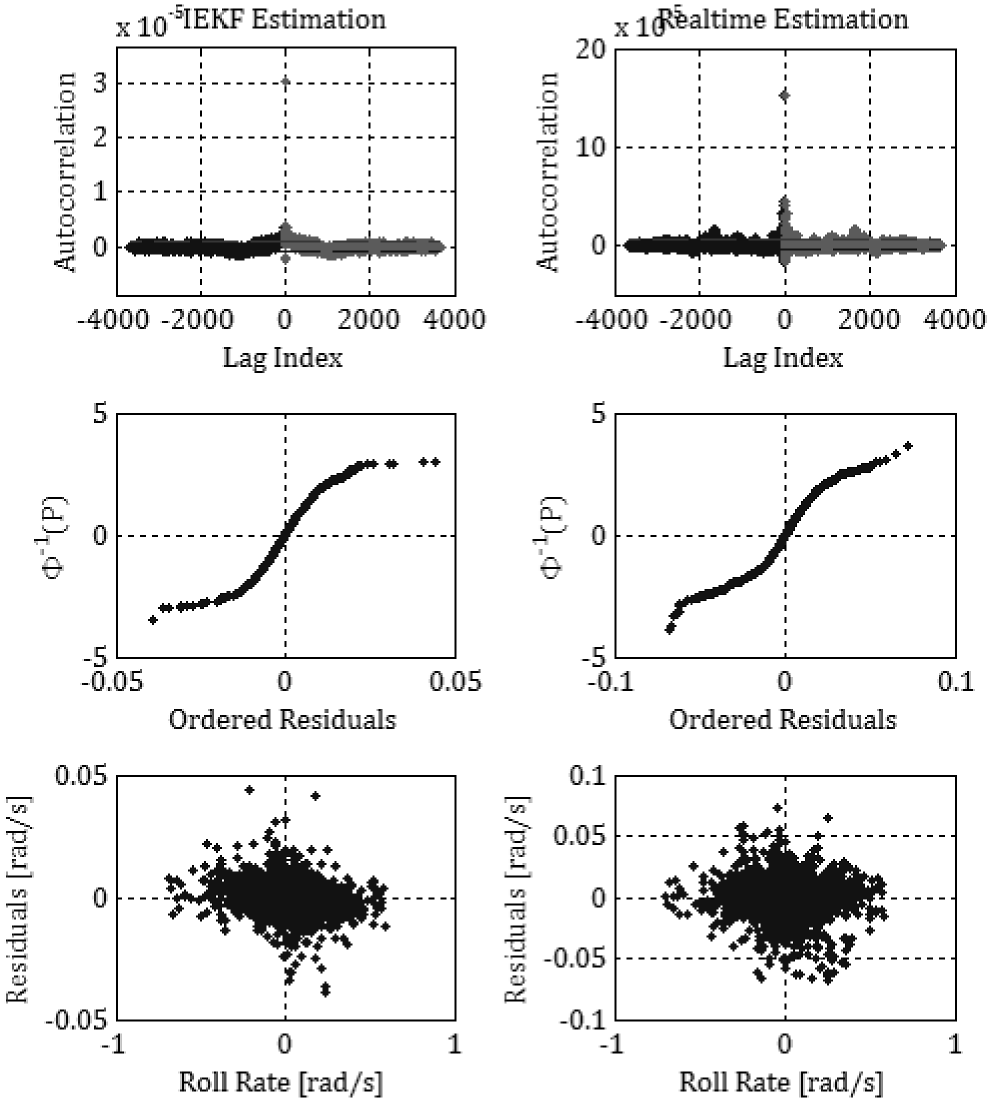

Figure G-39 Angular Rate Evaluations - Box Manoeuvre 1 - Roll Rate

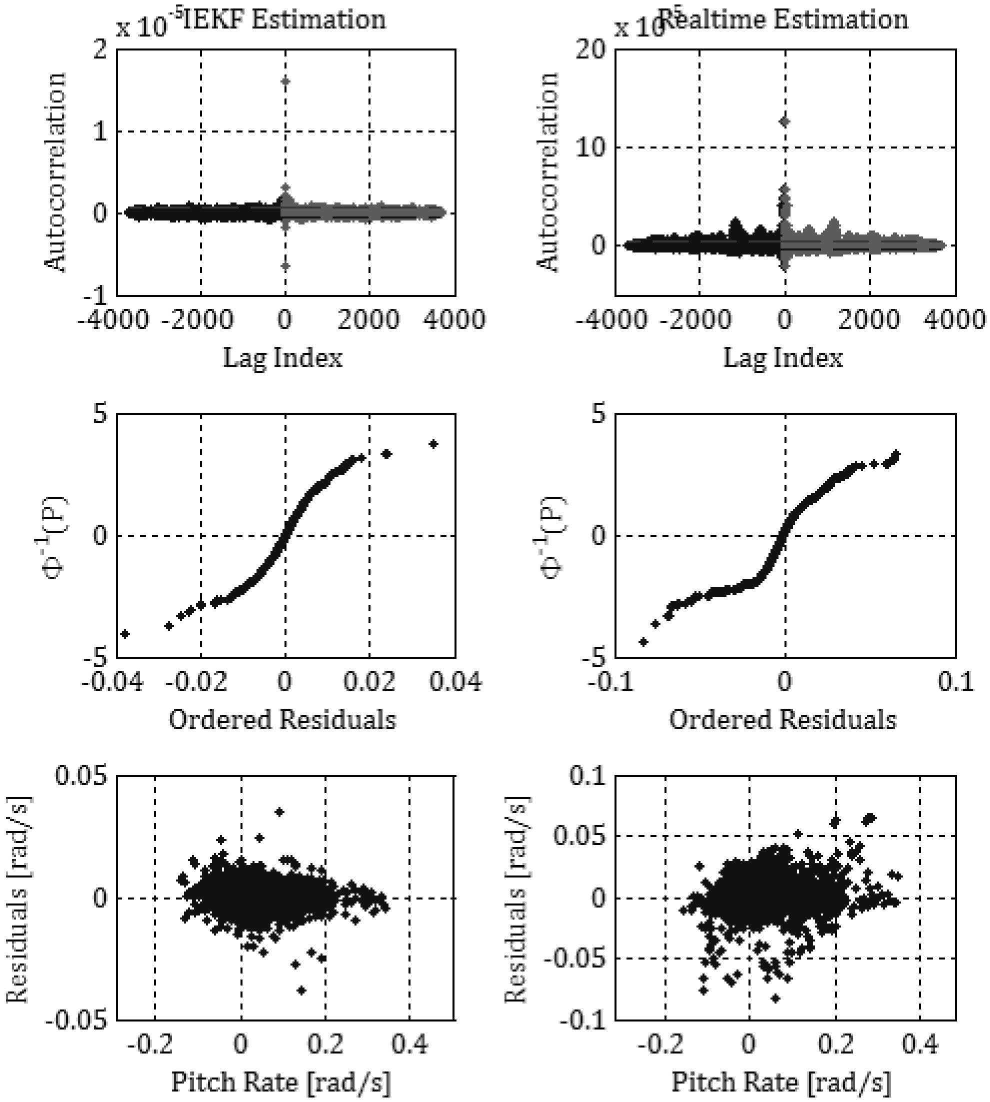

Figure G-40 Angular Rate Evaluations - Box Manoeuvre 1 - Pitch Rate

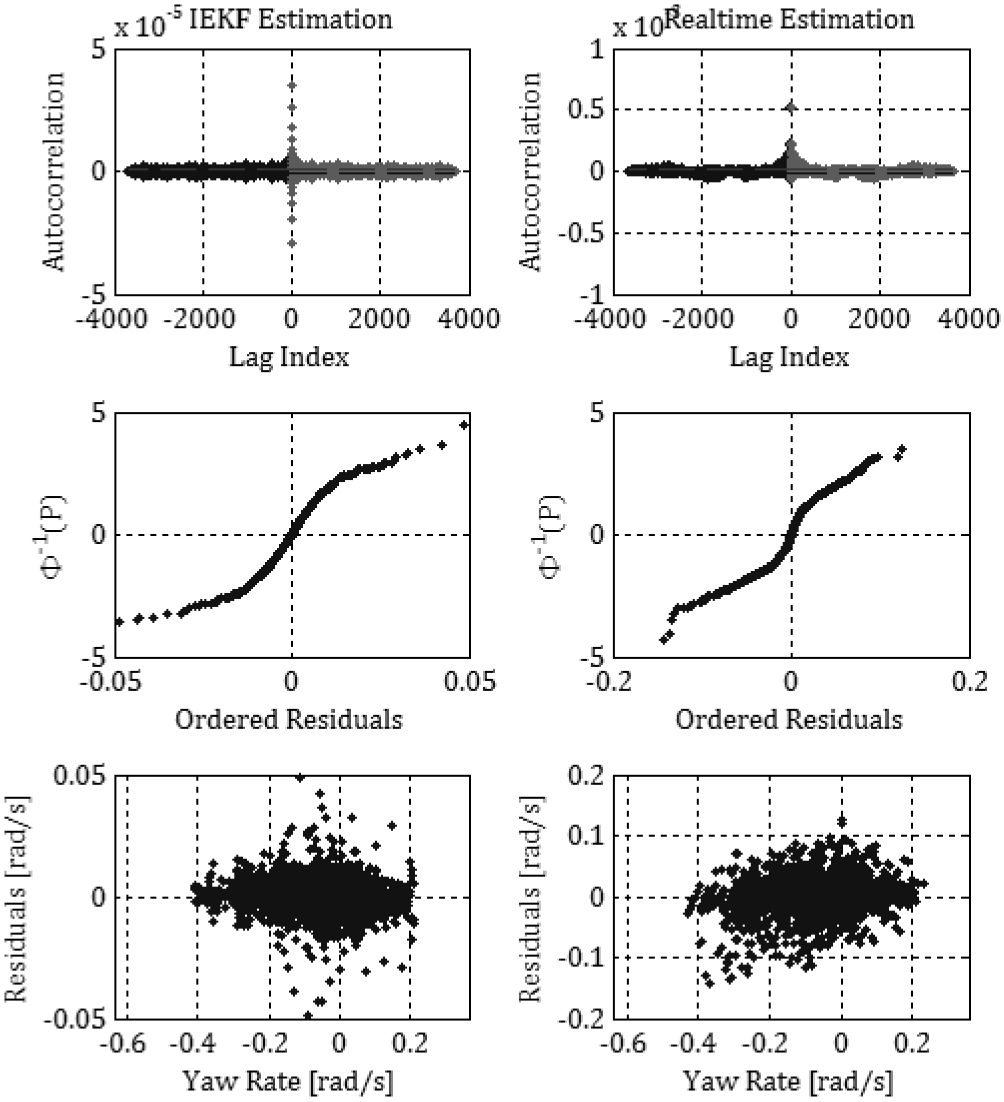

Figure G-41 Angular Rates Evaluations - Box Manoeuvre 1 - Yaw Rate

G.4 FINAL MEASUREMENT VARIANCES

The final measurement variances achieved through the application of the optimal filtering process is presented in Table G-1 to Table G-5.

Table G-1 Accelerometer Variances Obtained via the Optimal Filtering Technique

Measurement	Variance, $[m/s^2]^2$
X acceleration	0.004613
Y acceleration	0.031477
Z acceleration	0.052003

Table G-2 Rate Gyroscope Variances Obtained via the Optimal Filtering Technique

Measurement	Variance, $[rad/s]^2$
Roll rate, p	0.000061
Pitch rate, q	0.000031
Yaw rate, r	0.000069

Table G-3 GPS Positional Variances Obtained via the Optimal Filtering Technique

Measurement	Variance, $[m]^2$
Altitude	0.103140
North	4.577304
East	9.580597

Table G-4 GPS velocities Obtained via the Optimal Filtering Technique

Measurement	Variance, $[m/s]^2$
Climb rate	2.062531
North Rate	0.059783
East Rate	0.044033

Table G-5 Magnetometer Variances Obtained via the Optimal Filtering Technique

Measurement	Variance, $[Gauss]^2$
Roll rate, p	0.071705E-6
Pitch rate, q	3.614481E-6
Yaw rate, r	0.021835E-6

H. PARAMETER IDENTIFICATION RESULTS

H.1 LINEAR REGRESSION

An important step in the aerodynamic identification method was to develop adequate linear aerodynamic model structures for the lateral and longitudinal manoeuvres as described in Sec. 2.2.2. Stepwise regression was utilised to estimate which of the first order aircraft states were required in the final linear aerodynamic models for each orthogonal force or moment. Parameters for the most plausible models were then estimated using orthogonal functions in an effort to reduce the adverse correlation effects.

The two lateral manoeuvres were analysed first to determine the lateral force and moments (i.e. C_Y, C_n, and C_l). The results for the C_Y models were presented in Sec. 4.4.4, therefore only the remaining two modelling procedures will be discussed in this section.

The model structures and initial parameter estimates for the rolling moment model was established. A consistent model structure was established for both lateral manoeuvres and is given below:

$$C_l = C_{l_0} + C_{l_\beta}\beta + C_{l_p}\left(\frac{pb}{2V_0}\right) + C_{l_{\dot{\beta}}}\dot{\beta} + C_{l_{\delta a}}\delta a \qquad \textbf{H-1}$$

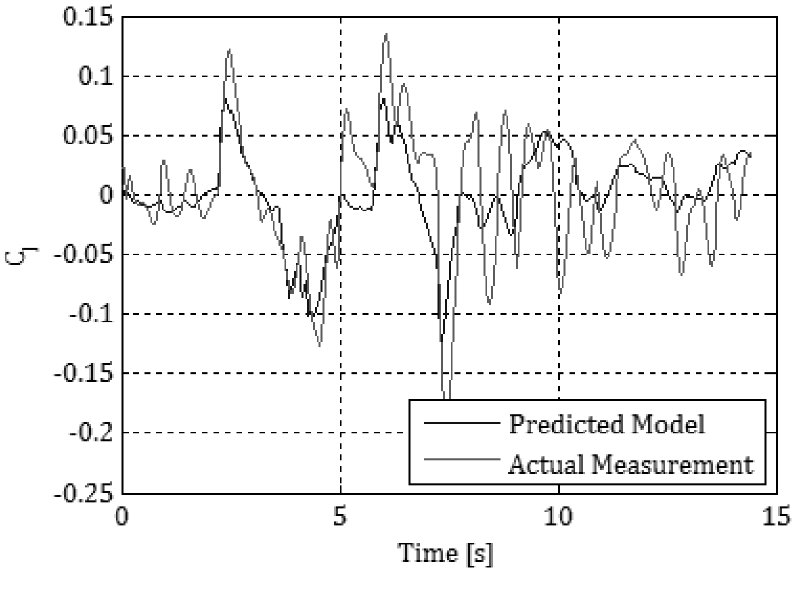

Figure H-1 C$_l$ Least Squares Fit - Lateral Manoeuvre 1

Table H-1 Stepwise Regression Results - C_l - Lateral Manoeuvre 1

C_l – Bank to Bank and Rudder Doublet – Manoeuvre 1 – No Wind Tunnel Data					
Regressor	θ^*	σ	θ	t_0	$100\left({}^{\sigma}/_{\theta^*}\right)$
β	-0.4962	0.032117	-0.0232	15.42885	6.472585
$pb/2V_0$	-0.9238	0.059561	-0.1388	15.49093	6.447425
$\dot{\beta}$	-0.3856	0.033338	-0.0919	11.55265	8.645803
δa	-1.3006	0.061617	-0.0805	21.08071	4.737561
* Standardised parameter					
R^2 [%]	62.1996				
σ	0.03121				
Condition No.	14.6523				
Correlation Coefficients					
	β	$pb/2V_0$	$\dot{\beta}$	δa	
β	1	0.0269	0.0816	0.1552	
$pb/2V_0$	0.0269	1	0.0271	0.8317	
$\dot{\beta}$	0.0816	0.0271	1	0.2188	
δa	0.1552	0.8317	0.2188	1	

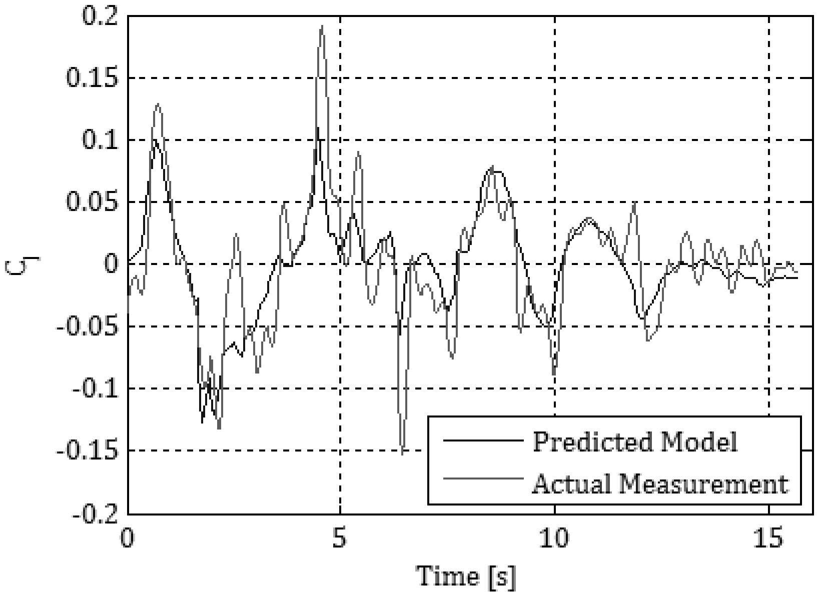

Figure H-2 C_l Least Squares Fit - Lateral Manoeuvre 2

Table H-2 Stepwise Regression Results - Cl - Lateral Manoeuvre 2

C_l – Bank to Bank and Rudder Doublet – Manoeuvre 2 – No Wind Tunnel Data					
Regressor	θ^*	σ	θ	t_0	$100(^{\sigma}/_{\theta^*})$
β	-0.5333	0.042433	-0.0236	12.54985	7.956612
$pb/2V_0$	-0.7467	0.084579	-0.1229	8.815637	11.32698
$\dot{\beta}$	-0.2282	0.046058	-0.0636	4.948096	20.18301
δa	-1.1672	0.08612	-0.0662	13.53464	7.378309
* Standardised parameter					
R^2 [%]	47.3206				
σ	0.0384				
Condition No.	21.84				
Correlation Coefficients					
	β	$pb/2V_0$	$\dot{\beta}$	δa	
β	1	-0.1841	0.2226	0.067	
$pb/2V_0$	-0.1841	1	-0.0608	0.8239	
$\dot{\beta}$	0.2226	-0.0608	1	0.2617	
δa	0.067	0.8239	0.2617	1	

The resulting model fits were poor with coefficients of determination of 62.2% and 47.32% respectively with large standard deviations. Correlation coefficients were not significantly high to expect any large adverse effects on the parameter estimates. The poor model fits could be attributed to the noisy measurement signal which had a strong component dependent on the numerical derivative of the roll rate rather than an actual measurement. The orthogonal function least squares results for both manoeuvres and the prior model data is given in Table H-3. The estimated parameters were consistent with the prior data except for the $C_{l_{\delta a}}$ and C_{l_β} being underestimated. If power effects on the wind tunnel estimate of the aileron effectiveness are considered minimal (a plausible assumption since the ailerons are situated out of the propeller slipstream for small sideslip angles), then the a priori result given in Table H-3 can be considered accurate and thus the $C_{l_{\delta a}}$ coefficients were significantly underestimated. In terms of the final model structure, the absence of the C_{l_r} parameter could potentially lead to erroneous Dutch roll characteristics and hence it was added to the final model structure. The resulting parameters were also consistent with laterally stable aircraft trends in terms of the signs of the estimates.

Table H-3 Final Least Squares Estimate for C_l

	Lateral	Lateral	A priori
C_{l_β}	-0.0232	-0.0236	-0.083
C_{l_p}	-0.1388	-0.1229	-0.113
$C_{l_{\dot\beta}}$	-0.0919	-0.0636	-
$C_{l_{\delta a}}$	-0.0805	-0.0662	-0.172
C_{l_r}	-	-	0.033

The resulting model fit evaluation for the yawing moment was good, yielding coefficients of determination of 90.37% and 84.46% respectively. The two model structures that were derived for the respective manoeuvres were:

$$C_n = C_{n_0} + C_{n_\beta}\beta + C_{n_r}\left(\frac{rb}{2V_0}\right) + C_{n_{\dot\beta}}\dot\beta + C_{n_{\delta r}}\delta r \qquad \textbf{H-2}$$

And

$$C_n = C_{n_0} + C_{n_\beta}\beta + C_{n_p}\left(\frac{pb}{2V_0}\right) + C_{n_r}\left(\frac{rb}{2V_0}\right) + C_{n_{\dot\beta}}\dot\beta + C_{n_{\delta r}} \qquad \textbf{H-3}$$

The difference could be attributed to the correlation between the aileron deflection and the roll rate as seen in the previous model structures. A high correlation between the yaw rate and rate of change of sideslip derivatives was also found for the second lateral manoeuvre. This correlation resulted in the noticeably higher standard deviations for these parameters.

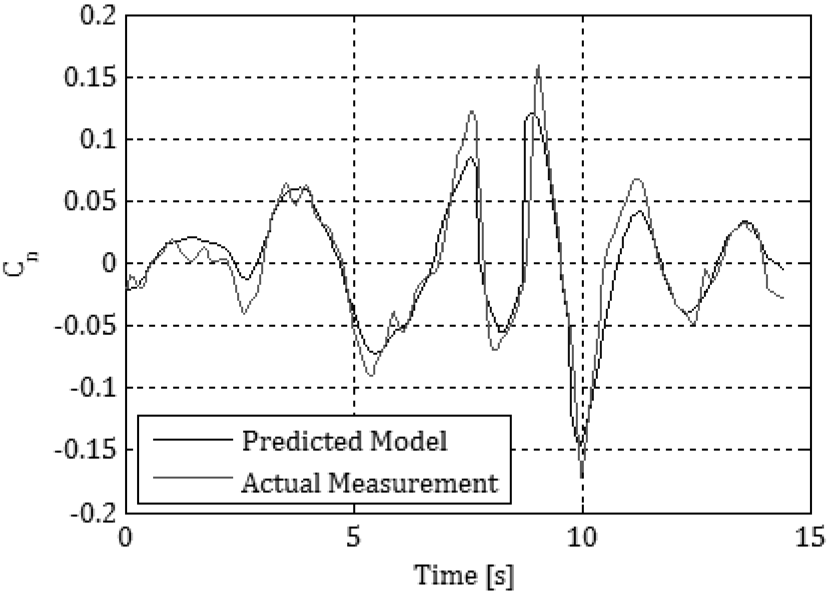

Figure H-3 C_n Least Squares Fit - Lateral Manoeuvre 1

Table H-4 Stepwise Regression Results - C_n - Lateral Manoeuvre 1

C_n – Bank to Bank and Rudder Doublet – Manoeuvre 1 – No Wind Tunnel Data					
Regressor	θ^*	σ	θ	t_0	$100(\sigma/\theta^*)$
β	0.9814	0.017233	0.066	56.87697	1.755919
$rb/2V_0$	-0.7762	0.036051	-0.2365	21.5034	4.644585
$\dot{\beta}$	-0.569	0.036233	-0.195	15.68326	6.367804
δa	0.1401	0.01861	0.0125	7.516701	13.28357
δr	-0.3616	0.01883	-0.0398	19.17714	5.207445
* Standardised parameter					
R^2 [%]	90.3681				
σ	0.01578				
Condition No.	23.0633				
Correlation Coefficients					
	β	$rb/2V_0$	$\dot{\beta}$	δa	δr
β	1	-0.2587	-0.1177	0.3334	-0.2146
$rb/2V_0$	-0.2587	1	0.8356	-0.2648	-0.0028
$\dot{\beta}$	-0.1177	0.8356	1	0.007	-0.2949
δa	0.3334	-0.2648	0.007	1	-0.2574
δr	-0.2146	-0.0028	-0.2949	-0.2574	1

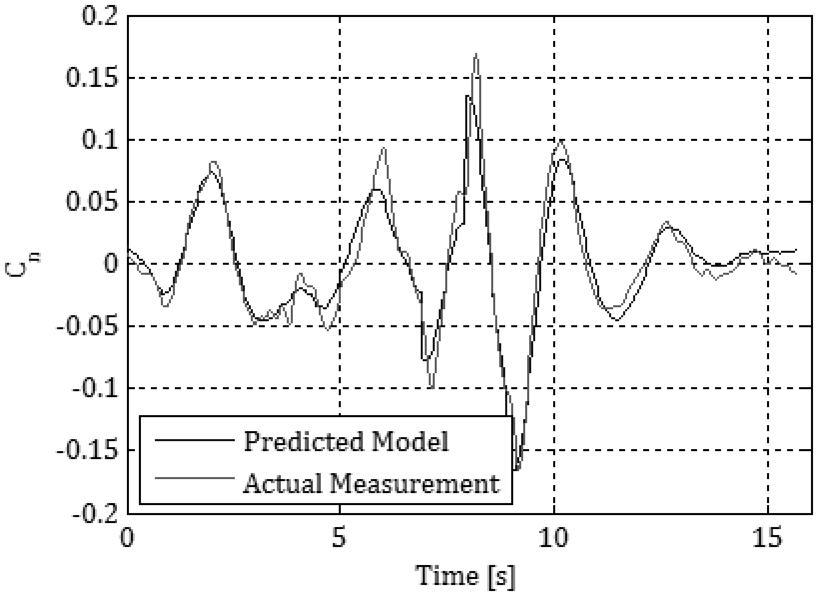

Figure H-4 C_n Least Squares Fit - Lateral Manoeuvre 2

Table H-5 Stepwise Regression Results - C_n - Lateral Manoeuvre 2

C_n – Bank to Bank and Rudder Doublet – Manoeuvre 2 – No Wind Tunnel Data					
Regressor	θ^*	σ	θ	t_0	$100(^{\sigma}/_{\theta^*})$
β	0.9472	0.023143	0.0493	40.86937	2.443263
$pb/2V_0$	-0.1726	0.025842	-0.0334	6.667929	14.97199
$rb/2V_0$	-0.5077	0.051083	-0.1384	9.925103	10.06157
$\dot{\beta}$	-0.3251	0.053692	-0.1064	6.046598	16.51562
δr	-0.4546	0.0212	-0.0336	21.41143	4.663516
* Standardised parameter					
R^2 [%]	85.4605				
σ	0.0202				
Condition No.	28.9174				
Correlation Coefficients					
	β	$pb/2V_0$	$rb/2V_0$	$\dot{\beta}$	δr
β	1	-0.4165	-0.2042	-0.071	-0.1615
$pb/2V_0$	-0.4165	1	-0.0835	-0.3138	0.2078
$rb/2V_0$	-0.2042	-0.0835	1	0.8918	-0.0825
$\dot{\beta}$	-0.071	-0.3138	0.8918	1	-0.1952
δr	-0.1615	0.2078	-0.0825	-0.1952	1

The final model structure and parameter estimates using orthogonal regressors are given in Table H-6. As can be seen there were large variances for the dynamic parameters (i.e. C_{n_p}, C_{n_r}, and $C_{n_{\dot{\beta}}}$), whilst the static parameters (i.e. C_{n_β}, $C_{n_{\delta a}}$ and $C_{n_{\delta r}}$) displayed more consistency between the three sources. As described in Roskam (1979) C_{n_p} is due mainly to two influences. These are the yawing moment increase due to an asymmetrical increase in drag due to effective changes in angle of attack of the left and right wing, and the increase in yawing moment due to an increase in angle of attack of the vertical tails due to a roll rate. C_{n_p} could therefore be positive or negative and a definite conclusion on the parameters could not be made using the least squares estimation without additional manoeuvres. The accuracy of the apriori estimates (including C_{n_p}) were low because they were based on low order analytical methods and therefore the apriori estimate of C_{n_p} was not weighted enough to definitively prove that the derivative should be positive. The C_{n_r} derivative also had a large variance but confidence in the estimate from the first lateral manoeuvre was higher than the remaining two sources since the t_0-statistic was relatively high and the estimated variance was low. Therefore, a value of -0.252 was considered the most probable. This once again highlighted the fact that the dynamic a priori data had questionable accuracy. The control derivatives showed greater consistency than the dynamic derivatives although the magnitude of the rudder effectiveness was underestimated for both lateral manoeuvres. The signs of the estimated parameters excluding C_{n_p}, were consistent with a laterally stable aircraft and therefore plausible.

Table H-6 Final Least Squares Result for C_n

	Lateral 1	Lateral 2	A Priori
C_{n_β}	0.066	0.050	0.097
C_{n_p}	0.014	-0.013	0.020
C_{n_r}	-0.252	-0.156	-0.085
$C_{n_{\dot\beta}}$	-0.210	-0.121	-
$C_{n_{\delta a}}$	0.018	0.009	0.010
$C_{n_{\delta r}}$	-0.039	-0.034	-0.065

Model structures for the longitudinal models were analysed next using standardised regressors and the stepwise regression algorithm. The model structures varied, therefore an average model based on the common plausible parameters with the highest t_0-statistics and consistent parameter estimates were used in the final least squares estimation using orthogonal functions. The results for the axial force model estimation are given in Table H-7 to Table H-10, depicting the stepwise analysis of the four longitudinal manoeuvres. It should be noted that the axial force model incorporated the thrust effects because the actual thrust was not available. This was deemed a satisfactory initial assumption since the throttle settings were constant and the angle of attack excursions were small.

Table H-7 Stepwise Regression Results - C_A – 3-2-1-1 Manoeuvre 1

<table>
<tr><td colspan="6">C_A – 3-2-1-1: ±4° Elevator Deflection – No Wind Tunnel Data</td></tr>
<tr><td>Regressor</td><td>θ^*</td><td>σ</td><td>θ</td><td>t_0</td><td>$100(\sigma/_{\theta^*})$</td></tr>
<tr><td>α</td><td>0.5648</td><td>0.013745</td><td>0.779</td><td>41.05745</td><td>2.433663</td></tr>
<tr><td>$\Delta V/V_0$</td><td>0.9564</td><td>0.011953</td><td>0.526</td><td>79.95461</td><td>1.249793</td></tr>
<tr><td>$q\bar{c}/2V_0$</td><td>-0.2187</td><td>0.016955</td><td>-13.7067</td><td>12.8865</td><td>7.752483</td></tr>
<tr><td>$\dot{\alpha}\bar{c}/2V_0$</td><td>0.124</td><td>0.014174</td><td>9.1521</td><td>8.744372</td><td>11.43049</td></tr>
<tr><td colspan="6">* Standardised parameter</td></tr>
<tr><td>R² [%]</td><td>92.1194</td><td colspan="4" rowspan="3">$C_A = C_{A_\alpha}\alpha + C_{A_V}\left(\Delta V/_{V_0}\right) + C_{A_q}\left(q\bar{c}/_{2V_0}\right) + C_{A_{\dot{\alpha}}}\left(\dot{\alpha}\bar{c}/_{2V_0}\right)$</td></tr>
<tr><td>σ</td><td>0.0109</td></tr>
<tr><td>Condition No.</td><td>7.6359</td></tr>
</table>

Table H-8 Stepwise Regression Results - C_A - 3-2-1-1 Manoeuvre 2

<table>
<tr><td colspan="6">C_A – 3-2-1-1: ±4° Elevator Deflection – No Wind Tunnel Data</td></tr>
<tr><td>Regressor</td><td>θ^*</td><td>σ</td><td>θ</td><td>t_0</td><td>$100(\sigma/_{\theta^*})$</td></tr>
<tr><td>α</td><td>0.7643</td><td>0.015969</td><td>0.5435</td><td>47.79651</td><td>2.089343</td></tr>
<tr><td>$\Delta V/V_0$</td><td>0.3609</td><td>0.016219</td><td>0.2802</td><td>22.2213</td><td>4.49417</td></tr>
<tr><td>$\dot{\alpha}\bar{c}/2V_0$</td><td>-0.1168</td><td>0.015043</td><td>-3.5858</td><td>7.75564</td><td>12.87893</td></tr>
<tr><td colspan="6">* Standardised parameter</td></tr>
<tr><td>R² [%]</td><td>91.97056</td><td colspan="4" rowspan="3">$C_A = C_{A_\alpha}\alpha + C_{A_V}\left(\Delta V/_{V_0}\right) + C_{A_{\dot{\alpha}}}\left(\dot{\alpha}\bar{c}/_{2V_0}\right)$</td></tr>
<tr><td>σ</td><td>0.01479</td></tr>
<tr><td>Condition No.</td><td>2.4074</td></tr>
</table>

Table H-9 Stepwise Regression Results - C_A - 1-1-2-3 Manoeuvre 1

<table>
<tr><td colspan="6">C_A – 1-1-2-3: ±6° Elevator Deflection – No Wind Tunnel Data</td></tr>
<tr><td>Regressor</td><td>θ^*</td><td>σ</td><td>θ</td><td>t_0</td><td>$100(\sigma/_{\theta^*})$</td></tr>
<tr><td>α</td><td>0.9488</td><td>0.028457</td><td>0.6843</td><td>33.30358</td><td>2.999298</td></tr>
<tr><td>β</td><td>-0.2246</td><td>0.018694</td><td>-0.1858</td><td>12.00164</td><td>8.323356</td></tr>
<tr><td>$\Delta V/V_0$</td><td>0.946</td><td>0.025669</td><td>0.3466</td><td>36.81172</td><td>2.713475</td></tr>
<tr><td>$q\bar{c}/2V_0$</td><td>-0.654</td><td>0.037168</td><td>-19.8924</td><td>17.57472</td><td>5.683224</td></tr>
<tr><td>$\dot{\alpha}\bar{c}/2V_0$</td><td>0.498</td><td>0.028257</td><td>20.3495</td><td>17.60305</td><td>5.674037</td></tr>
<tr><td>δe</td><td>0.2961</td><td>0.020827</td><td>0.2644</td><td>14.20083</td><td>7.033604</td></tr>
<tr><td colspan="6">* Standardised parameter</td></tr>
<tr><td>R² [%]</td><td>86.1579</td><td colspan="4" rowspan="3">$C_A = C_{A_\alpha}\alpha + C_{A_\beta}\beta + C_{A_V}\left(\Delta V/_{V_0}\right) + C_{A_q}\left(q\bar{c}/_{2V_0}\right)$
$+ C_{A_{\dot{\alpha}}}\left(\dot{\alpha}\bar{c}/_{2V_0}\right) + C_{A_{\delta e}}\delta e$</td></tr>
<tr><td>σ</td><td>0.01766</td></tr>
<tr><td>Condition No.</td><td>19.2508</td></tr>
</table>

Table H-10 Stepwise Regression Results - C_A - 1-1-2-3 Manoeuvre 2

C_A – 1-1-2-3: ±6° Elevator Deflection – No Wind Tunnel Data					
Regressor	θ^*	σ	θ	t_0	$100\left({}^{\sigma}/_{\theta^*}\right)$
α	0.7413	0.012232	0.5941	60.53183	1.650076
$\Delta V/V_0$	0.7169	0.010957	0.3935	65.34151	1.52845
$q\bar{c}/2V_0$	-0.3984	0.014846	-13.5592	26.80102	3.726492
$\dot{\alpha}\bar{c}/2V_0$	0.1844	0.013248	8.5671	13.89958	7.18454
* Standardised parameter					
R^2 [%]	95.5239	$C_A = C_{A_\alpha}\alpha + C_{A_V}\left({}^{\Delta V}/_{V_0}\right) + C_{A_q}\left({}^{q\bar{c}}/_{2V_0}\right) + C_{A_{\dot{\alpha}}}\left({}^{\dot{\alpha}\bar{c}}/_{2V_0}\right)$			
σ	0.01049				
Condition No.	5.8729				

The model structure used in the final orthogonal regressor least squares analysis based on the results above was:

$$C_A = C_{A_\alpha}\alpha + C_{A_V}\left({}^{\Delta V}/_{V_0}\right) + C_{A_q}\left({}^{q\bar{c}}/_{2V_0}\right) + C_{A_{\dot{\alpha}}}\left({}^{\dot{\alpha}\bar{c}}/_{2V_0}\right) \qquad \textbf{H-4}$$

The parameter estimation results are given in Table H-11. Minimum PSE values were reached before the addition of $\overset{\sqcup}{\alpha}$ and q for the 1-1-2-3 short period manoeuvres and before the addition of the $\overset{\sqcup}{\alpha}$ regressor for the first 3-2-1-1 manoeuvre hence they were removed from the respective model structures. Due to the selected removal and the inconsistent estimates obtained from the remaining manoeuvres, C_{A_q} and $C_{A_{\dot{\alpha}}}$ were dropped from the final model structure. The dependence of the axial force on angle of attack and velocity only was consistent with commonly used models as described in Roskam (1979) as long as a quasi-steady environment is maintained throughout the manoeuvre (i.e. oscillations are of relatively low frequency). As can be seen in Table H-11, the angle of attack derivative estimates were much higher than the a priori result. This was attributed to the absence of power effects in the wind tunnel data. Based on the t_0-statistic and the relative variances of each estimate for each manoeuvre, the most probable estimate of C_{A_α} was 0.4633 (1-1-2-3 Man.2) and C_{A_V} was 0.4903 (3-2-1-1 Man.1).

Table H-11 Final Least Squares Result for C_A

	3-2-1-1	3-2-1-1	1-1-2-3	1-1-2-3	A Priori
C_{A_α}	0.625	0.546	0.3809	0.4633	0.141
C_{A_V}	0.4903	0.2823	0.2455	0.3568	-
C_{A_q}	0.3022	-0.0555	-	-	-
$C_{A_{\dot{\alpha}}}$	-	-3.5458	-	-	-

Figure H-5 to Figure H-8 presents the model matching based on the parameters in Table H-11.

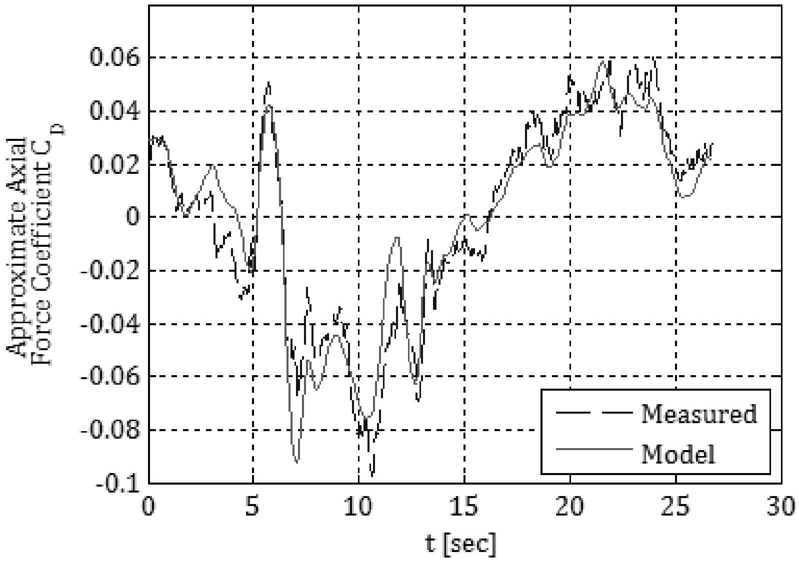

Figure H-5 Final Least Squares Result - C_A - (3-2-1-1 Man.1)

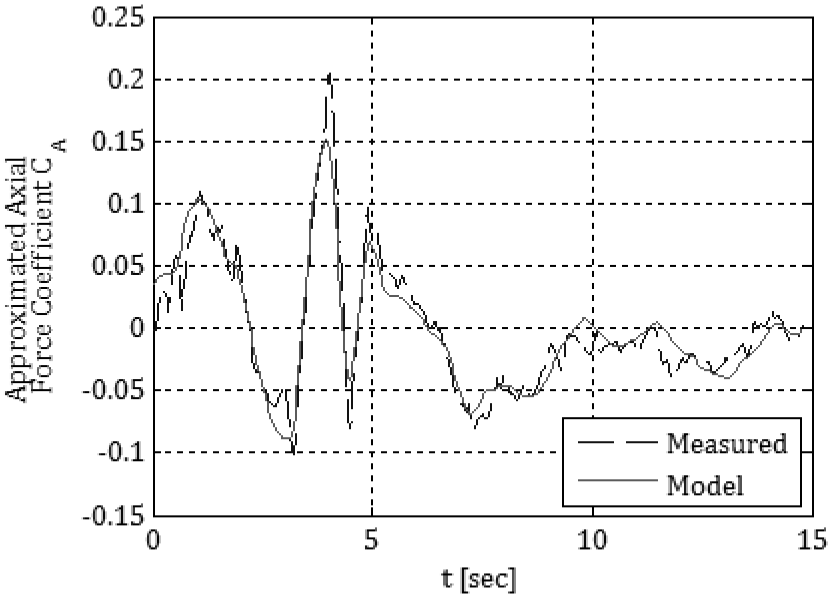

Figure H-6 Final Least Squares Result - C_A - (3-2-1-1 Man.2)

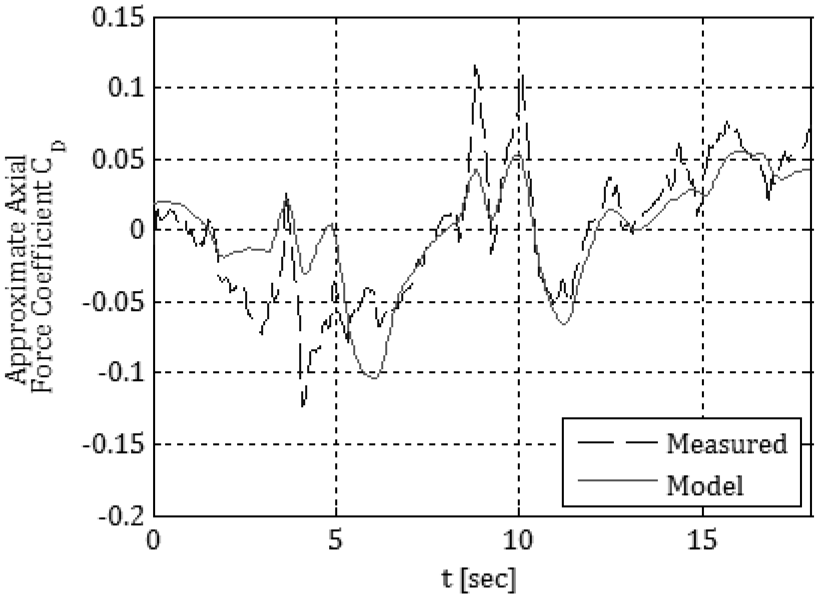

Figure H-7 Final Least Squares Result - C_A - (1-1-2-3 Man.1)

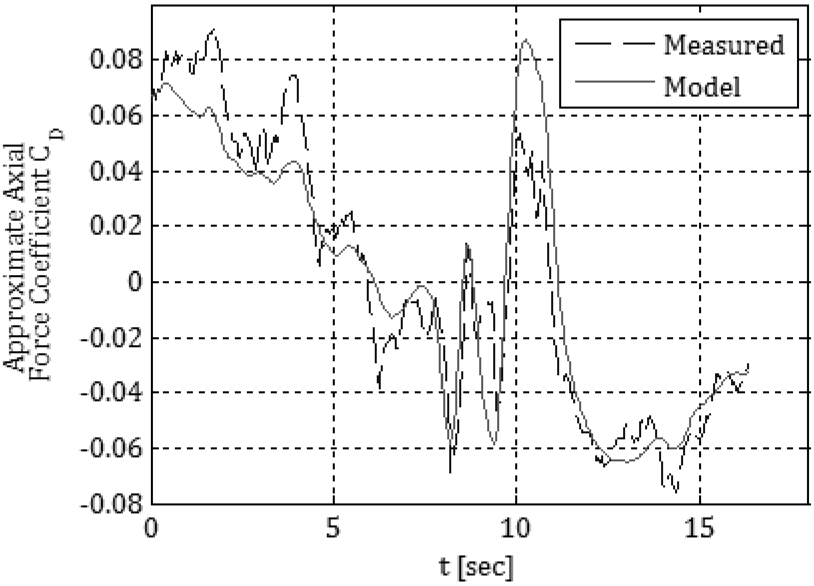

Figure H-8 Final Least Squares Result - C_A - (1-1-2-3 Man.2)

The inclusion of the thrust within the C_A model is evident in Figure H-5 to Figure H-8 where negative values were noted depicting a forward acceleration due to a thrust residual. The good matches between the measurements and the model outputs meant that the thrust inclusion assumption may have been valid for these particular short period manoeuvres.

Results from the lift force model structure are given in Table H-12 to Table H-15.

Table H-12 Stepwise Regression Results - C_L - (3-2-1-1 Man.1)

C_L – 3-2-1-1: ±4° Elevator Deflection – No Wind Tunnel Data					
Regressor	θ^*	σ	θ	t_0	$100(\sigma/_{\theta^*})$
$pb/2V_0$	0.0736	0.004108	0.9692	17.90383	5.581306
$q\bar{c}/2V_0$	1.1393	0.004935	163.9629	230.6987	0.433152
$\dot{\alpha}\bar{c}/2V_0$	-0.9505	0.004952	-161	191.7813	0.521011
* Standardised parameter					
R² [%]	98.883	$C_L = C_{L_0} + C_{L_p}\left({}^{pb}/_{2V_0}\right) + C_{L_q}\left({}^{q\bar{c}}/_{2V_0}\right) + C_{L_{\dot{\alpha}}}\left({}^{\dot{\alpha}\bar{c}}/_{2V_0}\right)$			
σ	0.0041				
Condition No.	3.5997				

Table H-13 Stepwise Regression Results - C_L - (3-2-1-1 Man.2)

C_L – 3-2-1-1: ±4° Elevator Deflection – No Wind Tunnel Data					
Regressor	θ^*	σ	θ	t_0	$100\left({}^{\sigma}/_{\theta^*}\right)$
$pb/2V_0$	-0.0897	0.003967	-1.836	22.54119	4.422555
$q\bar{c}/2V_0$	1.3138	0.005089	187.81	257.3494	0.387334
$\dot{\alpha}\bar{c}/2V_0$	-0.9838	0.005147	-193.866	190.5336	0.523169
* Standardised parameter					
R^2 [%]	99.7738	$C_L = C_{L_0} + C_{L_p}\left({}^{pb}/_{2V_0}\right) + C_{L_q}\left({}^{q\bar{c}}/_{2V_0}\right) + C_{L_{\dot{\alpha}}}\left({}^{\dot{\alpha}\bar{c}}/_{2V_0}\right)$			
σ	0.0038				
Condition No.	5.252				

Table H-14 Stepwise Regression Results - C_L - (1-1-2-3 Man.1)

C_L – 1-1-2-3: ±6° Elevator Deflection – No Wind Tunnel Data					
Regressor	θ^*	σ	θ	t_0	$100\left({}^{\sigma}/_{\theta^*}\right)$
$q\bar{c}/2V_0$	1.1316	0.010684	167.5072	105.7991	0.944127
$\dot{\alpha}\bar{c}/2V_0$	-0.8065	0.010684	-160.39	75.4064	1.324704
* Standardised parameter					
R^2 [%]	96.3158	$C_L = C_{L_0} + C_{L_q}\left({}^{q\bar{c}}/_{2V_0}\right) + C_{L_{\dot{\alpha}}}\left({}^{\dot{\alpha}\bar{c}}/_{2V_0}\right)$			
σ	0.0091				
Condition No.	3.2573				

Table H-15 Stepwise Regression Results - C_L - (1-1-2-3 Man.2)

C_L – 1-1-2-3: ±6° Elevator Deflection – No Wind Tunnel Data					
Regressor	θ^*	σ	θ	t_0	$100\left({}^{\sigma}/_{\theta^*}\right)$
α	0.0592	0.003886	0.2299	15.21549	6.564867
$\Delta V/V_0$	0.0595	0.003776	0.1583	15.7362	6.345938
$pb/2V_0$	0.1018	0.003711	2.2357	27.39967	3.645422
$q\bar{c}/2V_0$	1.0904	0.004653	179.8612	234.0409	0.426761
$\dot{\alpha}\bar{c}/2V_0$	-0.8044	0.004187	-181.147	191.8761	0.520538
* Standardised parameter					
R^2 [%]	99.5613	$C_L = C_{L_0} + C_{L_\alpha}\alpha + C_{L_V}\left({}^{\Delta V}/_{V_0}\right) + C_{L_p}(pb/2V_0) + C_{L_q}\left({}^{q\bar{c}}/_{2V_0}\right) + C_{L_{\dot{\alpha}}}\left({}^{\dot{\alpha}\bar{c}}/_{2V_0}\right)$			
σ	0.00329				
Condition No.	3.2573				

The excellent model matches were misleading because unrealistically high C_{L_q} and $C_{L_{\dot{\alpha}}}$ estimates were determined due to high levels of correlation between the parameters. Because of this high correlation, the model structure could not be optimised using the least squares regression technique. Therefore, the model structure was based on a conventional linear lift coefficient model, using the initial estimates from a priori data.

A similar effect was found upon analysis of the pitching moment. The linear dependence between the pitching moment and rate of change of angle of attack lead to poor estimates of the respective moment derivatives using the least squares approach. The poor plausibility of the estimates was contrary to the good coefficients of determination and low variances as seen in Table H-16 to Table H-19.

Table H-16 Stepwise Regression Results - C$_m$ - (3-2-1-1 Man.1)

C$_m$ – 3-2-1-1: ±4° Elevator Deflection – No Wind Tunnel Data					
Regressor	θ^*	σ	θ	t_0	$100\left({}^{\sigma}/_{\theta^*}\right)$
α	-0.1223	0.024626	-0.0732	4.964643	20.13548
$q\bar{c}/2V_0$	-0.4953	0.030173	-13.4653	16.402	6.091825
$\dot{\alpha}\bar{c}/2V_0$	0.5747	0.028096	18.3928	20.441	4.888834
δe	-0.5319	0.0251	-0.381	21.17537	4.71893
* Standardised parameter					
R^2 [%]	72.0179	$C_m = C_{m_0} + C_{m_\alpha}\alpha + C_{m_q}\left({}^{q\bar{c}}/_{2V_0}\right) + C_{L_{\dot{\alpha}}}\left({}^{\dot{\alpha}\bar{c}}/_{2V_0}\right) + C_{m_{\delta e}}\delta e$			
σ	0.0205				
Condition No.	7.398				

Table H-17 Stepwise Regression Results - C$_m$ - (3-2-1-1 Man.2)

C$_m$ – 3-2-1-1: ±4° Elevator Deflection – No Wind Tunnel Data					
Regressor	θ^*	σ	θ	t_0	$100\left({}^{\sigma}/_{\theta^*}\right)$
$pb/2V_0$	0.2172	0.023633	0.5943	9.179241	10.88059
$q\bar{c}/2V_0$	-0.7122	0.029545	-19.8571	24.07262	4.14846
$\dot{\alpha}\bar{c}/2V_0$	0.727	0.032902	27.1075	22.06684	4.525669
δe	-0.5786	0.027373	-0.5308	21.10694	4.730935
* Standardised parameter					
R^2 [%]	81.52858	$C_m = C_{m_0} + C_{m_p}(pb/2V_0) + C_{m_q}\left({}^{q\bar{c}}/_{2V_0}\right) + C_{L_{\dot{\alpha}}}\left({}^{\dot{\alpha}\bar{c}}/_{2V_0}\right) + C_{m_{\delta e}}\delta e$			
σ	0.022465				
Condition No.	6.8775				

Table H-18 Stepwise Regression Results - C_m - (1-1-2-3 Man.1)

C_m – 1-1-2-3: ±6° Elevator Deflection – No Wind Tunnel Data					
Regressor	θ^*	σ	θ	t_0	$100\left({}^{\sigma}/_{\theta^*}\right)$
$q\bar{c}/2V_0$	-0.5291	0.029773	-14.2948	17.75137	5.627058
$\dot{\alpha}\bar{c}/2V_0$	0.5275	0.031257	19.1444	16.85609	5.925428
δe	-0.6371	0.02898	-0.5054	21.95961	4.548773
* Standardised parameter					
R^2 [%]	72.5416	$C_m = C_{m_0} + C_{m_q}\left({}^{q\bar{c}}/_{2V_0}\right) + C_{L_{\dot{\alpha}}}\left({}^{\dot{\alpha}\bar{c}}/_{2V_0}\right) + C_{m_{\delta e}}\delta e$			
σ	0.02478				
Condition No.	4.3491				

Table H-19 Stepwise Regression Results - C_m - (1-1-2-3 Man.2)

C_m – 1-1-2-3: ±6° Elevator Deflection – No Wind Tunnel Data					
Regressor	θ^*	σ	θ	t_0	$100\left({}^{\sigma}/_{\theta^*}\right)$
$q\bar{c}/2V_0$	-0.5939	0.026666	-17.2189	22.24339	4.489966
$\dot{\alpha}\bar{c}/2V_0$	0.6664	0.028101	26.3786	23.68537	4.216764
δe	-0.5681	0.026292	-0.519	21.58175	4.628067
* Standardised parameter					
R^2 [%]	80.06625	$C_m = C_{m_0} + \left({}^{q\bar{c}}/_{2V_0}\right) + C_{L_{\dot{\alpha}}}\left({}^{\dot{\alpha}\bar{c}}/_{2V_0}\right) + C_{m_{\delta e}}\delta e$			
σ	0.02213				
Condition No.	4.449				

The final least squares results using orthogonal functions are given in Table H-20 as described above, large discrepancies were evident between the prior results and the estimated results. However, consistent results for the elevator control derivative were achieved for three of the manoeuvres. A difference between the prior control derivative and the estimated control derivative was expected since the wind tunnel data did not contain any power effects (i.e. propeller slipstream influences). However in the general case, the slipstream effect would tend to increase this particular derivative due to an increase in the effective velocity over the elevator. Therefore the plausibility of the control derivative being reduced due to slipstream effects was unlikely at these angles of attack. The erroneous control derivative could be attributed largely to the absence of the actual control deflection, instead using the commanded input.

Table H-20 Final Least Squares Result – C_m

	3-2-1-1	3-2-1-1	1-1-2-3	1-1-2-3	A Priori
C_{m_α}	-0.0732	-0.0798	-0.0899	-0.0579	-1.218
C_{m_q}	-13.4653	-16.1432	-11.4246	-15.6941	-17.421
$C_{m_{\dot{\alpha}}}$	18.3928	22.548	17.1652	25.3812	-1.687
$C_{m_{\delta e}}$	-0.381	-0.5305	-0.5026	-0.5144	-1.377

H.2 MAXIMUM LIKELIHOOD

Once the optimised model structure was established for the forces and moments, the output error method was utilised to estimate the preliminary aerodynamic parameters more accurately. As described in Sec. 4.4.5, the longitudinal and lateral output error analyses were separated. The lateral analyses will be presented first. Three different solution procedures were used. The first utilised the linearized equations of motion without the addition of wind tunnel data. The next solution was based on estimating all model parameters utilising the generic model structure with the non-linear equations of motion. The last solution was also based on the generic model structure and non-linear equations of motion but was limited to only estimating the dynamic coefficients.

All three methods for the lateral analyses led to convergent output error solutions. The aircraft state time histories are given for each method in Figure H-9 to Figure H-11. A comparison between the apriori model and the output error models was analysed via the validation criteria i.e. Goodness of fit parameters and Theil's inequality coefficients. These results were given and discussed in Figure 4-30.

The parameters were then analysed in terms of parameter plausibility checks and residual checks. The plausibility of each parameter was based on comparing the estimated coefficients with force and moment derivatives obtained from the static wind tunnel tests and three other conventional configuration inherently stable aircraft documented in Roskam (1979). This comparison is given in Table H-21. For the static derivatives, a greater weighting was given to the wind tunnel data since it was aircraft specific and the lack of power effects was expected to have minimal impact on the actual values for the lateral case.

The aerodynamic coefficient estimates that differed significantly in magnitude or had a different sign to that of the secondary aircraft data (see Table H-21) were C_{Y_p},$C_{Y_{\delta a}}$,$C_{Y_{\delta a}}$,C_{n_p} and $C_{n_{\delta a}}$. The reason for the poor estimates of C_{Y_p} and $C_{Y_{\delta a}}$ was attributed to the strong correlation between these parameters, also evident in the least squares analysis. $C_{l_{\delta a}}$ and $C_{n_{\delta a}}$ had a plausible magnitude but a different sign to the aircraft from Roskam (1979). This was attributed to a different sign convention for aileron deflections used in Roskam (1979). $C_{n_p}$and $C_{n_{\delta a}}$ as described in the least squares analysis is a weak parameter that has little influence on the dynamics of the aircraft. This is evident by the small values of the secondary aircraft C_{n_p} coefficients. Thus, with the exception of C_{Y_p} and $C_{Y_{\delta a}}$ the estimates obtained from the output error methods were plausible.

Table H-21 Lateral Model Estimates - Plausibility Check

Parameter	Estimate	Apriori	Aircraft 1	Aircraft 2	Aircraft 3
C_{Y_α}	0.0329	-	-	-	-
C_{Y_β}	-0.5222	-0.5820	-0.3100	-0.5900	-0.7300
C_{Y_p}	0.6013	-0.0060	-0.0370	-0.1900	0.0000
$C_{Y_{\delta a}}$	0.3517	-0.0450	0.0000	0.0000	0.0000
$C_{Y_{\delta r}}$	0.1875	0.2100	0.1870	0.1440	0.1400
C_{Y_r}	-	0.0800	0.2100	0.3900	0.4000
C_{l_β}	-0.0266	-0.0830	-0.0890	-0.1300	-0.1000
C_{l_p}	-0.3631	-0.1130	-0.4700	-0.5000	-0.4500
$C_{l_{\dot{\beta}}}$	-0.0162	-	-	-	-
$C_{l_{\delta a}}$	-0.1394	-0.1720	0.1780	0.1560	0.1780
C_{l_r}	0.0519	0.0330	0.0960	0.1400	0.1400
$C_{l_{\delta r}}$	-	0.0200	0.0147	0.0106	0.0210
C_{n_β}	0.0663	0.0970	0.0650	0.0800	0.1240
C_{n_p}	0.0019	0.0200	-0.0300	0.0190	-0.0220
C_{n_r}	-0.2092	-0.0850	-0.0990	-0.1970	-0.2000
$C_{n_{\dot{\beta}}}$	-0.0873	-	-	-	-
$C_{n_{\delta a}}$	0.0249	0.0100	-0.0530	-0.0012	-0.2000
$C_{n_{\delta r}}$	-0.0552	-0.0650	-0.0657	-0.0758	-0.0740

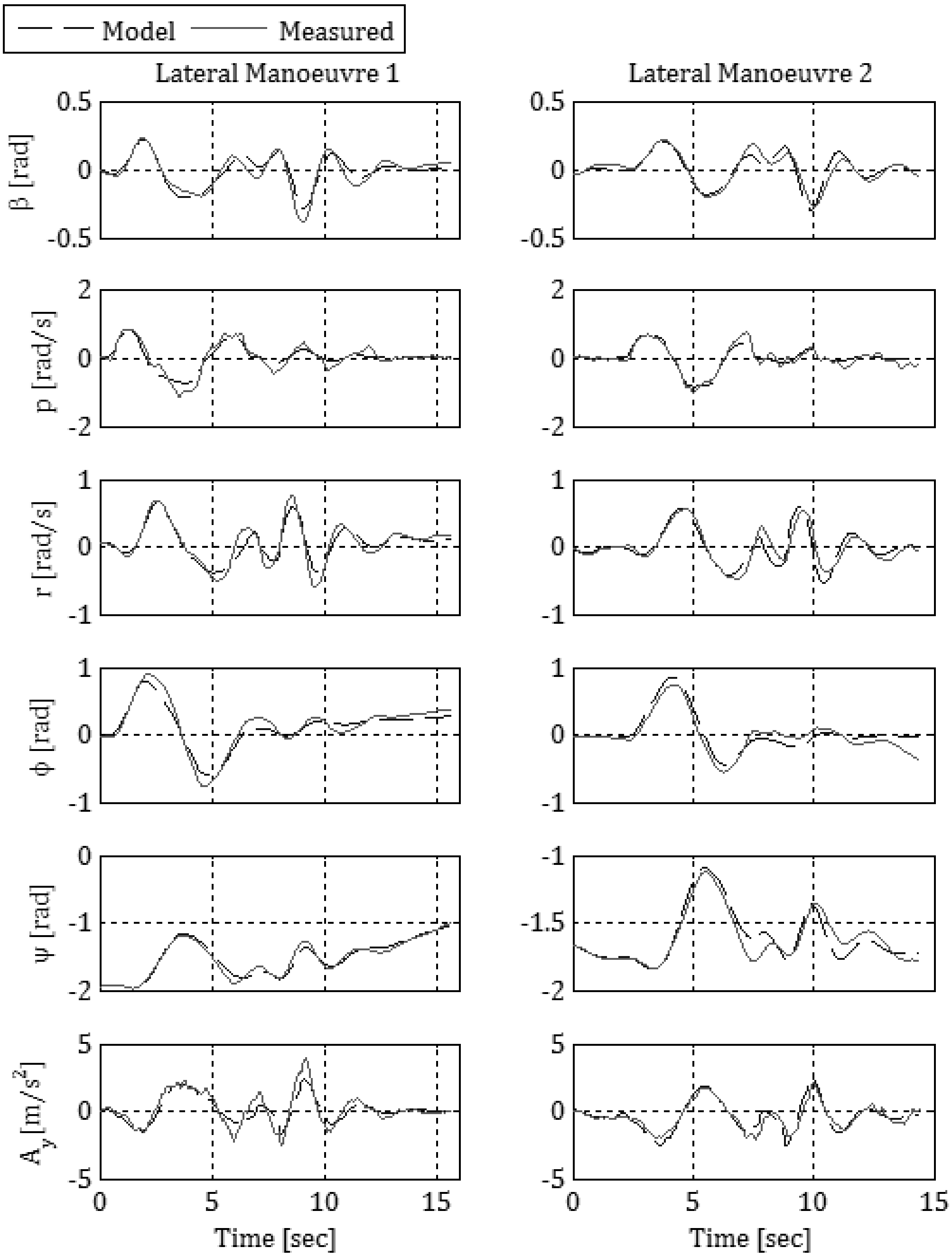

Figure H-9 Output Error Results – Aircraft Lateral Analysis – Linearized Equations of Motion

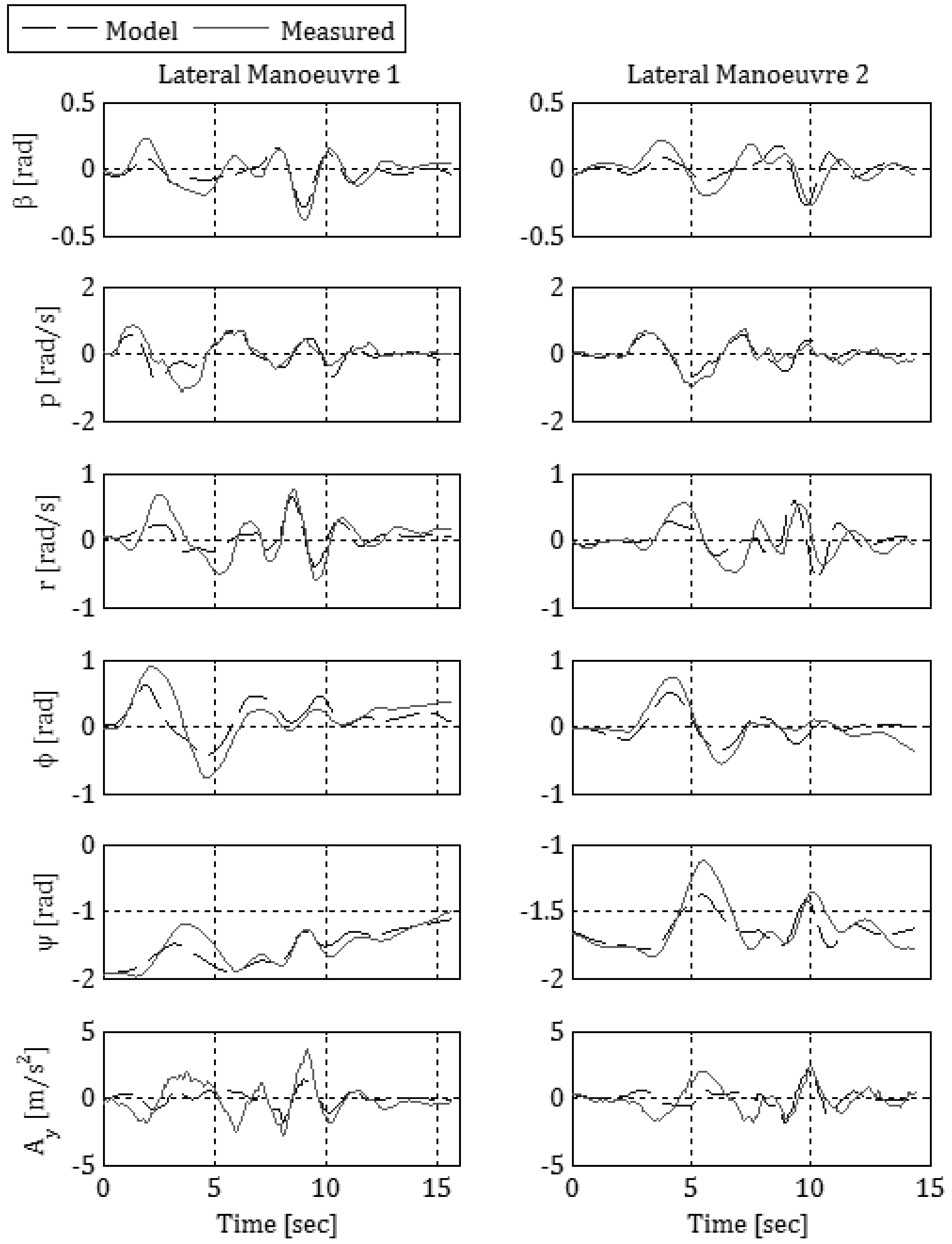

Figure H-10 Output Error Results – Aircraft Lateral Analysis – Non-linear Equations of Motion, Wind Tunnel Data and Estimation of all Parameters

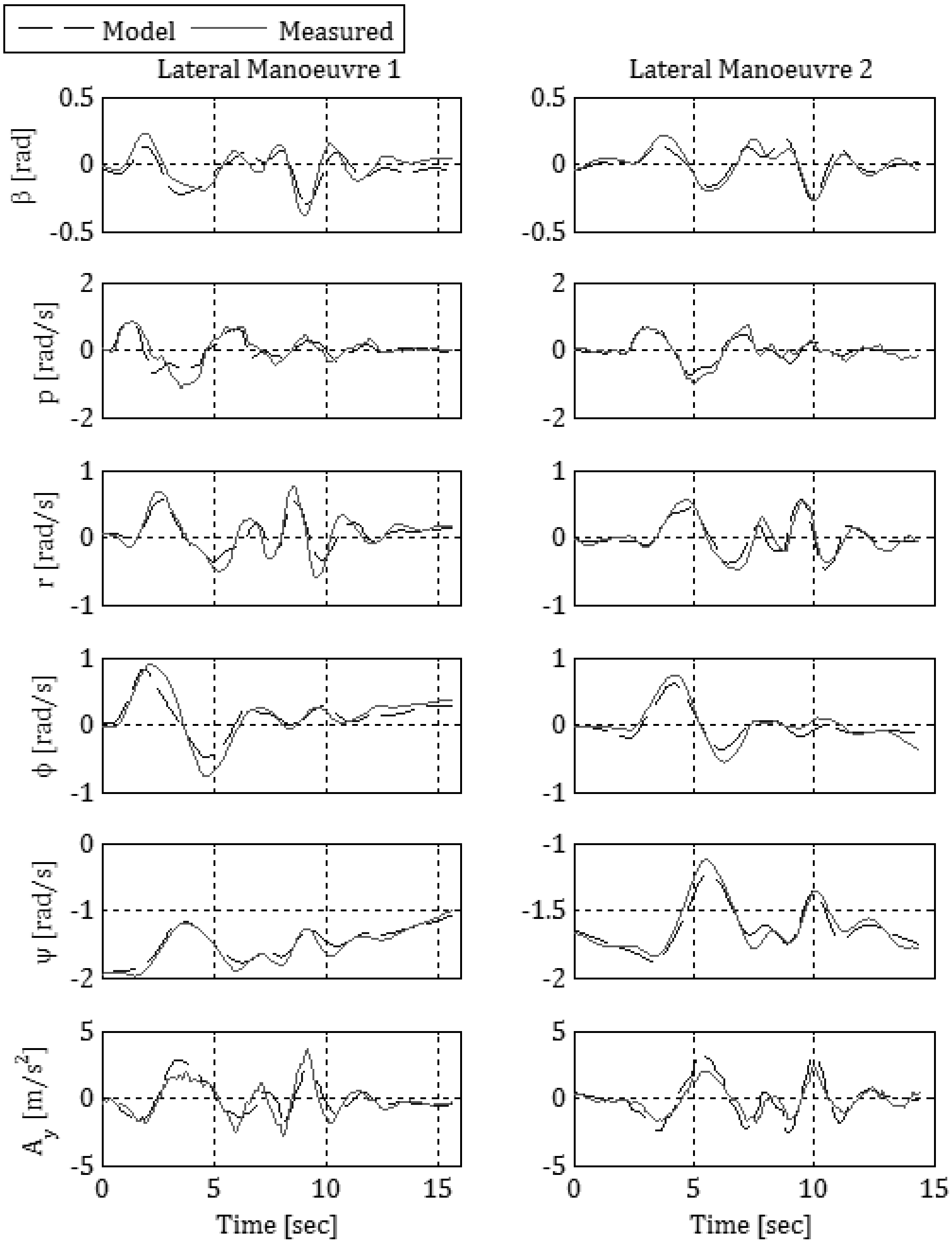

Figure H-11 Output Error Results – Aircraft Lateral Analysis – Non-linear Equations of Motion, Wind Tunnel Data and Estimation of Only Dynamic Parameters

Poor residuals are also evident in Figure H-12. These residuals alluded to systematic errors within the estimated model and thus further iterations of the parameter identification procedure are necessary to obtain approximately white residuals. The Cramer-Rao bounds were also corrected for these coloured residuals via autocorrelation correction factors.

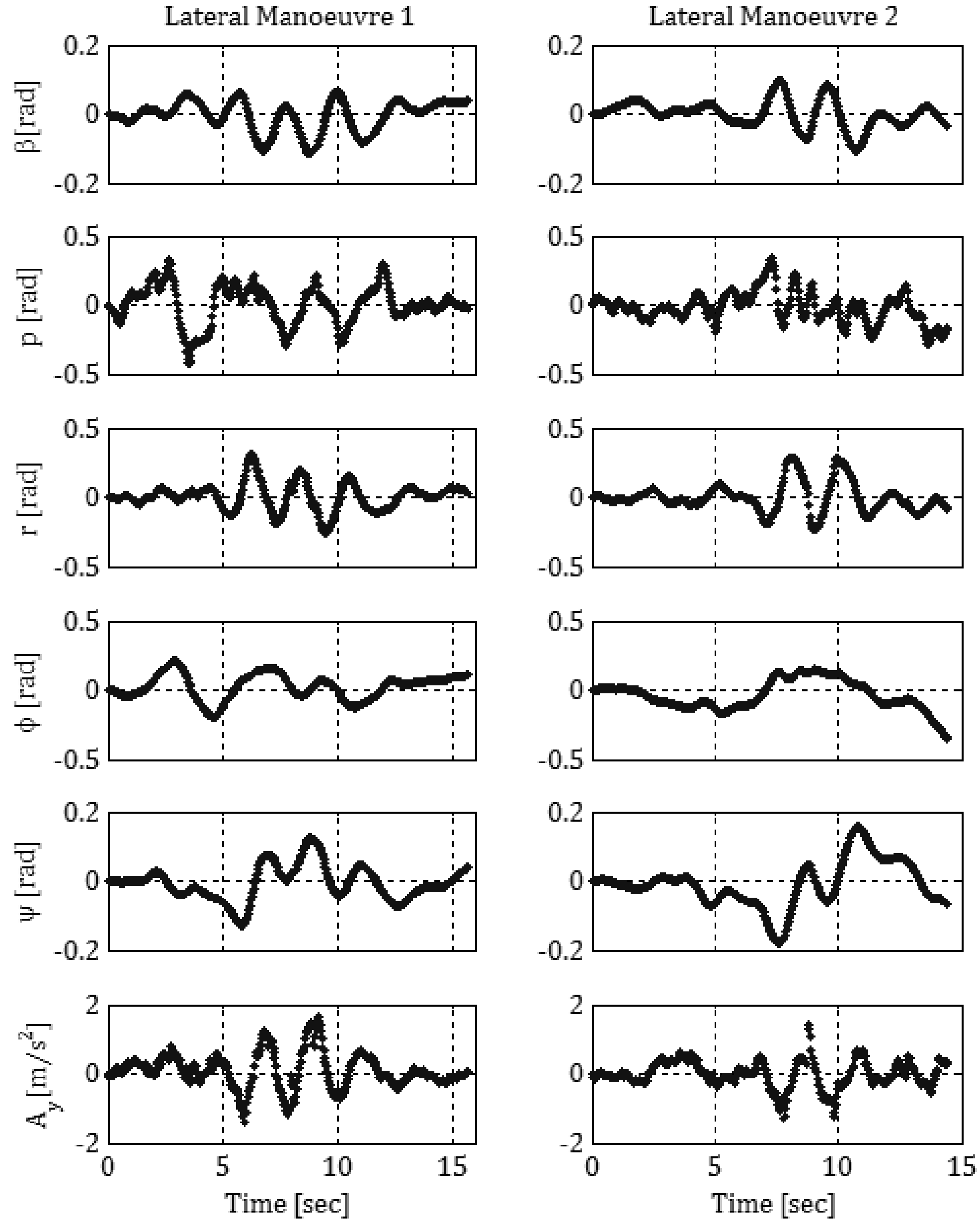

Figure H-12 Output Error Residual Results – Aircraft Lateral Analysis – Linearized Equations of Motion

The longitudinal model estimates were then estimated. The two datasets with the least lateral influence were chosen for the analysis. These consisted of the two 3-2-1-1 manoeuvres. A similar procedure to that of the lateral estimates was implemented where the output error estimation solutions were based on a single run using linearized longitudinal equations without wind tunnel data followed by two solutions using the non-linear longitudinal equations of motion and the wind tunnel data.

Due to the near linear relationship between the pitch rate and rate of change in angle of attack aircraft states the linear solution diverged. The pitch damping parameters were then removed from the estimation parameter vector thus keeping the damping derivatives constant.

As described, the next solution made use of the wind tunnel data and non-linear equations of motion estimating all the model parameters. The result yielded plausible parameter estimates but poor aircraft state matches as seen in Figure H-14. Finally, the static wind tunnel bias parameters were removed from the parameter vector of the second solution (i.e. only dynamic parameters were estimated) and a new solution was derived. The result is given in Figure H-15. Due to the poor results obtained from the non-linear solutions, the parameter set deemed the most probable was that derived from the linearized equations of motion using the apriori pitch damping derivatives. The results obtained from this solution process are given in Table H-22, whilst the residuals are given in Figure H-16.

The poor overall results meant that further analysis needed to be carried out with emphasis placed on decoupling the longitudinal damping derivatives possibly via non-linear force and moment models as discussed in Jategaonkar (2006).

Table H-22 Output Error Results - Longitudinal, Linearized, Decoupled Dynamics

Parameter	Initial	Final Analysis	Corrected σ	$100\times\left(\frac{\sigma}{\theta}\right)$
C_{L_α}	4.987	4.344	4.15E-01	9.563
C_{L_V}	0	0.7783	1.15E-01	14.752
C_{L_p}	0	1.7282	7.37E-01	42.630
C_{L_q}	4.639	-	-	-
$C_{L_{\dot\alpha}}$	1.372	-	-	-
C_{m_α}	-1.218	-0.357	4.87E-02	13.645
C_{m_q}	-17.421	-	-	-
$C_{m_{\dot\alpha}}$	-1.687	-	-	-
$C_{m_{\delta e}}$	-1.377	-0.9773	3.09E-02	3.164
τ	0	-	-	-

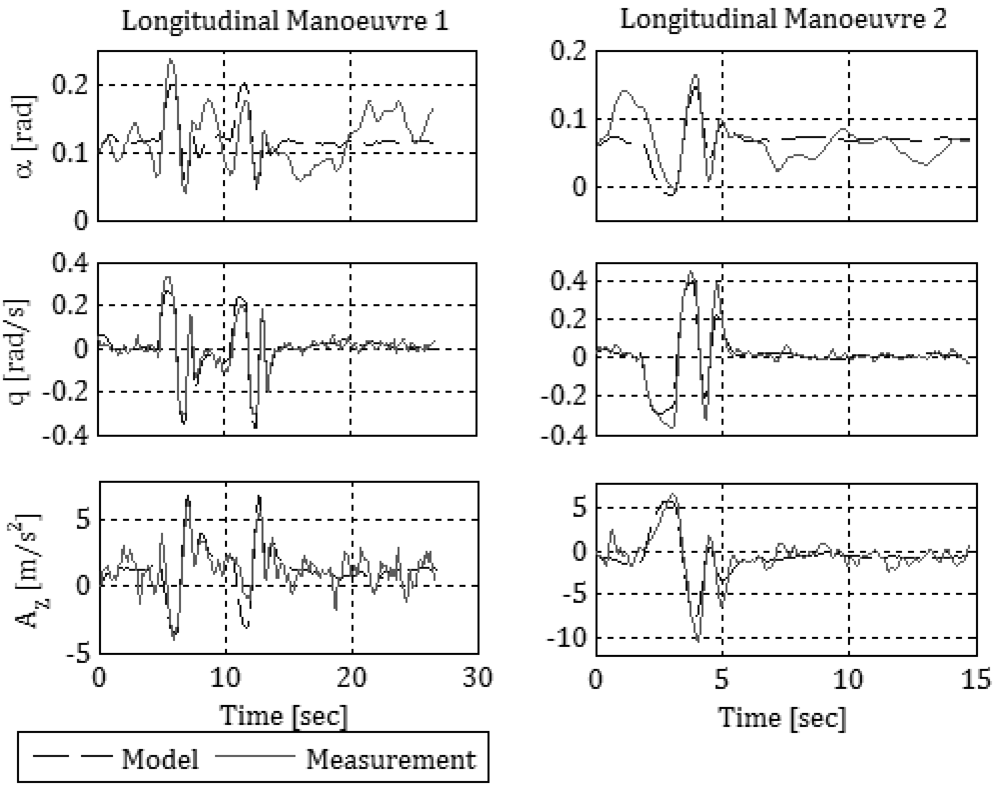

Figure H-13 Output Error Results - Longitudinal Analysis – Linearized Equations of Motion

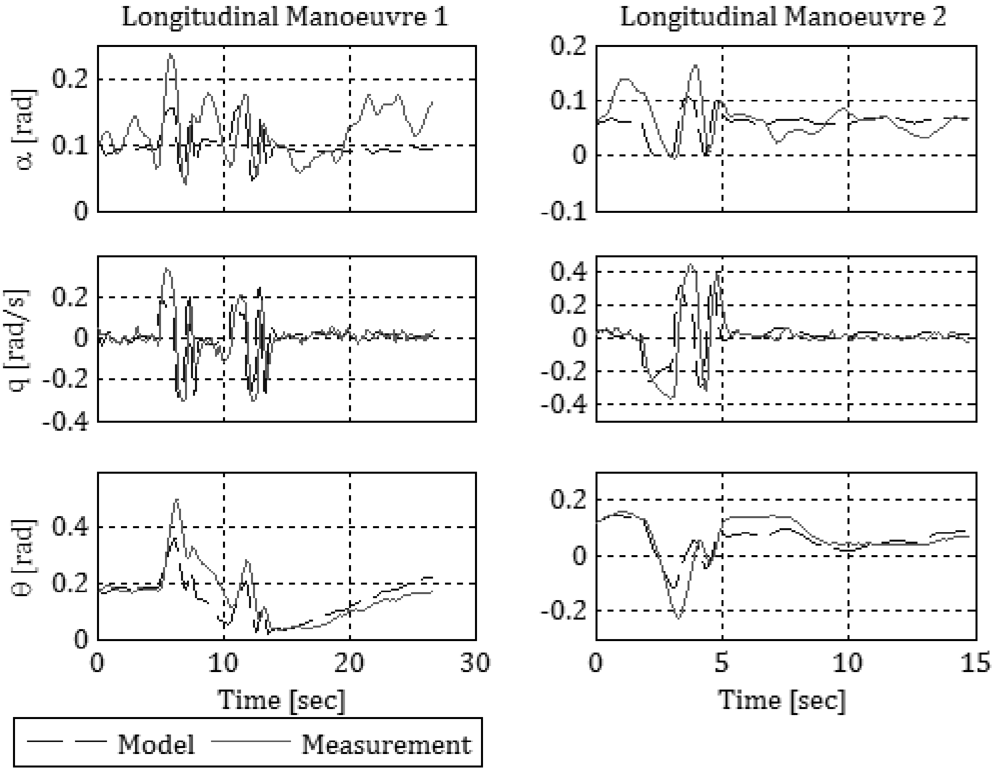

Figure H-14 Output Error - Longitudinal Analysis – Non-linear EOM, All parameters

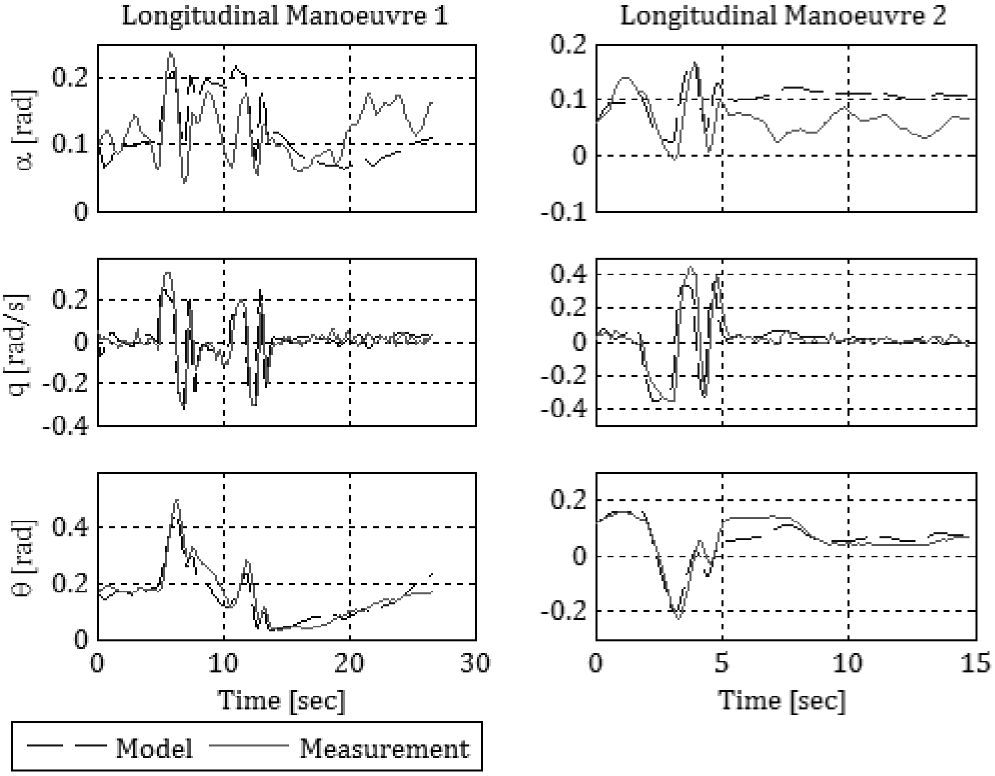

Figure H-15 Output Error - Longitudinal Analysis – Non-linear EOM, only dynamic parameters

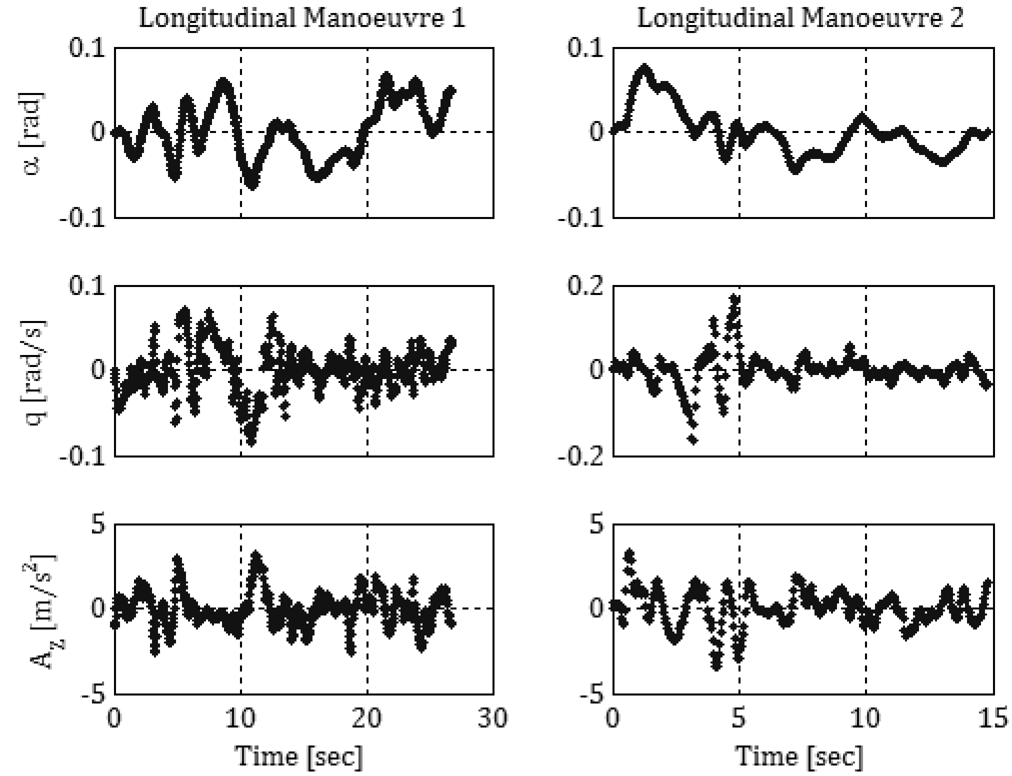

Figure H-16 Output Error Residual Results - Aircraft Longitudinal Analysis – Linear Dynamics

The final output error analysis dealt with the estimation of the approximate axial force derivatives. As was noted in the least squares analysis, the axial force coefficient included the thrust force. A single output error simulation was carried out yielding a good model match for the velocity and low variances for the force coefficients. The non-linear velocity equation was used in conjunction with and measured data when other states were required. A comparison between the measured velocity and that obtained via the output error analysis is given in Figure H-17 for the two 3-2-1-1 manoeuvres. The resulting residuals were coloured and are presented in Figure H-18. As with the previous output error results, the Cramer-Rao bounds were corrected for this colouring via an autocorrelation correction factor. The Theil's inequality coefficients were also determined for the velocity matches and are provided in Table H-23. Excellent results are evident with the Theil's inequality coefficients well below a common threshold of 0.3 and Theil's variance proportion coefficients below 0.1. The estimated standard deviations for the velocity are also low, thus describing a good model fit. The plausibility of the estimates through comparison with common values was not possible because the thrust force was incorporated into the model.

Table H-23 Output Error Results – Axial Force, Non-linear Dynamics

Parameter	Initial	Final Analysis	Corrected σ	$100\times\left(\frac{\sigma}{\theta}\right)$
C_{A_α}	0.577	0.722	7.60E-02	10.520
C_{A_V}	0.3652	0.5252	1.46E-02	2.771

Table H-24 Axial Force Model Residual Analyses

Manoeuvre	Parameter	σ	Theil's Inequality	Theil's Variance Proportion	Theil's Covariance Proportion
1	Velocity	0.223903	0.005917	0.029937	0.970063
2	Velocity	0.159527	0.003594	0.009219	0.989886

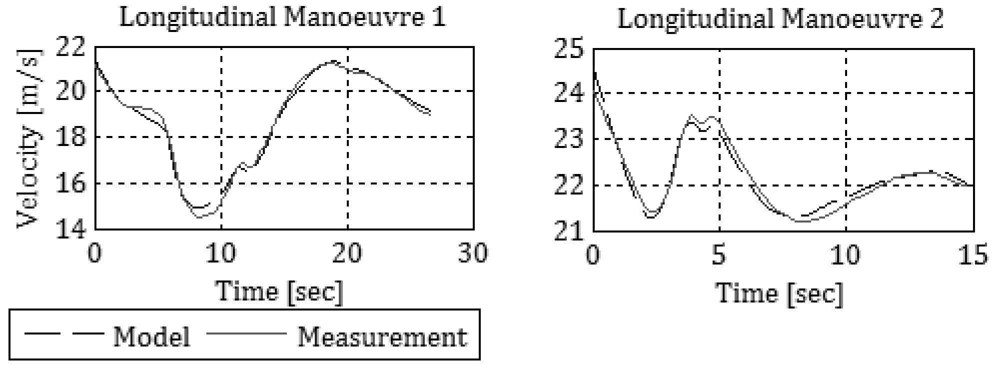

Figure H-17 Output Error Results – Axial Force Analysis

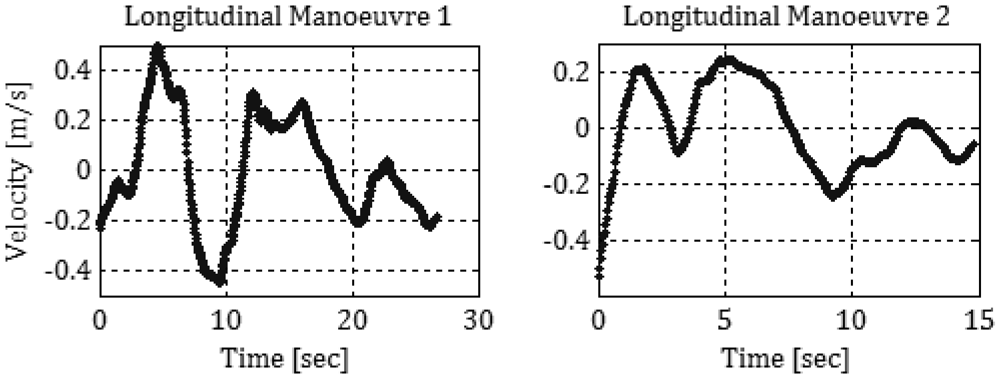

Figure H-18 Output Error Residual Results – Axial Force Analysis